Hadronic Correlation Functions with Quark-disconnected Contributions in Lattice QCD

Dissertation

zur Erlangung des Grades

„Doktor

der Naturwissenschaften“

am Fachbereich Physik, Mathematik, Informatik

der JOHANNES GUTENBERG-UNIVERSITÄT
in Mainz

VERA MAGDALENA GÜLPERS

geboren in Wiesbaden

Mainz, den 4. März 2015

Vera Magdalena Gülpers: *Hadronic Correlation Functions with Quark-disconnected Contributions in Lattice QCD*, Mainz **D77**

BERICHTERSTATTER:

TAG DER MÜNDLICHEN PRÜFUNG:

14. September 2015

ABSTRACT

One of the fundamental interactions in the Standard Model of particle physics is the strong force, which can be formulated as a non-abelian gauge theory called Quantum Chromodynamics (QCD). In the low-energy regime, where the QCD coupling becomes strong and quarks and gluons are confined to hadrons, a perturbative expansion in the coupling constant is not possible. However, the introduction of a four-dimensional Euclidean space-time lattice allows for an *ab initio* treatment of QCD and provides a powerful tool to study the low-energy dynamics of hadrons. Some hadronic matrix elements of interest receive contributions from diagrams including quark-disconnected loops, i.e. disconnected quark lines from one lattice point back to the same point. The calculation of such quark loops is computationally very demanding, because it requires knowledge of the all-to-all propagator. In this thesis we use stochastic sources and a hopping parameter expansion to estimate such propagators. We apply this technique to study two problems which relay crucially on the calculation of quark-disconnected diagrams, namely the scalar form factor of the pion and the hadronic vacuum polarization contribution to the anomalous magnet moment of the muon.

The scalar form factor of the pion describes the coupling of a charged pion to a scalar particle. We calculate the connected and the disconnected contribution to the scalar form factor for three different momentum transfers. The scalar radius of the pion is extracted from the momentum dependence of the form factor. The use of several different pion masses and lattice spacings allows for an extrapolation to the physical point. The chiral extrapolation is done using chiral perturbation theory (χPT). We find that our pion mass dependence of the scalar radius is consistent with χPT at next-to-leading order. Additionally, we are able to extract the low energy constant $\bar{\ell}_4$ from the extrapolation, and our result is in agreement with results from other lattice determinations. Furthermore, our result for the scalar pion radius at the physical point is consistent with a value that was extracted from $\pi\pi$-scattering data.

The hadronic vacuum polarization (HVP) is the leading-order hadronic contribution to the anomalous magnetic moment a_μ of the muon. The HVP can be estimated from the correlation of two vector currents in the time-momentum representation. We explicitly calculate the corresponding disconnected contribution to the vector correlator. We find that the disconnected contribution is consistent with zero within its statistical errors. This result can be converted into an upper limit for the maximum contribution of the disconnected diagram to a_μ by using the expected time-dependence of the correlator and comparing it to the corresponding connected contribution. We find the disconnected contribution to be smaller than $\approx 5\%$ of the connected one. This value can be used as an estimate for a systematic error that arises from neglecting the disconnected contribution.

ZUSAMMENFASSUNG

Die starke Kraft ist eine der fundamentalen Wechselwirkungen im Standardmodell der Teilchenphysik. Sie kann als nicht-abelsche Eichtheorie – die Quantenchromodynamik – formuliert werden. Im Niederenergiebereich, in dem die QCD Kopplung groß wird und Quarks und Gluonen in Hadronen gebunden sind, ist es nicht möglich die QCD in einer Störungsreihe in der Kopplungskonstanten zu entwickeln. Die Formulierung der QCD auf einem vierdimensionalen Raum-Zeit Gitter erlaubt eine theoretische Beschreibung der starken Wechselwirkung und ermöglicht es, die Dynamik der Hadronen im Niederenergiebereich zu studieren. Einige hadronische Matrixelemente enthalten Beiträge von Diagrammen mit quark-unverbundenen Schleifen, d.h. Quarklinien von einem Gitterpunkt zurück zum selben Gitterpunkt. Die Berechnung solcher Quarkschleifen ist sehr aufwendig, da man hierfür den Propagator von jedem Gitterpunkt zu allen Gitterpunkten (*all-to-all propagator*) benötigt. In der vorliegenden Arbeit benutzen wir stochastische Quellen und eine Hopping Parameter-Entwicklung um solche Propagatoren abzuschätzen. Diese Methode wird verwendet, um zwei Probleme zu erfoschen, die wesentlich von der Berechnung unverbundener Beiträge abhängen, nämlich der skalare Formfaktor des Pions und der Beitrag der hadronische Vakuumpolarisation zum anomalen magnetischen Moment des Myons.

Der skalare Formfaktor des Pions beschreibt die Kopplung eines geladenen Pions an ein skalares Teilchen. Wir berechnen den verbundenen und den unverbundenen Beitrag zum skalaren Formfaktor für drei verschiedene Impulsüberträge. Aus der Impulsabhängigkeit des Formfaktors kann der skalare Radius des Pions bestimmt werden. Da wir verschiedene Pionmassen und Gitterabstände verwenden, können wir unsere Ergebnisse zum physikalischen Punkt extrapolieren. Für die chirale Extrapolation verwenden wir chirale Störungstheorie (χPT). Unsere Werte sind konsistent mit χPT zur *next-to-leading* Ordung. Zusätzlich können wir aus der Extrapolation die Niederenergiekonstante $\bar{\ell}_4$ bestimmen. Unser Ergebnis ist konsistent mit Resultaten anderer Gitterrechnungen. Das entsprechende Resultat für den skalaren Pionradius am physikalischen Punkt stimmt mit einem Wert überein, der aus $\pi\pi$-Streuung bestimmt wurde.

Die hadronische Vakuumpolarisation (HVP) ist der führende hadronische Beitrag zum anomalen magnetischen Moment a_μ des Myons. Die HVP kann aus der Korrelation zweier Vektorströme bestimmt werden. Wir berechnen explizit den unverbundenen Anteil des Vektorkorrelators. Wir erhalten einen unverbundene Beitrag, der innerhalb der statistischen Fehler mit null verträglich ist. Daraus lässt sich eine obere Schranke für den maximalen Beitrag des unverbundenen Diagramms zu a_μ ermitteln, indem wir die erwartete Zeitabhängigkeit des Korrelators verwenden und ihn mit dem entsprechenden verbundenen Anteil vergleichen. Der unverbundene Beitrag ist kleiner als $\approx 5\%$ des verbundenen Anteils. Dieser Wert kann als systematischer Fehler verwendet werden, der aus der Vernachlässigung des unverbundenen Diagramms resultiert.

PUBLICATIONS

Parts of the results presented in this thesis have already been published in

[1] V. Gülpers, G. von Hippel and H. Wittig, *The scalar Pion form factor with Wilson Fermions*, PoS **LAT2012**, (2012) 181

[2] V. Gülpers, G. von Hippel and H. Wittig, *The scalar radius of the pion in two-flavor Wilson lattice QCD* , PoS **LAT2013**, (2013) 283

[3] V. Gülpers, G. von Hippel and H. Wittig, *The scalar pion form factor in two-flavor lattice QCD* , Phys.Rev. **D89**, (2014) 094503

[4] A. Francis, V. Gülpers, G. Herdoíza, H. Horch, B. Jäger, H. Meyer and H. Wittig, *The leading hadronic contribution to (g-2) of the muon: The chiral behavior using the mixed representation method*, PoS **LAT2014**, (2014) 127

[5] A. Francis, V. Gülpers, B. Jäger, H. Meyer, G. von Hippel and H. Wittig, *The leading disconnected contribution to the anomalous magnetic moment of the muon*, PoS **LAT2014**, (2014) 128

[6] A. Francis, V. Gülpers, G. Herdoíza, G. von Hippel, H. Horch, B. Jäger, H. Meyer, E. Shintani and H. Wittig, *Lattice QCD Studies of the Leading Order Hadronic Contribution to the Muon g-2*, (2014), [arXiv:1411.3031]

CONTENTS

INTRODUCTION

The recent discovery of the Higgs boson [7, 8] at the Large Hadron Collider (LHC) at CERN was a big success for the Standard Model of particle physics. Nearly 50 years after the prediction of such a boson by Higgs [9], Brout and Englert [10], and Guralnik, Hagen and Kibble [11], the existence of the last missing particle of the Standard Model was experimentally confirmed. In 2013 Higgs and Englert received the Nobel prize in physics for the prediction of the Higgs boson.
The Standard Model of particle physics contains all the known elementary particles and the three fundamental forces, the electromagnetic, the weak and the strong interaction. In 1979 Glashow, Salam and Weinberg received the Nobel prize for the unification of the electromagnetic and the weak interaction to the electroweak force [12–14]. The fundamental interactions in the Standard Model can be described as gauge theories. On the side of the elementary particles the Standard Model contains the leptons and quarks which are the building blocks of matter, the gauge bosons that mediate the fundamental interactions, and the Higgs, which is related to the generation of the masses of the fundamental particles.

For the search for physics beyond the Standard Model (BSM) there are two possible approaches. One is the search for new particles, such as supersymmetric partners for the Standard Model particles, at high energies as done at the LHC; the other approach is the search for signatures of BSM physics at low energies. The latter requires high-precision tests to resolve possible deviations of experimental results from the corresponding Standard Model predictions.

In this thesis we will concentrate on the strong interaction, whose quantum field theory is called Quantum Chromodynamics (QCD). The QCD Lagrangian is invariant under local gauge transformations and the corresponding gauge bosons are the gluons. Gluons couple to particles that carry color, the charge of the strong interaction. Besides the quarks, gluons also carry color and thus gluon self-interactions are possible. The strong coupling constant α_s depends on the energy regime where the interaction takes place. For large energies the coupling is small, and quarks and gluons become asymptotically free. In 2004 Gross and Wilczek received the Nobel prize for the discovery of the asymptotic freedom [15]. For small energies the strong coupling is large, and quarks and gluons are bound into hadrons. This is called confinement. So far it has not been possible to isolate a single quark in an experiment. Clearly, the structure of hadrons has to be determined in the low-energy regime. However, due to the large coupling constant a perturbative expansion in α_s is not possible in this regime.

In 1974 Wilson proposed to formulate QCD on a discretized space-time lattice [16], which allows for a non-perturbative treatment of QCD in the low-

energy regime. Nowadays with growing computer power, lattice QCD (LQCD) has become a powerful tool for calculating observables concerning the strong interaction at low energies from first principles. This allows for a determination of hadron masses or hadron structure quantities such as form factors.
At the level of the quarks, many quantities of interest include diagrams where not all vertices are connected with each other by quark lines. Such quantities are called quark-disconnected. These diagrams are not disconnected in the quantum field theoretical sense, since they are still connected by gluons. However, such quark-disconnected diagrams are computationally more demanding, since they require calculating the quark propagator from every lattice point to every other lattice point – the all-to-all propagator. The Dirac operator on the lattice is a large matrix with a rank of $\mathcal{O}(10^8)$ to $\mathcal{O}(10^9)$ for a typical lattice calculation. Obviously, an exact inversion of such a large matrix is not feasible even with modern supercomputers. Thus, one has to resort to stochastic methods for the calculation of the required all-to-all propagators.

In this thesis we will concentrate on two observables that include a quark-disconnected contribution, the scalar form factor of the pion, and the hadronic vacuum polarization.
The scalar form factor of the pion describes the coupling of a charged pion to a scalar particle, such as the Higgs boson. However, a Higgs with a mass of $m_H \approx 125$ GeV is far too heavy to affect the low-energy regime of QCD. Thus, there is no experimental data available for the scalar pion form factor. So far only one lattice calculation of the total form factor including the disconnected diagram has been performed by the JLQCD/TWQCD collaboration [17–19]. However, the lattices that have been used are rather small and have only 32×16^3 lattice points. Thus, an independent calculation of the scalar pion form factor on bigger lattices is desirable. We will explicitly calculate the quark-connected and the quark-disconnected contribution to the scalar form factor. The required disconnected quark loop is estimated using stochastic sources and a generalized hopping parameter expansion [20]. From the Q^2-dependence of the form factor it is possible to determine the scalar radius of the pion, which is given by the slope of the form factor at vanishing momentum transfer. In partially quenched chiral perturbation theory it was estimated that the disconnected contribution to the scalar radius is of the same order as the connected one [21, 22]. Thus, it would be interesting to check this in an explicit lattice calculation.
Although the scalar form factor and thus the scalar radius cannot be measured directly in an experiment, the scalar radius can be related to $\pi\pi$-scattering amplitudes [23–26] and the most recent value from [27] can be compared with our results. Since the lattices that are used for our calculations have unphysically large pion masses, we have to extrapolate our results to the physical point. This can be done with the help of chiral perturbation theory. At next-to-leading order the scalar radius of the pion depends only on one low-energy constant $\bar{\ell}_4$ [23, 28], which can be determined from the extrapolation. Additionally, we have to perform a continuum limit to reach the physical point, and thus we use lattices with three different lattice spacings a to be able to extrapolate to $a = 0$.

The anomalous magnetic moment of the muon a_μ is one of the most precisely measured quantities in physics and can therefore serve as a precision check of the Standard Model of particle physics. On the theory side, a_μ receives the largest error from the hadronic contribution, whose leading order is determined by the hadronic vacuum polarization (HVP). Currently, the best estimate of the HVP has been obtained by a semi-phenomenological approach from the cross section of $e^+ e^- \to$ hadrons using the optical theorem. However, a calculation from first principles without relying on experimental data would be preferable. The two-point function that determines the HVP receives a quark-disconnected contribution besides the connected one. However, the disconnected contribution is generally neglected in lattice calculations of the hadronic vacuum polarization. In partially quenched chiral perturbation theory it was estimated that the disconnected contribution could be of order -10% of the connected one [29, 30]. To be compatible with the determination of the HVP from the cross section approach, one requires a precision of 1% and thus the disconnected contribution may no longer be negligible. In this thesis the mixed representation method [31–33] will be used, where the HVP is determined from the vector correlator in a mixed time-momentum representation. We will explicitly calculate the disconnected contribution to the vector correlator for light and strange quarks. Comparing our result with the corresponding connected contribution and using the expected behavior of the disconnected correlator for infinite times, we will be able to quote an upper limit for the maximum disconnected contribution to the anomalous magnetic moment of the muon.

Part I

THEORETICAL BACKGROUND

1

QCD IN THE CONTINUUM

Quantum Chromodynamics (QCD) is the established theory describing the strong interaction, one of the three fundamental forces included in the Standard Model of particle physics. The strong force is mediated by gluons, which couple to particles that carry color charge. Three different colors are possible, which are conventionally called red, green and blue. Every quark carries one of these colors. The Standard Model includes six different quark flavors, which are listed in table 1.1. Quarks are bound to "colorless" states, which are called hadrons. So far it has not been possible to isolate a single quark in an experiment. Two different kinds of hadrons are known, meson which consist of a quark and an anti-quark of the corresponding anti-color, and baryons which consist of three quarks (green, red and blue). Further colorless bound quark states with more quarks are possible within QCD, such as tetraquarks ($\overline{q}\overline{q}qq$) or pentaquarks ($qqqq\overline{q}$), however, such states have so far not been established experimentally. Additionally, gluons carry a color and an anti-color, and bound states of gluons, i.e. glueballs, may exist in nature.

	flavor	charge $[e]$	mass $[MeV]$
1st generation	u	$2/3$	$2.3^{+0.7}_{-0.5}$
	d	$-1/3$	$4.8^{+0.5}_{-0.3}$
2nd generation	s	$-1/3$	95 ± 5
	c	$2/3$	$(1.275 \pm 0.025) \times 10^3$
3rd generation	b	$-1/3$	$(4.18 \pm 0.03) \times 10^3$
	t	$2/3$	$(173.21 \pm 0.51 \pm 0.71) \times 10^3$

Table 1.1: The six different quark flavors [34]. The masses of up, down and strange are given in the $\overline{MS}$ scheme at a scale of $\mu = 2$ GeV. The masses of charm and bottom are given in the $\overline{MS}$ scheme at a scale of the masses itself, i.e. $\mu = m_c$ and $\mu = m_b$, respectively. The top quark mass has been determined by direct measurements at the Tevatron. For further details see [34].

1.1 THE QCD LAGRANGIAN

In the following we will derive the QCD Lagrangian, starting from free quarks and demanding invariance under local gauge transformations.
As fermions, free quarks obey the Dirac Lagrangian, which is given by [35]

$$\mathcal{L}_{\text{free quarks}} = \overline{q}^{(f)}_{\alpha,c}(x)\left(i\gamma^{\mu}_{\alpha\alpha'}\partial_{\mu} - m_f\delta_{\alpha\alpha'}\right) q^{(f)}_{\alpha',c}(x) \tag{1.1}$$

with a quark field $q^{(f)}_{\alpha,c}$ with spin index $\alpha = \{1,2,3,4\}$ and the quark flavor f. The standard model includes 6 different quark flavors, which can be ordered in three generations each consisting of two quarks. A list of the different quark flavors including their masses and electric charges is given in table 1.1. Additionally, quarks carry color - the charge of the strong interaction - indicated by the color-index $c = \{1,2,3\}$.
To construct QCD as a gauge theory, we demand that the QCD Lagrangian is invariant under local $SU(3)$-transformations in color space,

$$\begin{aligned} q^{(f)}(x) \quad &\rightarrow \quad q'^{(f)}(x) = \exp\left(-i\theta_a(x)\,\frac{\lambda_a}{2}\right) q^{(f)}(x) \equiv \Omega(x) q^{(f)}(x) \\ q^{(f)}(x)^\dagger \quad &\rightarrow \quad q^{(f)}(x)^\dagger \Omega(x)^\dagger\,, \end{aligned} \tag{1.2}$$

where the eight *Gell-Mann matrices* λ_a (cf. equation (A.5)) are the generators of $SU(3)$. The matrices $\Omega(x)$ as defined in (1.2) are elements of the group $SU(3)$ and act in color space.
Inserting the transformations (1.2) in the Lagrangian for free quarks (1.1), one obtains

$$\mathcal{L}_{\text{free quarks}} \rightarrow \mathcal{L}'_{\text{free quarks}} = \mathcal{L}_{\text{free quarks}} + i\overline{q}^{(f)}\gamma^\mu \Omega^\dagger(x)\,(\partial_\mu \Omega(x))\,q^{(f)}\,, \tag{1.3}$$

i.e. the Lagrangian (1.1) is not invariant under local $SU(3)$-transformations.
On the other hand, if we replace the derivative ∂_μ in the Lagrangian by the covariant derivative

$$D_\mu = \partial_\mu - ig\frac{\lambda_a}{2} A_{a,\mu}(x) \tag{1.4}$$

with the gauge field

$$A_\mu(x) \equiv \frac{\lambda_a}{2} A_{a,\mu}(x)\,, \tag{1.5}$$

which transforms as

$$A_\mu \rightarrow \Omega(x) A_\mu \Omega(x)^\dagger - \frac{i}{g}\,(\partial_\mu \Omega(x))\,\Omega(x)^\dagger \tag{1.6}$$

under $SU(3)$ gauge transformations, we find a Lagrangian which is invariant under the $SU(3)$ gauge transformations (1.2) and (1.6).
The additional term in the Lagrangian that has been introduced via the covariant derivative to obtain gauge invariance is of the form

$$\mathcal{L}_{\text{interaction}} = g\,\overline{q}^{(f)}\gamma^\mu A_\mu q^{(f)} \tag{1.7}$$

with the strong coupling constant g and describes the interaction of a quark field $q^{(f)}$ with a gluon field A_μ, as depicted schematically in figure 1.1.

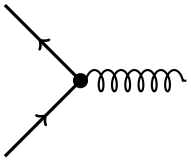

Figure 1.1: Schematic picture of the quark gluon vertex.

Additionally we must introduce a kinetic term for the gauge fields. Starting from the commutator of two covariant derivatives (1.4)

$$[D_\mu, D_\nu] = -ig\,\mathcal{F}_{a,\mu\nu}\,\frac{\lambda_a}{2} \tag{1.8}$$

one finds the field strength tensor

$$\mathcal{F}_a^{\mu\nu} = \partial^\mu A_a^\nu - \partial^\nu A_a^\mu + g\,f_{abc} A_b^\mu A_c^\nu\,, \tag{1.9}$$

with the $SU(3)$ structure constants f_{abc} (cf. table A.1). The field strength tensor itself is not invariant under gauge transformation (1.6). However, one can construct a gauge invariant combination of the gluon fields, that contains the correct kinetic term for a massless gauge boson

$$\mathcal{L}_{\text{gluons}} = \frac{1}{4}\mathcal{F}_{a,\mu\nu}\mathcal{F}_a^{\mu\nu}\,. \tag{1.10}$$

In contrast to the corresponding photon term in Quantum Electrodynamics (QED), the term 1.10 introduces three- and four-gluon vertices as drawn in figure 1.2, representing the gluon self-interaction.

Figure 1.2: Schematic picture of the three and four gluon vertices

Thus, in total the full QCD Lagrangian is given by

$$\mathcal{L}_{\text{QCD}} = \sum_f \overline{q}^{(f)}(x)\left(i\not{D} - m_f\right) q^{(f)}(x) - \frac{1}{4}\mathcal{F}_{a,\mu\nu}\mathcal{F}_a^{\mu\nu}\,. \tag{1.11}$$

1.2 THE RUNNING COUPLING

As in any quantum field theory the strong coupling g is not constant but depends on the energy scale, i.e. $g(\mu)$. The running of the coupling is determined by the renormalization group equation [35, 36]

$$\mu\frac{d}{d\mu}g(\mu) = \beta(g)\,, \tag{1.12}$$

where the β-function for QCD is given by

$$\beta(g) = -\frac{g^3}{(4\pi)^2}\left[11 - \frac{2}{3}N_f\right] \tag{1.13}$$

with the number of quark flavors $N_f = 6$. Solving the QCD renormalization group equation one finds

$$\alpha_s(\mu) \equiv \frac{g^2(\mu)}{4\pi} = \frac{\alpha_s(\Lambda)}{1 + \frac{\alpha_s(\Lambda)}{4\pi}(11 - \frac{2}{3}N_f)\ln\left(\frac{\mu^2}{\Lambda^2}\right)} \tag{1.14}$$

where we have defined the fine structure constant α_s.

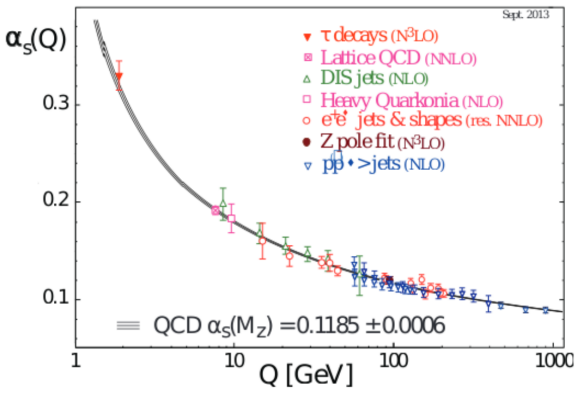

Figure 1.3: Compilation of the the world data for the strong coupling $\alpha_s(Q^2)$. The plot is taken from [34].

Figure 1.3 shows a compilation of the world data for the strong coupling constant plotted against the energy scale $Q = \mu$. For large energies the coupling α_s becomes small and quarks and gluons are asymptotically free. In this regime, one can use a perturbative expansion in the coupling constant α_s. Such a perturbative treatment of QCD is not possible in the low-energy regime, where the coupling becomes large. In this regime, quarks and gluons are confined to hadrons.

1.3 CHIRAL SYMMETRY

For massless quarks $m = 0$, the QCD Lagrangian (cf. equation (1.11)) is given by

$$\mathcal{L}_{m=0} = \overline{q}(x)\, i\gamma_\mu \left(\partial^\mu - igA^\mu(x)\right) q(x) = \overline{q}(x) D q(x)\,. \tag{1.15}$$

This Lagrangian can be split into a left-handed and a right-handed part:

$$\mathcal{L}_{m=0} = \overline{q}_L(x) D q_L(x) + \overline{q}_R(x) D q_R(x)\,. \tag{1.16}$$

Left- and right-handed fields are defined as

$$q_L(x) = \frac{1-\gamma_5}{2}\, q(x) \qquad \text{and} \qquad q_R(x) = \frac{1+\gamma_5}{2}\, q(x)\,. \tag{1.17}$$

The massless Lagrangian (1.15) is invariant under chiral transformations in flavor space

$$q_{L/R} \to e^{i\alpha_i \gamma_5 t_i} q_{L/R} \qquad\qquad \overline{q}_{L/R} \to \overline{q}_{L/R}\, e^{i\alpha_i \gamma_5 t_i} \tag{1.18}$$

with the generators t_i, $i = 1, \ldots, N_f^2 - 1$ of $SU(N_f)$ and the number of flavors N_f. Left- and right-handed quark fields can be transformed separately, and thus the massless Lagrangian obeys a $SU(N_f)_L \times SU(N_f)_R$ symmetry. However, the QCD vacuum is not invariant under the full symmetry group $SU(N_f)_L \times SU(N_f)_R$ since the quark condensate

$$\langle 0|\overline{q}q|0\rangle = \langle 0|\overline{q}_L q_R + \overline{q}_R q_L|0\rangle \neq 0 \tag{1.19}$$

mixes left- and right-handed fields, and the $SU(n_f)_L \times SU(n_f)_R$ is spontaneously broken to $SU(N_f)$. Therefore, one expects $N_f^2 - 1$ massless Goldstone bosons [37]. However, since quarks are not massless, chiral symmetry is additionally broken explicitly by the mass term in the Lagrangian

$$m\bar{q}q = m\,(\bar{q}_L q_R + \bar{q}_R q_L) \tag{1.20}$$

and the Goldstone bosons receive a mass (pseudo-Goldstone bosons). For $N_f = 2$, i.e. only up and down quarks, these Goldstone bosons are the three pions. Including also the strange quark, one has additionally the kaons and the η and thus in total eight Goldstone bosons.

2

QCD ON THE LATTICE

In the previous chapter we have discussed that the strong coupling α_s becomes large in the low-energy regime, such that a perturbative expansion in α_s is no longer applicable. In 1974, Kenneth Wilson proposed to formulate QCD on a Euclidean space-time lattice [16]

$$\Lambda = \left\{ n \in \mathbb{N}^4 \,|\, n_1, n_2, n_3 = 0, 1, ..., L-1 \,;\, n_0 = 0, 1, ..., T-1 \right\} , \tag{2.1}$$

with L lattice points in the spatial and T lattice points in the time direction. The lattice points are separated by the lattice spacing a, i.e. the lattice has a size of $L \cdot a$ in spatial and $T \cdot a$ in time direction. Lattice QCD provides a tool for a non-perturbative treatment of QCD and thus it allows to study the low-energy regime from first principles.
The introduction of a discretized space-time leads also to discrete momenta

$$\Lambda^* = \left\{ p \in \mathbb{R}^4 \middle| p_0 = \frac{2\pi}{Ta} \left(n_0 - \frac{T}{2} + 1 \right) \,;\, p_i = \frac{2\pi}{La} \left(n_i - \frac{L}{2} + 1 \right) \right\} , \tag{2.2}$$

which are in the range of

$$-\frac{\pi}{a} < p_\mu \leqslant \frac{\pi}{a} , \tag{2.3}$$

and thus the lattice provides a momentum cutoff.

2.1 DISCRETIZATION OF THE DIRAC OPERATOR

In this section we will discuss how the Dirac operator D can be discretized on a space-time lattice and how gauge invariance can be realized for the discretized version of D. For this derivation we will follow [38][1].
Our starting point is the Lagrangian for a free quark with mass m_0 in Euclidean metric[2],

$$\mathcal{L} = \overline{\Psi}(x) \left(\gamma_\mu \partial_\mu + m_0 \right) \Psi(x) . \tag{2.4}$$

To discretize the Lagrangian (2.4), one replaces the space-time variable x by a discrete variable n, where n is a point of the Euclidean lattice Λ and $x = a \cdot n$. Furthermore, the derivative ∂_μ is replaced by a finite difference,

$$\partial_\mu \Psi(x) \longrightarrow \frac{1}{2a} \left(\Psi(n + \hat{\mu}) - \Psi(n - \hat{\mu}) \right) , \tag{2.5}$$

where $n + \hat{\mu}$ denotes the neighboring lattice point of n in μ-direction and a is the lattice spacing. Thus, the discretized Lagrangian for free quarks is given by

$$\mathcal{L} = \overline{\Psi}(n) \left(\sum_{\mu=0}^{3} \gamma_\mu \frac{\Psi(n + \hat{\mu}) - \Psi(n - \hat{\mu})}{2a} + m_0 \Psi(n) \right) . \tag{2.6}$$

1 Similar derivations can be found e.g. in [39–41]
2 Note, that in Euclidean metric there is no difference between covariant and contravariant variables, i.e. $a_\mu = a^\mu$

In the (naive) continuum limit $a \to 0$, the continuum expression (2.4) is recovered.

As in the continuum, we require the Lagrangian to be invariant under the local gauge transformation

$$\Psi(n) \to \Psi'(n) = \Omega(n)\Psi(n) \,, \qquad \overline{\Psi}(n) \to \overline{\Psi}'(n) = \overline{\Psi}(n)\Omega(n)^\dagger \tag{2.7}$$

with a $SU(3)$ matrix $\Omega(n)$. Clearly, only the mass term in the discretized Lagrangian (2.6) is invariant under such a transformation. For the derivative term one finds

$$\overline{\Psi}(n)\Psi(n+\hat{\mu}) \to \overline{\Psi}'(n)\Psi'(n+\hat{\mu}) = \overline{\Psi}(n)\Omega(n)^\dagger\Omega(n+\hat{\mu})\Psi(n+\hat{\mu}). \tag{2.8}$$

However, if one introduces a gauge field $U_\mu(n)$, which transforms according to

$$U_\mu(n) \to U'_\mu(n) = \Omega(n)U_\mu(n)\Omega(n+\hat{\mu})^\dagger \tag{2.9}$$

one can construct gauge invariant terms of the form

$$\overline{\Psi}(n)U_\mu(n)\Psi(n+\hat{\mu}) \to \overline{\Psi}'(n)U'_\mu(n)\Psi'(n+\hat{\mu}) = \overline{\Psi}(n)U_\mu(n)\Psi(n+\hat{\mu})\,. \tag{2.10}$$

Such gauge fields $U_\mu(n)$ are elements of the gauge group $SU(3)$ and connect two neighboring lattice points n and $n+\hat{\mu}$. Note that one can also define a gauge field pointing in a negative direction as $U_{-\mu}(n) \equiv U_\mu(n-\hat{\mu})^\dagger$. Figure 2.1 shows a schematic picture of the gauge fields $U_\mu(n)$ and $U_{-\mu}(n)$. Since the gauge fields are attached to the links between the lattice points, one often refers to them as *link variables*.

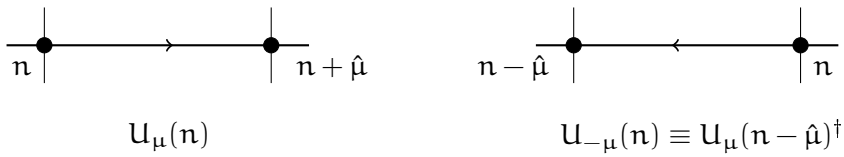

Figure 2.1: Schematic picture of link variables.

The link variable $U_\mu(n)$ can be interpreted as the parallel transporter from one lattice point to a neighboring point. In the continuum, a general parallel transporter from x to y is given by

$$G(x,y) = \text{P.O.} \exp\left(i \int_x^y dz\, A_\mu(z) \right) \,, \tag{2.11}$$

where P.O. stands for "path ordering" and $A_\mu(z)$ is a gluon field. The link variables $U_\mu(n)$ are parallel transporters from one lattice site n to the neighboring site $n+\hat{\mu}$,

$$U_\mu(n) = \exp(iaA_\mu(n))\,. \tag{2.12}$$

Using the link variables $U_\mu(n)$ we can construct a gauge invariant version of the discretized Lagrangian,

$$\mathcal{L} = \overline{\Psi}(n) \left(\sum_{\mu=0}^{3} \gamma_\mu \frac{U_\mu(n)\Psi(n+\hat{\mu}) - U_{-\mu}(n)\Psi(n-\hat{\mu})}{2a} + m_0\Psi(n) \right) \tag{2.13}$$

$$= \sum_{m\in\Lambda} \overline{\Psi}(n) D(n,m) \Psi(m)\,. \tag{2.14}$$

The corresponding Dirac operator $D(n,m)$ is given by

$$D(n,m) = \sum_{\mu=0}^{3} \gamma_\mu \frac{U_\mu(n)\delta_{n+\hat{\mu},m} - U_{-\mu}(n)\delta_{n-\hat{\mu},m}}{2a} + m_0\delta_{n,m} \tag{2.15}$$

and can be written as a matrix that has entries for the interaction of a lattice point n with a lattice point m (as well as every color and every Dirac index). Thus it is a matrix of rank $3 \times 4 \times V$ (# color $\times$ # spin $\times$ # lattice points).

The lattice version of the fermionic part of the action is therefore given by

$$S_F[\Psi,\overline{\Psi},U] = a^4 \sum_{n,m\in\Lambda} \overline{\Psi}(n) D(n,m) \Psi(m)\,. \tag{2.16}$$

2.2 THE WILSON GAUGE ACTION

In addition to the fermionic action we need an action for the gauge fields. In the previous section we have introduced the gauge fields $U_\mu(n)$ that link neighboring lattice points. The shortest possible closed path that can be constructed using the link variables is a *plaquette* $U_{\mu\nu}(n)$ and consists of four gauge fields

$$U_{\mu\nu}(n) \equiv U_\mu(n) U_\nu(n+\hat{\mu}) U_\mu(n+\hat{\nu})^\dagger U_\nu(n)^\dagger\,. \tag{2.17}$$

A schematic picture of a plaquette is given in figure 2.2.

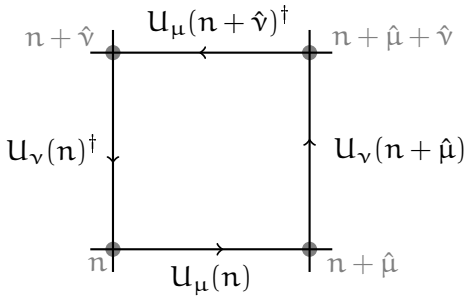

Figure 2.2: Schematic picture of a plaquette.

Under a gauge transformation (2.9) such a plaquette transforms as

$$U_{\mu\nu}(n) \to U'_{\mu\nu}(n) = \Omega(n)\, U_{\mu\nu}(n) \Omega(n)^\dagger\,, \tag{2.18}$$

and thus, the trace of a plaquette is gauge invariant. Using such plaquettes the *Wilson gauge action* can be constructed:

$$S_G[U] = \frac{2}{g_0^2} \sum_{n\in\Lambda} \sum_{\mu<\nu} \mathrm{Re}\,\mathrm{Tr}\,[\mathbb{1} - U_{\mu\nu}(n)]\ , \tag{2.19}$$

where g_0 is the bare strong coupling constant. One can show [38] that the Wilson gauge action (2.19) approaches its continuum counterpart for $a \to 0$:

$$S_G[U] \overset{a\to 0}{\longrightarrow} \frac{a^4}{2g_0^2} \sum_{n\in\Lambda} \sum_{\mu<\nu} \mathrm{Tr}\,[F_{\mu\nu}(n)\, F_{\mu\nu}(n)]\ . \tag{2.20}$$

2.3 FERMION DOUBLING AND THE WILSON-DIRAC OPERATOR

The Dirac operator in momentum space can be obtained by inserting a Fourier transformation for the spatial indices of the lattice Dirac operator,

$$\tilde{D}(p,q) = \frac{1}{V} \sum_{n,m\in\Lambda} e^{-ip\cdot an}\, D(n,m)\, e^{iq\cdot am} \tag{2.21}$$

with $V = T \times L^3$ the total number of lattice points. Inserting the lattice Dirac operator (2.15), one finds for trivial gauge fields $U_\mu(n) = \mathbb{1}$, i.e. free quarks,

$$\tilde{D}(p,q) = \frac{1}{V} \sum_{n\in\Lambda} e^{-i(p-q)\cdot an} \left(\sum_{\mu=0}^{3} \gamma_\mu \frac{e^{iq_\mu a} - e^{-iq_\mu a}}{2a} + m_0 \right) \tag{2.22}$$

$$= \delta(p-q) \underbrace{\left(\frac{i}{a} \sum_{\mu=0}^{3} \gamma_\mu \sin(p_\mu a) + m_0 \right)}_{\tilde{D}(p)}\ . \tag{2.23}$$

One can easily write down the inverse of $\tilde{D}(p)$, which is given by

$$\tilde{D}(p)^{-1} = \frac{-\frac{i}{a} \sum_{\mu=0}^{3} \gamma_\mu \sin(p_\mu a) + m_0}{\frac{1}{a^2} \sum_{\mu=0}^{3} \sin^2(p_\mu a) + m_0^2}\ . \tag{2.24}$$

Since the lattice contains discrete momenta in the range

$$-\frac{\pi}{a} < p_\mu \leqslant \frac{\pi}{a}\,, \tag{2.25}$$

the inverse $\tilde{D}(p)^{-1}$ of the Dirac operator in momentum space has in total 16 poles for massless quarks $m_0 = 0$ at

$$p = (0,0,0,0)\,,\ (0,0,0,\pi/a)\,,\ \ldots\,,\ (\pi/a,\pi/a,\pi/a,\pi/a) \tag{2.26}$$

instead of only one pole $(0,0,0,0)$ in the continuum,

$$\tilde{D}(p)^{-1}\big|_{m_0=0} \overset{a\to 0}{\longrightarrow} \frac{-\frac{i}{a} \sum_{\mu=0}^{3} \gamma_\mu p_\mu}{\frac{1}{a^2} \sum_{\mu=0}^{3} p^2}\,. \tag{2.27}$$

The 15 additional poles in the lattice Dirac operator correspond to 15 unphysical fermion species on the lattice and are called *doublers*.

However, it is possible to remove those doublers [16] by adding an additional term to the Dirac operator that vanishes in the continuum limit:

$$\tilde{D}_W(p) = \frac{i}{a}\sum_{\mu=0}^{3}\gamma_\mu \sin(p_\mu a) + \frac{1}{a}\sum_{\mu=0}^{3}(1-\cos(p_\mu a)) + m_0\,. \tag{2.28}$$

Using the inverse Fourier transformation, $\tilde{D}_W(p)$ can be transformed back to position space, where one obtains an additional term for the Dirac operator, the *Wilson term*. This term can be written down in a gauge invariant way and it is given by

$$-a\sum_{\mu=0}^{3}\frac{U_\mu(n)\delta_{n+\hat{\mu},m} - 2\delta_{n,m} + U_{-\mu}(n)\delta_{n-\hat{\mu},m}}{2a^2}\,. \tag{2.29}$$

Including the Wilson term in the discretized version of the Dirac operator (2.13), one obtains the *Wilson-Dirac operator*

$$\begin{aligned} D_W(n,m) = &\left(m_0 + \frac{4}{a}\right)\delta_{m,n} \\ &-\frac{1}{2a}\sum_{\mu=0}^{3}(1-\gamma_\mu)U_\mu(n)\delta_{n+\hat{\mu},m} - \frac{1}{2a}\sum_{\mu=0}^{3}(1+\gamma_\mu)U_{-\mu}(n)\delta_{n-\hat{\mu},m}\,. \end{aligned} \tag{2.30}$$

As one can see, the Wilson-Dirac operator (2.30) has two types of terms, one which is proportional to a unit matrix (first line of equation (2.30)), and one which connects neighboring lattice points (second line of equation (2.30)). Thus it can be written as

$$a\,D_W = \frac{1}{2\kappa}\mathbb{1} - \frac{1}{2}H\,. \tag{2.31}$$

The matrix H contains all the terms that couple neighboring points and is called *hopping matrix*. The *hopping parameter* κ is related to the bare quark mass m_0:

$$\kappa = \frac{1}{2(am_0+4)}\,. \tag{2.32}$$

2.4 CHIRAL SYMMETRY BREAKING AND THE NIELSEN-NINOMIYA NO-GO THEOREM

In the previous section we have introduced the Wilson term to remove the fermion doublers. However, this additional term explicitly breaks the chiral symmetry (cf. section 1.3) even for massless quarks, i.e.

$$\gamma_5\,D_W|_{m_0=0} + D_W|_{m_0=0}\,\gamma_5 \neq 0 \tag{2.33}$$

with the Wilson-Dirac operator D_W from equation (2.30).

Ideally, a lattice discretization of the Dirac operator D should fulfill the following conditions:

- D is local,
- in the continuum limit $a \to 0$ the discretized operator D recovers its continuum counterpart,
- the theory is free of doublers, and
- the Lagrangian obeys chiral symmetry, $\gamma_5 D + D\gamma_5 = 0$, for massless quarks.

However, Nielsen and Ninomiya showed in their *No-Go Theorem* [42] that it is not possible to construct a lattice version of the Dirac operator that fulfills all of these four conditions simultaneously.
Thus one has to resort to a Dirac operator on the lattice which violates at least one of these conditions. Some commonly used discretizations are

WILSON ACTION (2.30): The theory is free of doublers, but chiral symmetry is explicitly broken even for massless quarks.

STAGGERED FERMION ACTION [43]: The number of doublers is reduced to four. Simultaneously, a subgroup of chiral symmetry is retained.

GINSPARG-WILSON ACTION [44]: The theory is free of doublers. Additionally the Dirac operator for massless quarks fulfills a modified formulation of chiral symmetry $\gamma_5 D + D\gamma_5 = a\, D\gamma_5\, D$.

In this thesis we will use the Wilson action, i.e. chiral symmetry is explicitly broken.

2.5 O(a)-IMPROVEMENT OF THE WILSON-DIRAC OPERATOR

The aim of the Symanzik improvement program [45] is to reduce discretization errors from $\mathcal{O}(a)$ to higher orders. The main idea is to add additional terms to the action that vanish in the continuum limit $a \to 0$:

$$S = a^4 \sum_{n \in \Lambda} \left(\mathcal{L}^{(0)}(n) + a\mathcal{L}^{(1)}(n) + a^2 \mathcal{L}^{(2)}(n) + \dots \right) , \tag{2.34}$$

where $\mathcal{L}^{(0)}$ is the unimproved Lagrangian (i.e. the Wilson Lagrangian in our case). The additional terms $\mathcal{L}^{(k)}$ can be build from products of quark and gluon fields (and in general the quark mass m_0). Since the action has to be dimensionless, these terms have to have the dimension length $l^{-(4+k)}$.
Sheikholeslami and Wohlert have shown that for $\mathcal{O}(a)$-improvement of the Wilson Lagrangian it is sufficient to add a single term [46],

$$\mathcal{L}^{(1)}(n) = c_{SW} \frac{i}{4} \sum_{\mu<\nu} \underbrace{\overline{\Psi}(n)}_{l^{-3/2}} \sigma_{\mu\nu} \underbrace{\hat{F}_{\mu\nu}(n)}_{l^{-2}} \underbrace{\Psi(n)}_{l^{-3/2}} \tag{2.35}$$

with $\sigma_{\mu\nu} = i/2\,[\gamma_\mu, \gamma_\nu]$. The *Sheikholeslami-Wohlert coefficient* c_{SW} is a real number and has to be tuned for every lattice spacing a to achieve $\mathcal{O}(a)$-improvement [47]. This can be done non-perturbatively [48] and we will use the values determined by [49].

The lattice version of the field strength tensor $\hat{F}_{\mu\nu}(n)$ can be written as

$$\hat{F}_{\mu\nu}(n) = \frac{1}{8a^2}\left(Q_{\mu\nu}(n) - Q_{\nu\mu}(n)\right) , \tag{2.36}$$

where $Q_{\mu\nu}(n)$ is a sum over four plaquettes:

$$Q_{\mu\nu}(n) \equiv U_{\mu\nu}(n) + U_{\nu(-\mu)}(n) + U_{(-\mu)(-\nu)}(n) + U_{(-\nu)\mu}(n) . \tag{2.37}$$

Figure 2.3 shows a schematic picture of $Q_{\mu\nu}(n)$. Due to the form of this term, which resembles a clover leaf, one often refers to the Sheikholeslami-Wohlert term as the *clover term*.

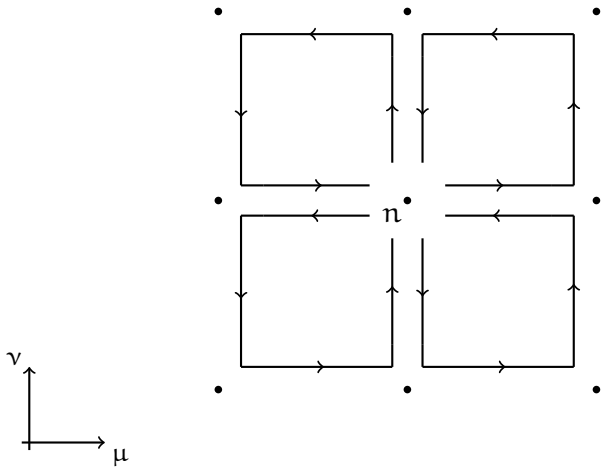

Figure 2.3: Schematic picture of the clover term $Q_{\mu\nu}(n)$.

In total, the $\mathcal{O}(a)$-improved Wilson-Dirac action is given by

$$\begin{aligned} S_{SW}[\Psi, \overline{\Psi}, U] = a^4 \sum_{n,m\in\Lambda} \overline{\Psi}(n) D_W(n,m) \Psi(m) \\ + a^5 \sum_{n,m\in\Lambda} c_{SW} \frac{i}{4} \sum_{\mu<\nu} \overline{\Psi}(n)\, \sigma_{\mu\nu}\, \hat{F}_{\mu\nu}(n)\, \Psi(n) \end{aligned} \tag{2.38}$$

with the unimproved Wilson-Dirac operator $D_W(n,m)$ (2.30). The corresponding $\mathcal{O}(a)$-improved operator is

$$D_{SW}(n,m) = D_W(n,m) + a\, c_{SW} \frac{i}{4} \sum_{\mu<\nu} \sigma_{\mu\nu}\, \hat{F}_{\mu\nu}(n)\, \delta_{n,m} . \tag{2.39}$$

In this thesis, the $\mathcal{O}(a)$-improved Wilson-Dirac operator (2.39) will be used for the quark fields.

3

CORRELATION FUNCTIONS ON THE LATTICE

In the following, we will discuss how correlation functions can be calculated in lattice QCD using path integrals. In the Euclidean path integral formalism the expectation value of an operator $\mathcal{O}$ is given as

$$\langle \mathcal{O} \rangle = \frac{1}{Z} \int \mathcal{D}[\Phi]\, \mathcal{O}[\Phi]\, e^{-S_E[\Phi]} \tag{3.1}$$

with the Euclidean action $S_E[\Phi]$ and the partition function

$$Z = \int \mathcal{D}[\Phi]\, e^{-S_E[\Phi]}\,. \tag{3.2}$$

The integration measure $\mathcal{D}[\Phi] = \mathcal{D}[U]\mathcal{D}[\Psi, \overline{\Psi}]$ contains the integration measure

$$\mathcal{D}[\Psi, \overline{\Psi}] = \prod_{n \in \Lambda} d\Psi(n) d\overline{\Psi}(n) \tag{3.3}$$

for the quark fields on every lattice point n and the Haar measure

$$\mathcal{D}[U] = \prod_{n \in \Lambda} \prod_{\mu=0}^{3} dU_\mu(n) \tag{3.4}$$

for the link variables. Since the Euclidean action is a sum of a fermionic and a gluonic part, i.e. $S_E[\Psi, \overline{\Psi}, U] = S_G[U] + S_F[\Psi, \overline{\Psi}, U]$, equation (3.1) can be split into a fermionic and a gluonic expectation value as follows

$$\langle \mathcal{O} \rangle = \langle \langle \mathcal{O} \rangle_F \rangle_G = \left\langle \frac{1}{Z_F[U]} \int \mathcal{D}[\Psi, \overline{\Psi}]\, \mathcal{O}[\Psi, \overline{\Psi}, U]\, e^{-S_F[\Psi, \overline{\Psi}, U]} \right\rangle_G \tag{3.5}$$

with the fermionic partition function

$$Z_F[U] = \int \mathcal{D}[\Psi, \overline{\Psi}]\, e^{-S_F[\Psi, \overline{\Psi}, U]}\,. \tag{3.6}$$

To obtain the full expectation value (3.1) the gluonic expectation value then is defined as

$$\langle A \rangle_G = \frac{1}{Z} \int \mathcal{D}[U]\, Z_F[U]\, A[U]\, e^{-S_G[U]}\,. \tag{3.7}$$

To calculate the fermionic expectation value, one can make use of Wick's Theorem, which will be derived in the next section 3.1. In section 3.2, we will discuss how the gluonic expectation value can be obtained using Monte Carlo methods.

3.1 FERMIONIC EXPECTATION VALUE AND WICK'S THEOREM

In the following, we will derive Wick's Theorem for the calculation of fermionic correlation functions. As a starting point, we will consider the fermionic partition function (3.6)

$$Z_F[U] = \int \mathcal{D}[\Psi, \overline{\Psi}]\, e^{-S_F[\Psi,\overline{\Psi},U]}\,. \tag{3.8}$$

The fermionic lattice action can be written in the form

$$S_F[\Psi, \overline{\Psi}, U] = \sum_{n,m\in\Lambda} \overline{\Psi}(n)\, D(n,m)\, \Psi(m) \tag{3.9}$$

where n and m are summed over all points of the lattice Λ. Hence the fermionic partition function is given by

$$Z_F[U] = \int \prod_{x\in\Lambda} d\Psi(x) d\overline{\Psi}(x)\, \exp\left(-\sum_{n,m\in\Lambda} \overline{\Psi}(n)\, D(n,m)\, \Psi(m)\right)\,. \tag{3.10}$$

Since the quark fields are fermionic degrees of freedom, one has to take into account that the Ψ anticommute with each other when evaluating the integral (3.10). Such anticommuting numbers are called Grassmann variables and have the properties[1]

$$\eta_i \eta_j = -\eta_j \eta_i \quad \Rightarrow \quad \eta_i^2 = 0 \tag{3.11}$$

$$\int d\eta_i 1 = 0 \qquad \int d\eta_i\, \eta_i = 1\,. \tag{3.12}$$

Now one can use the transformation

$$\Psi'(n) = -\sum_{m\in\Lambda} D(n,m)\, \Psi(m) \tag{3.13}$$

for the variables in the integral (3.10). The measure of the integral transforms accordingly:

$$\prod_{x\in\Lambda} d\Psi(x) d\overline{\Psi}(x) = \det(D) \prod_{x\in\Lambda} d\Psi'(x) d\overline{\Psi}(x)\,. \tag{3.14}$$

With this transformation, the fermionic partition functions is given by

$$\begin{aligned} Z_F[U] &= \det(D) \int \prod_{x\in\Lambda} d\Psi'(x) d\overline{\Psi}(x)\, \exp\left(\sum_{n\in\Lambda} \overline{\Psi}(n)\, \Psi'(n)\right) \\ &= \det(D) \prod_{x\in\Lambda} \int d\Psi'(x) d\overline{\Psi}(x)\, \exp\left(\overline{\Psi}(x)\, \Psi'(x)\right)\,. \end{aligned} \tag{3.15}$$

The exponential function can now be expanded into a Taylor series. Due to the fermionic nature of the Ψ and Ψ' and the property (3.11) of Grassman variables, only the first two terms in the series are non-vanishing,

$$\exp\left(\overline{\Psi}(x)\, \Psi'(x)\right) = 1 + \overline{\Psi}(x)\, \Psi'(x)\,. \tag{3.16}$$

1 A more detailed introduction to Grassmann numbers can be found for example in [35] or [38].

Thus, the integral we have to solve is given by

$$Z_F[U] = \det(D) \prod_{x\in\Lambda} \int d\Psi'(x) d\overline{\Psi}(x) \; \left(1 + \overline{\Psi}(x)\,\Psi'(x)\right) . \tag{3.17}$$

Using the properties (3.12) one finds that the fermionic partition function can be written as

$$Z_F[U] = \det(D) \prod_{x\in\Lambda} \int d\Psi'(x) d\overline{\Psi}(x) \; \left(1 + \overline{\Psi}(x)\,\Psi'(x)\right) = \det(D)\,, \tag{3.18}$$

where $\det(D)$ is called the *fermion determinant*.

As the next step, we want to evaluate the fermionic expectation value of two quark fields $\left\langle \overline{\Psi}(z)\Psi(y)\right\rangle_F$, i.e.

$$\begin{aligned} &\left\langle \overline{\Psi}(z)\Psi(y)\right\rangle_F \\ &= \frac{1}{Z_F[U]} \int \prod_{x\in\Lambda} d\Psi(x) d\overline{\Psi}(x) \; \overline{\Psi}(z)\Psi(y) \; \exp\left(- \sum_{n,m\in\Lambda} \overline{\Psi}(n)\, D(n,m)\, \Psi(m) \right) \end{aligned} \tag{3.19}$$

Using the same variable transformation (3.13) and (3.14) as before and $Z_F[U] = \det(D)$, one finds:

$$\begin{aligned} &\left\langle \overline{\Psi}(z)\Psi(y)\right\rangle_F \\ &= \sum_{b\in\Lambda} (-D^{-1}(y,b)) \int \prod_{x\in\Lambda} d\Psi'(x) d\overline{\Psi}(x) \; \overline{\Psi}(z)\Psi'(b) \; \exp\left(\sum_{n\in\Lambda} \overline{\Psi}(n)\,\Psi'(n) \right) \\ &= \sum_{b\in\Lambda} (-D^{-1}(y,b)) \int \prod_{x\in\Lambda} d\Psi'(x) d\overline{\Psi}(x) \; \overline{\Psi}(z)\Psi'(b) \prod_{n\in\Lambda} \left(1 + \overline{\Psi}(n)\,\Psi'(n)\right) , \end{aligned} \tag{3.20}$$

where we have used the Taylor series expansion (3.16) in the last step. Due to the properties (3.11) and (3.12) of the Grassman variables, only integrals of the form

$$\int \prod_{x\in\Lambda} d\Psi'(x) d\overline{\Psi}(x) \prod_{y\in\Lambda} \Psi'(y)\overline{\Psi}(y) = \prod_{x\in\Lambda} \int d\Psi'(x) d\overline{\Psi}(x) \; \Psi'(x)\overline{\Psi}(x) = 1$$

are non-vanishing. In equation (3.20) such an integral can only occur if $b = z$ and for the one summand of $\prod \left(1 + \overline{\Psi}(n)\,\Psi'(n)\right)$ where $\overline{\Psi}(z)\Psi'(z)$ is missing. Thus, one obtains

$$\left\langle \overline{\Psi}(z)\Psi(y)\right\rangle_F = \sum_{b\in\Lambda} (-D^{-1}(y,b))\,\delta_{zb} = -D^{-1}(y,z)\,, \tag{3.21}$$

i.e. the fermionic expectation value of two quark fields $\left\langle \overline{\Psi}(z)\Psi(y)\right\rangle_F$ is given by the propagator $D^{-1}(y,z)$ from y to z.

For N-point functions $\left\langle \overline{\Psi}(y_1)\ldots\overline{\Psi}(y_N)\,\Psi(x_1)\ldots\Psi(x_N)\right\rangle$ equation (3.21) can be generalised to *Wick's Theorem*

$$\begin{aligned} &\left\langle \overline{\Psi}(y_1)\ldots\overline{\Psi}(y_N)\,\Psi(x_1)\ldots\Psi(x_N)\right\rangle \\ &= (-1)^N \sum_{\mathcal{P}(1,\ldots,N)} \operatorname{sign}(\mathcal{P}) \; D^{-1}(x_1, y_{\mathcal{P}_1}) \cdots D^{-1}(x_N, y_{\mathcal{P}_N})\,. \end{aligned} \tag{3.22}$$

Thus, the N-point function can be calculated as the sum over all possible permutations $\mathcal{P}$ of pair-wise contrations (Wick contractions) of quark and anti-quark fields.

3.2 GLUONIC EXPECTATION VALUE

3.2.1 *Gauge Average*

In the previous section we have developed Wick's Theorem for the calculation of the fermionic expectation value. To obtain the complete expectation value (3.5), the gauge expectation value

$$\langle A \rangle_G = \frac{1}{Z} \int \mathcal{D}[U]\, Z_F[U]\, A[U]\, e^{-S_G[U]} = \frac{1}{Z} \int \mathcal{D}[U]\, \det(D[U])\, A[U]\, e^{-S_G[U]} \quad (3.23)$$

is needed as well. Equation (3.23) indicates, that the calculation of the gauge expectation value requires the determination of a high-dimensional integral. Such integrations can be done using Monte Carlo techniques.

One generates gauge configurations U (a gauge configuration contains gauge fields $U_\mu(x)$ for every link of the lattice) in a Markov chain [50]

$$U_0 \to U_1 \to U_2 \to \dots . \quad (3.24)$$

One has to make sure, that the gauge configurations are distributed according to their statistical weight

$$P(U) = \frac{1}{Z} \det(D[U]) e^{-S_G[U]} . \quad (3.25)$$

The gauge expectation value of an observable A can be estimated by determining A on every configuration U of quark fields and averaging over the gauge configurations,

$$\langle A \rangle_G \approx \frac{1}{N_{cfg}} \sum_{n=1}^{N_{cfg}} A[U_n] . \quad (3.26)$$

A set of such N_{cfg} gauge configurations is called a gauge ensemble. The gauge noise, i.e. the statistical error from the averaging over the gauge configurations, is expected to scale like $1/\sqrt{N_{cfg}}$. The statistical errors in this thesis are calculated using the jackknife procedure (cf. section A.4 in the appendix).

Since the calculation of the fermion determinant $\det(D)$, which is required for the generation of gauge configurations, is expensive in computer time, early simulations used $\det(D) = 1$. This approximation is called *quenchend approximation* and corresponds to having only gluons and no quark - antiquark pairs in the sea sector. Nowadays simulations with $N_f = 2$ up to $N_f = 2+1+1$ flavors of dynamical quarks have become state of the art.

3.2.2 *CLS Ensembles*

The gauge ensembles that have been used in this thesis have been generated within the Coordinated Lattice Simulation (CLS) effort. These ensembles have been generated using the DD-HMC [51, 52] code[2]. This code uses a Hybrid Monte Carlo (HMC) [53] algorithm together with domain decomposition (DD) [52]. The CLS gauge configurations include $N_f = 2$ dynamical quark flavors, i.e. only the light (up and down with $m_u = m_d$) quarks are contained in the sea. For the generation of the ensembles, the $\mathcal{O}(a)$-improved Wilson-Dirac action (cf. equation (2.39)) and the Wilson gauge action (cf. equation (2.19)) have been used for quark and gauge fields, respectively. The lattices are constructed with (anti-)periodic boundary conditions to mimic an infinite geometry. For the gauge fields (bosons) periodic boundary conditions are used in spatial and time directions:

$$U_\mu(n + L\hat{k}) = U_\mu(n) \qquad U_\mu(n + T\hat{0}) = U_\mu(n)\,. \tag{3.27}$$

For the quark fields (fermions) periodic boundary conditions in spatial direction and anti-periodic boundary conditions in time direction are used:

$$\Psi(n + L\hat{k}) = \Psi(n) \qquad \Psi(n + T\hat{0}) = -\Psi(n)\,. \tag{3.28}$$

An overview over the CLS ensembles used in this thesis is given in table 3.1.

β	a[fm]	c_{SW}	lattice	m_π[MeV]	$m_\pi L$	κ	label
5.2	0.079	2.01715	64×32^3	473	6.0	0.13580	A3
5.2	0.079	2.01715	64×32^3	363	4.7	0.13590	A4
5.2	0.079	2.01715	64×32^3	312	4.0	0.13594	A5
5.2	0.079	2.01715	96×48^3	267	5.1	0.13597	B6
5.3	0.063	1.90952	64×32^3	650	6.6	0.13605	E3
5.3	0.063	1.90952	64×32^3	605	6.2	0.13610	E4
5.3	0.063	1.90952	64×32^3	456	4.7	0.13625	E5
5.3	0.063	1.90952	96×48^3	325	5.0	0.13635	F6
5.3	0.063	1.90952	96×48^3	277	4.3	0.13638	F7
5.3	0.063	1.90952	128×64^3	193	4.0	0.13642	G8
5.5	0.050	1.75150	96×48^3	430	5.2	0.13660	N5
5.5	0.050	1.75150	96×48^3	332	4.1	0.13667	N6
5.5	0.050	1.75150	128×64^3	261	4.2	0.13671	O7

Table 3.1: Overview of the CLS ensembles used in this thesis. The table quotes the inverse gauge coupling $\beta = 6/g_0^2$, the lattice spacing a, the coefficient c_{SW} for the $\mathcal{O}(a)$-improvement, the number of lattice points, the pion mass, $m_\pi \cdot L$ with the box size L, the hopping parameter κ and the label of the lattice.

2 The code can be downloaded from `http://luscher.web.cern.ch/luscher/DD-HMC/index.html`.

As one can see, there are three sets of ensembles each with a different gauge coupling β:

- $\beta = 5.2$: labels A, B,
- $\beta = 5.3$: labels E, F, G,
- $\beta = 5.5$: labels N, O.

In each of these sets, an ascending letter in alphabet corresponds to a larger lattice volume. Ascending numbers in the labels denote larger values of the hopping parameter κ, i.e. smaller quark masses. The lattice spacing for every value of the gauge coupling has been determined by matching the mass of the Ω-baryon with its physical value [54]. Similar results for the lattice spacings have been found by the ALPHA collaboration using the kaon decay constant f_K [55].

All CLS ensembles used in this thesis fulfill $m_\pi L \geqslant 4$, which is a rule of thumb [38] that the volume of the lattice is large enough such that one can expect finite-volume effects to be negligible. Thus, we do not perform a finite-volume extrapolation $V \to \infty$ of our lattice results.
Furthermore, the use of ensembles with different pion masses and lattice spacings allows for extrapolating to the physical point, i.e. a chiral extrapolation $m_\pi \to m_\pi^{\text{phys}}$, and a continuum extrapolation $a \to 0$.

3.3 TWO-POINT FUNCTIONS

3.3.1 *Mesonic Two-Point Functions*

For an arbitrary hadron creation operator $O^\dagger$, the two-point function is given as the correlation function

$$C_{2pt} = \left\langle O(y) O^\dagger(x) \right\rangle , \tag{3.29}$$

i.e. a hadron with quantum numbers specified by the operator O is created at x and annihilated at y.

In the following, we will concentrate on mesonic two-point functions. In general, one can also determine n-point functions of baryons by introducing the corresponding three-quark creation operators.

Mesons consist of a quark and an anti-quark. Therefore, a meson creation operator $\phi(x)$ is constructed as a Dirac bilinear

$$\phi(x) = \overline{q}(x)\, \Gamma\, q'(x) = \overline{q}(x)^c_\alpha\, \Gamma_{\alpha\beta}\, q'(x)^c_\beta . \tag{3.30}$$

with quarks of the flavors q and q'. Greek and Latin indices denote the spin and the color, respectively. Γ is one of the 16 Dirac matrices, i.e. $\Gamma = \{\mathbb{1}, \gamma_\mu, \gamma_5, \gamma_\mu\gamma_5, \gamma_i\gamma_j\}$, and is used to make sure that the operator creates a meson with the desired quantum numbers J^{PC}. An overview over the Dirac matrices and the corresponding quantum numbers is given in table 3.2.

State	J^{PC}	Γ	Particles
Scalar	0^{++}	$\mathbb{1}, \gamma_0$	$f_0, a_0, K_0^*, \ldots$
Pseudoscalar	0^{-+}	$\gamma_5, \gamma_0\gamma_5$	$\pi^\pm, \pi_0, \eta, K^\pm, K^0, \ldots$
Vector	1^{--}	$\gamma_i, \gamma_0\gamma_i$	$\rho^\pm, \rho^0, \omega, K^*, \phi, \ldots$
Axial vector	1^{++}	$\gamma_i\gamma_5$	$a_1, f_1, \ldots$
Tensor	1^{+-}	$\gamma_i\gamma_j$	$h_1, b_1, \ldots$

Table 3.2: Quantum numbers J^{PC} of the meson interpolating operators $\bar{q}\,\Gamma\,q'$ [38].

For example, the pion, which is the lightest pseudoscalar meson, can be created using

$$\phi^\dagger(x)_{ps} = \bar{u}(x)\,\gamma_5\,d(x) \quad , \qquad \phi(x)_{ps} = \bar{d}(x)\,\gamma_5\,u(x) \tag{3.31}$$

for a π^- or π^+, respectively. Note, that the operator (3.31) does not only create a pion, but also excited states with the same quantum numbers.
Since the meson creation operator (3.30) is given in position space, it contains contributions from mesons with all possible momenta. For many applications, such as hadron spectroscopy or form factor calculations, one is interested in a meson with a certain momentum. To obtain the meson creation operator (3.30) in momentum space, one uses a spatial Fourier transformation, which on the lattice requires a sum over all spatial lattice points $\mathbf{x}$,

$$\phi^\dagger(t, \mathbf{p}) = \sum_{\mathbf{x}} e^{i\mathbf{p}\cdot\mathbf{x}}\ \bar{q}(x)\,\Gamma\,q'(x)\,. \tag{3.32}$$

The Fourier-transformed operator $\phi^\dagger(t, \mathbf{p})$ creates a meson at time t with momentum $\mathbf{p}$. The corresponding annihilation operator $\phi(t, \mathbf{p})$ is given by

$$\phi(t, \mathbf{p}) = \sum_{\mathbf{x}} e^{-i\mathbf{p}\cdot\mathbf{x}}\ \bar{q}'(x)\,\Gamma^\dagger\,q(x)\,. \tag{3.33}$$

In the corresponding two-point function, a meson with momentum $\mathbf{p}$ is created at time t_0 and annihilated at the sink time t_s,

$$\begin{aligned} C_{2pt}(t_s, t_0, \mathbf{p}) &= \langle \phi(t_s, \mathbf{p})\phi^\dagger(t_0, \mathbf{p})\rangle \\ &= \sum_{\mathbf{y},\mathbf{x}} e^{-i\mathbf{p}\cdot(\mathbf{y}-\mathbf{x})}\langle \phi(t_s, \mathbf{y})\phi^\dagger(t_0, \mathbf{x})\rangle\,. \end{aligned} \tag{3.34}$$

Usually, in lattice calculations one sets the source position $(t_0, \mathbf{x})$ to a fixed value and neglects the sum over $\mathbf{x}$ for simplicity. In this approach one relies on the gauge average to project on the correct momentum at the source, since all unphysical momentum channels are not gauge invariant and therefore vanish in the gauge average. Equation (3.34) then is simplified to

$$C_{2pt}(t_s, t_0, \mathbf{p}) = \sum_{\mathbf{y}} e^{-i\mathbf{p}\cdot(\mathbf{y}-\mathbf{x})}\langle \phi(t_s, \mathbf{y})\phi^\dagger(t_0, \mathbf{x})\rangle\,. \tag{3.35}$$

Following Wick's Theorem, the expectation value $\langle \phi(t_s, \mathbf{y}) \phi^\dagger(t_0, \mathbf{x}) \rangle$ can be written as

$$\begin{aligned}
\langle \phi(t_s, \mathbf{y}) \phi^\dagger(t_0, \mathbf{x}) \rangle &= \langle \overline{q}'(y)\, \Gamma^\dagger\, q(y)\ \ \overline{q}(x)\, \Gamma\, q'(x) \rangle \\
&= \langle \overline{q}'(y)^c_\alpha\, \Gamma^\dagger_{\alpha\beta}\, q(y)^c_\beta\ \ \overline{q}(x)^d_\gamma\, \Gamma_{\gamma\delta}\, q'(x)^d_\delta \rangle \\
&= \langle \overline{q}'(y)^c_\alpha\, \Gamma^\dagger_{\alpha\beta}\, q(y)^c_\beta\ \ \overline{q}(x)^d_\gamma\, \Gamma_{\gamma\delta}\, q'(x)^d_\delta \rangle \\
&= -\left\langle S'(y,x)^{dc}_{\delta\alpha}\ \Gamma^\dagger_{\alpha\beta}\ S(x,y)^{cd}_{\beta\gamma}\ \Gamma_{\gamma\delta} \right\rangle_G \\
&= -\left\langle \mathrm{Tr}_{CD}\left[S'(y,x)\ \Gamma^\dagger\ S(x,y)\ \Gamma \right] \right\rangle_G ,
\end{aligned} \tag{3.36}$$

where Tr_{CD} denotes the trace in Dirac- and color space. Due to an odd number of exchanges of quark fields, one obtains a minus sign when performing the required Wick contraction. The propagator $S(x,y) \equiv D^{-1}(x,y)$ in (3.36) refers to a quark with flavor q, which propagates from y to x, and the propagator $S'(y,x)$ belongs to a quark q' propagating from x to y (or, equally, an anti-quark $\overline{q}'$ propagating from y to x).
If the quark flavors q and q' are the same, a second Wick contraction is possible, and the two-point function is

$$\begin{aligned}
\langle \phi(t_s, \mathbf{y}) \phi^\dagger(t_0, \mathbf{x}) \rangle =& \langle \overline{q}(y)^c_\alpha\, \Gamma^\dagger_{\alpha\beta}\, q(y)^c_\beta\ \ \overline{q}(x)^d_\gamma\, \Gamma_{\gamma\delta}\, q(x)^d_\delta \rangle \\
&+ \langle \overline{q}(y)^c_\alpha\, \Gamma^\dagger_{\alpha\beta}\, q(y)^c_\beta\ \ \overline{q}(x)^d_\gamma\, \Gamma_{\gamma\delta}\, q(x)^d_\delta \rangle \\
=& -\left\langle \mathrm{Tr}_{CD}\left[S(y,x)\ \Gamma^\dagger\ S(x,y)\ \Gamma \right] \right\rangle_G \\
&+ \left\langle \mathrm{Tr}_{CD}\left[S(y,y)\ \Gamma^\dagger \right] \cdot \mathrm{Tr}_{CD}\left[S(x,x)\ \Gamma \right] \right\rangle_G ,
\end{aligned} \tag{3.37}$$

where propagators like $S(x,x)$ refer to quarks that propagate from one point back to same same point. The two contributions (3.37) to the two-point function are shown in figure 3.1. Wick contractions like the second line in (3.37) are called *quark-disconnected*, since they include vertices which are not connected by each other via quark lines. However, since we have calculated only the fermionic expectation value in (3.37) the quark lines are still connected via gluons as schematically shown in figure 3.2. For simplicity, we will denote such quark-disconnected contributions simply as "disconnected" contributions in the following.

Figure 3.1: Sketch of a meson two-point function: The corresponding meson is created at x and annihilated at y. The left and the right diagram show the connected and the disconnected contribution, respectively.

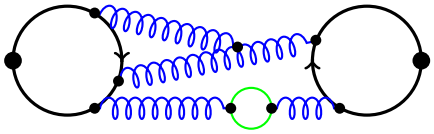

Figure 3.2: Example for a disconnected meson two-point function: Curled blue lines show gluons, green lines show virtual quark anti-quark pairs.

3.3.2 *The Time-Dependence of the Two-Point Function*

In addition, one can examine the dependence of the two-point function

$$C_{2pt}(t_s, t_0, \mathbf{p}) = \langle \phi(t_s, \mathbf{p}) \phi^\dagger(t_0, \mathbf{p}) \rangle = \langle 0 | \phi(t_s, \mathbf{p}) \phi^\dagger(t_0, \mathbf{p}) | 0 \rangle \tag{3.38}$$

on the source and sink time t_0 and t_s. Using the Euclidean time evolution for operators, i.e. $O(t) = \exp(t\hat{H})\, O(0) \exp(-t\hat{H})$ with the Hamilton operator $\hat{H}$, equation (3.38) can be written as

$$\begin{aligned} C_{2pt}(t_s, t_0, \mathbf{p}) &= \langle 0 | e^{t_s \hat{H}} \phi(0, \mathbf{p}) e^{-t_s \hat{H}}\ e^{t_0 \hat{H}} \phi^\dagger(0, \mathbf{p}) e^{-t_0 \hat{H}} | 0 \rangle \\ &= \sum_j \frac{1}{2E_j(\mathbf{p})} \langle 0 | e^{t_s \hat{H}} \phi(0, \mathbf{p}) e^{-(t_s - t_0)\hat{H}} | j \rangle \langle j | \phi^\dagger(0, \mathbf{p}) e^{-t_0 \hat{H}} | 0 \rangle , \end{aligned} \tag{3.39}$$

where in the second line of equation (3.39) a complete set $|j\rangle$ of eigenstates of the Hamiltonian $\hat{H}$ was inserted

$$\mathbb{1} = \sum_j \frac{1}{2E_j(\mathbf{p})} |j\rangle\langle j| . \tag{3.40}$$

Additionally, we want the states $|j\rangle$ to be ordered according to their energies, i.e. $E_1 < E_2 < E_3 \cdots$. We obtain

$$\begin{aligned} &C_{2pt}(t_s, t_0, \mathbf{p}) \\ &= \sum_j \frac{1}{2E_j(\mathbf{p})} e^{-(t_s - t_0)E_j(\mathbf{p})} e^{-(t_0 - t_s)E_0} \langle 0 | \phi^\dagger(0, \mathbf{p}) | j \rangle \langle j | \phi(0, \mathbf{p}) | 0 \rangle \\ &= \sum_j \frac{Z_j^2(\mathbf{p})}{2E_j(\mathbf{p})} e^{-(t_s - t_0)E_j}, \end{aligned} \tag{3.41}$$

where the energy of the vacuum $E_0 = 0$, and the prefactor

$$Z_j^2(\mathbf{p}) = \langle 0 | \phi(0, \mathbf{p}) | j \rangle \langle j | \phi^\dagger(0, \mathbf{p}) | 0 \rangle = \left| \langle j | \phi^\dagger(0, \mathbf{p}) | 0 \rangle \right|^2 \tag{3.42}$$

is the probability for the operator $\phi^\dagger$ to create the meson state $|j\rangle$ from the vacuum. As already mentioned above, the operator $\phi^\dagger$ also contains contributions from excited states, as one can see in (3.41). Since $E_1 < E_2 < E_3 \cdots$, one can rely on the excited states having died out exponentially for sufficiently large source-sink separations $t_s - t_0$, such that only the ground state $|1\rangle$ survives,

$$C_{2pt}(t_s, t_0, \mathbf{p}) \underset{t_s \gg t_0}{=} \frac{Z_1^2(\mathbf{p})}{2E_1(\mathbf{p})} e^{-(t_s - t_0)E_1(\mathbf{p})}, \tag{3.43}$$

e.g. the pion in the case of a pseudoscalar meson creation operator $\phi^\dagger(x)_{ps} = \overline{u}(x)\, \gamma_5\, d(x)$.

Since we use periodic boundary conditions in the time-direction in our lattice calculations, we allow the meson to propagate in negative time-direction as well and reach the sink from the back. This modifies equation (3.43) to

$$C_{2pt}(t_s, t_0, \mathbf{p}) \underset{t_s \gg t_0}{=} \frac{Z_1^2(\mathbf{p})}{2E_1(\mathbf{p})} \left(e^{-(t_s - t_0)E_1(\mathbf{p})} + e^{-(T-(t_s-t_0))E_1(\mathbf{p})} \right), \quad (3.44)$$

with the length T of the lattice in time-direction.

The two-point functions with vanishing momentum $\mathbf{p} = 0$ can be used to determine the masses of the hadrons. For large source-sink separations, the effective mass

$$a\, m_{\text{eff}}(t_s) = \ln\left(\frac{C_{2pt}(t_s, t_0, 0)}{C_{2pt}(t_s + 1, t_0, 0)} \right) \underset{t_s \gg t_0}{\longrightarrow} a\, m_{\text{lat}} \quad (3.45)$$

determines the mass of the ground state in lattice units $a\, m_{\text{lat}}$. In reverse this can also be used to determine the lattice spacing a of a given lattice by requiring a certain hadron to recieve its phyical value. Then the lattice spacing is given by

$$a = \frac{a\, m_{\text{lat}}}{m_{\text{phys}}}. \quad (3.46)$$

For the CLS ensembles we will use the lattice spacings that have been obtained using the Ω-baryon[3] mass [54].

3.4 THREE-POINT FUNCTIONS

3.4.1 *Mesonic Three-Point Functions*

To determine quantities like form factors, one needs three-point functions. Again, a hadron is created at the source $(t_0, \mathbf{x})$ and annihilated at the sink $(t_s, \mathbf{y})$. At a time t with $t_0 < t < t_s$ an operator

$$\mathcal{O}(t, \mathbf{q}) = \sum_{\mathbf{z}} \mathcal{O}(t, \mathbf{z}) e^{i\mathbf{q}\cdot\mathbf{z}} \quad (3.47)$$

can be inserted. The corresponding three-point function is given by

$$C_{3pt}(t_s, t, t_0, \mathbf{p}_i, \mathbf{p}_f) = \sum_{\mathbf{x},\mathbf{y},\mathbf{z}} e^{i\mathbf{q}\cdot\mathbf{z}} e^{-i\mathbf{p}_f\cdot\mathbf{y}} e^{i\mathbf{p}_i\cdot\mathbf{x}} \langle \phi(t_s, \mathbf{y}) \mathcal{O}(t, \mathbf{z}) \phi^\dagger(t_0, \mathbf{x}) \rangle, \quad (3.48)$$

where momentum conservation has to be considered, i.e. $\mathbf{q} = \mathbf{p}_f - \mathbf{p}_i$. However, as in the two-point function one usually drops the sum over the source position $\mathbf{x}$ and relies on the gauge average to project on the physical kinematics, i.e where the momentum is conserved. In the following we will focus on operators of the form $\mathcal{O}(z) = \overline{q}(z)\Gamma^{\mathcal{O}} q(z)$, where $\Gamma^{\mathcal{O}}$ is one of the 16 Dirac matrices. If the operator $\mathcal{O}$ is chosen to transform as a vector, i.e. $\Gamma^{\mathcal{O}} = \gamma_\mu$, the three-point function (3.48) contains information on the corresponding vector form factor. If one is interested in the scalar form factor, e.g. of the pion, the scalar operator with $\Gamma^{\mathcal{O}} = \mathbb{1}$ has to be inserted.

3 The Ω-baryon consists of three strange quarks and its mass is $m_\Omega = 1672.43 \pm 0.32$ MeV [34].

Using Wick's Theorem to calculate the correlation function in (3.48) one obtains

$$\begin{aligned}
&\langle \phi(t_s, \mathbf{y})\ \mathcal{O}(t, \mathbf{z})\ \phi^\dagger(t_0, \mathbf{x})\rangle \\
&= \langle \overline{q}'(y)^c_\alpha\, \Gamma^\dagger_{\alpha\beta}\, q(y)^c_\beta \quad \overline{q}(z)^d_\gamma\, \Gamma^{\mathcal{O}}_{\gamma\delta}\, q(z)^d_\delta \quad \overline{q}(x)^e_\epsilon\, \Gamma_{\epsilon\zeta}\, q'(x)^e_\zeta\rangle \\
&= \langle \overline{q}'(y)^c_\alpha\, \Gamma^\dagger_{\alpha\beta}\, q(y)^c_\beta \quad \overline{q}(z)^d_\gamma\, \Gamma^{\mathcal{O}}_{\gamma\delta}\, q(z)^d_\delta \quad \overline{q}(x)^e_\epsilon\, \Gamma_{\epsilon\zeta}\, q'(x)^e_\zeta\rangle \\
&\quad + \langle \overline{q}'(y)^c_\alpha\, \Gamma^\dagger_{\alpha\beta}\, q(y)^c_\beta \quad \overline{q}(z)^d_\gamma\, \Gamma^{\mathcal{O}}_{\gamma\delta}\, q(z)^d_\delta \quad \overline{q}(x)^e_\epsilon\, \Gamma_{\epsilon\zeta}\, q'(x)^e_\zeta\rangle \\
&= + \left\langle \mathrm{Tr}_{CD}\left[S'(y,x)\ \Gamma^\dagger\ S(z,y)\ \Gamma^{\mathcal{O}}\ S(x,z)\ \Gamma\right]\right\rangle_G \\
&\quad - \left\langle \mathrm{Tr}_{CD}\left[S'(y,x)\ \Gamma^\dagger\ S(x,y)\ \Gamma\right]\cdot \mathrm{Tr}_{CD}\left[S(z,z)\ \Gamma^{\mathcal{O}}\right]\right\rangle_G
\end{aligned} \tag{3.49}$$

with the assumption that q' and q are different quark flavors as it is for a charged pion. Both contributions to the mesonic three-point function, the connected and the disconnected one, are shown in figure 3.3. The disconnected contribution contains a meson two-point function and a disconnected loop, which are connected only via gluon lines as depicted in figure 3.4.

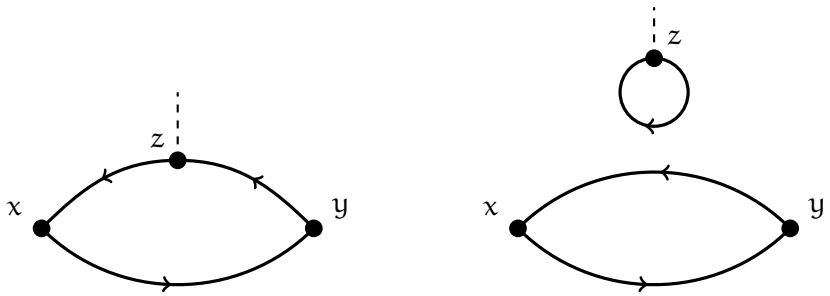

Figure 3.3: Sketch of a meson three-point function: The corresponding meson is created at x, an operator is inserted at z and the meson is annihilated at y. The connected contribution is shown on the left, the quark-disconnected contribution on the right.

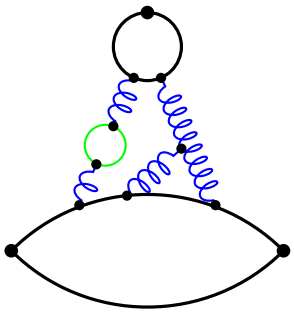

Figure 3.4: Example for a disconnected meson three-point function: Curled blue lines show gluons, green lines show virtual quark-antiquark pairs.

Note that in the case of the scalar form factor, i.e. $\mathcal{O}_S(z) = \overline{q}(z)q(z)$, the vacuum contribution to the three-point function,

$$C_{vac}(t_s, t, t_0, \mathbf{p}_i, \mathbf{p}_f) = C_{2pt}(t_s, t_0, \mathbf{p}_f) \sum_{\mathbf{y}} e^{i\mathbf{q}\cdot\mathbf{z}} \langle \mathcal{O}_S(t, \mathbf{z})\rangle\ , \tag{3.50}$$

is non-zero for vanishing momentum transfer and has to be subtracted from the scalar three-point function. In terms of expectation values, the vacuum contribution can be written as

$$-\left\langle \mathrm{Tr}_{CD}\left[S'(y,x)\;\Gamma^{\dagger}\;S(x,y)\;\Gamma\right]\right\rangle_G \cdot \left\langle \mathrm{Tr}_{CD}\left[S(z,z)\;\mathbb{1}\right]\right\rangle_G , \tag{3.51}$$

i.e. one has two separate gauge averages, one for the two-point function and one for the quark loop. Thus, the vacuum contribution is also disconnected in the quantum field-theoretical sense since no gluons are connecting the quark lines. The scalar pion form factor is obtained from a three-point function

$$C_{3pt}^{subtr}(t_s,t,t_0,\mathbf{p}_i,\mathbf{p}_f) = C_{3pt}(t_s,t,t_0,\mathbf{p}_i,\mathbf{p}_f) - C_{vac}(t_s,t,t_0,\mathbf{p}_i,\mathbf{p}_f) \tag{3.52}$$

with subtracted vacuum contribution.

3.4.2 *The Time-Dependence of the Three-Point Function*

As for the two-point function, we can study the time-dependence of the three-point function

$$\begin{aligned} C_{3pt}(t_s,t,t_0,\mathbf{p}_i,\mathbf{p}_f) &= \langle \phi(t_s,\mathbf{p}_f)\mathcal{O}(t,\mathbf{p}_f-\mathbf{p}_i)\phi^{\dagger}(t_0,\mathbf{p}_i)\rangle \\ &= \langle 0|\phi(t_s,\mathbf{p}_f)\mathcal{O}(t,\mathbf{p}_f-\mathbf{p}_i)\phi^{\dagger}(t_0,\mathbf{p}_i)|0\rangle . \end{aligned} \tag{3.53}$$

Applying the time evolution operator and inserting complete sets of eigenstates of the Hamiltonian $\hat{H}$, one obtains

$$\begin{aligned} &C_{3pt}(t_s,t,t_0,\mathbf{p}_i,\mathbf{p}_f) \\ &= \sum_{i,j} \frac{1}{4E_i(\mathbf{p}_f)E_j(\mathbf{p}_i)} \langle 0|e^{\hat{H}t_s}\,\phi(0,\mathbf{p}_f)\,e^{-\hat{H}t_s}|i\rangle\langle i|e^{\hat{H}t}\,\mathcal{O}(0,\mathbf{p}_f-\mathbf{p}_i)\,e^{-\hat{H}t}|j\rangle \\ &\qquad\qquad \times \langle j|e^{\hat{H}t_0}\,\phi^{\dagger}(0,\mathbf{p}_i)\,e^{\hat{H}t_0}|0\rangle \\ &= \sum_{i,j} \frac{Z_i^{\dagger}(\mathbf{p}_f)Z_j(\mathbf{p}_i)}{4E_i(\mathbf{p}_f)E_j(\mathbf{p}_i)}\, e^{-(t_s-t)E_i(\mathbf{p}_f)}\, e^{-(t-t_0)E_j(\mathbf{p}_i)} \langle i|\mathcal{O}(0,\mathbf{p}_f-\mathbf{p}_i)|j\rangle \end{aligned} \tag{3.54}$$

If we consider only the ground state $i = j = 1$, the time-dependence of the three-point function is

$$\begin{aligned} &C_{3pt}(t_s,t,t_0,\mathbf{p}_i,\mathbf{p}_f) \\ &= \frac{Z_1^{\dagger}(\mathbf{p}_f)Z_1(\mathbf{p}_i)}{4E_1(\mathbf{p}_f)E_1(\mathbf{p}_i)}\, e^{-(t_s-t)E_1(\mathbf{p}_f)}\, e^{-(t-t_0)E_1(\mathbf{p}_i)} \langle 1|\mathcal{O}(0,\mathbf{p}_f-\mathbf{p}_i)|1\rangle . \end{aligned} \tag{3.55}$$

Note that for the scalar operator $\mathcal{O}_S = \bar{q}q$ with zero momentum transfer $Q^2 = 0$, i.e. $\mathbf{p}_i = \mathbf{p}_f$, equation (3.55) is only true after subtracting the vacuum contribution (3.50). Otherwise, one also obtains a term with $i = j = 0$,

$$\frac{Z_0^{\dagger}(\mathbf{p})Z_0(\mathbf{p})}{4E_0(\mathbf{p})E_0(\mathbf{p})}\, e^{-(t_s-t)E_0(\mathbf{p})}\, e^{-(t-t_0)E_0(\mathbf{p})} \langle 0|\mathcal{O}(0,0)|0\rangle , \tag{3.56}$$

which is exactly canceled by the vacuum contribution, and (3.55) is the remaining leading term in the three-point function.

For the pseudoscalar meson creation operator $\phi^\dagger(x)_{ps} = \overline{u}(x)\,\gamma_5\,d(x)$ and the operator $\mathcal{O}(t,\boldsymbol{z}) = 2/3\,\overline{u}\gamma_\mu u - 1/3\,\overline{d}\gamma_\mu d$, the matrix element $\langle\pi|\mathcal{O}(0,\mathbf{p}_f-\mathbf{p}_i)|\pi\rangle$ in (3.55) determines the electromagnetic vector form factor of the pion, i.e.

$$F_v^\pi\left(Q^2\right) \equiv \left\langle\pi^+\left(p_f\right)\right|\frac{2}{3}\,\overline{u}\gamma_\mu u - \frac{1}{3}\,\overline{d}\gamma_\mu d\,\left|\pi^+\left(p_i\right)\right\rangle\,. \tag{3.57}$$

Using the scalar operator $\mathcal{O}(t,\boldsymbol{z}) = m_d\overline{d}d + m_u\overline{u}u$ one obtains information on the scalar pion form factor

$$F_s^\pi\left(Q^2\right) \equiv \left\langle\pi^+\left(p_f\right)\right|\,m_d\overline{d}d + m_u\overline{u}u\,\left|\pi^+\left(p_i\right)\right\rangle\,. \tag{3.58}$$

To extract the matrix element in (3.55) from three-point functions calculated in a lattice simulation, one builds ratios from appropriate three- and two-point functions. This will be explained in chapter 6.

3.4.3 *The Disconnected Contribution to the Pion Vector Form Factor*

From the Wick contractions (3.49) we obtained a connected and a disconnected contribution for the three-point function. In the following we will show that the disconnected contribution vanishes in the case of the vector form factor due to charge conjugation invariance [56].

Under charge conjugation particles transform to their antiparticles:

$$q(x) \xrightarrow{C} C^{-1}\,\overline{q}(x)^T\,, \qquad \overline{q}(x) \xrightarrow{C} -q(x)^T\,C\,, \tag{3.59}$$

$$U_\mu(n) \xrightarrow{C} U_\mu(n)^*\,, \tag{3.60}$$

with the charge conjugation matrix C, which acts on the Dirac indices and is defined such that

$$C\,\gamma_\mu\,C^{-1} = -\gamma_\mu^T \qquad \Rightarrow \qquad C\,\gamma_5\,C^{-1} = \gamma_5^T\,. \tag{3.61}$$

The Dirac operator transforms under charge conjugation as

$$D(x,y;U) \xrightarrow{C} C\,D(x,y;U)\,C^{-1} = D^T(y,x;U^*)\,, \tag{3.62}$$

where we have explicitly written the dependence on the gauge fields U. It is straightforward to check that the action

$$S = a^4 \sum_{x,y\in\Lambda} \overline{q}(x)\,D(x,y;U)\,q(y) \tag{3.63}$$

is invariant under charge conjugation. Relation (3.62) is also true for the inverse of the Dirac operator, i.e.

$$S(x,y;U) \xrightarrow{C} C\,S(x,y;U)\,C^{-1} = S^T(y,x;U^*)\,. \tag{3.64}$$

The disconnected three-point function for the pion vector form factor is determined by (cf. equation (3.49))

$$G_{disc}(U) = \mathrm{Tr}\left[S(y,x;U)\;\gamma_5\;S(x,y;U)\;\gamma_5\right]\cdot\mathrm{Tr}\left[S(z,z;U)\;\gamma_\mu\right]\,. \tag{3.65}$$

Using equations (3.61) and (3.64) and the cyclicity of the trace one can write:

$$\begin{aligned} G_{\text{disc}}(U) &= \text{Tr}\left[S(y,x;U)\ \gamma_5\ S(x,y;U)\ \gamma_5\right] \cdot \text{Tr}\left[S(z,z;U)\ \gamma_\mu\right] \\ &= \text{Tr}\left[S^T(x,y;U^*)\,\gamma_5^T\,S^T(y,x;U^*)\,\gamma_5^T\right] \cdot \text{Tr}\left[S^T(z,z;U^*)\ \left(-\gamma_\mu^T\right)\right] \\ &= -\,G_{\text{disc}}(U^*)\,. \end{aligned} \tag{3.66}$$

Additionally, the gauge action $S_G[U]$ (cf. equation (2.19)) is invariant under charge conjugation $U \to U^*$ and thus, the weight

$$\det(D[U])e^{-S_G[U]} = \det(D[U^*])e^{-S_G[U^*]} \tag{3.67}$$

of the configuration U is the same as the weight of U^*. However, if U and U^* have the same weight, one can write [56]

$$\langle G_{\text{disc}}(U)\rangle_G = \frac{1}{2}\,\langle G_{\text{disc}}(U) + G_{\text{disc}}(U^*)\rangle_G \overset{(3.66)}{=} 0 \tag{3.68}$$

with the gauge average $\langle\rangle_G$. Thus, one can conclude that the disconnected contribution to the vector form factor of the pion vanishes in the gauge average. For the scalar pion form factor one finds $G_{\text{disc}}(U) = G_{\text{disc}}(U^*)$ instead of (3.66), and thus we expect a non-vanishing disconnected contribution to the scalar form factor.

4

PROPAGATOR CALCULATION

According to Wick's Theorem (3.22) the computation of correlation functions such as two- and three-point functions requires the calculation of appropriate propagators $S(x,y) = D^{-1}(x,y)$, i.e. the Dirac operator has to be inverted. On the lattice the Dirac operator is a very large matrix with a rank of $12V$, where V is the total number of lattice points and $12 = \#\,\text{color} \times \#\,\text{Dirac components}$. For typical lattice simulations this is $12V \gtrsim \mathcal{O}(10^8)$. An exact calculation of the full inverse of such a large matrix is not feasible in computational costs. In the following, some methods for the calculation of the propagators are introduced.

4.1 POINT SOURCES

For some applications, such as connected two-point functions (cf. equation (3.36))

$$\begin{aligned} C_{2pt}(t_s, t_0, \mathbf{p}) &= -\sum_{\mathbf{y}} e^{-i\mathbf{p}\cdot(\mathbf{y}-\mathbf{x})} \left\langle \mathrm{Tr}_{CD}\left[S(y,x)\ \Gamma^\dagger\ S(x,y)\ \Gamma\right]\right\rangle_G \\ &= -\sum_{\mathbf{y}} e^{-i\mathbf{p}\cdot(\mathbf{y}-\mathbf{x})} \left\langle \mathrm{Tr}_{CD}\left[S(y,x)\ \Gamma^\dagger\ \gamma_5 S^\dagger(y,x)\gamma_5\ \Gamma\right]\right\rangle_G , \end{aligned} \tag{4.1}$$

it is sufficient to have knowledge of the point-to-all propagator, i.e. the propagator $S(y,x)$ from a fixed lattice point x to all other points y. In the second row of (4.1) we have used the γ_5-hermiticity of the propagator, i.e. $S(x,y) = \gamma_5 S^\dagger(y,x)\gamma_5$, which follows from the γ_5-hermiticity of the Wilson-Dirac operator. The point-to-all propagator can be calculated using point sources

$$\xi_{\alpha\alpha_0 cc_0 x x_0} = \delta^{(4)}_{x x_0}\delta_{\alpha\alpha_0}\delta_{cc_0}\ , \tag{4.2}$$

i.e. a vector, which has only one non-vanishing entry for a given lattice point x_0, Dirac index α_0 and color index c_0. The solution of the Dirac equation for the point source (4.2) provides the propagator from the lattice point x_0, Dirac index α_0 and color index c_0 to all other points x, Dirac indices α and color indices c according to

$$\sum_{y,\beta,d} D(x,y)^{cd}_{\alpha\beta}\ D^{-1}(y,x_0)^{dc_0}_{\beta\alpha_0} = \delta^{(4)}_{x x_0}\delta_{\alpha\alpha_0}\delta_{cc_0}\,. \tag{4.3}$$

$D^{-1}(y,x_0)^{dc_0}_{\beta\alpha_0} = S(y,x_0)^{dc_0}_{\beta\alpha_0}$ in equation (4.3) is the $\{x_0,\alpha_0,c_0\}$ column of the propagator matrix. To obtain the full point-to-all propagator as needed in the calculation of the two-point function (4.1), 12 point sources have to be used, one for every combination of Dirac and color indices.

4.2 SMEARING

As discussed in the previous chapter, a hadron creation operator $\phi^\dagger$ does not only create the ground state but also excited states with the same quantum numbers. If one calculates for example the two-point function (3.41)

$$C_{2pt}(t_s, t_0, \mathbf{p}) = \sum_j \frac{Z_j^2(\mathbf{p})}{2E_j(\mathbf{p})}\, e^{-(t_s - t_0)E_j}, \tag{4.4}$$

using point sources, the overlap factors Z_j for $j > 1$, and therefore the contamination with excited states, might be large, and a large time separation between source and sink is needed to rely on excited states to have sufficiently died out. The idea of *smearing* [57] is to enhance the ground state compared to the excited states by maximizing Z_1/Z_j for $j > 1$. This can be achieved by applying appropriate smearing operators $M(x,y)^{cd}_{\alpha\beta}$ to the quark fields,

$$\tilde{q}(x)^c_\alpha = M(x,y)^{cd}_{\alpha\beta}\, q(y)^d_\beta\,, \tag{4.5}$$

to obtain the smeared quark field $\tilde{q}$. For Gaussian smearing [58–60] one choses

$$M = (\mathbb{1} + \kappa_G\, H)^k\,, \tag{4.6}$$

with the hopping matrix H and a real number κ_G. If the number k of iterations is large enough, this results in an approximately Gaussian shape of the quark field. Besides k, one can tune the parameter κ_G such that one obtains good overlap with the ground state. In this thesis we use the smearing parameters that have been tuned by Benjamin Jäger [61].
Technically, smearing of the quark fields at the source can be achieved by solving the Dirac equation with a smeared source instead of a point source,

$$\sum_{y,\beta,d} D(x,y)^{cd}_{\alpha\beta}\;\; \tilde{S}(y,x_0)^{dc_0}_{\beta\alpha_0} = M(x,z)^{ce}_{\alpha\gamma}\, \delta^{(4)}_{zx_0}\delta_{\gamma\alpha_0}\delta_{ec_0}, \tag{4.7}$$

to obtain a source-smeared propagator $\tilde{S}$. Applying the smearing operator also to the source-smeared propagator,

$$\tilde{\tilde{S}}(x,z)^{ce}_{\alpha\gamma} = M(x,y)^{cd}_{\alpha\beta}\;\; \tilde{S}(y,z)^{de}_{\beta\gamma}\,, \tag{4.8}$$

one obtains the smeared-smeared quark propagator $\tilde{\tilde{S}}$, which is smeared at the source and the sink.

In the following, we will refer to correlation functions, which have been calculated without smearing as local-local (LL), correlation functions with smearing only at the source as smeared-local (SL) and correlation functions with smearing on source and sink as smeared-smeared (SS).

4.3 THE EXTENDED PROPAGATOR METHOD

Beside propagators starting from a fixed source point x, the connected three-point function (cf. equation (3.49))

$$C^{con}_{3pt} = \sum_{y,z} e^{iq\cdot(z-x)} e^{-ip\cdot(y-x)} \left\langle \mathrm{Tr}_{CD}\left[S(y,x)\;\Gamma^\dagger\; S(z,y)\;\Gamma^{\mathcal{O}}\; S(x,z)\;\Gamma\right]\right\rangle_G \tag{4.9}$$

also includes the propagator $S(y,z)$, which would naively require the propagator from every lattice point to all lattice points. However, one can avoid the calculation of the all-to-all propagator for three-point functions by using the extended propagator method [62]. The three-point function (4.9) can be rewritten as

$$C_{3pt}^{con} = \sum_{z} e^{iq\cdot(z-x)} \left\langle Tr_{CD}\left[\Sigma(z,x)\ \Gamma^{\mathcal{O}}\ S(x,z)\ \Gamma\right]\right\rangle_{G} \tag{4.10}$$

with the extended propagator

$$\Sigma(z,x) = \sum_{y} e^{-ip\cdot(y-x)}\, S(y,x)\ \Gamma^{\dagger}\ S(z,y)\,. \tag{4.11}$$

After the point-to-all propagator $S(y,x)$ has been calculated using a point source (or smeared point source) at the lattice point x, the extended propagator can be obtained by another inversion of the Dirac operator,

$$\sum_{z} D(m,z)\Sigma(z,x) = e^{-ip\cdot(m-x)}\,\Gamma^{\dagger}\,S(m,x)\,, \tag{4.12}$$

where the point-to-all propagator is used as a source. A sketch of the extended propagator $\Sigma(z,x)$ is given in figure 4.1.

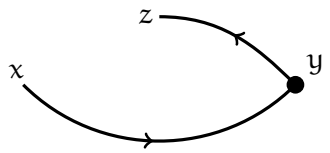

Figure 4.1: Sketch of the extended propagator $\Sigma(z,x)$ for mesons.

From equation (4.12) it is clear that a new extended propagator has to be calculated for every sink momentum $\mathbf{p}$ and Γ-structure.

4.4 STOCHASTIC SOURCES

As soon as a disconnected loop $L(\mathbf{q},z_0)$ is involved in a correlation function, e.g. in the disconnected three-point functions (cf. equation (3.49)), it is essential to have knowledge of the propagator from every lattice point to every lattice point (*all-to-all propagator*) to estimate the trace

$$L(\mathbf{q},z_0) = \sum_{z} e^{i\mathbf{q}\cdot z}\ Tr_{CD}\left[S(z,z)\ \Gamma\right]\,. \tag{4.13}$$

A calculation with point sources (4.2) would require to solve the Dirac equation $12V$ times, where V is the total number of lattice points. For a typical lattice (cf. table 3.1), $12V$ is of the order $\mathcal{O}(10^8)$ to $\mathcal{O}(10^9)$, and thus a calculation with point sources is clearly unacceptable in computational costs. However, the full all-to-all propagator can be obtained using the method of stochastic sources [63–66].

For the calculation of the propagator with stochastic sources, one needs N random vectors η_i with $i = 1,\cdots,N$. The random numbers have to be chosen such that

(a) for every entry (x, α, c) the mean over the N sources has to vanish in the limit $N \to \infty$,

$$\lim_{N\to\infty} \frac{1}{N} \sum_{i=1}^{N} \eta_i(x)^c_\alpha = 0\,, \tag{4.14}$$

(b) in the limit $N \to \infty$ the random vectors fulfill

$$\lim_{N\to\infty} \frac{1}{N} \sum_{i=1}^{N} \eta_i(x)^c_\alpha \; \eta_i^\dagger(y)^d_\beta = \delta^{(4)}_{x,y} \delta_{\alpha\beta} \delta_{cd}\,. \tag{4.15}$$

Suitable choices for stochastic sources are for example $Z_2 \otimes Z_2$ sources, where the random numbers are picked from

$$Z_2 \otimes Z_2 = \left\{ \frac{1}{\sqrt{2}} (\pm 1 \pm i) \right\}, \tag{4.16}$$

or $U(1)$ sources. For $U(1)$ sources every entry of the stochastic source η_i is a random $U(1)$-number, i.e.

$$\eta_i(x)^c_\alpha = e^{i\phi} \tag{4.17}$$

with a randomly chosen phase $\phi \in [0, 2\pi)$. It is straightforward to check the conditions (4.14) and (4.15) for $Z_2 \otimes Z_2$ as well as for $U(1)$ sources, where both choices lead to comparable stochastic noise [67] and are thus equally well suited for the calculation of the all-to-all propagator. In this work we use $U(1)$ stochastic sources.
For every stochastic source, one has to solve the Dirac equation

$$\sum_{y,\beta,d} D(x,y)^{cd}_{\alpha\beta} \; s_i(y)^d_\beta = \eta_i(x)^c_\alpha\,. \tag{4.18}$$

Multiplying equation (4.18) with $\eta_i^\dagger(z)^e_\gamma$ from the right and taking the mean over N stochastic sources, one obtains

$$\begin{aligned} \lim_{N\to\infty} \frac{1}{N} \sum_{i=1}^{N} \sum_{y,\beta,d} D(x,y)^{cd}_{\alpha\beta} \; s_i(y)^d_\beta \; \eta_i^\dagger(z)^e_\gamma &= \lim_{N\to\infty} \frac{1}{N} \sum_{i=1}^{N} \eta_i(x)^c_\alpha \; \eta_i^\dagger(z)^e_\gamma \\ &= \delta^{(4)}_{x,z} \delta_{\alpha\gamma} \delta_{ce}\,, \end{aligned} \tag{4.19}$$

where in the last step the condition (4.15) for stochastic sources has been used. Equation (4.19) implies that the propagator can be calculated as

$$S(y,z)^{de}_{\beta\gamma} = D^{-1}(y,z)^{de}_{\beta\gamma} = \lim_{N\to\infty} \frac{1}{N} \sum_{i=1}^{N} s_i(y)^d_\beta \; \eta_i^\dagger(z)^e_\gamma\,. \tag{4.20}$$

For the estimate of a disconnected loop (4.13), which is required for e.g. the scalar form factor of the pion, the trace of the propagator calculated with stochastic sources is simply the scalar product

$$\begin{aligned} &\sum_z e^{iq\cdot z} \; \mathrm{Tr}_{CD} \left[\Gamma \; S(z,z)\right] = \sum_z e^{iq\cdot z} \; \mathrm{Tr}_{CD} \left[\Gamma \sum_{i=1}^{N} s_i(z) \; \eta_i^\dagger(z)\right] \\ &= \sum_{i=1}^{N} \sum_z e^{iq\cdot z} \; \mathrm{Tr}_{CD} \left[\eta_i^\dagger(z) \; \Gamma \; s_i(z)\right] = \sum_{i=1}^{N} \sum_z e^{iq\cdot z} \; \left(\eta_i^\dagger(z) \cdot \Gamma \; s_i(z)\right) \end{aligned} \tag{4.21}$$

due to the cyclicity of the trace. Thus, for the practical computation of the disconnected loop, one has to follow the steps

1. create a random source η_i,
2. solve the Dirac equation for this source, i.e. $D\, s_i = \eta_i$,
3. calculate the scalar product of $\eta_i^\dagger$ and $\Gamma\, s_i$ and sum over the spatial lattice points including the Fourier phase.
4. repeat steps 1. to 3. N times, sum the results and normalize by N.

For N random sources, the statistical error from the inversion with stochastic sources is expected to scale like $1/\sqrt{N}$. Note that in general the gauge average and the stochastic average commute. Thus, a gauge average also includes an average over different stochastic sources, and it is sufficient to use only a few stochastic sources per gauge configuration for the propagator calculation.

As indicated in equation (4.13), we need the loop $L(\mathbf{q}, z_0)$ for every time z_0 on the lattice. Thus, we use N time-diluted stochastic sources that have entries on only one single timeslice and repeat the calculation for every time z_0. In total we need $T \cdot N$ inversions for the calculation of the disconnected loop, where T is the temporal extend of the lattice and N is the number of stochastic sources. N can be chosen small, such that $T \cdot N \ll 12V$.

Since the method of stochastic sources provides the all-to-all propagator, it is also possible to calculate connected diagrams using stochastic sources. For the calculation of connected two-point functions using stochastic sources, one usually applies the "one-end-trick" [68, 69]. However, the two-point functions used in this thesis have been calculated with (smeared) point sources as explained in section 4.1.

4.5 THE HOPPING PARAMETER EXPANSION

When calculating the all-to-all propagator using stochastic sources, the Dirac equation has to be solved for every source. Since solving the Dirac equation is expensive in computational costs, one is interested in using as few stochastic sources as possible. However, a decrease of the number N of sources results in an increase of the statistical error $\propto 1/\sqrt{N}$. Therefore, one needs noise reduction methods to achieve a sufficient accuracy of the results without significantly increasing the required computer time. In the past few years several different noise reduction techniques have been tested, such as different dilution schemes [70, 71], truncated solver methods [67, 72], low-mode averaging [73–75] and hopping parameter expansions [67, 76]. In our previous work [20], we found that the hopping parameter expansion is a powerful tool for the reduction of the statistical error in the calculation of disconnected loops using stochastic sources. In the following the hopping parameter expansion is explained for the unimproved and the $\mathcal{O}(a)$-improved Wilson-Dirac Operator.

4.5.1 *The unimproved Wilson-Dirac Operator*

The unimproved Wilson-Dirac operator (2.30) has the general form

$$D_W = \frac{1}{2\kappa}\mathbb{1} - \frac{1}{2}H \tag{4.22}$$

with the hopping parameter κ and the hopping matrix H, which contains the couplings between neighboring lattice points. In (4.22) we have set $a = 1$ for simplicity. Since one is interested in the inverse of the Dirac-operator,

$$D_W^{-1} = \left(\frac{1}{2\kappa}\mathbb{1} - \frac{1}{2}H\right)^{-1}, \tag{4.23}$$

one can apply a geometric series expansion in κ [67, 76], the *hopping parameter expansion* (HPE)

$$D_W^{-1} = 2\kappa \sum_{i=0}^{\infty} (\kappa H)^i \tag{4.24a}$$

$$= 2\kappa \sum_{i=0}^{k-1} (\kappa H)^i + 2\kappa \sum_{i=k}^{\infty} (\kappa H)^i . \tag{4.24b}$$

Since the hopping matrix H allows to "hop" from one lattice point to a neighboring point, equation (4.24a) implies that the propagator from x to y can be written as the sum over all possible paths between those two lattice points as depicted schematically in figure 4.2. Every path is weighted with κ^i, where i is the length of the path in lattice units. Since the hopping parameter $\kappa < 1$, the leading term in the propagator is given by the shortest paths.

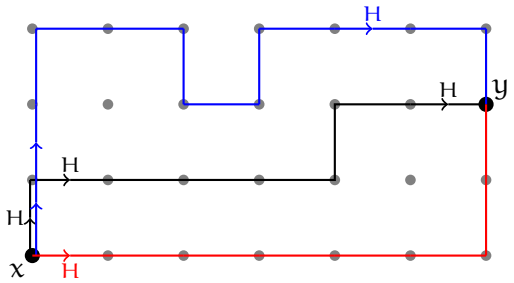

Figure 4.2: Some possible paths between x and y on a two-dimensional lattice. Different paths are denoted by different colors. The propagator D_W^{-1} can be written as the sum over all possible paths between x and y (4.24a).

The idea of the hopping parameter expansion is, to calculate the shortest paths explicitly and estimate the rest of the paths using stochastic sources by rewriting equation (4.24b)

$$D_W^{-1} = 2\kappa \sum_{i=0}^{k-1} (\kappa H)^i + (\kappa H)^k \cdot D_W^{-1} . \tag{4.25}$$

The inverse D_W^{-1} one the right-hand side can be calculated using stochastic sources while paths with length $i < k$ are calculated exactly. The stochastic noise in the calculation of D_W^{-1} one the right-hand side is suppressed by κ^k. Therefore the HPE can be used to reduce the statistical error in the calculation of the all-to-all propagator.

4.5.2 *The $\mathcal{O}(a)$-improved Wilson-Dirac Operator*

Due to the additional clover term, the $\mathcal{O}(a)$-improved Wilson-Dirac operator is not of the form (4.22), but of the form (cf. equation (2.39))

$$D_{sw} = \frac{1}{2\kappa}\mathbb{1} - \frac{1}{2}H + c_{sw}B \tag{4.26}$$

with the $\mathcal{O}(a)$-improvement term $c_{sw}B$. The matrix B is local, i.e. it does not couple different lattice points. To perform a geometric series as done for the unimproved case, we have to rewrite the improved operator (4.26) as

$$D_{sw} = A - \frac{1}{2}H = A\left(\mathbb{1} - \frac{1}{2}A^{-1}H\right), \tag{4.27}$$

with the matrix

$$A = \frac{1}{2\kappa}\mathbb{1} + c_{sw}B\,. \tag{4.28}$$

The form of the right-hand side of equation (4.27) implies that a geometric series expansion can be performed for the expression in the brackets, which leads to the following expansion for the $\mathcal{O}(a)$-improved Wilson-Dirac operator

$$D_{sw}^{-1} = \sum_{i=0}^{k-1}\left(\frac{1}{2}A^{-1}H\right)^i A^{-1} + \left(\frac{1}{2}A^{-1}H\right)^k D_{sw}^{-1}\,. \tag{4.29}$$

Again, the inverse D_{sw}^{-1} on the right hand side can be estimated using the method of stochastic sources, whereas the largest contributions to the propagator

$$X = \sum_{i=0}^{k-1}\left(\frac{1}{2}A^{-1}H\right)^i A^{-1} \tag{4.30}$$

can be calculated explicitly. Practically, one can also estimate the trace of this term with stochastic sources using (4.15)

$$\frac{1}{N}\sum_{i=1}^{N}|\eta_i\rangle\langle\eta_i| \approx \mathbb{1} \tag{4.31}$$

and

$$\begin{aligned}
\mathrm{Tr}\,[X] &= \mathrm{Tr}\left[\sum_{i=0}^{k-1}\left(\frac{1}{2}A^{-1}H\right)^i A^{-1}\right] \\
&\approx \frac{1}{N}\sum_{i=1}^{N}\mathrm{Tr}\left[\sum_{i=0}^{k-1}\left(\frac{1}{2}A^{-1}H\right)^i A^{-1}|\eta_i\rangle\langle\eta_i|\right] \\
&= \frac{1}{N}\sum_{i=1}^{N}\langle\eta_i|\sum_{i=0}^{k-1}\left(\frac{1}{2}A^{-1}H\right)^i A^{-1}|\eta_i\rangle\,.
\end{aligned} \tag{4.32}$$

Since this estimate is cheap in computational costs compared to the inversion of the Dirac operator, we use a large number of sources $N = 50$.

For the hopping parameter expansion of the $\mathcal{O}(a)$-improved Wilson-Dirac operator (4.29), we additionally need to calculate the inverse of the matrix A defined in (4.28). Since the $\mathcal{O}(a)$-improvement term is local, i.e. it does not couple different lattice points, A is diagonal in position space. In Dirac and color space it is given by (cf. equation (2.39))

$$A = \frac{1}{2\kappa} + c_{sw} \frac{i}{4} \sigma_{\mu\nu} \hat{F}_{\mu\nu} \,. \tag{4.33}$$

If one inserts the Euclidean gamma matrices in the chiral representation (cf. A.3) in the definition of the matrix A (4.33), one obtains the following block diagonal form in Dirac space [77]

$$A = \begin{pmatrix} \tilde{A}_+ & 0 \\ 0 & \tilde{A}_- \end{pmatrix} . \tag{4.34}$$

The matrices $\tilde{A}_\pm$ are 6×6 matrices

$$\tilde{A}_\pm = \left(\frac{1}{2\kappa} + c_{sw} \frac{i}{16} \sum_{k=1}^{3} \sigma_k \left(\mathcal{E}_k \mp \mathcal{B}_k \right) \right) , \tag{4.35}$$

with the Pauli matrices σ_k and the electric $\mathcal{E}_k$ and magnetic $\mathcal{B}_k$ components of the field strength tensor,

$$\mathcal{E}_k = 8\hat{F}_{0k} \,, \qquad \mathcal{B}_k = \sum_{i,j=1}^{3} 4\epsilon_{ijk} \hat{F}_{ij} \,. \tag{4.36}$$

This block-diagonal form of the matrix A implies that the calculation of A^{-1} requires the inversion of two 6×6 matrices for every lattice point. These inversions are cheap compared to solving the Dirac equation and can be done e.g. using the Householder triangularization. For this purpose we were able to use existing code [77] implemented in the DD-HMC program by Martin Lüscher.

If one sets the $\mathcal{O}(a)$-improvement parameter $c_{sw} = 0$ one obtains

$$A = \frac{1}{2\kappa} \mathbb{1} \qquad \Rightarrow \qquad A^{-1} = 2\kappa \, \mathbb{1} \,. \tag{4.37}$$

Inserting this into (4.29) one recovers the hopping parameter expansion (4.25) for the unimproved Wilson-Dirac operator. In the following we will refer to the hopping parameter expansion for the $\mathcal{O}(a)$-improved Wilson-Dirac operator as the *generalized hopping parameter expansion* (gHPE).

To optimize the calculation of the disconnected loop contribution with stochastic sources and the gHPE, one can tune two parameters – the order of the hopping parameter expansion k and the number of stochastic sources N for the estimate of the remaining inverse D_{sw}^{-1}. In our previous work [20], we tested different combinations of k and N. In figure 4.3 the relative error on the scalar loop (i.e. $\Gamma = \mathbb{1}$)

$$L(\mathbf{p} = 0, t = 0) = \sum_{x} \mathrm{Tr}_{CD} \left[S(x, x) \right] \tag{4.38}$$

for $t = 0$ and vanishing momentum $\mathbf{p} = 0$ is plotted against $1/\sqrt{N}$ for a light quark (u,d) propagator. For this study the gauge average has been taken on 33 gauge configurations of the E4 ensemble (cf. table 3.1). This gauge average has been calculated for $k = 2, 4, 6$ as well as without gHPE (i.e. stochastic estimate only), each with $N = 3, 5, 7$ stochastic sources.

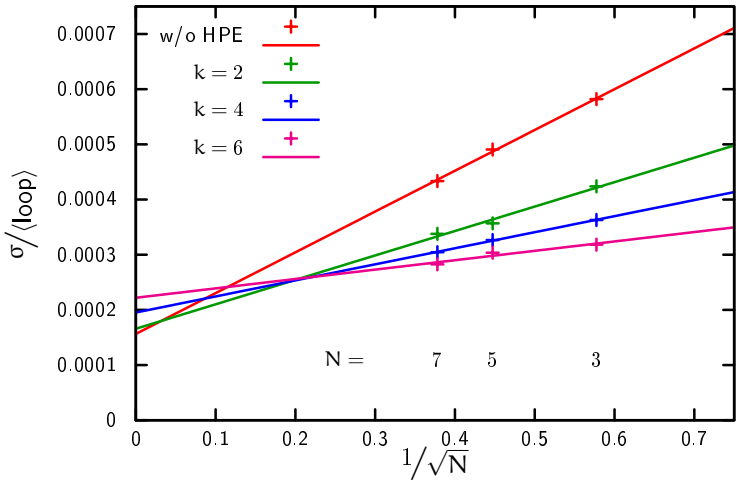

Figure 4.3: The relative error for the loop (4.38) calculated with order $k = 2, 4, 6$ terms in the gHPE as well as without hopping parameter expansion. For each case $N = 3, 5, 7$ stochastic sources have been used. The data are taken from [20].

From the plot one can clearly see the gain of the generalized hopping parameter expansion. The higher the order k of the gHPE, the larger is the reduction of the statistical uncertainty. Furthermore one can observe the expected dependence in the number of stochastic sources $\sigma \propto 1/\sqrt{N}$, which is indicated by linear curves fitted to the data to guide the eye. The remaining stochastic error at $1/\sqrt{N} = 0$, i.e. $N \to \infty$, is the gauge noise from averaging over a finite number of configurations of the gauge fields.
Since the most expensive part of the calculation of the disconnected loop is to solve the Dirac equation for every source, one is interested in using as few sources as possible. From figure 4.3 we can conclude that $N = 3$ sources is enough when using the gHPE. Using $k = 6$ compared to the stochastic method only, we achieve a reduction of the error by a factor ≈ 2. To have a good balance of the required computational costs and the stochastic accuracy, we use $N = 3$ stochastic sources and $k = 6$ for the calculation of the disconnected loops.
Note that this study has been made for the light (u,d) quark. For heavier quarks, which have a smaller hopping parameter κ, the optimal choice of the parameters N and k is different [78]. For the calculation of the disconnected contribution to the anomalous magnetic moment of the muon we will also use strange quark loops. Although our choice of $N = 3$ and $k = 6$ is not optimal for the strange quark, we find that for the disconnected contribution to the hadronic vacuum polarization it is advantageous to have light and strange quark loops, that have been calculated with exactly the same stochastic sources (cf. section 9.1.2). Thus, the strange quark loops used in this thesis are estimated using the same stochastic sources as the light quarks, i.e. $N = 3$ and $k = 6$.

Part II

SCALAR PION FORM FACTOR

5

INTRODUCTION

Lattice techniques are a powerful tool to study QCD in the low-energy regime, where a perturbative expansion in the strong coupling is not possible. This allows for a first-principles calculation of quantities concerning the structure of hadrons. In the following, we will concentrate on the scalar form factor of the pion, which is defined as

$$F_s(Q^2) \equiv \langle \pi(p_f) | \, \overline{q}q \, | \pi(p_i) \rangle \tag{5.1}$$

with the four-momentum transfer

$$Q^2 = -(p_f - p_i)^2 \, . \tag{5.2}$$

Due to the euclidean space-time used in lattice calculations, one has access only to space-like momentum transfers $Q^2 \geqslant 0$.
The scalar form factor of the pion occurs in the coupling of a charged pion to a scalar particle, such as the Higgs boson, which has been recently discovered at the Large Hadron Collider at CERN. However, a Higgs with a mass of $m_H \approx 125$ GeV [7, 8] is far too heavy to be detectable in the low energy regime of QCD, and thus a direct experimental evaluation of the scalar form factor is currently not possible.

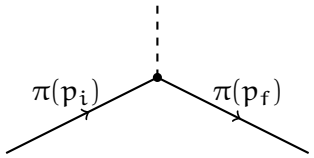

Figure 5.1: Feynman diagram of the coupling of a scalar particle to a pion.

As already discussed in section 3.4, the matrix element of the form

$$\langle \overline{q}\gamma_5 q \, \overline{q}q \, \overline{q}\gamma_5 q \rangle \, , \tag{5.3}$$

which determines the scalar pion form factor, receives a quark-connected and a quark-disconnected contribution.
So far only one lattice calculation of the full scalar pion form factor including disconnected contributions has been performed by the JLQCD/TWQCD collaboration [17–19] on rather small 32×16^3 lattices. Thus, an independent computation with bigger lattices, such as the CLS ensembles, is desirable.

In this thesis, we will calculate the scalar form factor of the pion on the lattice by explicitly calculating the connected and the disconnected contribution to the matrix element (5.1). The use of different momentum transfers Q^2 will allow us to study the momentum dependence of the scalar form factor and to extract the scalar radius of the pion.

The scalar form factor for vanishing momentum transfer $Q^2 = 0$ can also be estimated using the Feynman-Hellman Theorem [79]. For the scalar pion form factor the Feynman-Hellman Theorem yields [27, 80, 81]

$$F_s(0) = \frac{\partial M_\pi^2}{\partial m_{ud}}\,, \tag{5.4}$$

with the light quark mass m_{ud}. Thus, an accurate calculation of the scalar form factor for vanishing momentum transfer using the Feynman-Hellman Theorem (5.4) would ideally require to determine the pion mass from lattices with only slightly different quark masses. Such lattices are not available within the CLS ensembles. Therefore the Feynman-Hellman Theorem is not used in this work and we estimate the form factor for $Q^2 = 0$ also from a direct calculation of the corresponding matrix element (5.1) on the lattice. However, with the appropriate data it could serve as a check of our results for $F_s(0)$.

Once the scalar form factor of the pion has been computed for different values of the momentum transfer Q^2, one can determine the pion scalar radius $\langle r^2 \rangle_s^\pi$, which is defined as the slope of the form factor for vanishing momentum transfer:

$$\langle r^2 \rangle_s^\pi \equiv -\frac{6}{F_s^\pi(0)} \frac{\partial F_s^\pi(Q^2)}{\partial Q^2}\Big|_{Q^2=0}\,. \tag{5.5}$$

Since so far it has not been possible to determine the scalar form factor in an experiment, there is no experimental result for the scalar radius from a direct measurement. However, it is possible to relate the scalar radius of the pion to $\pi\pi$-scattering amplitudes [23–26] and the most recent result is [27]

$$\langle r^2 \rangle_s^\pi = 0.61 \pm 0.04 \text{ fm}^2\,. \tag{5.6}$$

This value can be used as a comparison with our result from a first-principles determination of the scalar pion radius using lattice QCD.

5.1 THE VECTOR FORM FACTOR FROM LATTICE QCD

The electromagnetic form factor of the pion $F_v^\pi\left(Q^2\right)$ has been studied more extensively on the lattice [17, 82–93] than the scalar form factor due to the absence of disconnected diagrams. In addition, it can be measured experimentally, and thus, lattice results can be compared with experimental data. The pion electromagnetic form factor describes the coupling of a charged pion to the vector current and is defined as (cf. (3.57))

$$F_v^\pi\left(Q^2\right) \equiv \left\langle \pi^+\left(p_f\right)\right| \frac{2}{3}\,\bar{u}\gamma_\mu u - \frac{1}{3}\,\bar{d}\gamma_\mu d \left|\pi^+\left(p_i\right)\right\rangle\,. \tag{5.7}$$

The vector form factor of the pion at vanishing momentum transfer corresponds to its electric charge, i.e.

$$F_v^\pi(0) = 1. \tag{5.8}$$

Experimentally the form factor can be measured in the scattering of electrons and pions. The corresponding Feynman diagram is shown in figure 5.2.

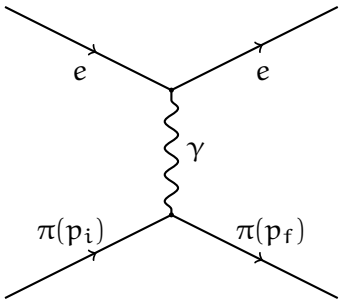

Figure 5.2: Feynman diagram of pion electron scattering.

The slope of the electromagnetic form factor at vanishing momentum transfer $Q^2 = 0$ determines the vector radius of the pion,

$$\left\langle r^2 \right\rangle_V^\pi = -6 \, \frac{\partial F_V^\pi(Q^2)}{\partial Q^2}\Big|_{Q^2=0} . \tag{5.9}$$

Clearly, a fine momentum resolution close to $Q^2 = 0$ of the form factor is desirable to estimate the pion radius. The momenta which are available on the lattice via Fourier transformation are restricted to discrete values (cf. equation (2.2)). However, the introduction of partially twisted boundary conditions in the spatial directions [94, 95] for the valence quarks,

$$q(x + L \cdot \hat{k}) = e^{i\theta_k} q(x) , \tag{5.10}$$

allows tuning the momenta continuously,

$$p_i = \frac{2\pi}{La} \, n_i + \frac{\theta_i}{La} . \tag{5.11}$$

This method has been successfully applied to the calculation of the vector radius of the pion [84, 87–89, 92].
However, the use of partially twisted boundary conditions is not possible for the disconnected contribution to the scalar form factor, since the effect of twisting cancels in flavor singlet quantities. Thus, we have to resort to the use of Fourier momenta in our calculation of the scalar radius of the pion.

Figure 5.3 shows a compilation of various lattice results for the vector radius of the pion. The black point shows the most accurate experimental result

$$\left\langle r^2 \right\rangle_V^\pi = 0.439 \pm 0.008 \text{ fm}^2 \tag{5.12}$$

which has been obtained from the NA7 experiment at CERN in 1989 [96] for a comparison. Clearly, all lattice results show a good agreement with the experimental value, although the errors of all lattice results are larger than the error on the experimentally determined radius.

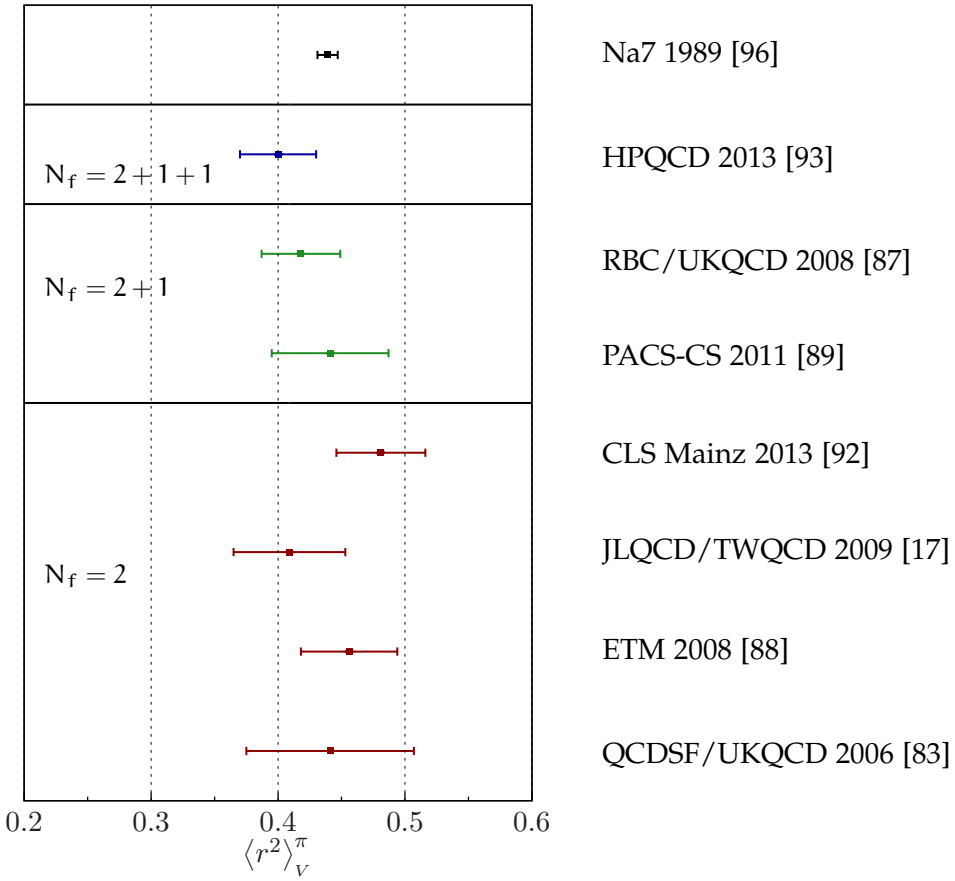

Figure 5.3: The results for the vector radius of the pion from different lattice collaborations compared with the experimental value from the NA7 experiment, which is shown in the upper panel. The three lower panels show results for $N_f = 2+1+1$, $2+1$ and 2 dynamical quark flavors.

5.2 THE SCALAR FORM FACTOR IN CHIRAL PERTURBATION THEORY

Chiral Perturbation Theory[1] (χPT) is an effective field theory for QCD in the low-energy regime. The fundamental degrees of freedom are the low-energy degrees of freedom of QCD, i.e. light mesons and baryons. In χPT one constructs the most general Lagrangian which is consistent with the symmetries of QCD, e.g. the chiral symmetry. These Lagrangians contain low-energy constants, which are *a priori* unknown from the effective theory itself, but can be determined by the underlying theory, i.e. QCD.
Since lattice simulations are usually performed with pions which are heavier than the physical pion one has to extrapolate the obtained results to the physical mass. Such extrapolations can be done using the expressions obtained in chiral perturbation theory. Additionally, results from lattice simulations allow to extract χPT low-energy constants from first principles.

1 An introduction to Chiral Perturbation Theory can be found e.g. in [97].

5.2.1 *Next-to-leading Order*

At next-to-leading order (NLO) in chiral perturbation theory, the scalar radius of the pion is given by [23, 28]

$$\left\langle r^2 \right\rangle_s^\pi = -\frac{1}{(4\pi F)^2}\,\frac{13}{2} + \frac{6}{(4\pi F)^2}\left[\bar{\ell}_4 + \ln\left(\frac{m_{\pi,phys}^2}{m_\pi^2}\right)\right] \tag{5.13}$$

with the pion decay constant $F = 92.2$ MeV [34]. The scalar radius in NLO chiral perturbation theory (cf. equation (5.13)) depends only on one low-energy constant $\bar{\ell}_4$. Thus, a calculation of the scalar pion radius, e.g. from the lattice, provides also a determination of this low-energy constant, alternatively to the determination of $\bar{\ell}_4$ from pseudoscalar meson decay constants. The current FLAG[2] report [98] quotes a value of

$$\bar{\ell}_4|_{N_f=2} = 4.62 \pm 0.22 \tag{5.14}$$

for two dynamical flavors of quarks.

The corresponding NLO χPT formula for the vector radius of the pion is given by [23, 28]

$$\left\langle r^2 \right\rangle_v^\pi = -\frac{1}{(4\pi F)^2} + \frac{1}{(4\pi F)^2}\left[\bar{\ell}_6 + \ln\left(\frac{m_{\pi,phys}^2}{m_\pi^2}\right)\right]. \tag{5.15}$$

Thus, from a calculation of the vector radius the low energy constant $\bar{\ell}_6$ can be determined as done e.g. in [92]. Comparing the χPT formulae of scalar and vector radius, one finds that the pion mass dependence in the chiral logarithm is enhanced by a factor of six for the scalar radius. Thus, one expects a more pronounced pion mass dependence in the scalar case.

The scalar and vector radius of the pion are also known at next-to-next-to-leading order (NNLO) in chiral perturbation theory [25, 80]. The corresponding expressions can be found in the appendix in section B.3. However, we will use NLO chiral perturbation theory for the extrapolation of the scalar radius to the physical pion mass, since the amount of our data is insufficient to constrain all low-energy constants at NNLO.

5.2.2 *Partially Quenched Chiral Perturbation Theory*

Additionally, partially quenched chiral perturbation theory (pqχPT) [99–101] allows to consider different Wick contractions of matrix elements separately with χPT methods. The idea is to introduce an additional quark flavor ν, which has the same mass as the light quarks. However, quarks of different flavors cannot be contracted with each other. In the case of the scalar pion form factor,

2 The Flavour Lattice Averaging Group (FLAG) reviews and summarizes the status of lattice results concerning low-energy physics.

the matrix element $\langle \bar{u}\gamma_5 d\, \bar{d} d\, \bar{d}\gamma_5 u \rangle$ is split into two matrix elements, where one is purely connected and one purely disconnected:

$$\langle \bar{u}\gamma_5 d\, \bar{d} d\, \bar{d}\gamma_5 u \rangle = \langle \bar{u}\gamma_5 v\, \bar{v} d\, \bar{d}\gamma_5 u \rangle + \langle \bar{u}\gamma_5 d\, \bar{v} v\, \bar{d}\gamma_5 u \rangle \,. \tag{5.16}$$

The first term on the right-hand side of equation (5.16) represents the connected contribution and the second term the disconnected one. The sum of both yields the physical scalar form factor. These summands can be calculated separately in chiral perturbation theory. For the scalar form factor this has been done recently [21, 22]. The results are shown in figures 5.4 and 5.5. Both plots are taken from [21].

Figure 5.4 shows the scalar form factor plotted against the four-momentum transfer $t = -Q^2$ for physical pion mass. The connected contribution is shown as the dotted blue line and the disconnected contribution as a dashed green line. The sum of both curves is shown in red and corresponds to the total form factor. For this plot the form factor is normalized such that $F_s(0) = 1$ for vanishing momentum transfer. One can see, that the disconnected contribution is small compared to the connected one. Note that on the lattice, we have only access to space-like momenta $t < 0$, i.e. the left hand-side of this plot. On the right hand-side in the time-like region one can clearly see the two-pion threshold at $t = (2\,m_\pi)^2$.

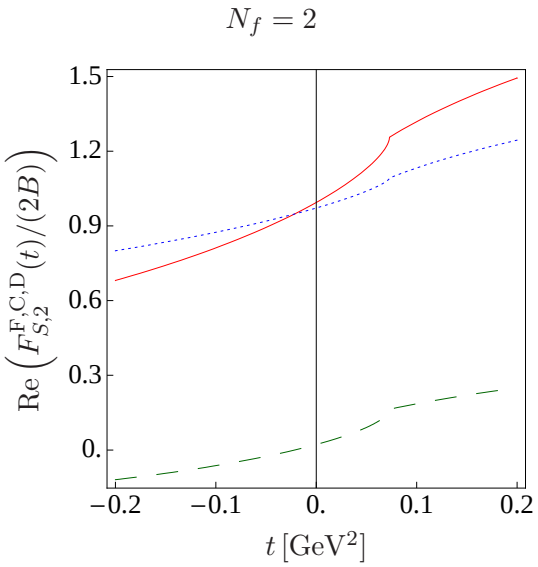

Figure 5.4: The connected (dotted blue), disconnected (dashed green) and total (red) scalar pion form factor from pqχPT plotted against the four momentum transfer $t = -Q^2$ at physical pion mass. The form factor is normalized such that $F_s(0) = 1$. Note that on the lattice one has only access to space-like momenta $t < 0$, i.e. the left side of the plot. In the time-like region one can see the two-pion threshold $t = (2\,m_\pi)^2$. The plot is taken from [21].

In figure 5.5, the scalar pion radius from partially quenched chiral perturbation theory is plotted against the pion mass m_π^2. The dotted blue line shows the connected contribution, the dashed green line the disconnected one. The red

line is the scalar radius from the complete form factor and corresponds to the result from NLO χPT (cf. equation (5.13)). One can see that the disconnected and the connected contribution to the scalar radius, i.e. the slope of the form factor at vanishing momentum transfer, are of the same order. This indicates the importance of the disconnected contribution for the scalar pion radius. Thus, a meaningful result for $\langle r^2 \rangle_s^\pi$ can only be obtained when calculating both the connected and the disconnected contribution.

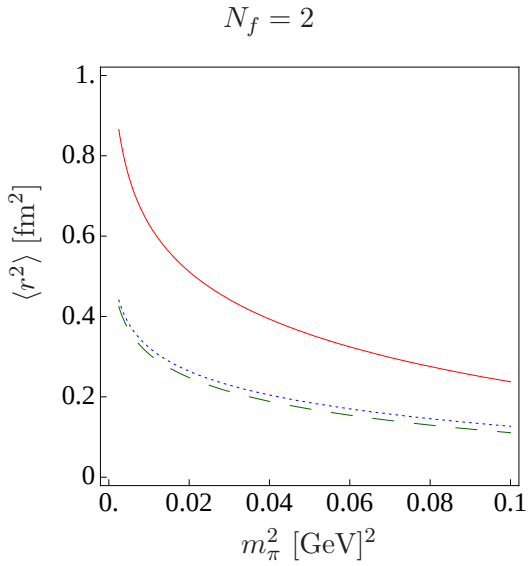

Figure 5.5: The scalar radius of the pion from pqχPT. The dotted blue line shows the connected contribution, the dashed green line the disconnected one. The red line is the scalar radius from the complete form factor. The plot is taken from [21].

6

RESULTS

In the following, we will discuss how the scalar form factor of the pion can be extracted from the three- and two-point functions that can be calculated on the lattice. We will present results for the connected and disconnected contribution to the form factor for three different momentum transfers Q^2. From the Q^2-dependence of the form factor, the scalar pion radius can be determined. The use of gauge ensembles with different pion masses and three different lattice spacings will allow for a chiral and continuum extrapolation to the physical point.

As already discussed in section 3.4, the scalar form factor of the pion appears in the pion three-point function

$$\begin{aligned} C_{3pt}(t_s, t, \mathbf{p}_i, \mathbf{p}_f) &= \langle \pi(t_s, \mathbf{p}) \;\; \mathcal{O}(t, \mathbf{p}_f - \mathbf{p}_i) \;\; \pi(0, \mathbf{p} - \mathbf{q}) \rangle \\ &= \frac{Z_\pi^\dagger(\mathbf{p}_f) Z_\pi(\mathbf{p}_i)}{4 E_\pi(\mathbf{p}_f) E_\pi(\mathbf{p}_i)} \, e^{-(t_s - t) E_\pi(\mathbf{p}_f)} \, e^{-t E_\pi(\mathbf{p}_i)} \langle \pi(\mathbf{p}_f) | \mathcal{O}(\mathbf{p}_f - \mathbf{p}_i) | \pi(\mathbf{p}_i) \rangle \,, \end{aligned} \tag{6.1}$$

where we have placed the pion source at $t_0 = 0$ for simplicity. The matrix element $\langle \pi(\mathbf{p}_f) | \mathcal{O}(\mathbf{p}_f - \mathbf{p}_i) | \pi(\mathbf{p}_i) \rangle$ provides the scalar pion form factor for the momentum transfer $Q^2 = -q^2 = -(E_f - E_i)^2 + (\mathbf{p}_f - \mathbf{p}_i)^2$. This matrix element can be extracted by building ratios of appropriate mesonic three- and two-point functions. In this work we have used two different ratios, which we call R_1 and R_3 along the lines of [102]:

$$R_1(t, t_s, \mathbf{p}_i, \mathbf{p}_f) = \sqrt{\frac{C_{3pt}(t, t_s, \mathbf{p}_i, \mathbf{p}_f) C_{3pt}(t, t_s, \mathbf{p}_f, \mathbf{p}_i)}{C_{2pt}(t_s, \mathbf{p}_i) C_{2pt}(t_s, \mathbf{p}_f)}} \,, \tag{6.2}$$

$$\begin{aligned} R_3(t, t_s, \mathbf{p}_i, \mathbf{p}_f) = &\frac{C_{3pt}(t, t_s, \mathbf{p}_i, \mathbf{p}_f)}{C_{2pt}(t_s, \mathbf{p}_f)} \\ &\times \sqrt{\frac{C_{2pt}(t_s, \mathbf{p}_f) C_{2pt}(t, \mathbf{p}_f) C_{2pt}((t_s - t), \mathbf{p}_i)}{C_{2pt}(t_s, \mathbf{p}_i) C_{2pt}(t, \mathbf{p}_i) C_{2pt}((t_s - t), \mathbf{p}_f)}} \,. \end{aligned} \tag{6.3}$$

In sections 6.1 and 6.2 we will show that, neglecting excited state contributions, these ratios are constant and proportional to the scalar form factor $F_S^\pi(Q^2)$, except for a time-dependent factor, which is an artifact of the periodic boundary conditions used in our lattice calculations. These time-dependencies are analytically known and will be investigated in 6.1.1 and 6.1.2 for the connected and the disconnected contribution, respectively.

As already mentioned in section 2.4, the Wilson fermions that we use in our calculations break the chiral symmetry explicitly even in the case of massless quarks. Due to the chiral symmetry breaking, the scalar operator $\mathcal{O}_S = \bar{q}q$ can mix with the identity and thus, the scalar operator obtains an additive renormalization besides the multiplicative one

$$\left\langle \mathcal{O}_S^R \right\rangle = Z_S \left\langle \mathcal{O}_S - b_0 \right\rangle \,. \tag{6.4}$$

However, as already mentioned in section 3.4, we have to subtract the vacuum contribution from the three-point function in the scalar case. The vacuum contribution

$$C_{vac}(t_s, t, \mathbf{p}_i, \mathbf{p}_f) = C_{2pt}(t_s, \mathbf{p}_f) \sum_{\mathbf{y}} e^{i\mathbf{q}\cdot\mathbf{z}} \langle \mathcal{O}_S(t, \mathbf{z}) \rangle \tag{6.5}$$

undergoes the same additive renormalization and thus the subtraction of the vacuum also subtracts the additive renormalization constant b_0. Thus, we are left with the multiplicative renormalization Z_S for the scalar form factor. Since Z_S has not been determined for the CLS gauge ensembles yet, all the form factor data presented in this thesis are not renormalized. However, in the calculation of the scalar radius of the pion

$$\langle r^2 \rangle_S^\pi = -\frac{6}{F_S^\pi(0)} \frac{\partial F_S^\pi(Q^2)}{\partial Q^2}\Big|_{Q^2=0} \tag{6.6}$$

the multiplicative renormalization drops out, i.e. the scalar radius is independent of the renormalization.

6.1 VANISHING MOMENTUM TRANSFER

Vanishing momentum transfer $Q^2 = 0$ corresponds to choosing the initial and final momentum of the pion to be the same, i.e. $\mathbf{p}_f = \mathbf{p}_i \equiv \mathbf{p}$. Clearly, both ratios R_1 and R_3 are equal in this case

$$R(t, t_s, \mathbf{p}, \mathbf{p}) \equiv R_1(t, t_s, \mathbf{p}, \mathbf{p}) = R_3(t, t_s, \mathbf{p}, \mathbf{p}) = \frac{C_{3pt}(t, t_s, \mathbf{p}, \mathbf{p})}{C_{2pt}(t_s, \mathbf{p})}\,. \tag{6.7}$$

If we insert the expected time behaviors of the three-point (3.55) and the two-point (3.44) function, we obtain

$$R(t, t_s, \mathbf{p}, \mathbf{p}) = \frac{\langle \pi(\mathbf{p})|\mathcal{O}(0)|\pi(\mathbf{p})\rangle}{2E_\pi(\mathbf{p})} \cdot \frac{e^{-t_s E_\pi(\mathbf{p})}}{\left(e^{-t_s E_\pi(\mathbf{p})} + e^{-(T-t_s)E_\pi(\mathbf{p})}\right)}\,. \tag{6.8}$$

Thus, all overlap factors $Z_\pi(\mathbf{p}) = \langle 0|\phi^\dagger(\mathbf{p})|\pi\rangle$ have been canceled. Additionally, the dependence on the time t of the operator insertion drops out, i.e. the ratio R is independent of t. Note that this is only true if excited state contributions are neglected, as was done here. The remaining t_s dependent factor

$$f(t_s) = \frac{e^{-t_s E_\pi(\mathbf{p})}}{\left(e^{-t_s E_\pi(\mathbf{p})} + e^{-(T-t_s)E_\pi(\mathbf{p})}\right)} \tag{6.9}$$

is a consequence of the backward propagating pion in the two-point function due to the periodic boundary conditions used in our lattice calculations. For an infinite lattice $T \to \infty$ this time dependent factor $f(t_s)$ approaches 1 and thus the ratio

$$R(t, t_s, \mathbf{p}, \mathbf{p}) \to \frac{\langle \pi(\mathbf{p})|\mathcal{O}|\pi(\mathbf{p})\rangle}{2E_\pi(\mathbf{p})} \tag{6.10}$$

is the desired form factor up a factor of $(2E_\pi(\mathbf{p}))^{-1}$ for large time separations $0 \ll t \ll t_s$, where excited states can be neglected. Since the pion energy $E_\pi(\mathbf{p})$

can be extracted from the exponential t_s-dependence of the pion two-point function,

$$C_{2pt}(t_s, \mathbf{p}) = \frac{Z_\pi^2(\mathbf{p})}{2E_\pi(\mathbf{p})} \left(e^{-t_s E_\pi(\mathbf{p})} + e^{-(T-t_s)E_\pi(\mathbf{p})} \right) , \tag{6.11}$$

the form factor $F_s(Q^2 = 0)$ can be determined from lattice results for $C_{2pt}(t_s, \mathbf{p})$ and $C_{3pt}(t, t_s, \mathbf{p}, \mathbf{p})$ using the ratio R.

6.1.1 *The Connected Contribution: t_s-Dependence*

In figure 6.1 the ratio R for the connected three-point function is plotted against the operator insertion time t for a fixed value of the pion sink time $t_s = 24$. As an example, we show data for the E5 ensemble with a pion mass of $m_\pi = 456$ MeV, since we have the highest statistics of gauge configurations for this ensemble (cf. table 3.1). We have set the initial and final momentum of the pion to $\mathbf{p} = 0$ and put the pion source at $(0, 0, 0, 0)$. The connected three-point function has been calculated using the extended propagator method. We have applied Gaussian smearing at the pion source and use a local pion sink.

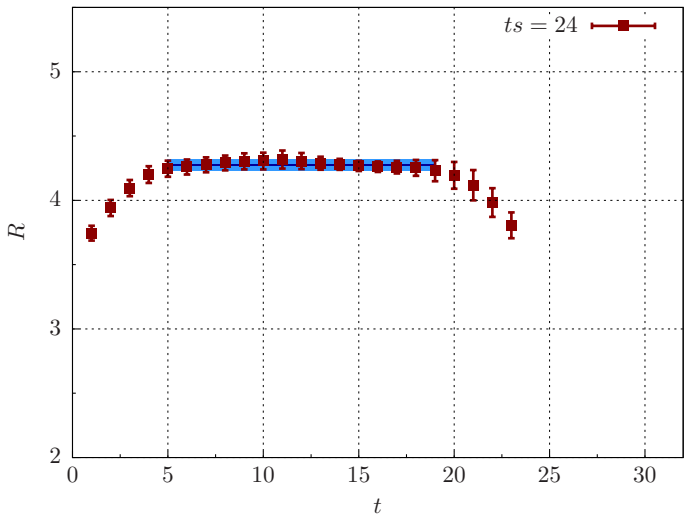

Figure 6.1: The ratios for the connected contribution plotted against the operator insertion time t for a fixed source-sink separation $t_s = 24$. The blue line indicates a fit to the plateau region.

As one can see in figure 6.1, our data form a plateau, when the operator insertion t is far enough away from the source at $t = 0$ and the sink at $t = t_s$. For small times t and large times t close to t_s, there are deviations from the constant, due to excited states. Near the pion source and the pion sink, excited state contributions are still large, before the excited states have died out exponentially. To estimate the value of the ratio for the plateau region, a constant function has been fitted to the data, as indicated by the blue line in figure 6.1. The error on the fit result is shown as a blue band.

To investigate the expected behavior of the ratio on t_s (cf. equation (6.8)) and to check for the influence of excited states, we have repeated this analysis for

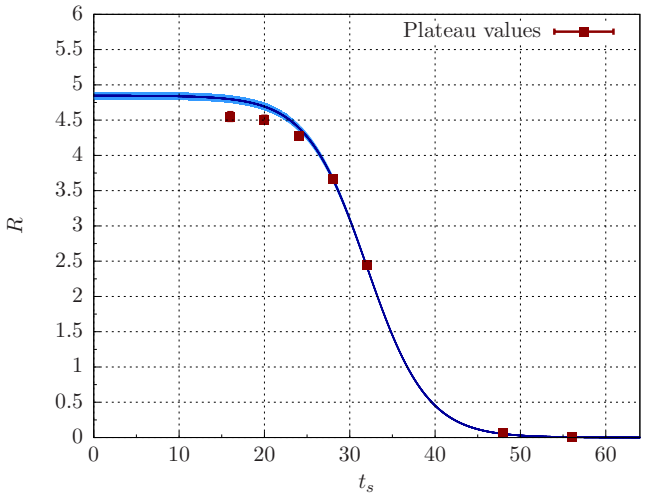

Figure 6.2: The plateau values for the connected contribution plotted against different source-sink separations t_s. A function of the form (6.12) has been fitted to the data to show the expected t_s-dependence.

several values of $t_s = \{16, 20, 24, 28, 32, 48, 56\}$. In figure 6.2 the plateau values are plotted against t_s. A function of the form

$$F(t_s) = A \cdot \frac{e^{-t_s E_\pi(0)}}{\left(e^{-t_s E_\pi(0)} + e^{-(T-t_s)E_\pi(0)}\right)} \tag{6.12}$$

has been fitted to the results to show the expected t_s-dependence. Here, the only fit parameter is A, and the pion mass $E_\pi(0) = m_\pi$ has been taken from a determination using the two-point functions.
As one can see in figure 6.2, the plateau values fulfill this behavior for $t_s \gtrsim 24$. For the smaller values of t_s, our data deviate from the fit function. From this, we can conclude that a small source-sink separation of $t_s < 24$ is not sufficient for the excited states having died out sufficiently such that the data reach a reliable plateau.

6.1.2 *The Disconnected Contribution: t_s-Dependence*

The disconnected contribution to the three-point function factorizes into a quark loop and a connected two-point function. The disconnected quark loop was calculated with $N = 3$ stochastic sources and the order $k = 6$ in the generalized hopping parameter expansion as described in section 4.5. For this purpose we could make use of two-point functions that have been calculated as parts of the projects of Benjamin Jäger [61] and Bastian Knippschild [103]. For both pion source and sink, Gaussian smearing with the same smearing parameters has been used. These pion two-point functions have been calculated for four different pion source positions[1] per gauge configuration, namely

$$(0,0,0,0)\,, \quad (T/4, L/2, L/2, L/2)\,, \quad (T/2, 0, 0, 0)\,, \quad (3T/4, L/2, L/2, L/2)\,,$$

1 For the G8 ensemble we have data for 12 different source positions.

which have been chosen such that they are maximally apart from each other. Since we have calculated the loop on every timeslice anyway, this enables us to increase the statistics for the disconnected contribution by a factor 4 without any additional calculation.

For the disconnected contribution we have performed the same analysis and investigation of the t_s-dependence as for the connected one.
As an example, figure 6.3 shows the ratios obtained for the source-sink separation $t_s = 24$ plotted against t. One can see clearly, that the data fluctuates more than in the connected case, i.e. the relative statistical error is larger. Again, the blue band shows the result of a constant fit to our data. Since both the pion source and sink are smeared with the same parameters, and since $\mathbf{p}_f = \mathbf{p}_i$, we chose a symmetric fit interval for determining the plateau value.

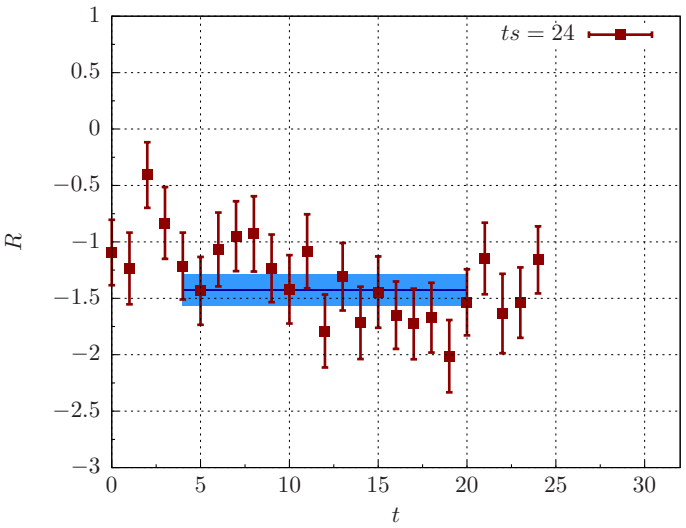

Figure 6.3: The ratios for the disconnected contribution plotted against the operator insertion time t for a fixed source-sink separation $t_s = 24$. The blue line indicates a fit to the plateau region.

Since for the disconnected contribution the values of t_s are not as restricted as for the connected part, where the three-point function is calculated with the extended propagator method and each t_s needs a separate inversion, we used more values of t_s for studying the t_s-dependence:

$$t_s = \{16, 18, 20, 22, 24, 26, 28, 30, 32, 34, 36, 40, 48, 56\}.$$

The plateau values obtained are plotted in figure 6.4 against t_s and a function of the form (6.12) has been fitted to the data as shown by the blue line. As for the connected contribution our results show the expected t_s-dependence for ratios with $t_s \gtrsim 24$. Although the relative statistical error is larger than in the connected case, we can see deviations from the blue line for small values of t_s, indicating the presence of excited states.

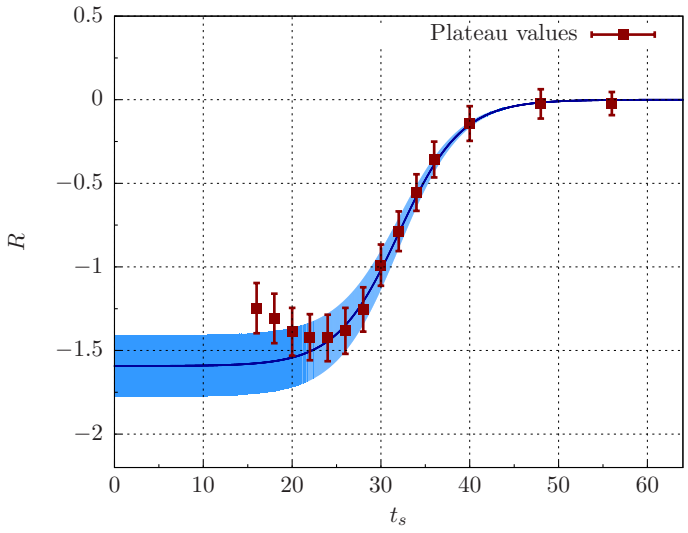

Figure 6.4: The plateau values for the disconnected contribution plotted against different source-sink separations t_s. A function of the form (6.12) has been fitted to the data to show the expected t_s-dependence.

6.1.3 *Global Plateau Fit for Vanishing Momentum Transfer*

As described above, our data for the connected contribution as well as for the disconnected one show the expected dependence on the source-sink separation t_s,

$$R(t, t_s, 0, 0) = A \cdot \frac{e^{-t_s m_\pi}}{\left(e^{-t_s m_\pi} + e^{-(T-t_s)m_\pi}\right)} \equiv A \cdot f(t_s)\,. \tag{6.13}$$

For our final analysis of the scalar form factor for vanishing momentum transfer $Q^2 = 0$, we divide the ratios by the time dependent factor $f(t_s)$, such that any other deviation from a constant is an effect of excited states which have not been considered in the derivation of the time dependence of the three- and two-point functions. The results for $R(t, t_s, 0, 0)/f(t_s)$ are shown for different values of t_s in figure 6.5 for the E5 ensemble.
The trend already observed when investigating the t_s-dependence, namely that the plateaus have not reached the correct value for small values $t_s < 24$, is clearly visible for the connected ratios on the left hand side of figure 6.5. A similar effect has also been observed e.g. for nucleons [104]. For the disconnected contribution this trend is somewhat hidden in the larger statistical fluctuations of the data.

To obtain a final result for the scalar pion form factor at vanishing momentum transfer, we perform a global fit to the plateau regions for the ratios for $t_s \geqslant 24$. Smaller source-sink separations have been excluded from the analysis to avoid systematics from excited states. All t_s values that have been used in the fits, are listed in table 6.1. For the ensembles with different lattice spacings than E5, we have chosen to use only values of t_s with at least the same physical distance as $t_s = 24a \approx 1.5$ fm for E5. The complete fit ranges in t for each ensemble and t_s are given in the appendix in tables B.10-B.16.

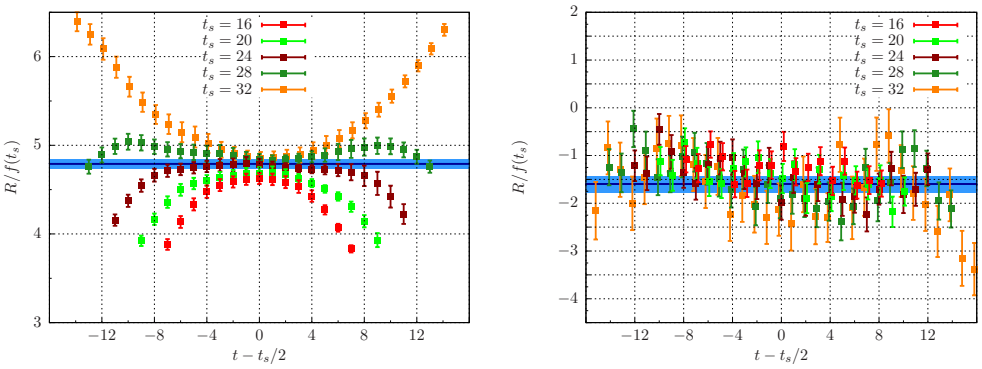

Figure 6.5: The ratios for E5 for $Q^2 = 0$ divided by the t_s-dependent factor (6.9) for the connected part on the left and the disconnected on the right. The blue line indicates the result of a global fit to the ratios for $t_s \geqslant 24$.

ensemble		t_s values used for global fit
A3 - A5	connected	20, 24, 28, 32
	disconnected	20, 22, 24, 26, 28, 30, 32
B6	connected	20, 28, 36, 40, 44, 48
	disconnected	20, 24, 28, 32, 36, 40, 44, 48
E3 - E5	connected	24, 28, 32
	disconnected	24, 26, 28, 30, 32
F6, F7	connected	28, 36, 40, 44, 48
	disconnected	24, 28, 32, 36, 40, 44, 48
G8	connected	24, 32, 40, 48, 56, 64
	disconnected	24, 28, 32, 36, 40, 44, 48, 52, 56, 60, 64
N5, N6	connected	36, 40, 44, 48
	disconnected	32, 36, 40, 44, 48
O7	connected	32, 40, 48, 56, 64
	disconnected	32, 36, 40, 44, 48, 52, 56, 60, 64

Table 6.1: The values of t_s that have been used for the global fits.

The blue lines in figure 6.5 show the result of the global fit. From the fit result, one can obtain the connected and disconnected contribution to the form factor using

$$A_{\text{con/disc}} = \frac{F_S^\pi(0)_{\text{con/disc}}}{2m_\pi} \,. \tag{6.14}$$

For the E5 ensemble we find

$$F_S^\pi(0)_{\text{con}} = 1.36 \pm 0.01 \qquad \text{and} \qquad F_S^\pi(0)_{\text{disc}} = -0.45 \pm 0.04 \,. \tag{6.15}$$

The numerical results for all ensembles are given in the appendix in B.1.7. Similar plots as figure 6.5 for all other ensembles can be found in the appendix in B.1.1 and B.1.2 for connected and disconnected contributions, respectively.

6.1.4 *Comparison of Disconnected and Connected Contribution*

Equation (6.15) indicates, that the disconnected contribution to the scalar form factor at $Q^2 = 0$ is not negligible. We find that it is

$$\frac{F_S^\pi(0)_{\text{disc}}}{F_S^\pi(0)_{\text{con}}} \approx 33\% \tag{6.16}$$

of the connected one for the E5 ensemble. In figure 6.6 the relative contribution of the disconnected compared to the connected contribution $F_S^\pi(0)_{\text{disc}}/F_S^\pi(0)_{\text{con}}$ is plotted against the pion mass for all ensembles. Different lattice spacings are shown in different colors.

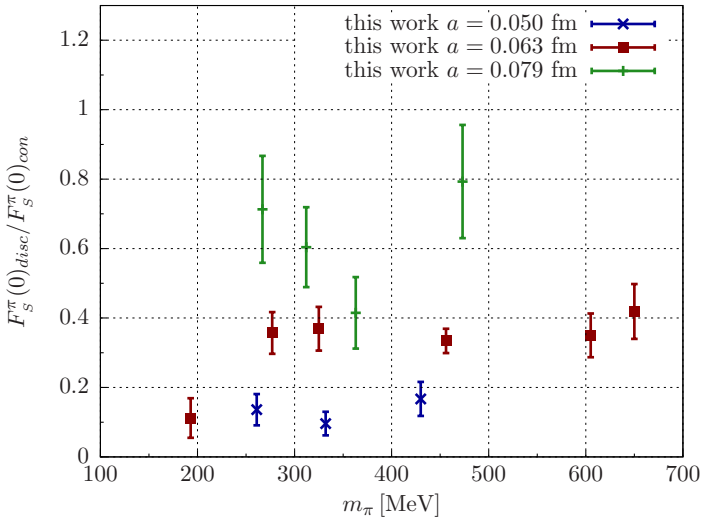

Figure 6.6: The disconnected contribution $F_S^\pi(0)_{\text{disc}}$ to the scalar pion form factor at $Q^2 = 0$ divided by the corresponding connected contribution. Blue, red and green points denote different values of the lattice spacing $a = 0.050$ fm, 0.063 fm and 0.079 fm, respectively.

Except for the lightest ensemble (G8), which might simply be an outlier, we find no significant dependence on the pion mass. However, the relative contribution of the disconnected diagram has a very pronounced dependence on the lattice spacing. The smaller the lattice spacing, the smaller is $F_S^\pi(0)_{\text{disc}}/F_S^\pi(0)_{\text{con}}$. This is in qualitative agreement with the result from partially quenched chiral perturbation theory [21] (cf. figure 5.4), where the disconnected contribution at $Q^2 = 0$ turns out to be very small compared to the connected one in the continuum. This result is also in agreement with a preliminary result of the HPQCD collaboration [105] at physical pion mass. They find a small disconnected contribution to the form factor at $Q^2 = 0$. For their calculation they use a highly improved staggered quark (HISQ) action [106]. Lattice artifacts for the HISQ action are of order $\mathcal{O}(a^4, \alpha_s a^2)$ [107]. Although their lattices are generally coarser then ours, one can expect smaller lattice artifacts in their calculation compared to our results.

6.2 NON-VANISHING MOMENTUM TRANSFER

Since we are interested in the scalar radius of the pion, i.e. the momentum dependence, we also need the scalar form factor for non-vanishing momentum transfer

$$Q^2 = -q^2 = -(p_f - p_i)^2 = -\left((E_\pi(\mathbf{p}_f) - E_\pi(\mathbf{p}_i))^2 - (\mathbf{p}_f - \mathbf{p}_i)^2\right) , \quad (6.17)$$

with the initial and final momentum of the pion $\mathbf{p}_i$ and $\mathbf{p}_f$, respectively. Considering the ratios R_1 and R_3 (compare equations (6.2) and (6.3)),

$$R_1(t, t_s, \mathbf{p}_i, \mathbf{p}_f) = \sqrt{\frac{C_{3pt}(t, t_s, \mathbf{p}_i, \mathbf{p}_f) C_{3pt}(t, t_s, \mathbf{p}_f, \mathbf{p}_i)}{C_{2pt}(t_s, \mathbf{p}_i) C_{2pt}(t_s, \mathbf{p}_f)}} , \quad (6.18)$$

$$R_3(t, t_s, \mathbf{p}_i, \mathbf{p}_f) = \frac{C_{3pt}(t, t_s, \mathbf{p}_i, \mathbf{p}_f)}{C_{2pt}(t_s, \mathbf{p}_f)} \times \sqrt{\frac{C_{2pt}(t_s, \mathbf{p}_f) C_{2pt}(t, \mathbf{p}_f) C_{2pt}((t_s - t), \mathbf{p}_i)}{C_{2pt}(t_s, \mathbf{p}_i) C_{2pt}(t, \mathbf{p}_i) C_{2pt}((t_s - t), \mathbf{p}_f)}} , \quad (6.19)$$

one has to take into account that the overlap factors $Z_\pi(\mathbf{p}) = \langle 0|\phi^\dagger(\mathbf{p})|\pi\rangle$ depend on the source type (e.g. local or smeared) [108]. Considering only the overlap factors, we find that

$$R_1 \propto \sqrt{\frac{Z_\pi(p_i)^{\text{source}} \, Z_\pi(p_f)^{\text{sink}} \, Z_\pi(p_f)^{\text{source}} \, Z_\pi(p_i)^{\text{sink}}}{Z_\pi(p_i)^{\text{source}} \, Z_\pi(p_i)^{\text{sink}} \, Z_\pi(p_f)^{\text{source}} \, Z_\pi(p_f)^{\text{sink}}}} = 1 , \quad (6.20)$$

i.e. in R_1 all overlap factors cancel, as long as all required three- and two-point functions have been calculated with the same source and with the same sink. However, source and sink do not have to be the same. Doing the same for R_3 one obtains

$$\begin{aligned} R_3 \propto & \frac{Z_\pi(p_i)^{\text{source}} Z_\pi(p_f)^{\text{sink}}}{Z_\pi(p_f)^{\text{source}} Z_\pi(p_f)^{\text{sink}}} \\ & \times \sqrt{\frac{Z_\pi(p_f)^{\text{source}} Z_\pi(p_f)^{\text{sink}} Z_\pi(p_f)^{\text{source}} Z_\pi(p_f)^{\text{sink}} Z_\pi(p_i)^{\text{source}} Z_\pi(p_i)^{\text{sink}}}{Z_\pi(p_i)^{\text{source}} Z_\pi(p_i)^{\text{sink}} Z_\pi(p_i)^{\text{source}} Z_\pi(p_i)^{\text{sink}} Z_\pi(p_f)^{\text{source}} Z_\pi(p_f)^{\text{sink}}}} \\ = & \sqrt{\frac{Z_\pi(p_i)^{\text{source}} Z_\pi(p_f)^{\text{sink}}}{Z_\pi(p_f)^{\text{source}} Z_\pi(p_i)^{\text{sink}}}} = \begin{cases} 1 & \text{LL, SS} , \\ \sqrt{\frac{Z_\pi(p_i)^S Z_\pi(p_f)^L}{Z_\pi(p_f)^S Z_\pi(p_i)^L}} & \text{SL} . \end{cases} \end{aligned} \quad (6.21)$$

In R_3 all overlap factors cancel only when the both pion source and sink have been calculated with the same sources, i.e. local-local (LL) or smeared-smeared (SS) with the same smearing on both sides. In the smeared-local case, some overlap factors remain for non-vanishing momentum transfer. Since these factors are *a priori* unknown, R_3 cannot be used for correlation functions that have been calculated with a smeared source and a point-like sink. For the connected contribution we have only data for smeared-local correlation functions available and thus we have to use R_1.

For the disconnected correlation function, we have SS data, thus we can use both R_1 and R_3. An obvious disadvantage of R_1 is the overall square root,

which hides the sign of the form factor. In R_3 the sign is determined by the sign of the three-point function $C_{3pt}(t, t_s, \mathbf{p}_i, \mathbf{p}_f)$. Nevertheless, one can still use $R_1(t, t_s, \mathbf{p}_i, \mathbf{p}_f)$ and assign to the ratio the sign of the corresponding three-point function $C_{3pt}(t, t_s, \mathbf{p}_i, \mathbf{p}_f)$. In figure 6.7 both ratios are shown for the E5 ensemble for a source-sink separation of $t_s = 24$ at a momentum transfer of $Q^2 = 0.278$ GeV^2. One can see, that the errors on R_3 are significantly smaller than the errors on R_1 over a wide range of t. For the values of t where no data point is shown for R_1, the expression under the square root was negative. The reason for this are opposite signs in the three-point functions $C_{3pt}(t, t_s, \mathbf{p}_i, \mathbf{p}_f)$ and $C_{3pt}(t, t_s, \mathbf{p}_f, \mathbf{p}_i)$. Altogether one can conclude that in the case of the disconnected contribution R_3 is superior and thus we will use R_3 in the analysis of the disconnected contribution with non-vanishing momentum transfer.

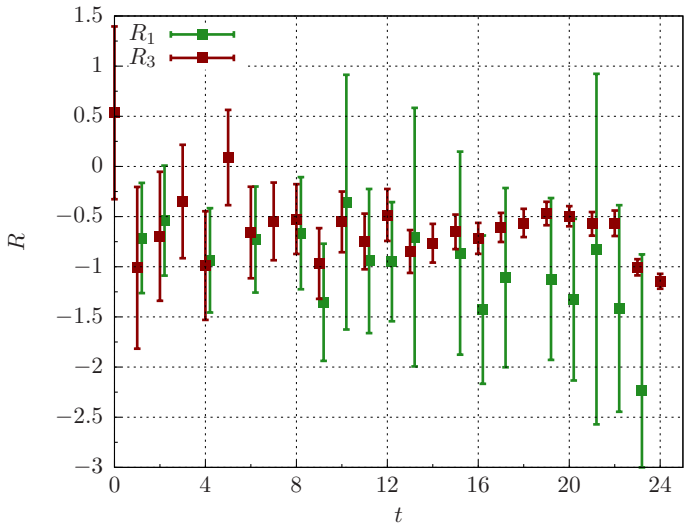

Figure 6.7: Comparison of the ratios R_1 and R_3 for the disconnected contribution. The data shown are for the E5 ensemble for $t_s = 24$ with a momentum transfer of $Q^2 = 0.278$ GeV^2.

To summarize, we use smeared-local data for R_1 to compute the connected part and smeared-smeared data for R_3 for the disconnected contribution to the scalar form factor at non-vanishing momentum transfer.

As in the case of $Q^2 = 0$, both ratios have a remaining time-dependence due to the periodic boundary conditions on our lattice. Inserting the corresponding three- and two-point functions, one finds

$$R_1(t, t_s, \mathbf{p}_i, \mathbf{p}_f) = \frac{\langle \pi(\mathbf{p}_f) | \mathcal{O} | \pi(\mathbf{p}_i) \rangle}{2\sqrt{E_\pi(\mathbf{p}_i) E_\pi(\mathbf{p}_f)}} \times \sqrt{\frac{e^{-E_\pi(\mathbf{p}_i) t_s} e^{-E_\pi(\mathbf{p}_f) t_s}}{(e^{-E_\pi(\mathbf{p}_i) t_s} + e^{-E_\pi(\mathbf{p}_i)(T-t_s)}) \cdot (e^{-E_\pi(\mathbf{p}_f) t_s} + e^{-E_\pi(\mathbf{p}_f)(T-t_s)})}} \,. \tag{6.22}$$

and

$$R_3(t, t_s, \mathbf{p}_i, \mathbf{p}_f) = \frac{\langle \pi(\mathbf{p}_f) | \mathcal{O} | \pi(\mathbf{p}_i) \rangle}{2\sqrt{E_\pi(\mathbf{p}_i) E_\pi(\mathbf{p}_f)}} f(t, t_s) \,, \tag{6.23}$$

with the factor

$$
\begin{aligned}
f(t,t_s) = & \frac{e^{-(t_s-t)E_\pi(\mathbf{p}_f)}\, e^{-tE_\pi(\mathbf{p}_i)}}{\left(e^{-t_s E_\pi(\mathbf{p}_f)} + e^{-(T-t_s)E_\pi(\mathbf{p}_f)}\right)} \\
& \times \sqrt{\frac{\left(e^{-t_s E_\pi(\mathbf{p}_f)} + e^{-(T-t_s)E_\pi(\mathbf{p}_f)}\right)\left(e^{-tE_\pi(\mathbf{p}_f)} + e^{-(T-t)E_\pi(\mathbf{p}_f)}\right)}{\left(e^{-t_s E_\pi(\mathbf{p}_i)} + e^{-(T-t_s)E_\pi(\mathbf{p}_i)}\right)\left(e^{-tE_\pi(\mathbf{p}_i)} + e^{-(T-t)E_\pi(\mathbf{p}_i)}\right)}} \\
& \times \sqrt{\frac{\left(e^{-(t_s-t)E_\pi(\mathbf{p}_i)} + e^{-(T-(t_s-t))E_\pi(\mathbf{p}_i)}\right)}{\left(e^{-(t_s-t)E_\pi(\mathbf{p}_f)} + e^{-(T-(t_s-t))E_\pi(\mathbf{p}_f)}\right)}}
\end{aligned}
\tag{6.24}
$$

for R_1 and R_3 respectively. Again, these factors include the energies of the pion for a given momentum and can be divided out of our results.

For the calculation of the disconnected contribution to the scalar form factor we are restricted to the use of Fourier momenta, since the effect of twisted boundary conditions cancels for flavor-singlet quantities. Thus, we also use only Fourier momenta for the connected contribution (although it would be possible to use momenta from twists) to have both contributions for the same momentum transfers.

6.2.1 *Smallest Non-Vanishing Momentum Transfer*

The smallest non-vanishing momentum transfer on the lattice with Fourier momenta can be achieved with a pion with momentum $|\mathbf{p}_f| = 2\pi/L$ at the sink and momentum $\mathbf{p}_i = 0$ at the source. In the case of the connected contribution, we inserted momentum $(0,0,1)\,2\pi/L$ at the sink. For the disconnected three-point function, we have data for $\mathbf{p}_f = (0,0,1)\,2\pi/L,\ (0,1,0)\,2\pi/L,\ (1,0,0)\,2\pi/L$. The three-point functions with these momenta can be averaged. Together with the four different pion source positions we have $3 \times 4 = 12$ times[2] the statistics for the disconnected form factor with momentum transfer compared to the connected one.

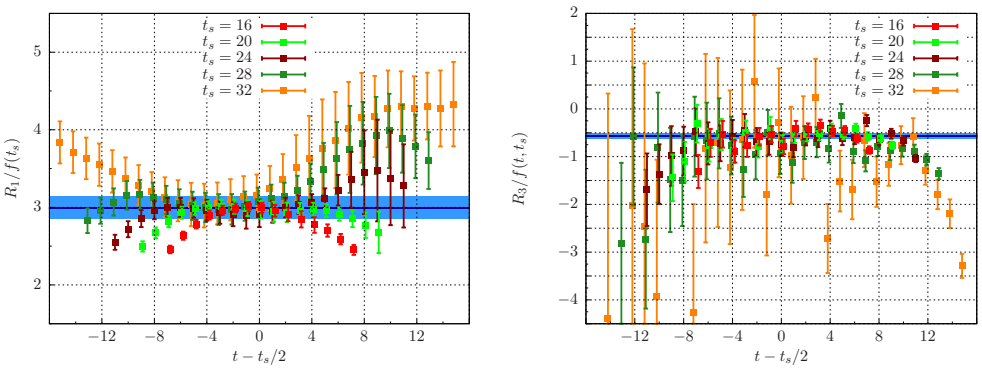

Figure 6.8: The ratios for E5 for the smallest non-vanishing momentum transfer $Q^2 = 0.278$ GeV divided by the t_s-dependent factor (6.22) and (6.24) for the connected and the disconnected part, respectively. The blue line indicates the result of a global fit to the ratios for $t_s \geqslant 24$.

2 We have 12 source positions for G8, i.e. $3 \times 12 = 36$ times the statistics.

Our results for the ratios for different source-sink separations are shown in figure 6.8 for the E5 ensemble. These ratios are already divided by the time-dependent factors (compare equations (6.22) and (6.24)).
Although we cannot observe a trend in the plateau value for increasing t_s as for vanishing momentum transfer, we use only ratios from $t_s \geqslant 24$ for the analysis to be sure that excited states are suppressed. Thus, we use the same source-sink separations as for $Q^2 = 0$ (c.f. table 6.1).
Similar plots as figure 6.8 for the other ensembles can be found in the appendix in B.1.3 and B.1.4. Numerical results for the form factor are given in B.1.8.

6.2.2 *Higher Momentum Transfer*

Additionally, we have also three- and two-point function data for a third momentum transfer, where the pion has a final momentum of $|\mathbf{p}_f| = \sqrt{2}\ 2\pi/L$. However, for non-zero momenta the noise-to-signal ratio for the pion two-point function increases exponentially with the source-sink separation t_s [109–111]

$$R_{NS}(t_s) \propto \exp\left[\left(\sqrt{m_\pi^2 + \mathbf{p}^2} - m_\pi\right)\ t_s\right]. \tag{6.25}$$

In figure 6.9 the pion two-point function is shown for $\mathbf{p} = (0,1,1)\,2\pi/L$. One can clearly see the growing error as t_s approaches the middle $T/2$ in the temporal direction. For large t_s the error can also be larger then the value itself and some points even are negative (and thus are not shown in the plot with a logarithmic axis).

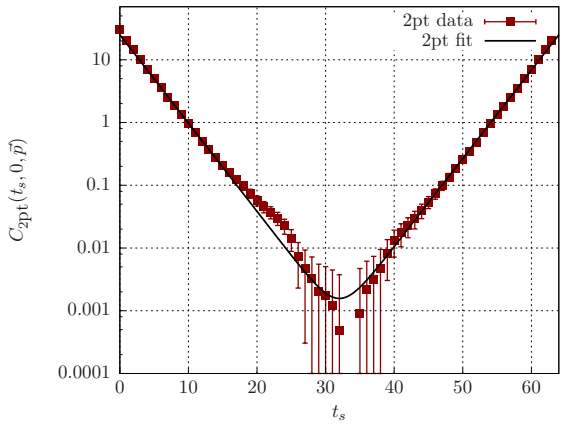

Figure 6.9: The smeared local two-point function for $\mathbf{p} = (0,1,1)\,2\pi/L$ for the E5 ensemble. The black line shows the result of fitting an exponential function of the form (6.26) to the data.

However, depending on the source-sink separation we need the two-point function also in this region for the ratios R_1 and R_3. To avoid using values for the two-point function with large errors or even the wrong sign, we fit an exponential function of the form

$$g(t_s) = A \cdot \left(e^{-E\cdot t_s} + e^{-E\cdot(T-t_s)}\right) \tag{6.26}$$

to the data and use results from the fit instead of the data itself for two-point functions $C_{2pt}(t_s, \mathbf{p}_f)$ with momentum $|\mathbf{p}_f| = \sqrt{2}\, 2\pi/L$ for building the ratios. In figure 6.10 the results for the ratios are shown for the E5 ensemble with a global fit to the plateau regions for $t_s \geqslant 24$. For the disconnected contribution we can again average over four different source positions and three momentum channels.

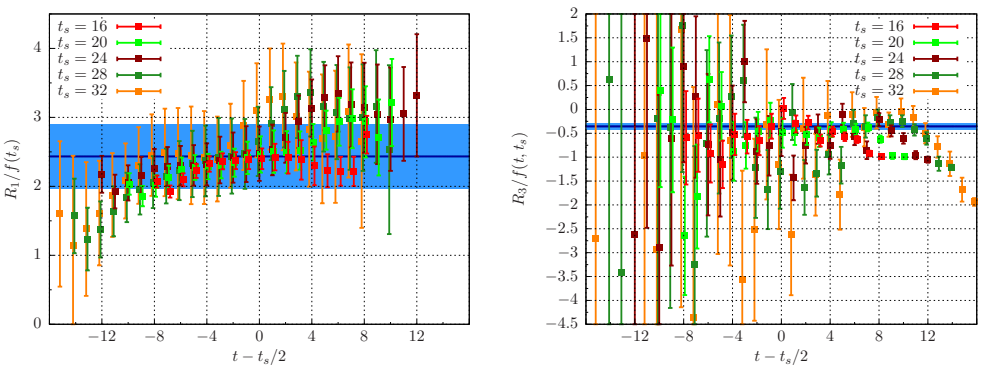

Figure 6.10: The ratios for E5 for $Q^2 = 0.471$ GeV divided by the t_s-dependent factor (6.22) and (6.24) for the connected and the disconnected contribution, respectively. The blue line indicates the result of a global fit to the ratios for $t_s \geqslant 24$.

Similar plots for the other ensembles can be found in B.1.5 and B.1.6. Numerical results are given in B.1.9. For the G8 ensemble the noise of the connected three-point function with $\mathbf{p}_f = (0, 1, 1)\, 2\pi/L$ was already too large to obtain a useful signal from which the form factor can be extracted. Thus, we have to resort to using only two different momentum transfers for the G8 ensemble.

6.3 Q^2-DEPENDENCE AND SCALAR RADIUS

The scalar radius of the pion is defined as the slope of the form factor at vanishing momentum transfer,

$$\left\langle r^2 \right\rangle_s^\pi = -\frac{6}{F_s^\pi(0)} \frac{\partial F_s^\pi(Q^2)}{\partial Q^2}\Big|_{Q^2=0} . \tag{6.27}$$

To determine the radius $\left\langle r^2 \right\rangle_s^\pi$ from our data, we need a parameterization of the Q^2-dependence of the form factor $F_s^\pi(Q^2)$. The simplest ansatz is a polynomial function in Q^2. Since we have only three different momentum transfers available, we choose a function which is linear in Q^2,

$$F_s^\pi(Q^2) = F_s^\pi(0) \left(1 - \frac{1}{6} \left\langle r^2 \right\rangle_s^\pi Q^2 + \mathcal{O}(Q^4)\right) . \tag{6.28}$$

Clearly, the parameterization (6.28) fulfills the definition of the radius (6.27). Thus, we can obtain an estimate for the scalar radius of the pion by fitting a function of the form (6.28) to our results for the form factor.

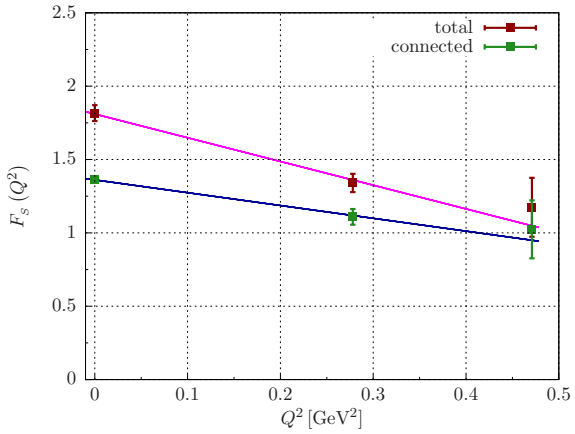

Figure 6.11: The Q^2-dependence of the scalar form factor for the E5 ensemble. A linear function of the form (6.28) has been fitted to the data to determine the scalar radius. The red points and the purple line show the results for the total form factor, the green points and the blue line show the results for the connected contribution only.

In figure 6.11 the results for the scalar form factor for the E5 ensemble are plotted against Q^2 for the connected contribution and the total form factor. A linear function of the form (6.28) has been fitted to the data to obtain the scalar radius. For the connected contribution alone as well as for the total form factor, we find our data to be consistent with a linear curve within the statistical accuracy. Any possible curvature of $\mathcal{O}(Q^4)$ cannot be resolved in our data. Furthermore, we find that the descending slope of the fitted curve is steeper when we include the disconnected contribution, resulting in a larger scalar radius. The numerical results for the scalar form factor for all ensembles and the scalar radii obtained from the linear fit can be found in the appendix in section B.2.1.

Although we do not observe a deviation from a linear Q^2-dependence in our data, we additionally fit a vector meson dominance (VMD) inspired function of the form

$$F_S^\pi(Q^2) = F_S^\pi(0)\,\frac{1}{\left(1+\left(\frac{Q^2}{M^2}\right)\right)^2} \tag{6.29}$$

to our data. This functional form has a built in curvature and thus allows us to investigate the systematic effect in the determination of the scalar radius from the ansatz for the Q^2-dependence. In this parameterization the scalar radius is given by

$$\left\langle r^2\right\rangle_S^\pi = \frac{12}{M^2}\,. \tag{6.30}$$

The fitted curve is shown in figure 6.12 for the E5 ensemble. Due to the intrinsic curvature of the function (6.29), we obtain a scalar radius which is slightly larger than the result from the linear fit.

In figure 6.13 we show a comparison of the scalar radius obtained from different ansätze for the E and F ensembles:

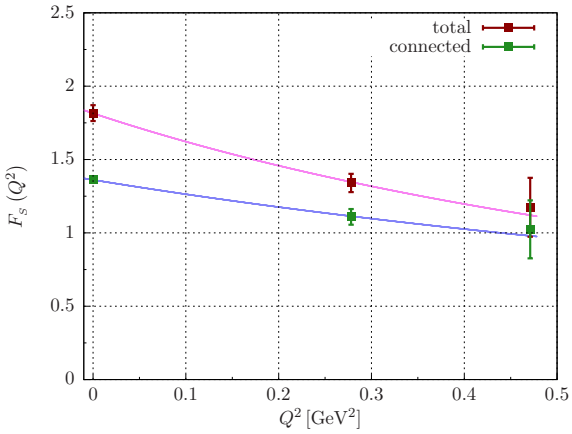

Figure 6.12: A VMD-inspired function of the form (6.29) has been fitted to the Q^2-dependence of the scalar pion form factor. The red points and the purple line show the results for the total form factor, the green points and the blue line show the results for the connected contribution only.

- a linear curve matched to the form factor for $Q^2 = 0$ and the smallest non-vanishing Q^2,
- a linear curve fitted to all three values of the momentum transfer Q^2,
- a vector meson dominance inspired function (6.29) fitted to the data.

A similar plot as figure 6.13 for the other two values of the lattice spacing can be found in B.2.3.

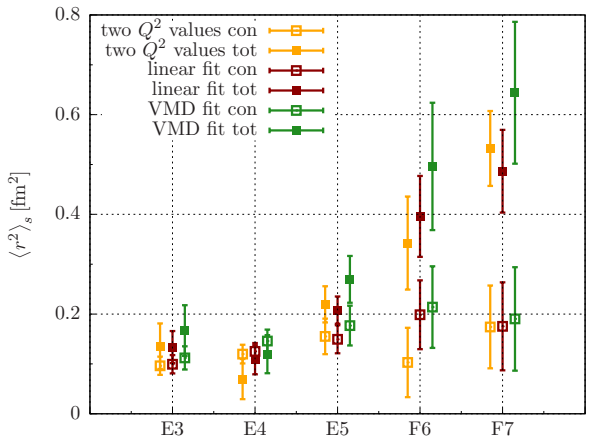

Figure 6.13: Comparison of the scalar radii obtained from different ansätze for the Q^2-dependence for the E and F ensembles. Yellow points show the results from the first two Q^2 values only, red points show the results from a linear fit to all three Q^2 values, and green points show the results from a vector meson dominance fit. Open and closed symbols denote results from the connected and total form factor, respectively.

As one can see, for all ensembles the results from all three methods agree within the statistical errors. Thus, we can be confident that a linear Q^2-dependence is a good description of our data. Therefore, we use the results from the linear fits to all three Q^2 values as our results for the scalar radius.

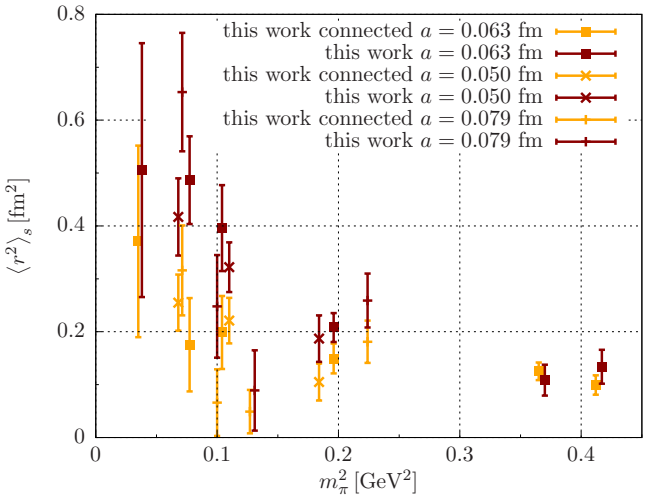

Figure 6.14: The results for the scalar radii plotted against the pion mass. Yellow points show the results from connected contributions only, red points show the results obtained from the full form factor. Different symbols denote different lattice spacings.

In figure 6.14 the results for the scalar radius from the linear fits are plotted against the pion mass m_π^2. Values obtained from the total form factor are shown in red, values from the connected contribution only are shown in yellow. One can see that we find significant contributions of the disconnected diagrams especially for the smaller pion masses. Unfortunately, our result at the smallest pion mass ($m_\pi = 193$ MeV) has a large error, such that this trend cannot be resolved for this point. Thus, for the future it would be important to increase the statistics for the G8 ensemble. Nevertheless, from the other ensembles we can state, that the disconnected contribution to the scalar pion radius is not negligible. This is in qualitative agreement with the result from partially quenched chiral perturbation theory (cf. figure (5.5)).

For most ensembles, the error on the scalar radius from the total form factor is only slightly larger than the error on the radius determined from the connected results only. Although the relative error on the disconnected contribution of the form factor is in general larger than the relative error on the corresponding connected contribution, the total error on the form factor especially for non-vanishing momentum transfer is dominated by the total error on the connected contribution. To further reduce the error on the scalar radius, we thus have to increase the statistics on the connected contribution by including more source positions as already done for the disconnected contribution.

6.4 CHIRAL AND CONTINUUM EXTRAPOLATION

Table 6.2 shows an overview of the CLS gauge ensembles that have been used for the calculation of the scalar radius of the pion. The use of several different pion masses and three lattice spacings allows for a chiral extrapolation $m_\pi \to m_{\pi,\text{phys}}$ and a continuum extrapolation $a \to 0$. In general one also has to perform a extrapolation to infinite volume, however, as already mentioned in section 3.2.2,

we expect finite-volume effects to be negligible since all our ensembles fulfill $m_\pi L \geqslant 4$.

β	a[fm]	lattice	m_π[MeV]	$m_\pi L$	κ	Label	N_{cfg}
5.2	0.079	96×48^3	473	6.1	0.13580	A3	133
5.2	0.079	96×48^3	363	4.7	0.13590	A4	200
5.2	0.079	96×48^3	312	4.0	0.13594	A5	250
5.2	0.079	96×48^3	267	5.1	0.13597	B6	159
5.3	0.063	64×32^3	650	6.6	0.13605	E3	156
5.3	0.063	64×32^3	605	6.2	0.13610	E4	162
5.3	0.063	64×32^3	456	4.7	0.13625	E5	1000
5.3	0.063	96×48^3	325	5.0	0.13635	F6	300
5.3	0.063	96×48^3	277	4.3	0.13638	F7	351
5.3	0.063	128×64^3	193	4.0	0.13642	G8	348
5.5	0.050	96×48^3	430	5.2	0.13660	N5	477
5.5	0.050	96×48^3	332	4.1	0.13667	N6	946
5.5	0.050	128×64^3	261	4.2	0.13671	O7	490

Table 6.2: Overview of the CLS ensembles that have been used for the calculation of the scalar radius of the pion

6.4.1 *Chiral Extrapolation*

For the chiral extrapolation $m_\pi \to m_{\pi,\text{phys}}$ we can make use of the expression for the scalar radius from chiral perturbation theory. As discussed above, at next-to-leading order the scalar radius is given by (cf. equation (5.13))

$$\langle r^2 \rangle_s^\pi = -\frac{1}{(4\pi F)^2}\,\frac{13}{2} + \frac{6}{(4\pi F)^2}\left[\bar{\ell}_4 + \ln\left(\frac{m_{\pi,\text{phys}}^2}{m_\pi^2}\right)\right]. \tag{6.31}$$

To obtain the scalar radius at the physical pion mass, a function of the form (6.31) can be fitted to our results. The low-energy constant $\bar{\ell}_4$ serves as a fit parameter and can thus be estimated from our fit. Note that this is a one-parameter fit. We use $F = 92.2$ MeV [34] for the pion decay constant, and the mass of the charged pion $m_{\pi,\text{phys}} = 139.57$ MeV [34].

We have fitted a function of the form (6.31) to our data for the scalar radius for all three lattice spacings separately. The obtained fit curves are shown in figure 6.15 for $a = 0.079$ fm (top left), $a = 0.063$ fm (top right), and $a = 0.050$ fm (bottom).

Once the low-energy constant $\bar{\ell}_4$ is known from the fits, the scalar radius of the pion at the physical pion mass is given by (cf. equation (6.31))

$$\langle r^2 \rangle_s^\pi \Big|_{m_\pi = m_{\pi,\text{phys}}^2} = -\frac{1}{(4\pi F)^2}\,\frac{13}{2} + \frac{6}{(4\pi F)^2}\,\bar{\ell}_4\,. \tag{6.32}$$

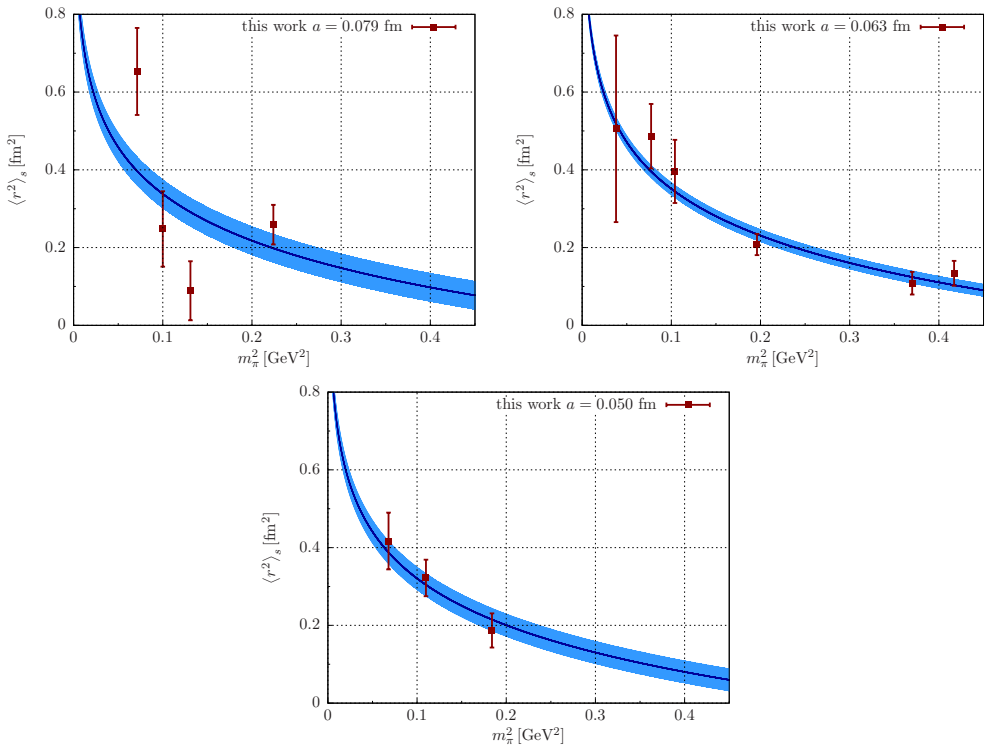

Figure 6.15: Chiral fits to the scalar radius. The plots show fits for $a = 0.079$ fm (top left), $a = 0.063$ fm (top right), and $a = 0.050$ fm (bottom). The corresponding results for the chirally extrapolated radii and the χ^2 values of the fits are given in table 6.3.

The results for $\bar{\ell}_4$ and $\langle r^2 \rangle_S^\pi$ at the physical mass, as well as the χ^2 values from the fits, are given in table (6.3).

Note that the fit parameter $\bar{\ell}_4$ only changes the offset of the curve. The curvature, i.e. the pion mass dependence is completely fixed by the summand

$$\langle r^2 \rangle_S^\pi = \text{const} + \frac{6}{(4\pi F)^2} \left[\ln \left(\frac{m_{\pi,\text{phys}}^2}{m_\pi^2} \right) \right] \tag{6.33}$$

in the chiral perturbation theory expression (6.31). Especially for $a = 0.063$ fm and $a = 0.050$ fm we find a very good agreement of our data with the fit curve. For the $a = 0.079$ fm data, the trend in the scalar radius is not as clear as for the other ensembles (cf. the plot top left of figure 6.15). We are planning to increase statistics for these ensembles in the future to investigate this behavior.

Despite a possible dependence of the scalar radius on the lattice spacing, we can also fit NLO χPT to the data points for all ensembles combined without taking their lattice spacings into account. The corresponding plot is shown in figure 6.16, and the values for $\bar{\ell}_4$ and the scalar radius are given in table 6.3. As one can see, the results for all three different lattice spacings as well as the result for a chiral fit to all ensembles agree within their statistical errors. This indicates that the dependence of the scalar radius on the lattice spacing is small.

a [fm]	$\bar{\ell}_4$	$\langle r^2 \rangle_s^\pi$ [fm^2]	χ^2/dof
0.079	4.67 ± 0.21	0.623 ± 0.036	$14.59/3$
0.063	4.74 ± 0.09	0.636 ± 0.016	$3.72/5$
0.050	4.57 ± 0.17	0.605 ± 0.029	$0.71/2$
all	4.70 ± 0.08	0.627 ± 0.013	$19.85/12$

Table 6.3: The results of the fits for the chiral extrapolation. For every lattice spacing the result for $\bar{\ell}_4$ and the scalar radius at physical pion mass is given as well as the reduced χ^2 of the corresponding fits. The last line shows the result of a simultaneous fit to the data of all three lattice spacings combined.

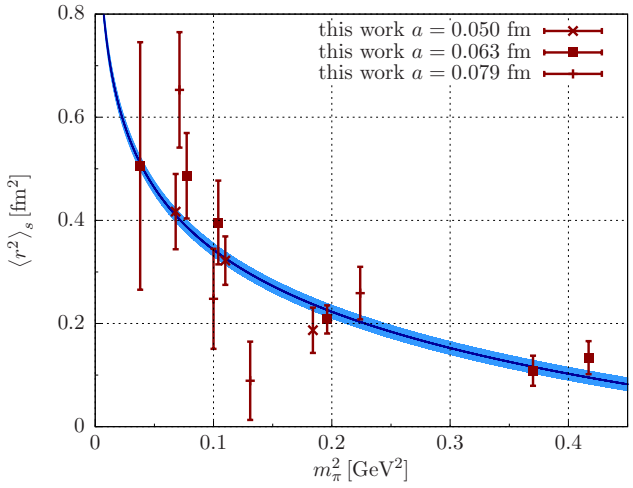

Figure 6.16: Chiral fit to the scalar radius for all ensembles without taking the lattice spacing into account.

One might question the validity of chiral perturbation theory at large pion masses, such as $m_\pi = 605$ MeV and $m_\pi = 650$ MeV for the E3 and E4 ensembles, respectively. To check for a possible source of systematic error when including those two ensembles, we repeated the same analysis with a mass cut of $m_\pi < 500$ MeV, i.e. E3 and E4 were excluded. The results are given in table 6.4 and are consistent within their statistical uncertainties with the results without the mass cut (cf. table 6.3).

a [fm]	$\bar{\ell}_4$	$\langle r^2 \rangle_s^\pi$ [fm^2]	χ^2/dof
0.063	4.70 ± 0.14	0.627 ± 0.024	$2.4/3$
all	4.65 ± 0.10	0.618 ± 0.017	$18.1/10$

Table 6.4: The results of the fits for the chiral extrapolation with mass cut $m_\pi < 500$ MeV. The low-energy constant and scalar radius at physical pion mass is given for $a = 0.063$ fm as well as the result of a fit to the data of all three lattice spacings combined. The results are consistent with the results without mass cut. The mass cut does not affect the results for $a = 0.050$ fm and 0.079 fm, since no ensembles have to be excluded.

6.4.2 *Continuum Extrapolation*

Although the results for the scalar radius at physical pion mass that we obtained for the different lattice spacings as well as the result from the fit to all ensembles regardless of their lattice spacing agree within their statistical errors, it is necessary to perform a continuum extrapolation $a \to 0$ in order to take lattice artifacts properly into account.
To obtain a first idea on the lattice spacing dependence of the scalar radius, one can look at ensembles with roughly the same pion mass and different lattice spacings. Within the CLS ensembles we have two sets of such ensembles:

- $m_\pi \approx 270$ Mev: B6, F7, O7,
- $m_\pi \approx 325$ Mev: A5, F6, N6.

In figure 6.17 the results for the scalar pion radius for these ensembles are plotted against the lattice spacing a^2. The plot on the left and on the right hand-side show the radii for $m_\pi \approx 270$ and $m_\pi \approx 325$, respectively. While for the smaller pion mass, one can see a clear trend in the scalar radius for an increasing lattice spacing, we do not observe such a trend for $m_\pi = 325$ MeV. Thus, it is unclear how much the scalar radius actually depends on the lattice spacing.

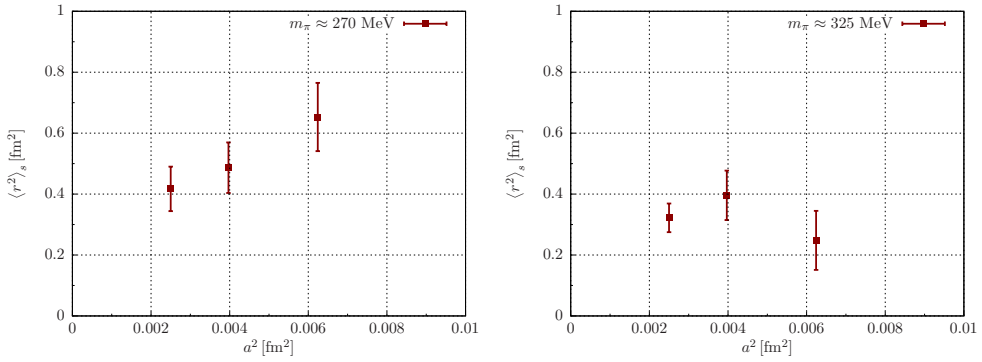

Figure 6.17: The scalar radius for fixed m_π plotted against the lattice spacing a. The plot on the left shows results for a pion mass of ≈ 270 MeV (B6,F7,O7); the plot on the right shows results for $m_\pi \approx 325$ MeV (A5,F6,N6).

Nevertheless, one can try a continuum extrapolation of the scalar radii at the physical pion mass obtained above. Since our quark action is $\mathcal{O}(a)$-improved, we expect a quadratic dependence on the lattice spacing. The left hand-side of figure 6.18 shows our results for $\langle r^2 \rangle_s^\pi$ at the physical pion mass plotted against the squared lattice spacing a^2. A function

$$\langle r^2 \rangle_s^\pi = \langle r^2 \rangle_s^\pi \Big|_{a=0} + b\, a^2 \tag{6.34}$$

with a linear dependence on a^2 has been fitted to the data as indicated by the blue line. We obtain a scalar radius of

$$\langle r^2 \rangle_s^\pi \Big|_{a=0} = 0.596 \pm 0.069 \text{ fm}^2 \tag{6.35}$$

in the continuum limit $a = 0$ from the fit. Note that the result for the factor b multiplying the a^2 term

$$b = 9.1 \pm 19.1 \tag{6.36}$$

has an error of $> 100\%$ indicating a negligible dependence on the lattice spacing.

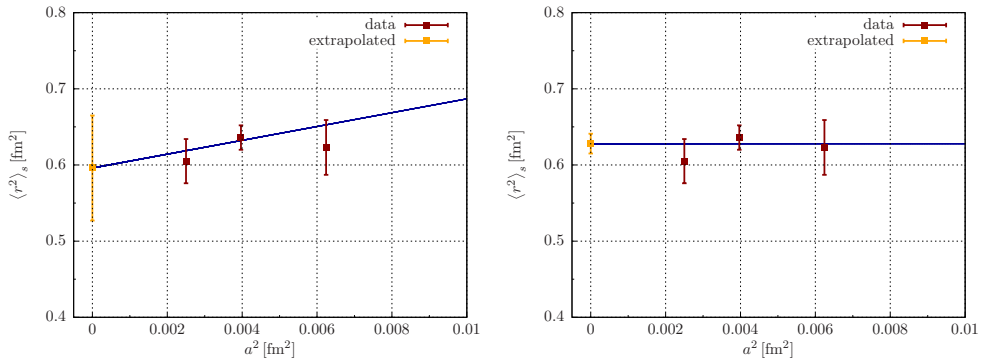

Figure 6.18: Continuum extrapolation for the scalar radius. Red points show the results of the scalar radius at the physical pion mass for the different lattice spacings. The blue curves on the left and on the right hand-side show the results of a linear and a constant fit, respectively. The yellow points show the corresponding extrapolated value at $a = 0$.

Since we do not observe a clear trend in the lattice spacing, we additionally fitted a constant to the results for the scalar radius as shown on the right hand-side of figure 6.18.
Table 6.5 summarizes both results from the continuum extrapolation as well as the results from the same analysis when including the mass cut. The muss cut only affects the scalar radius at $a = 0.063$ fm since the E4 and E3 ensembles are excluded.

			$m_\pi < 500$ MeV	
method	$\langle r^2 \rangle_s^\pi$ [fm^2]	b	$\langle r^2 \rangle_s^\pi$ [fm^2]	b
quadratic	0.596 ± 0.069	9.1 ± 19.1	0.590 ± 0.070	8.2 ± 19.1
constant	0.628 ± 0.013	–	0.619 ± 0.017	–

Table 6.5: Results from the continuum extrapolation using a quadratic and a constant function. The columns on the left and right show results without and with mass cut, respectively.

6.4.3 *Combined Chiral and Continuum Extrapolation*

To treat the pion mass dependence and the lattice artifacts simultaneously, one can perform a combined chiral and continuum extrapolation by including a

term proportional to the squared lattice spacing a^2 in the χPT formula for the scalar radius,

$$\langle r^2 \rangle_s^\pi = -\frac{1}{(4\pi F)^2}\frac{13}{2} + \frac{6}{(4\pi F)^2}\left[\bar{\ell}_4 + \ln\left(\frac{m_{\pi,\text{phys}}^2}{m_\pi^2}\right)\right] + b\,a^2\,. \tag{6.37}$$

This fit has two fit parameters $\bar{\ell}_4$ and b. The result of such a fit is shown in 6.19. Different colors denote different lattice spacings and the black line shows the pion mass dependence in the continuum $a = 0$. One can see only a small trend in the lattice spacing guided by the $b\,a^2$ term, which is compatible with zero $b = 4.6 \pm 12.7$.

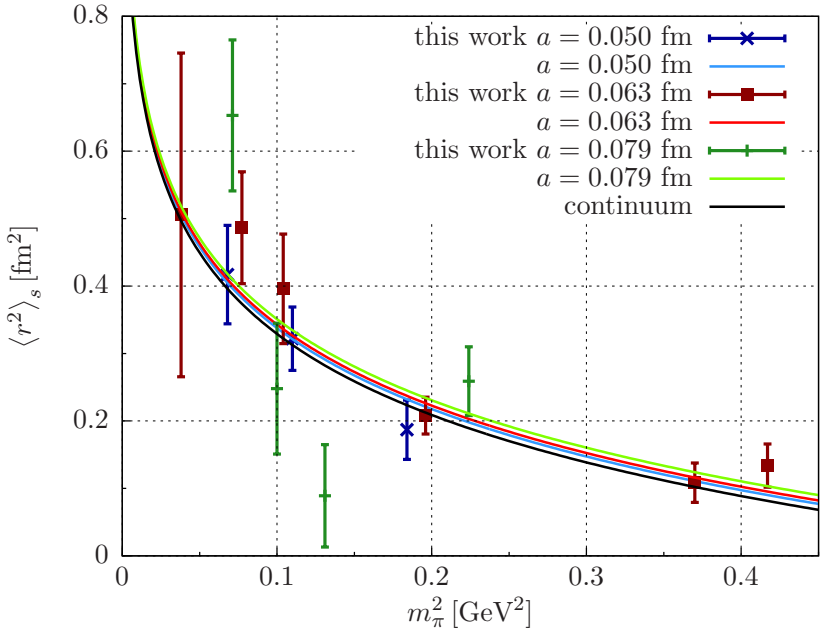

Figure 6.19: A combined chiral and continuum extrapolation for the scalar radius. Green, red and blue show the results for $a = 0.079$ fm, 0.063 fm and 0.050 fm, respectively. The black line denotes the pion mass dependence in the continuum $a = 0$.

The result of the combined chiral and continuum fit is given in table 6.6 once with and once without mass cut. Both results are consistent with each other.

	$\bar{\ell}_4$	$\langle r^2 \rangle_s^\pi$ [fm^2]	b	χ^2/dof
w/o mass cut	4.59 ± 0.30	0.608 ± 0.052	4.6 ± 12.7	$19.2/11$
with mass cut	4.54 ± 0.30	0.600 ± 0.052	4.7 ± 12.5	$17.9/9$

Table 6.6: The results from a combined chiral and continuum extrapolation for the scalar radius according to equation (6.37). The first line shows a fit to all ensembles, the second line a fit including the mass cut $m_\pi < 500$ MeV.

To better visualize the trend in the lattice spacing from the combined fit, figure 6.20 shows the results for the radius at physical pion mass for each lattice spacing from above plotted against a^2. The blue line shows the lattice spacing

dependence as obtained from the combined chiral and continuum extrapolation. The yellow point shows the radius for $a = 0$ and $m_\pi = m_{\pi,\text{phys}}$ from the combined fit. The dashed line in light blue shows the fit result for the continuum extrapolation of the scalar radii at the physical pion mass (cf. plot on the left-hand side of figure 6.18) as a comparison.

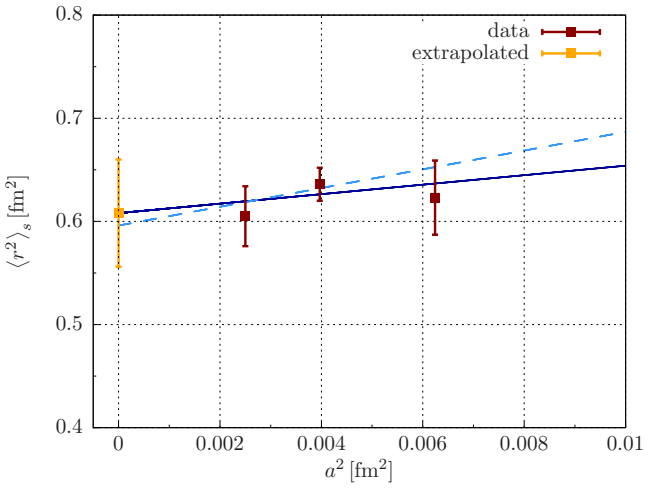

Figure 6.20: The scalar radius at physical pion mass plotted against the lattice spacing a^2. The blue line shows the lattice spacing dependence as obtained from the combined fit.

6.4.4 *Comparison and Final Result*

Figure 6.21 shows a compilation of our results for the scalar pion radius. The different methods that we have used to extrapolate to the physical point are explained above:

- method 1, 2, 3: Extrapolation to the physical mass using chiral perturbation theory for the different lattice spacings separately,
- method 4: Extrapolation to the physical mass using chiral perturbation theory for the results from all ensembles independent of the lattice spacing,
- method 5, 6: Continuum extrapolation of the results from method 1-3 once with a linear term in the squared lattice spacing a^2 and once with a constant,
- method 7: Combined chiral and continuum extrapolation.

Points in light and dark red show results with and without the mass cut of $m_\pi < 500$ MeV, respectively. As one can see, we find that all our results are consistent with each other and with the value

$$\left\langle r^2 \right\rangle_s^\pi = 0.61 \pm 0.04 \text{ fm}^2 \tag{6.38}$$

which was extracted from $\pi\pi$-scattering data in [27]. This value is shown in green in figure 6.21.

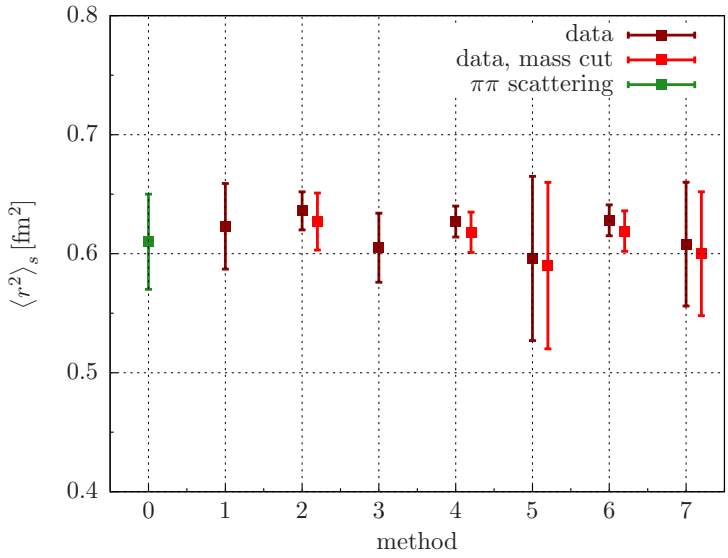

Figure 6.21: Comparison of different results for the scalar radius: Method 1,2 and 3 show the chiral extrapolation for $a = 0.079$ fm, 0.063 fm and 0.050 fm, method 4 is the chiral extrapolation for all ensembles, method 5 and 6 are the continuum extrapolation of the scalar radii at physical mass with a linear term in a^2 and a constant, and method 7 is the result from the combined fit. Dark red points show the results from the analysis of all ensembles and light red points denote results including the mass cut. The green point (method 0) is the value that was obtained from $\pi\pi$-scattering in [27].

The two results (methods 5 and 7) that include a linear dependence on the squared lattice spacing a^2 have larger errors than the other results since the lattice spacing dependence is not very well constrained by our data.
Although we find that lattice artifacts are smaller than our statistical uncertainty, there is no reason to believe that the scalar radius should be independent of a. For our final result we choose the scalar radius from the combined chiral and continuum extrapolation (method 7). To be sure that we only use data where it is justified that chiral perturbation theory can be applied, we use the result including the mass cut $m_\pi < 500$ MeV. Thus, we quote as our final result

$$\langle r^2 \rangle_s^\pi = 0.600 \pm 0.052 \text{ fm}^2 , \tag{6.39}$$

$$\bar{\ell}_4 = 4.54 \pm 0.30 . \tag{6.40}$$

7

CONCLUSIONS AND OUTLOOK

We have explicitly calculated the connected and the disconnected contribution to the scalar form factor of the pion for $N_f = 2$ dynamical flavors of Wilson quarks. The form factor can be extracted by building appropriate ratios of three- and two-point functions. The required all-to-all propagators for the quark loop in the disconnected three-point function have been estimated with stochastic sources and the generalized hopping parameter expansion. Using this method we are able to resolve the disconnected contribution to the scalar pion form factor for zero as well as for non-zero momentum transfer Q^2. For vanishing momentum transfer we find that the disconnected contribution is of order 10% of the connected contribution for our finest lattices up to order 70% for the coarser lattices.

From the Q^2-dependence of the scalar form factor, the scalar radius of the pion has been determined by a linear fit to our results, and we find our form factor results to be consistent with a linear curve for all ensembles. To check for a possible source of systematic error from the linear ansatz of the Q^2-dependence, we have compared these results also with results from a vector meson dominance inspired fit and we find the values to be consistent within their statistical errors (cf. figure 6.13). As our final results for the scalar radii we thus use the values from the linear fits.

Our results show that the disconnected contribution to the scalar radius is not negligible, especially for the smaller pion masses (cf. figure 6.14). This is in qualitative agreement with the result from partially quenched χPT [21] (cf. figure 5.5), that the disconnected contribution to the scalar radius is of the same order as the connected one.

Unfortunately, the statistics on our lightest ensemble (G8 with a pion mass of $m_\pi = 193$ MeV) is too small to resolve a significant difference between the radius from the total form factor and the radius from the connected contribution alone. It is important to further reduce the statistical error on this point also to better constrain a chiral extrapolation. For the disconnected contribution, we already have data from 12 different pion source-sink separations for G8. To further reduce the error on the scalar radius, we need to increase the statistics on the connected contribution. However, a reduction of the statistical error by a factor of 2 requires an increase in statistics by a factor of 4, i.e. data for 3 additional source positions.

To obtain the scalar radius of the pion at the physical point, i.e. at $m_\pi = m_{\pi,\text{phys}}$ and $a = 0$, a combined chiral and continuum extrapolation was performed. The dependence on the pion mass has been taken from next-to-leading order chiral perturbation theory, where the low-energy constant $\bar{\ell}_4$ serves as the only fit parameter. We expect a linear dependence on the squared lattice spacing a^2, and thus we have included a term $\propto a^2$ in the combined fit to all ensembles, although we do not observe significant lattice artifacts in the scalar radius. For the final result we have excluded data with $m_\pi > 500$ MeV to be sure that chiral

perturbation theory is valid, although the results including the heavier masses are consistent with those with the mass cut. From the combined chiral and continuum extrapolation with the mass cut we find

$$\langle r^2 \rangle_s^\pi = 0.600 \pm 0.052 \text{ fm}^2 , \tag{7.1}$$

which we quote as our final result at the physical point. This value is consistent with the scalar radius that was extracted from $\pi\pi$-scattering [27]:

$$\langle r^2 \rangle_s^\pi = 0.61 \pm 0.04 \text{ fm}^2 \qquad (\pi\pi\text{-scattering}) . \tag{7.2}$$

Figure 7.1 is the same figure as 6.19, but with the $\pi\pi$-scattering result included in orange. The other points show our own results for the scalar radius, where different colors denote different lattice spacings. The black line is the pion mass dependence in the continuum from our combined fit. One can clearly see the consistency of our results with the phenomenological value from $\pi\pi$-scattering.

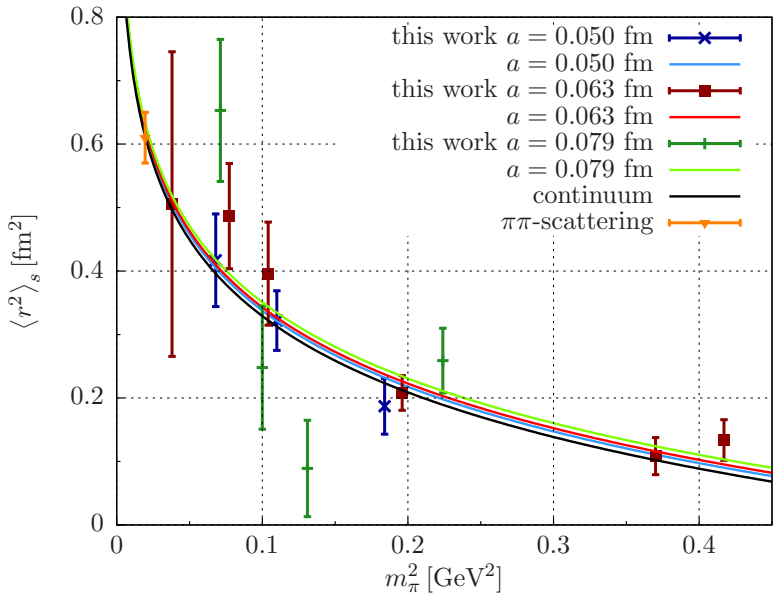

Figure 7.1: Our results for the scalar radius plotted against the pion mass m_π^2 including the result from a combined chiral and continuum extrapolation. The orange point at the physical pion mass shows the value from $\pi\pi$-scattering.

Furthermore, our data show the expected pion-mass dependence from chiral perturbation theory at next-to-leading order. This is different from the finding of the JLQCD/TWQCD collaboration where no pion mass dependence was observed. Their results for the scalar radius are shown on the right-hand side of figure 7.2. The plot is taken from [17]. The lower point at physical pion mass which is labeled with "expr't" is the $\pi\pi$-scattering value and is the same as the orange point in our own plot which is shown on the left of figure 7.2 as a comparison. The black lines show the fit of NLO chiral perturbation theory to their data and the corresponding error band. The black point at the physical pion mass is their chirally extrapolated result [17]:

$$\langle r^2 \rangle_s^\pi = 0.797 \pm 0.015 \text{ fm}^2 \qquad (\text{JLQCD/TWQCD}). \tag{7.3}$$

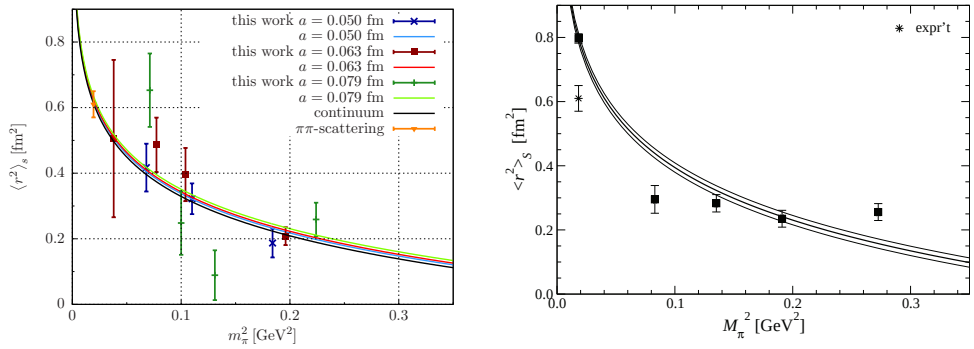

Figure 7.2: The chiral behavior of the scalar radius compared with the results of the JLQCD/TWQCD collaboration on the right-hand side (the plot is taken from [17]). Our results are shown on the left-hand side, and are plotted with same plot range as the plot on the right-hand side.

Note that the results from the JLQCD/TWQCD collaboration have been obtained using a single relatively coarse lattice spacing of $a = 0.1184$ fm. Thus, also no continuum extrapolation is included in their data. Furthermore, the lattices used by JLQCD/TWQCD have 32×16^3 lattice points, and although their lattices are coarser, they have in general smaller volumes than ours. Actually, for the two lightest points in the plot on the right-hand side $m_\pi L < 4$, and thus these points might be affected by finite volume effects. Whether this is the reason for the different chiral behavior remains unclear at this point.

However, we find a pion mass dependence which is consistent with χPT at NLO. One has to note that the pion mass dependent curvature is completely driven by χPT and the fit parameter $\bar{\ell}_4$ only influences the offset of the curve. From our combined fit we can determine this low-energy constant and we find

$$\bar{\ell}_4 = 4.54 \pm 0.30\,. \tag{7.4}$$

This value can be compared with other lattice results for this low-energy constant using $N_f = 2$ dynamical quark flavors. A summary of such results is given in the current FLAG report [98]. A compilation of all lattice results for $\bar{\ell}_4$ with $N_2 = 2$ dynamical fermions quoted in the FLAG report is given in figure 7.3. All published lattice results are plotted in the middle panel. The FLAG group assigns points a green color if they include the following points:

- chiral extrapolation,
- continuum extrapolation,
- finite volume effects under control.

The FLAG estimate, which is shown in the upper panel is the average of all green points

$$\bar{\ell}_4 = 4.62 \pm 0.22 \qquad \text{(FLAG estimate)}. \tag{7.5}$$

The upper point in the middle panel labeled with "Gülpers 2013" is our result from the 2013 publication [3] which included only the E and F lattices and thus

no continuum extrapolation. The point labeled with "Brandt 2013" is an estimate of $\bar{\ell}_4$ [92] using the pion decay constant

$$\frac{F_\pi}{F} = 1 + \frac{M_\pi^2}{4\pi F_\pi^2}\,\bar{\ell}_4 \tag{7.6}$$

calculated on the CLS ensembles. The blue point in the lower panel is the final result from this work. We find our value for the low-energy constant $\bar{\ell}_4$ to be consistent with the current FLAG estimate. Additionally, it is consistent with the result from the pion decay constant using the same CLS ensembles. The extraction of low-energy constants using different observables can serve as a consistency test of chiral perturbation theory.

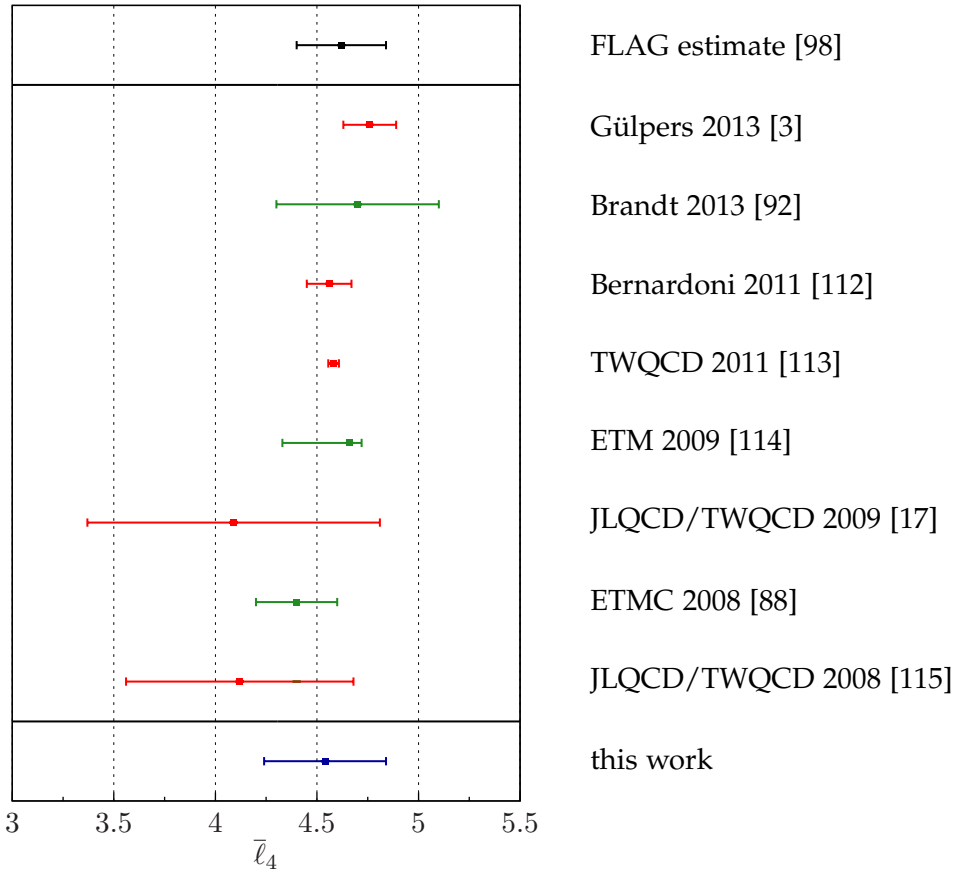

Figure 7.3: Comparison of lattice results for $\bar{\ell}_4$. The upper panel shows the current FLAG estimate for $N_f = 2$. The middle panel shows all published lattice results quoted in the FLAG report, including our result using only the E and F lattices (Gülpers 2013). Green points have been used by FLAG to build the average shown in the upper panel. The blue point in the lower panel shows the result from this work.

In general it would be desirable to use the NNLO χPT expression for the chiral extrapolation of the scalar radius instead of the NLO one. However, the amount of available data is too small to reliably constrain all the required low-energy constants at NNLO (cf. section B.3). In principle, it would be possible to perform a combined fit together with the vector form factor results from the

CLS ensembles [92] using NNLO χPT. Such an analysis remains to be done in the future.
However, since we see consistency of our data with χPT at NLO we resort to using NLO at this point. If the current statistics is significantly improved, one might be able to resolve a difference between NLO and NNLO.

Currently, the CLS initiative is generating a new set of gauge ensembles [116] with $N_f = 2+1$ dynamical flavors of $\mathcal{O}(a)$-improved Wilson fermions. Lattices with three different lattice spacings of $a \approx 0.086$ fm, 0.064 fm and 0.05 fm are generated. The pion masses will be in a range of $m_\pi \approx 420$ MeV down to the physical pion mass of 130 MeV. For the future we can use this new set of ensembles to calculate the scalar form factor and radius of the pion. Although a chiral extrapolation to the physical point is no longer necessary when including an ensemble at physical pion mass, the pion mass dependence of the scalar radius can still be used to test chiral perturbation theory and to determine the low-energy constant $\bar{\ell}_4$ for $N_f = 2+1$ sea quark flavors.

Part III

THE DISCONNECTED CONTRIBUTION TO THE HADRONIC VACUUM POLARIZATION

8

INTRODUCTION

8.1 THE ANOMALOUS MAGNETIC MOMENT OF THE MUON

The magnetic moment $\vec{\mu}$ of an elementary fermion with charge e, mass m and spin $\vec{s}$ is given by

$$\vec{\mu} = g \frac{e}{2m} \vec{s} \tag{8.1}$$

with the gyromagnetic factor g. In Dirac theory only the tree-level process (cf. figure 8.1) occurs and the g-factor for an elementary fermion, e.g. a muon, is given by $g = 2$.

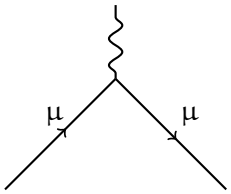

Figure 8.1: The tree level contribution to the gyromagnetic factor g_μ of the muon.

However, due to quantum corrections, the g-factor is slightly different from this value. One defines the anomalous magnetic moment a_l of an elementary particle l as the deviation of its g-factor from 2

$$a_l \equiv (g-2)/2\,. \tag{8.2}$$

The anomalous magnetic moment of the muon a_μ is one of the most precisely measured quantities in physics and can therefore serve as a high-precision check of the Standard Model of particle physics. A comprehensive overview can be found in [117].

The currently most precise experimental result has been measured at the Brookhaven National Laboratory using a storage ring with polarized muons in a magnetic field B. The anomalous magnetic moment of the muon is obtained from measuring the Larmor precession frequency

$$\omega_a = a_\mu \frac{eB}{m_\mu} \tag{8.3}$$

of the muon, and the result is given by [118]

$$a_\mu = (11659208.9 \pm 5.4 \pm 3.3) \times 10^{-10}\,. \tag{8.4}$$

8.1.1 *The Standard Model Estimate*

From the theoretical side, the anomalous magnetic moment of the muon receives contributions from electromagnetic, weak and strong interactions. The largest fraction of a_μ comes from QED, where the leading order contribution, the Schwinger term, has already been calculated in 1948 and its value is given by [119]

$$a_\mu^{\text{QED,LO}} = \frac{\alpha}{2\pi}\,. \tag{8.5}$$

The corresponding Feynman diagram is shown in figure 8.2.

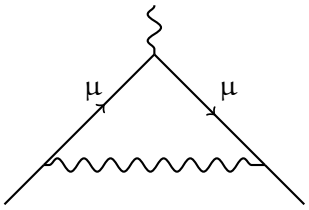

Figure 8.2: The leading order QED contribution to the anomalous magnetic moment of the muon.

By now, the electromagnetic contribution is known up to fifth order [120] in the fine structure constant α, and all together the QED part of the anomalous magnetic moment of the muon is given by [34]

$$a_\mu^{\text{QED}} = (11658471.895 \pm 0.008) \times 10^{-10}\,. \tag{8.6}$$

The weak contribution contains all diagrams where W- and Z-bosons as well as the Higgs boson is exchanged. It has been calculated up to two loops and is given by [121]

$$a_\mu^{\text{weak}} = (15.36 \pm 0.10) \times 10^{-10} \tag{8.7}$$

for a Higgs boson mass of $m_H \approx 126$ GeV.

Since the muon does not couple to gluons directly, QCD can only contribute to a_μ via quark loops. The leading-order QCD contribution to the anomalous magnetic moment of the muon is the hadronic vacuum polarization (HVP), which is shown in figure 8.3.

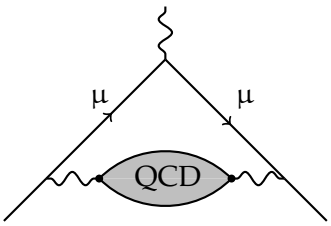

Figure 8.3: The hadronic vacuum polarization contribution to the anomalous magnetic moment of the muon.

For the calculation of the hadronic contribution to a_μ, perturbation theory cannot be applied in contrast to the electroweak contributions. Currently, the best estimate of the hadronic vacuum polarization is achieved by a semi-phenomenological approach, where the imaginary part of the hadronic vacuum polarization $\Pi(s)$ can be related to the cross section for $e^+ e^- \to$ hadrons using the optical theorem

$$\operatorname{Im}\Pi(s) = \frac{\alpha(s)}{3} R(s) \tag{8.8}$$

as depicted in figure 8.4. The R-ratio $R(s)$ is defined as the total cross section of $e^+ e^- \to$ hadrons normalized by the cross section of $e^+ e^- \to \mu^+\mu^-$,

$$R(s) = \frac{\sigma(e^+ e^- \to \text{hadrons}, s)}{\sigma(e^+ e^- \to \mu^+\mu^-, s)} . \tag{8.9}$$

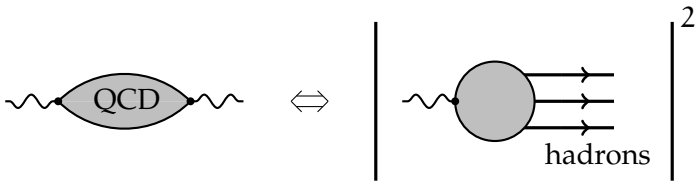

Figure 8.4: The optical theorem for the hadronic vacuum polarization.

Figure 8.5 shows a summary of the experimentally measured R-ratio. At low energies, one can see the resonances for ρ, ω and ϕ. At larger energies there are also resonances for excited states such as the ρ', and resonances for the heavier quark flavors, such as the J/Ψ for the charm or the Υ for the bottom sector.

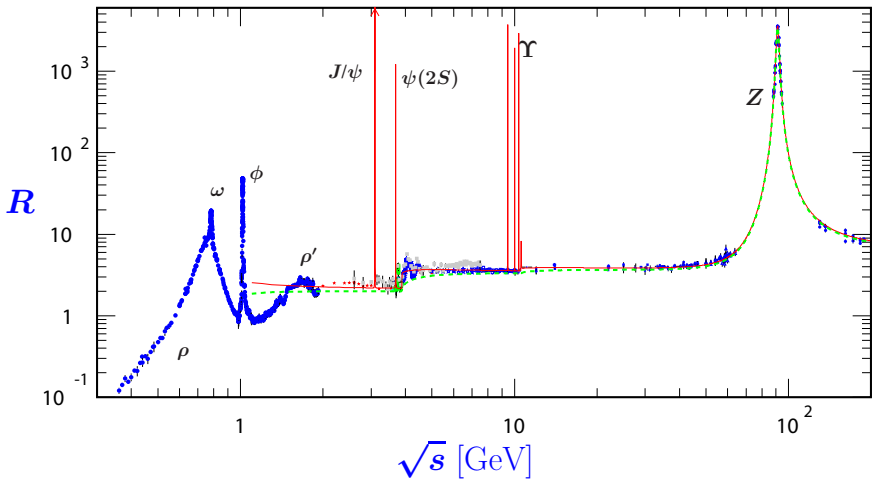

Figure 8.5: Compilation of the the world data for the R ratio. The plot is taken from [34].

At order α^2 one finds that the contribution of the hadronic vacuum polarization to the anomalous magnetic moment of the muon can be calculated as [117]

$$a_\mu^{\text{hvp}} = \left(\frac{\alpha m_\mu}{3\pi}\right)^2 \int_{m_\pi^2}^{\infty} ds \, \frac{R(s)K(s)}{s^2} \tag{8.10}$$

with an electromagnetic kernel function $K(s)$ [122]. Using a compilation of the world data for $e^+ e^- \to$ hadrons, the current estimate of the leading order hadronic contribution to a_μ is given by [123]

$$a_\mu^{\text{hvp}} = (692.3 \pm 4.2 \pm 0.3) \times 10^{-10}\,, \tag{8.11}$$

where the first error comes from the experimentally measured R-ratio and the second error is due to perturbative QCD, which is used to model the R-ratio for large energies, where no data are available.
In the same way, hadronic vacuum polarization contributions at order α^3 can be estimated and the value is [124]

$$a_\mu^{\text{hvp},\alpha^3} = (-9.84 \pm 0.06) \times 10^{-10}\,. \tag{8.12}$$

The hadronic vacuum polarization can also be calculated using lattice techniques, for more details see sections 8.2 and 8.3. Figure 8.6 shows recent results for the hadronic contribution to a_μ from different lattice calculations compared with the result from $e^+ e^- \to$ hadrons.

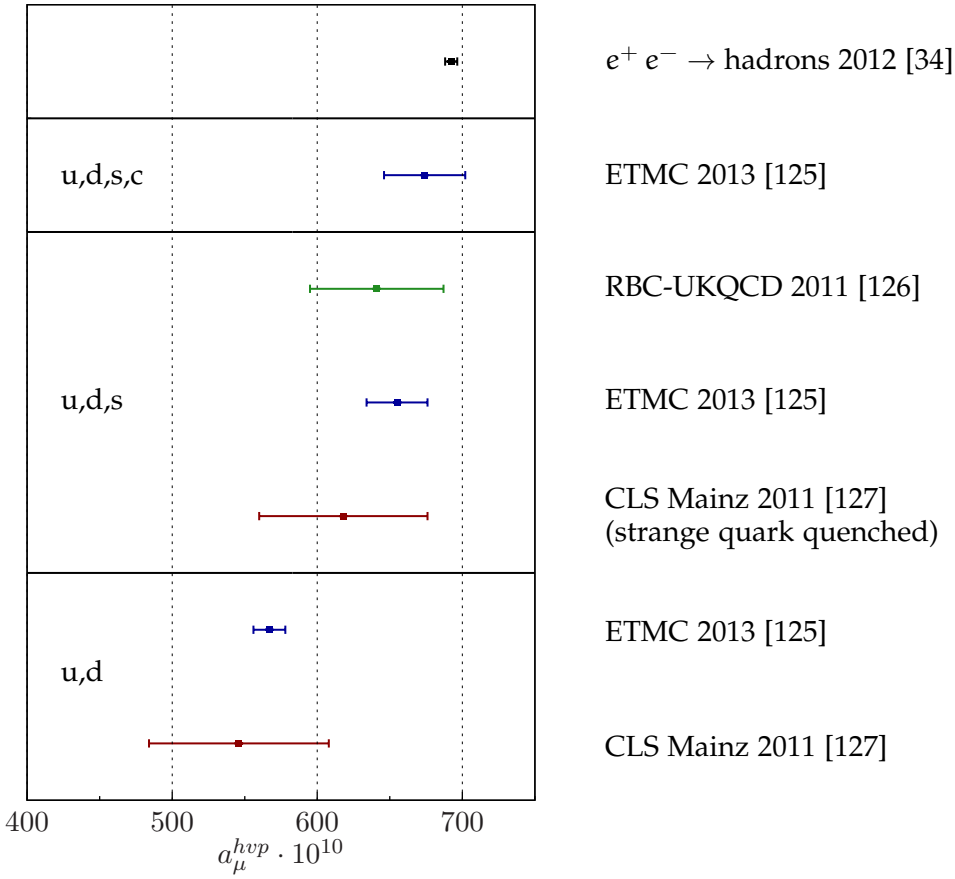

Figure 8.6: Recent results for a_μ^{hvp} from different lattice collaborations compared with the result from $e^+ e^-$, which is shown in the upper panel. The three lower panels show results for four, three and two valence quark flavors.

Clearly, lattice results are at this stage not able to achieve the same accuracy as the phenomenological estimate. Furthermore one can see that the lattice results

are closer to the $e^+ e^-$ result (which includes all quark flavors) when more quark flavors are used.

Another QCD contribution to the anomalous magnetic moment of the muon is the hadronic light-by-light scattering (lbl), which sets in at order α^3. The corresponding diagram is shown in figure 8.7.

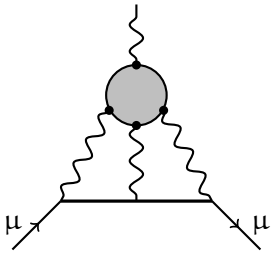

Figure 8.7: The hadronic light-by-light scattering contribution to the anomalous magnetic moment of the muon.

A theoretical estimate for the light-by-light scattering can be obtained from QCD in the large N_c limit and a recent result is given by [128]

$$a_\mu^{\text{lbl}} = (10.5 \pm 2.6) \times 10^{-10} \,. \tag{8.13}$$

A computation of the light-by-light scattering from lattice QCD is technically very complicated, since it requires the calculation of a four-point function. To avoid explicitly calculating four-point functions, an ansatz has been proposed by Blum *et al.* including QED on the lattice [129, 130].

8.1.2 *Comparison of Theory and Experiment*

Summing all individual contributions, the electromagnetic (8.6), the weak (8.7), the hadronic vacuum polarization at $\mathcal{O}(\alpha^2)$ (8.11) and $\mathcal{O}(\alpha^3)$ (8.12) as well as the light-by-light scattering (8.13), one obtains the current Standard Model estimate for the anomalous magnetic moment of the muon [34]

$$a_\mu^{\text{SM}} = (11659180.3 \pm 0.1 \pm 4.2 \pm 2.6) \times 10^{-10} \,, \tag{8.14}$$

where the first error is from electroweak contributions, the second from the leading order strong contribution, i.e. the hadronic vacuum polarization, and the third error is due to higher order hadronic contributions including light-by-light scattering. Clearly, the largest fraction of the error of the theoretical prediction originates from QCD, and thus a reduction of the overall error requires a better estimate of the hadronic contributions, e.g. from the lattice.
If one compares the Standard Model prediction (8.14) with the experimental result (8.4), one finds a discrepancy of $\approx 3.6\sigma$

$$\Delta a_\mu = a_\mu^{\text{exp}} - a_\mu^{\text{SM}} = (28.8 \pm 6.3 \pm 4.9) \times 10^{-10} \,. \tag{8.15}$$

This deviation leaves room for new physics such as Supersymmetry (SUSY) or the dark photon [131, 132]. The dark photon is a hypothetical $U(1)$ gauge boson, that couples to dark matter and mixes with the Standard Model photon.

It is crucial to reduce the error on both - the experiment and the theory - to either confirm a possible discrepancy or to reduce it. Currently, the muon storage ring from Brookhaven is being installed at Fermilab to reduce the experimental error by a factor of four [133]. From the theory side, a more precise calculation of the hadronic contributions is required. Here it would be desirable to have a first-principles calculation instead of having to rely on experimental input.
In the next two sections we will discuss two methods for calculating the hadronic vacuum polarization in lattice QCD, the *standard* and the *mixed-representation* method, where the latter will be used in this thesis to estimate the disconnected contribution to the hadronic vacuum polarization.

8.2 THE HADRONIC VACUUM POLARIZATION FROM LATTICE QCD

The hadronic vacuum polarization $\Pi(Q^2)$ can be written in terms of the hadronic vacuum polarization tensor

$$\Pi_{\mu\nu}(Q) \equiv \int d^4x \; e^{i\,Q\cdot x} \; \left\langle j_\mu^\gamma(x) \; j_\nu^\gamma(0) \right\rangle = (Q_\mu Q_\nu - \delta_{\mu\nu} Q^2)\, \Pi(Q^2)\,, \tag{8.16}$$

which is given by the correlation function of two electromagnetic currents

$$j_\mu^\gamma = \frac{2}{3}\bar{u}\gamma_\mu u - \frac{1}{3}\bar{d}\gamma_\mu d - \frac{1}{3}\bar{s}\gamma_\mu s + \cdots\,, \tag{8.17}$$

where the current for each quark flavor is weighted by the electric charge of the corresponding quark. Performing the corresponding Wick contractions of the correlation function $\left\langle j_\mu^\gamma(x) \; j_\nu^\gamma(0) \right\rangle$ of the vector current, one obtains a connected and a disconnected contribution, which are shown in figure 8.8.

Figure 8.8: Connected and disconnected contribution to the two-point function of the vector current.

From the subtracted vacuum polarization

$$\hat{\Pi}(Q^2) = 4\,\pi^2 \left[\Pi(Q^2) - \Pi(0)\right]\,, \tag{8.18}$$

the leading order hadronic contribution to $g-2$ can be calculated

$$a_\mu^{\text{had}} = \left(\frac{\alpha}{\pi}\right)^2 \int_0^\infty dQ^2\, K(Q^2)\, \hat{\Pi}(Q^2) \tag{8.19}$$

with an electromagnetic kernel $K(Q^2)$, which is analytically known [134]. Thus, a calculation of the vacuum polarization $\Pi(Q^2)$ from the lattice provides a result for the hadronic contribution to the anomalous magnetic moment of the muon from first principles.

Commonly, the hadronic vacuum polarization is calculated by performing the four-dimensional Fourier transformation of the correlation function $\left\langle j_\mu^\gamma(x) \; j_\nu^\gamma(0) \right\rangle$

to obtain the vacuum polarization tensor $\Pi_{\mu\nu}(Q)$ according to equation (8.16). This method has become state of the art, and many calculations of the connected contribution are available [125–127, 135–142]. In the following, we will refer to this method as the *standard method*. The drawback of this method is that the hadronic vacuum polarization

$$\Pi(Q^2) = \frac{\Pi_{\mu\nu}(Q)}{(Q_\mu Q_\nu - \delta_{\mu\nu} Q^2)} \tag{8.20}$$

cannot be calculated directly for $Q^2 = 0$. However, the calculation of the anomalous magnetic moment of the muon requires the subtracted vacuum polarization $\hat{\Pi}(Q^2)$ and therefore also $\Pi(0)$. Ideally, $\Pi(0)$ should be known very precisely. In the standard method an estimate of $\Pi(0)$ has to be obtained by extrapolating the hadronic vacuum polarization to zero momentum. However, the functional form of $\Pi(Q^2)$ is *a priori* unknown, and any extrapolation introduces a possible source of systematic error.
One approach to obtain better control of this systematic error is the use of partially twisted boundary conditions in the spatial directions [94, 95] for the valence quarks,

$$q(x + L \cdot \hat{k}) = e^{i\theta_k} q(x)\,, \tag{8.21}$$

instead of periodic boundary conditions. This allows tuning the momentum on the lattice continuously,

$$p_i = \frac{2\pi}{L} n_i + \frac{\theta_i}{L}\,. \tag{8.22}$$

Using zero momentum from the Fourier transformation, i.e $n_i = 0$ and non-vanishing twist angle θ_i one can also obtain momenta which are smaller than the lowest Fourier mode. In this way, one can achieve a better resolution of the hadronic vacuum polarization for small momenta and a better constraint on the extrapolation to $Q^2 = 0$ [140].
These extrapolations are often done using Padé-approximants to different orders, which have been shown to give good results [143, 144].

So far only the ETMC collaboration has done a lattice calculation of the disconnected diagram to the hadronic vacuum polarization using the standard method, where they found the disconnected contribution to be consistent with zero within the statistical errors [145].

In all other determinations, the disconnected contribution has been neglected. However, an estimate using quenched chiral perturbation theory indicates that the disconnected contribution could be as large as -10% of the connected contribution [29, 30]. Compared to the accuracy of recent lattice calculations (see also figure 8.6) of $< 10\%$, the disconnected contribution might not longer be negligible.

In the following section we will introduce an alternative approach for the calculation of the hadronic vacuum polarization using the time-momentum vector correlator. In section 9.2 we will discuss how this method allows for a systematic inclusion of the disconnected contribution.

8.3 THE TIME-MOMENTUM CORRELATOR

A different method for calculating the hadronic vacuum polarization on the lattice has been developed recently [31–33]. In this method the mixed time-momentum representation vector correlator is used for the calculation of the hadronic vacuum polarization. In the following, we will derive the relation between $\hat{\Pi}(Q^2)$ and the correlator $G^{\gamma\gamma}(t)$ of two vector currents

$$G^{\gamma\gamma}(t) = -\int d^3x \left\langle j_k^\gamma(x)\; j_k^\gamma(0)\right\rangle \qquad \text{for} \quad k = 1,2,3 \tag{8.23}$$

in time-momentum space following the derivation of [31]. The electromagnetic current in (8.23) is given by

$$j_k^\gamma = \frac{2}{3}\bar{u}\gamma_k u - \frac{1}{3}\bar{d}\gamma_k d - \frac{1}{3}\bar{s}\gamma_k s + \cdots . \tag{8.24}$$

The integral over the spatial components in (8.23) is a Fourier transformation and projects the vector two-point function on spatial momentum $\mathbf{q} = 0$. As we will show in section 9.1, the vector correlator $G^{\gamma\gamma}(t)$ contains a connected and a disconnected Wick contraction (cf. figure 8.8).
It is obvious that the correlator $G^{\gamma\gamma}(t)$ is related to the vacuum polarization tensor $\Pi_{\mu\nu}(Q)$ (8.16) by

$$\Pi_{kk}(\omega, \mathbf{q} = 0) = \int d^4x\; e^{i\omega t} \left\langle j_k^\gamma(x)\; j_k^\gamma(0)\right\rangle = -\int dt\; e^{i\omega t}\, G^{\gamma\gamma}(t)\,. \tag{8.25}$$

Furthermore, the tensor structure of the polarization tensor implies that

$$\Pi_{kk}(\omega, \mathbf{q} = 0) = (\underbrace{Q_k Q_k}_{=0} - \delta_{kk} Q^2)\,\Pi(Q^2) \overset{Q^2=\omega^2}{=} -\omega^2\,\Pi(\omega^2)\,. \tag{8.26}$$

Inserting equation (8.26) into the relation (8.25) between the vector correlator and the polarization tensor one obtains

$$\Pi(\omega^2) = \frac{1}{\omega^2} \int_{-\infty}^{\infty} dt\; e^{i\omega t}\, G^{\gamma\gamma}(t)\,. \tag{8.27}$$

For the calculation of a_μ^{hvp} we need the subtracted vacuum polarization (cf. equation (8.18)), i.e.

$$\hat{\Pi}(\omega^2) = 4\pi^2 \left[\Pi(\omega^2) - \Pi(0)\right] . \tag{8.28}$$

If we expand the exponent in equation (8.27) into a Taylor series, we obtain

$$\begin{aligned}\Pi(\omega^2) &\sim \frac{1}{\omega^2} \int_{-\infty}^{\infty} dt\; G^{\gamma\gamma}(t) - \frac{1}{2} \int_{-\infty}^{\infty} dt\; t^2\, G^{\gamma\gamma}(t) + \mathcal{O}(\omega^2) \\ &\overset{\omega\to 0}{=} \frac{1}{\omega^2} \int_{-\infty}^{\infty} dt\; G^{\gamma\gamma}(t) - \frac{1}{2} \int_{-\infty}^{\infty} dt\; t^2\, G^{\gamma\gamma}(t) = \Pi(0)\,,\end{aligned} \tag{8.29}$$

where we have used that $G^{\gamma\gamma}(t)$ is even in t, i.e. $G^{\gamma\gamma}(t) = G^{\gamma\gamma}(-t)$, and thus

$$\int_{-\infty}^{\infty} dt\ t^n\, G^{\gamma\gamma}(t) = 0 \tag{8.30}$$

for odd n. The subtracted vacuum polarization can now be written as

$$\Pi(\omega^2) - \Pi(0) = \int_{-\infty}^{\infty} dt\ G^{\gamma\gamma}(t) \left[\frac{e^{i\omega t} - 1}{\omega^2} + \frac{t^2}{2}\right]. \tag{8.31}$$

Splitting the exponential function $\exp(i\omega t)$ into a real and an imaginary part and considering that the integral vanishes for functions which are odd in t one obtains

$$\begin{aligned}\Pi(\omega^2) - \Pi(0) &= 2\int_0^{\infty} dt\ G^{\gamma\gamma}(t) \left[\frac{t^2}{2} - \frac{1-\cos(\omega t)}{\omega^2}\right] \\ &= \frac{1}{\omega^2} \int_0^{\infty} dt\ G^{\gamma\gamma}(t) \left[\omega^2 t^2 - 4\sin^2\left(\frac{1}{2}\,\omega t\right)\right].\end{aligned} \tag{8.32}$$

Equation (8.32) implies that the subtracted vacuum polarization can be calculated at arbitrary momenta $Q^2 = \omega^2$ if the correlator $G^{\gamma\gamma}(t)$ is known for zero spatial momentum $\mathbf{q} = 0$. The integral in (8.32) has to be carried out up to $t \to \infty$ and thus one has to model the correlator $G^{\gamma\gamma}(t)$ by an exponential decay $\propto \exp(-m_0 \cdot t)$ for large euclidean times t where no lattice data are available. For this purpose we will investigate the behavior of the correlator for $t \to \infty$ in section 9.2.
Once $\hat{\Pi}(Q^2)$ has been determined using the time-momentum correlator, one can obtain the leading order hadronic contribution to the anomalous magnetic moment of the muon via equation (8.19).

Since this method for the calculation of the hadronic vacuum polarization involves the vector correlator $G^{\gamma\gamma}(t)$, which according to the definition (8.23) is given in time-momentum space, we will refer to this method as the *mixed-representation method* in the following. So far it has successfully been used for the calculation of the connected contribution to the hadronic vacuum polarization [4, 32, 33].

However, this approach is particularly useful in the case of the disconnected contribution, since for disconnected diagrams one is restricted to Fourier momenta and cannot use partially twisted boundary conditions to resolve the vacuum polarization for very small values of Q^2. In the standard method it is important to resolve the vacuum polarization $\Pi(Q^2)$ for small values of Q^2 in order to reliably obtain $\Pi(0)$ from an extrapolation. In the mixed-representation method the subtracted vacuum polarization $\hat{\Pi}(Q^2)$ can be obtained directly from the vector correlator (cf. equation (8.32)).
Another more technical advantage of calculating the disconnected part of the hadronic vacuum polarization using the mixed-representation correlator is that

we can make use of the quark loops which we have calculated during the scalar form factor project. The insertion of different Dirac structures Γ in

$$L(\mathbf{q}, z_0) = \sum_{z} e^{iq\cdot z}\ \mathrm{Tr}_{CD}\left[S(z,z)\ \Gamma\right] \tag{8.33}$$

is cheap in terms of computer time, and thus we can calculate different Dirac structures in one computation.

8.4 THE VECTOR CORRELATOR AND THE QCD SPECTRUM

The spectral representation of the vector correlator $G^{VV}(t)$ is given by [31]

$$G^{VV}(t) = \int_0^\infty d\omega\, \omega^2 \rho(\omega)\, e^{-\omega|t|} \tag{8.34}$$

where the spectral function $\rho(\omega)$ is related to the R-ratio

$$\rho(\omega^2) = \frac{R(\omega^2)}{12\pi} \qquad \text{with} \qquad R(\omega^2) = \frac{\sigma(e^+e^- \to \text{hadrons}, \omega^2)}{\sigma(e^+e^- \to \mu^+\mu^-, \omega^2)}\,. \tag{8.35}$$

To determine which vector resonances contribute to the correlator $G^{VV}(t)$, one uses a flavor decomposition of the electromagnetic current

$$j^V_\mu \equiv j^l_\mu + j^s_\mu + \cdots\ . \tag{8.36}$$

For the light quarks, the current j^l_μ can be split into an isovector and an isoscalar part,

$$j^l_\mu = \underbrace{\frac{1}{2}\left(\bar{u}\gamma_\mu u - \bar{d}\gamma_\mu d\right)}_{I=1,\ j^\rho_\mu} + \underbrace{\frac{1}{6}\left(\bar{u}\gamma_\mu u + \bar{d}\gamma_\mu d\right)}_{I=0,\ \frac{1}{3}j^\omega_\mu}, \tag{8.37}$$

which corresponds to the ρ and the ω meson, respectively. Including the strange quark contribution to the electromagnetic current

$$j^s_\mu = -\frac{1}{3}\,\bar{s}\gamma_\mu s \tag{8.38}$$

one obtains the ϕ meson.

One can also add contributions for the heavier quark flavors, i.e. the charm and bottom quarks. Their ground state vector mesons are the J/Ψ and the Υ, respectively. However, in this thesis we will concentrate on the light and strange vector current, i.e. the mesons of interest are ρ, ω and ϕ.

9

RESULTS

9.1 CONNECTED AND DISCONNECTED VECTOR CORRELATOR

In the following, we will perform the Wick contractions and present our lattice results for the vector correlator. We will start with the light-quark (up, down) contributions only and add a strange quark later.

9.1.1 *Light Quark Contribution*

We define the mixed time-momentum vector correlator $G^l(x_0)$ for the light quarks as

$$G^l(x_0) \equiv -\int d^3x \ \langle j_k^l(x)\, j_k^l(0)\rangle \tag{9.1}$$

with the light-quark vector current

$$j_k^l(x) = \frac{2}{3}\bar{u}\gamma_k u - \frac{1}{3}\bar{d}\gamma_k d\,. \tag{9.2}$$

The prefactors $2/3$ and $-1/3$ correspond to the charges of the up and the down quark, respectively. Inserting the vector current in (9.1) and using Wick's Theorem (3.22) we find that

$$\begin{aligned}\langle j_k^l(x)\, j_k^l(0)\rangle = &\frac{4}{9}\langle \bar{u}\overbrace{(x)\gamma_k u(x)}\ \bar{u}\overbrace{(0)\gamma_k u(0)}\rangle + \frac{1}{9}\langle \bar{d}\overbrace{(x)\gamma_k d(x)}\ \bar{d}\overbrace{(0)\gamma_k d(0)}\rangle \\ &-\frac{2}{9}\langle \bar{u}\overbrace{(x)\gamma_k u(x)}\ \bar{d}\overbrace{(0)\gamma_k d(0)}\rangle - \frac{2}{9}\langle \bar{d}\overbrace{(x)\gamma_k d(x)}\ \bar{u}\overbrace{(0)\gamma_k u(0)}\rangle\,,\end{aligned} \tag{9.3}$$

where the first two terms of (9.3) have a connected and a disconnected Wick contraction, and the last two terms are purely disconnected. If we assume isospin symmetry, i.e. $S^u(x,y) = S^d(x,y) = S^l(x,y)$, as is the case in our lattice calculation, we can write the correlation of the light vector current as

$$\langle j_k^l(x)\, j_k^l(0)\rangle = -\frac{5}{9}\ \langle \mathrm{Tr}_{CD}\left[S^l(x,0)\ \gamma_k\ S^l(0,x)\ \gamma_k\right]\rangle_G \tag{9.4}$$

$$+\frac{1}{9}\ \langle \mathrm{Tr}_{CD}\left[S^l(x,x)\ \gamma_k\right]\cdot \mathrm{Tr}_{CD}\left[S^l(0,0)\ \gamma_k\right]\rangle_G \tag{9.5}$$

$$= \langle j_k^l(x)\, j_k^l(0)\rangle_{con} + \langle j_k^l(x)\, j_k^l(0)\rangle_{disc} \tag{9.6}$$

with a quark-connected (9.4) and a quark-disconnected (9.5) contribution (cf. figure 8.8). If one defines the connected and the disconnected vector correlator in the following way:

$$G^l_{con}(x_0) \equiv \int d^3x \ \langle \mathrm{Tr}_{CD}\left[S^l(x,0)\ \gamma_k\ S^l(0,x)\ \gamma_k\right]\rangle_G\,, \tag{9.7}$$

$$G^l_{disc}(x_0) \equiv \int d^3x \ \langle \mathrm{Tr}_{CD}\left[S^l(x,x)\ \gamma_k\right]\cdot \mathrm{Tr}_{CD}\left[S^l(0,0)\ \gamma_k\right]\rangle_G\,, \tag{9.8}$$

one finds for the total vector correlator for the two light quark flavors

$$G^l(x_0) = \frac{5}{9} G^l_{\text{con}}(x_0) - \frac{1}{9} G^l_{\text{disc}}(x_0)\,. \tag{9.9}$$

As already discussed above, the vector current can be split into an isovector and an isoscalar part,

$$j^l_k = \underbrace{\frac{1}{2}\left(\overline{u}\gamma_k u - \overline{d}\gamma_k d\right)}_{I=1,\ j^\rho_k} + \underbrace{\frac{1}{6}\left(\overline{u}\gamma_k u + \overline{d}\gamma_k d\right)}_{I=0,\ \frac{1}{3}j^\omega_k}\,. \tag{9.10}$$

If one performs the Wick contractions only for the isovector current j^ρ_k, one obtains the ρ-correlator

$$G^{\rho\rho}(x_0) \equiv -\int d^3x\ \left\langle j^\rho_k(x)\, j^\rho_k(0)\right\rangle = \frac{1}{2} G^l_{\text{con}}(x_0)\,, \tag{9.11}$$

which is a purely connected quantity, and all disconnected contributions are contained in the isoscalar part corresponding to the ω meson.

To construct the disconnected light vector correlator $G^l_{\text{disc}}(x_0)$ from the disconnected loops

$$L(\mathbf{q}, z_0) = \sum_{\mathbf{z}} e^{i\mathbf{q}\cdot\mathbf{z}}\ \text{Tr}_{\text{CD}}\left[\gamma_k\ S(z,z)\right]\,, \tag{9.12}$$

which we have calculated as part of the scalar form factor project[1], we have to correlate the loop for $\mathbf{q} = 0$ at a given timeslice x_0 with the loop on a different timeslice y_0,

$$f^l(x_0 - y_0) = \left\langle \left(\sum_{\mathbf{x}} \text{Tr}_{\text{CD}}\left[\gamma_k\, S(x,x)\right]\right)\cdot\left(\sum_{\mathbf{y}} \text{Tr}_{\text{CD}}\left[\gamma_k\, S(y,y)\right]\right)\right\rangle_G\,, \tag{9.13}$$

where the average $\langle\rangle_G$ denotes the gauge average. Since in equation (9.13) we have summed over the spatial coordinates of both the source and the sink, we have to divide by the spatial volume L^3 to obtain the same normalization as for the connected correlator, where one only sums over the sink position. Furthermore, the local vector current (9.2) is not conserved and thus we have to renormalize the vector current with the multiplicative renormalization constant Z_V. In total we find

$$G^l_{\text{disc}}(x_0 - y_0) = \frac{Z_V^2}{L^3}\left\langle \left(\sum_{\mathbf{x}} \text{Tr}_{\text{CD}}\left[\gamma_k\, S(x,x)\right]\right)\cdot\left(\sum_{\mathbf{y}} \text{Tr}_{\text{CD}}\left[\gamma_k\, S(y,y)\right]\right)\right\rangle_G\,. \tag{9.14}$$

For our $\beta = 5.3$ ensembles the renormalization constant has been determined non-perturbatively [146]

$$Z_V = 0.750 \pm 0.005\,. \tag{9.15}$$

1 Although the vector loops were not required for the scalar form factor project, we included $\Gamma = \gamma_k$ in our computation. The insertion of different Γ structures is cheap in computational cost.

In Figure 9.1 the result for the disconnected vector correlator $G^l_{\text{disc}}(x_0 - y_0)$ is shown for the E5 ensemble. Since we have calculated the disconnected loop on every timeslice, we can take the mean over all possible temporal source positions y_0. As one can see, we find that the disconnected contribution to the light vector correlator is consistent with zero within the statistical accuracy of our calculation.

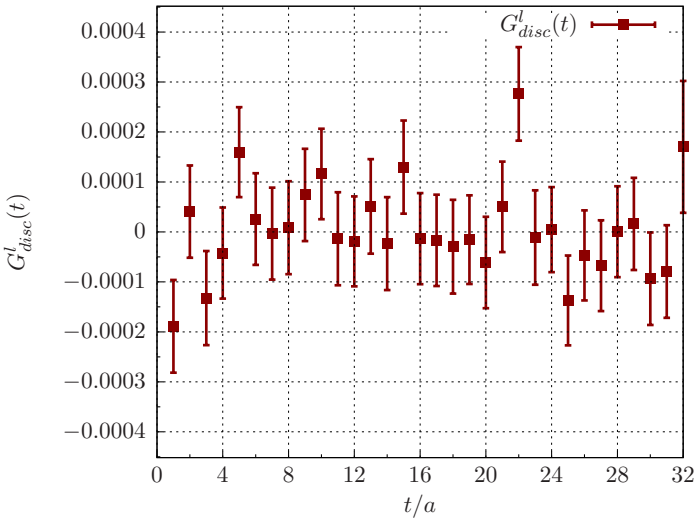

Figure 9.1: The disconnected vector correlator $G^l_{\text{disc}}(t)$ for the light-quark contribution calculated on 1000 E5 configurations.

However, we must add the disconnected and connected contribution to obtain the full light vector correlator. The connected correlator, which has been calculated by Anthony Francis and Benjamin Jäger [4], uses the local vector current (9.2) at the source and a point-split vector current of the form [136]

$$V^c_\mu(x) = \frac{1}{2}\left(\overline{q}(x + a\hat{\mu})(1+\gamma_\mu)U^\dagger_\mu(x)\, q(x) - \overline{q}(x)(1-\gamma_\mu)U_\mu(x)\, q(x + a\hat{\mu})\right) \quad (9.16)$$

at the sink. The point-split current is conserved on the lattice and fulfills a Ward-Takahashi identity

$$q_\mu V^c_\mu(x) = 0\,, \quad (9.17)$$

which is not true for the local vector current $\overline{q}\gamma_\mu q$. Since we use the connected correlator of one local and one conserved current, only one factor of Z_V is required for the renormalization of the connected part.

Our result for the connected as well as for the total vector correlator $G^l(x_0)$ is shown in figure 9.2. The connected vector correlator (red data points) shows the expected behavior of a two-point function, which can be described by a single exponential for larger times and additional excited states, which are visible at small source-sink separations t. To increase statistics, the mean over the forward and the backward propagating correlator has been taken. If we add the disconnected vector correlator to obtain the total vector correlator (yellow data points), the signal-to-noise ratio grows exponentially due to the roughly

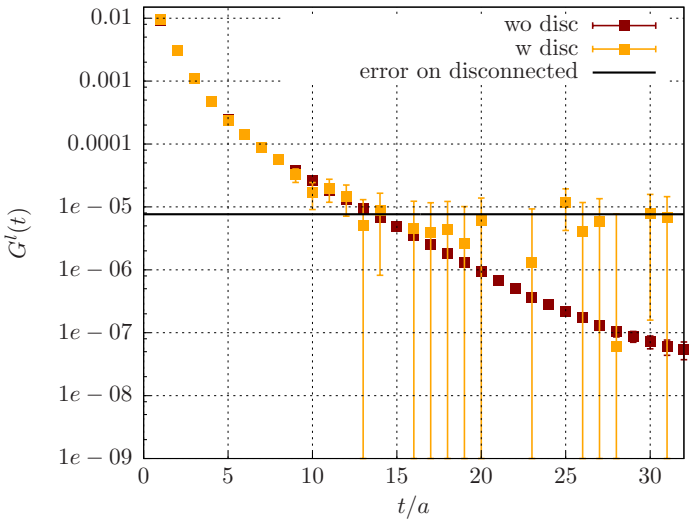

Figure 9.2: The connected (red) and total (yellow) vector correlator $G^l(t)$ for the light-quark contribution calculated on 1000 E5 configurations. The black line shows the error on the disconnected part.

constant error on the disconnected contribution. At $t \approx 14a \approx 0.9$ fm, the total vector correlator reaches the level of the error on the disconnected part, which is shown as a black line in figure 9.2. At this point our result for $G^l(t)$ is dominated by the error on $G^l_{\text{disc}}(t)$, and the signal for the total vector correlator is lost.

Although we do not find a signal for the disconnected contribution to the vector correlator and hence the hadronic vacuum polarization, we are still interested in an upper limit on the maximum contribution of the disconnected diagram. However, the vector correlator is dominated by noise already at early times, such that an estimate for an upper limit would be unsatisfactory in this case. Nevertheless, as we will see in the following, the situation can be significantly improved when adding the strange-quark contribution due to the structure of the disconnected Wick contractions.

9.1.2 *Light and Strange Quark Contribution*

We will now extend our study of the mixed-representation vector correlator to three quark flavors. The vector current for light-quark and strange-quark contribution is given by

$$j_k^{ls}(x) = j_k^l(x) + j_k^s(x) \qquad \text{with} \quad j_k^s(x) = -\frac{1}{3}\bar{s}\gamma_k s\,. \tag{9.18}$$

We define the light and strange vector correlator as the correlation of the three-flavor vector current $j_k^{ls}(x)$ with itself projected to zero spatial momentum,

$$G^{ls}(x_0) \equiv -\int d^3x\ \left\langle j_k^{ls}(x)\, j_k^{ls}(0)\right\rangle\,. \tag{9.19}$$

If one considers only connected Wick contractions, one obtains, besides the connected light-quark contribution, a connected contribution from the strange quark, which is given by

$$\langle j_k^s(x)\, j_k^s(0)\rangle_{\text{con}} = -\frac{1}{9}\,\langle \mathrm{Tr}_{\text{CD}}\,[S^s(x,0)\;\gamma_k\;S^s(0,x)\;\gamma_k]\rangle_G\;, \tag{9.20}$$

with strange-quark propagators $S^s(x,y)$.

For the disconnected part, it is advantageous to look at the combined contribution of all three quark flavors, which one can write as

$$\begin{aligned}
&\left\langle j_k^{ls}(x)\, j_k^{ls}(0)\right\rangle_{\text{disc}} \\
&= \frac{1}{9}\,\left\langle \mathrm{Tr}_{\text{CD}}\left[S^l(x,x)\;\gamma_k\right]\cdot \mathrm{Tr}_{\text{CD}}\left[S^l(0,0)\;\gamma_k\right]\right\rangle_G \\
&- \frac{1}{9}\,\left\langle \mathrm{Tr}_{\text{CD}}\left[S^l(x,x)\;\gamma_k\right]\cdot \mathrm{Tr}_{\text{CD}}\left[S^s(0,0)\;\gamma_k\right]\right\rangle_G \\
&- \frac{1}{9}\,\left\langle \mathrm{Tr}_{\text{CD}}\left[S^s(x,x)\;\gamma_k\right]\cdot \mathrm{Tr}_{\text{CD}}\left[S^l(0,0)\;\gamma_k\right]\right\rangle_G \\
&+ \frac{1}{9}\,\left\langle \mathrm{Tr}_{\text{CD}}\left[S^s(x,x)\;\gamma_k\right]\cdot \mathrm{Tr}_{\text{CD}}\left[S^s(0,0)\;\gamma_k\right]\right\rangle_G \\
&= \frac{1}{9}\,\Big\langle \left(\mathrm{Tr}_{\text{CD}}\left[S^l(x,x)\;\gamma_k\right] - \mathrm{Tr}_{\text{CD}}\left[S^s(x,x)\;\gamma_k\right]\right) \\
&\qquad\qquad \times \left(\mathrm{Tr}_{\text{CD}}\left[S^l(0,0)\;\gamma_k\right] - \mathrm{Tr}_{\text{CD}}\left[S^s(0,0)\;\gamma_k\right]\right)\Big\rangle_G\,.
\end{aligned} \tag{9.21}$$

Equation (9.21) implies that the disconnected correlation can also be written as the disconnected part of the correlation of the light minus the strange current,

$$\left\langle j_k^{ls}(x)\, j_k^{ls}(0)\right\rangle_{\text{disc}} = \left\langle \left(j_k^l(x) - j_k^s(x)\right)\left(j_k^l(0) - j_k^s(0)\right)\right\rangle_{\text{disc}}\,. \tag{9.22}$$

Thus, for our lattice calculation we only need differences of the all-to-all propagators for light and strange quarks,

$$\mathrm{Tr}_{\text{CD}}\left[S^l(x,x)\;\gamma_k - S^s(x,x)\;\gamma_k\right]. \tag{9.23}$$

Since we calculate the all-to-all propagators stochastically, we can calculate light and strange propagators with the same stochastic sources. In this way, one expects the statistical noise from the stochastic sources to be partially canceled in the difference of the light and strange-quark propagators.

The calculation of the strange-quark propagators requires the strange-quark mass m_s on a given lattice. The values used for this thesis have been determined [54] by tuning the strange hopping parameter κ_s such that the mass ratio

$$\frac{m_K^2 - \frac{1}{2}\,m_\pi^2}{m_\Omega^2} \tag{9.24}$$

receives its physical value. Furthermore one has to note that our strange quark is quenched, since our gauge ensembles contain only contributions from light quarks in the sea.

The plot on the left-hand side of figure 9.3 shows the light $G^l_{\text{disc}}(t)$ and strange $G^s_{\text{disc}}(t)$ disconnected correlators separately, i.e. the light data are the same as the

data in figure 9.1 from above. As expected, light and strange results are highly correlated, since they have been calculated with the same stochastic sources. The plot on the right-hand side shows the combined correlator using the differences of the light and strange propagators as explained above,

$$G^{ls}_{disc}(x_0 - y_0) = \frac{Z_V^2}{L^3} \left\langle \left(\sum_{\mathbf{x}} \left(\mathrm{Tr}_{CD}\left[S^l(x,x)\, \gamma_k \right] - \mathrm{Tr}_{CD}\left[S^s(x,x)\, \gamma_k \right] \right) \right. \right. \\ \left. \left. \times \sum_{\mathbf{y}} \left(\mathrm{Tr}_{CD}\left[S^l(y,y)\, \gamma_k \right] - \mathrm{Tr}_{CD}\left[S^s(y,y)\, \gamma_k \right] \right) \right) \right\rangle_G . \quad (9.25)$$

If one compares the orders of magnitude of the errors between the plots on the left and on the right, one finds that the error of the combined correlator $G^{ls}_{disc}(t)$ is roughly 95% smaller than the error on the individual light-quark or strange-quark contributions. This implies that indeed a significant amount of stochastic noise is canceled when calculating both propagators with the same noise sources. Nevertheless, we still find that the disconnected contribution to the vector correlator is consistent with zero within its errors and any possible signal cannot be resolved with our present accuracy.

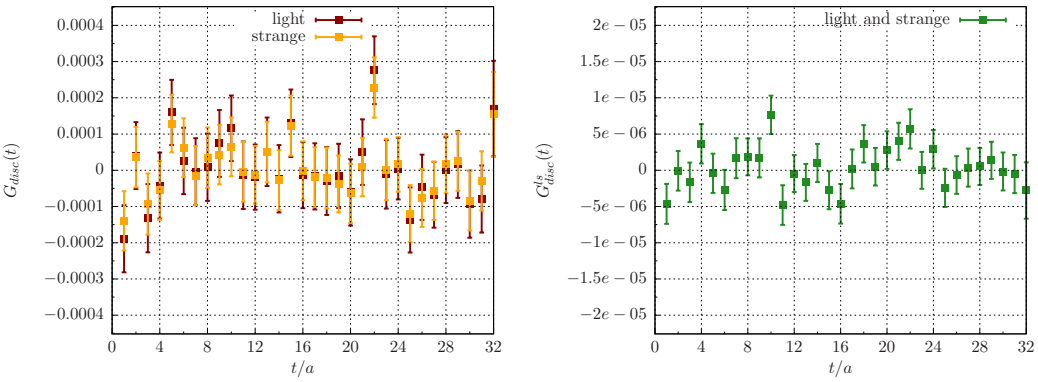

Figure 9.3: The light and strange disconnected vector correlator. On the left the contributions for light and strange quarks are shown separately. The plot on the right-hand side shows the disconnected vector correlator for light and strange quarks combined.

As for the light-quark vector correlator, we can add the disconnected contribution to the connected one as shown in figure 9.4. The total vector correlator is given by

$$G^{ls}(x_0) = \frac{5}{9} G^l_{con}(x_0) + \frac{1}{9} G^s_{con}(x_0) - \frac{1}{9} G^{ls}_{disc}(x_0) . \quad (9.26)$$

One can see that the region where the error of the disconnected contribution dominates starts at $t \approx 24a \approx 1.5$ fm. Compared to $14a$, which we found for the light quarks, this underlines how well the error reduction works when both light and strange quark loops are calculated with the same stochastic sources.

However, since we still cannot resolve a signal for the disconnected vector correlator, we have to resort to giving an upper limit for the error that arises when

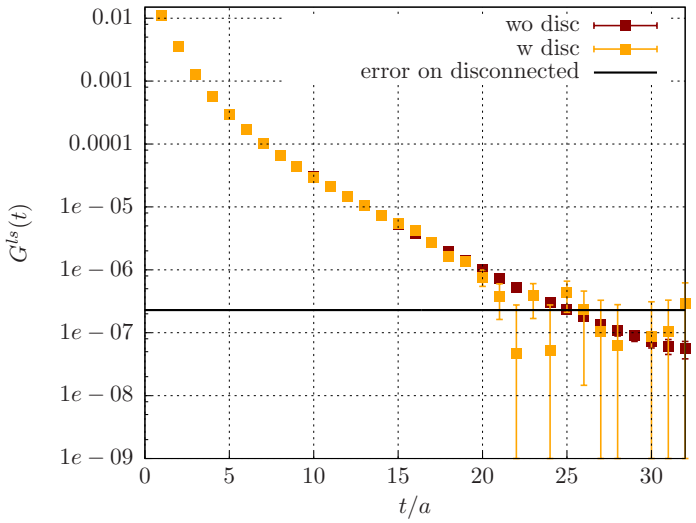

Figure 9.4: The connected (red) and total (yellow) vector correlator $G^{ls}(t)$ for the light and strange quark contribution calculated on 1000 E5 configurations. The black line shows the error on the disconnected part.

neglecting the disconnected diagrams. In the next section, we will discuss the behavior of the vector correlator for infinite Euclidean times and use this result combined with our data to estimate the maximum disconnected contribution.

9.2 THE VECTOR CORRELATOR AT LARGE EUCLIDEAN TIMES

In the following we will solely consider the case of light and strange quark flavors, for which we obtain a significantly smaller statistical error for the disconnected contribution as described above. From our data we know that the total vector correlator $G^{ls}(t)$ is well described by only the connected part for small source-sink separations. However, we found that for larger times $t \approx 1.5$ fm, the error on the disconnected contribution gets large compared to the connected correlator, and thus our data cannot exclude that the disconnected contribution becomes important at some point.
For the calculation of the hadronic vacuum polarization with the mixed-representation method, we need the vector correlator up to infinite times (cf. equation (8.32)) and thus we have to make an assumption for the disconnected contribution for large Euclidean times anyway. In the following, we will extend the arguments given in [32] about the behavior of the correlator to three quark flavors. For light quarks the authors stated that the disconnected contribution to the vector correlator is of the same order as the connected one for large Euclidean time separations.

As already discussed in section 8.4, the vector current can be split into an isovector and an isoscalar part

$$j_\mu^{ls} = \underbrace{\frac{1}{2}\left(\bar{u}\gamma_\mu u - \bar{d}\gamma_\mu d\right)}_{I=1,\ j_\mu^{I=1}} + \underbrace{\frac{1}{6}\left(\bar{u}\gamma_\mu u + \bar{d}\gamma_\mu d - 2\bar{s}\gamma_\mu s\right)}_{I=0,\ j_\mu^{I=0}} . \tag{9.27}$$

As long as isospin is an exact symmetry, which is the case in our lattice calculations, equation (9.27) implies that the correlator $G^{ls}(t)$ can be split into an isoscalar and an isovector part as well,

$$\begin{aligned} G^{ls}(x_0) &= -\int d^3x \ \left\langle j_k^{ls}(x)\, j_k^{ls}(0)\right\rangle \\ &= -\int d^3x \ \left\langle j_k^{I=1}(x)\, j_k^{I=1}(0) + j_k^{I=0}(x)\, j_k^{I=0}(0)\right\rangle \\ &= G^{I=1}(x_0) + G^{I=0}(x_0)\,. \end{aligned} \tag{9.28}$$

Since the spectral function $\rho(\omega)$ is related to the vector correlator via the spectral representation (cf. equation (8.34))

$$G^{\gamma\gamma}(t) = \int_0^\infty d\omega\, \omega^2 \rho(\omega)\, e^{-\omega|t|}\,, \tag{9.29}$$

this property directly translates to $\rho(\omega)$,

$$\rho^{ls}(\omega) = \rho^{I=I}(\omega) + \rho^{I=0}(\omega)\,, \tag{9.30}$$

which simply means that a final hadron state in $e^+ e^- \to$ hadrons is either isovector or isoscalar. Since two pions is the lightest possible final isovector state, the isovector channel opens at energies $\omega = 2m_\pi$ and thus

$$\rho^{I=1}(\omega) = 0 \qquad \text{for} \quad \omega < 2m_\pi. \tag{9.31}$$

For the production of an isoscalar hadronic state at least an energy of the mass of three pions is needed, and hence

$$\rho^{I=0}(\omega) = 0 \qquad \text{for} \quad \omega < 3m_\pi\,. \tag{9.32}$$

Combining the relations (9.31) and (9.32) we find that in the energy region between these two thresholds

$$\rho^{ls}(\omega) = \rho^{I=I}(\omega) \qquad \text{for} \quad 2m_\pi < \omega < 3m_\pi\,, \tag{9.33}$$

while $\rho^{ls}(\omega) = 0$ for $\omega < 2m_\pi$.

On the other hand, we obtain the following Wick contractions for the isoscalar correlator

$$\begin{aligned} G^{I=0}(x_0) &\equiv -\int d^3x \ \left\langle j_k^{I=0}(x)\, j_k^{I=0}(0)\right\rangle \\ &= \frac{1}{18} G^l_{con}(x_0) + \frac{1}{9} G^s_{con}(x_0) - \frac{1}{9} G^{ls}_{disc}(x_0)\,, \end{aligned} \tag{9.34}$$

which can be translated to the isoscalar spectral function,

$$\rho^{I=0}(\omega) = \frac{1}{18}\rho^l_{con}(\omega) + \frac{1}{9}\rho^s_{con}(\omega) - \frac{1}{9}\rho^{ls}_{disc}(\omega)\,. \tag{9.35}$$

If one compares this relation with the low-energy behavior of $\rho^{I=0}(\omega)$ from equation (9.32), it is obvious that

$$\rho^{ls}_{disc}(\omega) = \frac{1}{2}\rho^l_{con}(\omega) + \rho^s_{con}(\omega) \qquad \text{for} \quad \omega < 3m_\pi\,. \tag{9.36}$$

According to the spectral representation (9.29) the region of small energies in the spectral function is most important at large Euclidean times for the vector correlator. Therefore, for $x_0 \to \infty$, one expects the following behavior:

$$G^{ls}_{disc}(x_0) = \left(\frac{1}{2}G^{l}_{con}(x_0) + G^{s}_{con}(x_0)\right)\left(1 + \mathcal{O}(e^{-m_\pi x_0})\right). \tag{9.37}$$

This relation shows that for large Euclidean times the disconnected contribution to the vector correlator $G^{ls}(x_0)$ is of the same order of magnitude as the connected one. This is consistent with what has been found in [32] for the light quarks only.
Equation (9.37) can now be inserted into the expression for the total light and strange vector correlator

$$\begin{aligned} G^{ls}(x_0) &= \frac{5}{9}G^{l}_{con}(x_0) + \frac{1}{9}G^{s}_{con}(x_0) - \frac{1}{9}G^{ls}_{disc}(x_0) \\ &= \frac{1}{2}G^{l}_{con}(x_0)\left(1 + \mathcal{O}(e^{-m_\pi x_0})\right) \qquad \text{for} \quad x_0 \to \infty. \end{aligned} \tag{9.38}$$

Using that $1/2 G^{l}_{con}(x_0) = G^{\rho\rho}(x_0)$, the vector correlator for large Euclidean times can be rewritten in terms of the ρ correlator,

$$G^{ls}(x_0) = G^{\rho\rho}(x_0)\left(1 + \mathcal{O}(e^{-m_\pi x_0})\right), \tag{9.39}$$

which simply reflects that for large times only the isovector part survives due to its lower threshold energy.

The behavior of the vector correlator for large Euclidean times can help us to estimate the disconnected contribution. Nevertheless, to obtain a full evaluation of the maximum disconnected contribution to the anomalous magnetic moment of the muon, we have to investigate up to which timeslice x_0 the disconnected contribution can be neglected and from which time on we will use an asymptotic value to estimate it.
As a starting point, one can rewrite the expression for the full vector correlator $G^{ls}(x_0)$ (9.26) by dividing by the ρ correlator and rearranging the terms

$$-\frac{1}{9}\frac{G^{ls}_{disc}(x_0)}{G^{\rho\rho}(x_0)} = \frac{G^{ls}(x_0) - G^{\rho\rho}(x_0)}{G^{\rho\rho}(x_0)} - \frac{1}{9}\left(1 + 2\frac{G^{s}_{con}(x_0)}{G^{l}_{con}(x_0)}\right). \tag{9.40}$$

Equation (9.40) gives us a handle on the ratio of the disconnected correlator and the ρ correlator and is true for all times x_0. For $x_0 \to \infty$, the first term of the right-hand side of (9.40) vanishes, due to the large time behavior (9.39)

$$\frac{G^{ls}(x_0) - G^{\rho\rho}(x_0)}{G^{\rho\rho}(x_0)} \quad \longrightarrow \quad 0 \qquad \text{for} \quad x_0 \to \infty. \tag{9.41}$$

Additionally, we know that the ratio of the strange and the light connected correlators, $G^{s}_{con}(x_0)/G^{l}_{con}(x_0)$, has to vanish for large x_0,

$$\left(1 + 2\frac{G^{s}_{con}(x_0)}{G^{l}_{con}(x_0)}\right) \quad \longrightarrow \quad 1 \qquad \text{for} \quad x_0 \to \infty, \tag{9.42}$$

since the mass of the ϕ meson is larger than the lightest mesonic states build from light quarks, and $G^{s}_{con}(x_0)/G^{l}_{con}(x_0)$ is exponentially suppressed. Thus, the

large time behavior of the ratio (9.40) of disconnected and ρ correlator is given by

$$-\frac{1}{9}\frac{G^{ls}_{disc}(x_0)}{G^{\rho\rho}(x_0)} \quad \longrightarrow \quad -\frac{1}{9} \qquad \text{for} \qquad x_0 \to \infty\,. \tag{9.43}$$

In figure 9.5 this ratio is shown for our data for the E5 ensemble. As expected the ratio is consistent with zero within the errors. The error grows exponentially for larger timeslices t due to the roughly constant error $\Delta G^{ls}_{disc}(t)$ of the disconnected contribution and the exponentially falling ρ correlator. The green line in figure 9.5 shows the asymptotic value $-1/9$. One can easily distinguish the data from the asymptotic behavior up to $t = 15a \approx 1$ fm. For larger times our results are also consistent with $-1/9$. On the basis of these data we cannot discriminate between a slow approach to the asymptotic value and a sudden drop to $-1/9$ around $t \gtrsim 1$ fm.

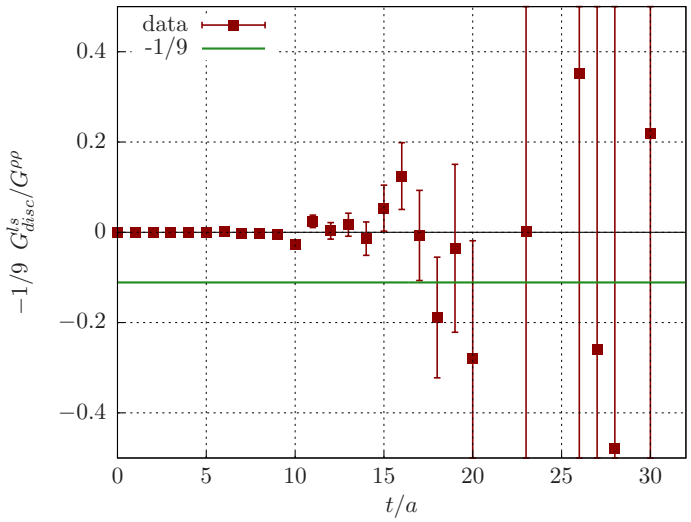

Figure 9.5: The ratio $-\frac{1}{9}\ G^{ls}_{disc}(t)/G^{\rho\rho}(t)$ for the E5 ensemble. The green line shows the asymptotic value $-1/9$ for large Euclidean times t.

We are interested in the scenario where the disconnected correlator contributes maximally to the hadronic vacuum polarization according to our data. Therefore we claim that the ratio is consistent with our data and we assume that the ratio falls monotonously to $-1/9$ at some point. Clearly, the disconnected contribution is the largest in the case, where at 1 fm the ratio suddenly jumps from basically zero to the asymptotic value $-1/9$. This is indicated by the blue line in figure 9.6, which shows the same data as the previous figure 9.5.

This allows us to give a conservative estimate on the maximum systematic error on the anomalous magnetic moment of the muon which arises from neglecting the disconnected contribution. For this, one has to calculate the hadronic vacuum polarization once with the connected contribution only and once with an estimate of the disconnected contribution, which follows the blue line in figure 9.6.

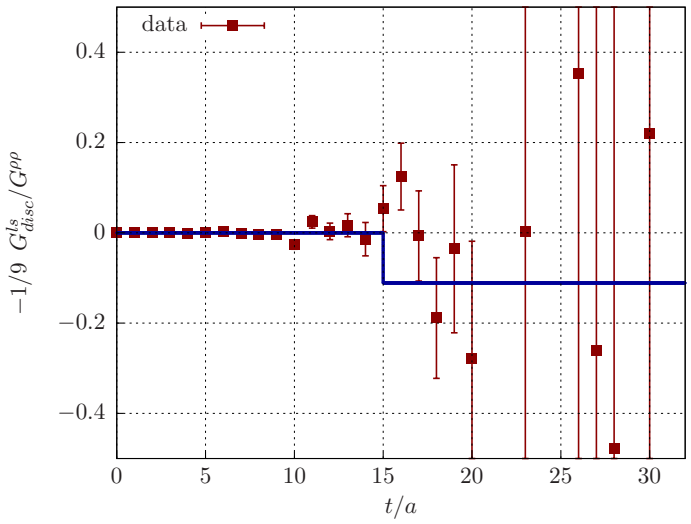

Figure 9.6: The ratio $-\frac{1}{9}\ G^{ls}_{disc}(t)/G^{\rho\rho}(t)$ for the E5 ensemble. The blue line shows our estimate for the disconnected contribution for the calculation of the hadronic vacuum polarization.

9.3 HADRONIC VACUUM POLARIZATION AND a_μ

In the mixed-representation method, which is described in section 8.3, the subtracted hadronic vacuum polarization can be calculated from the vector correlator using

$$\hat{\Pi}(Q^2) = \frac{1}{Q^2} \int_0^\infty dt\ G^{\gamma\gamma}(t) \left[Q^2 t^2 - 4 \sin^2\left(\frac{1}{2} Qt\right)\right] . \tag{9.44}$$

In the following, we will calculate $\hat{\Pi}(Q^2)$ for light and strange quarks, first for the connected vector correlator and second for the vector correlator with a disconnected estimate. Finally, we compute the leading order hadronic contribution to the anomalous magnetic moment of the muon from the vacuum polarization for both cases. The difference of both results can be used as an estimate for a maximum systematic error from neglecting the disconnected contribution in the calculation of a_μ.

9.3.1 *The Connected Contribution*

For the calculation of the connected contribution to the hadronic vacuum polarization from the connected vector correlator following equation (9.44), the correlator up to infinity is needed. From the lattice, which is a finite volume, we only have data for half the box size T in the time direction. Thus, we need an extrapolation of the correlator to infinity. Additionally, it is desirable to have an interpolation between different data points in the region where data is still available.

At the larger Euclidean times, where one expects that only the ground state has survived, it is convenient to fit an exponential function to the correlator. Since we consider the vector correlator for light and strange quarks

$$G^{ls}_{con}(t) = \frac{5}{9} G^{l}_{con}(t) + \frac{1}{9} G^{s}_{con}(t)\,, \tag{9.45}$$

we fit the light correlator and the strange correlator separately, each with a single exponential. Thus the connected light strange vector correlator is given by a sum of two exponentials

$$G^{ls}_{con}(t) = A_l\ e^{-m_l\, t} + A_s\ e^{-m_s\, t} \tag{9.46}$$

one for the light vector ground state (l) and one for the strange vector ground state (s). In the light channel, the vector ground state is the ρ meson, i.e $m_l = m_\rho$, since for the gauge ensembles E5, F6 and F7 used in this study the mass of the pion is large, such that the ρ cannot decay into two pions and thus is stable. In the strange channel, the ground state is given by the ϕ meson, i.e. $m_s = m_\phi$. The masses of ρ and ϕ obtained from these fits are shown in the appendix in figure C.6 for the three ensembles E5, F6 and F7 used in this analysis. For $t \geqslant 15a$ we will use the fit result for the correlator to calculate the hadronic vacuum polarization.

For smaller times, where excited states can still play a role, we use an interpolation of the data with cubic splines. At $t = 15a$ the cubic spline has been set to the fit value at that point and the slope to the slope of the fit function. This ensures that our interpolation is continuously differentiable at the point $t = 15a$ where splines and exponential fit are connected.
The connected light and strange vector correlator $G^{ls}_{con}(t)$ is plotted in figure 9.7 together with the result of the cubic splines (black curve) and the exponential fit (green curve).

The interpolated cubic splines and the result of the exponential fit can now be used to calculate the connected contribution to the hadronic vacuum polarization for light and strange quarks,

$$\hat{\Pi}^{ls}_{con}(Q^2) = \frac{1}{Q^2} \int_0^\infty dt\ G^{ls}_{con}(t) \left[Q^2 t^2 - 4 \sin^2\left(\frac{1}{2} Qt\right)\right]. \tag{9.47}$$

This integral is split into two parts, one where the vector correlator has been interpolated with cubic splines and one, where we use the fit result

$$\begin{aligned}\hat{\Pi}^{ls}_{con}(Q^2) = \frac{1}{Q^2} \sum_{i=0}^{14} \int_{i\cdot a}^{(i+1)\cdot a} dt\ G^{i}_{cubic}(t) \left[Q^2 t^2 - 4 \sin^2\left(\frac{1}{2} Qt\right)\right] \\ + \frac{1}{Q^2} \int_{15a}^{\infty} dt\ \left(A_l\, e^{-m_l\, t} + A_s\, e^{-m_s\, t}\right) \left[Q^2 t^2 - 4 \sin^2\left(\frac{1}{2} Qt\right)\right],\end{aligned} \tag{9.48}$$

where the correlator interpolated between two points $t = i \cdot a$ and $t = (i+1) \cdot a$,

$$G^{i}_{cubic}(t) = a_i t^3 + b_i t^2 + c_i t + d_i\,, \tag{9.49}$$

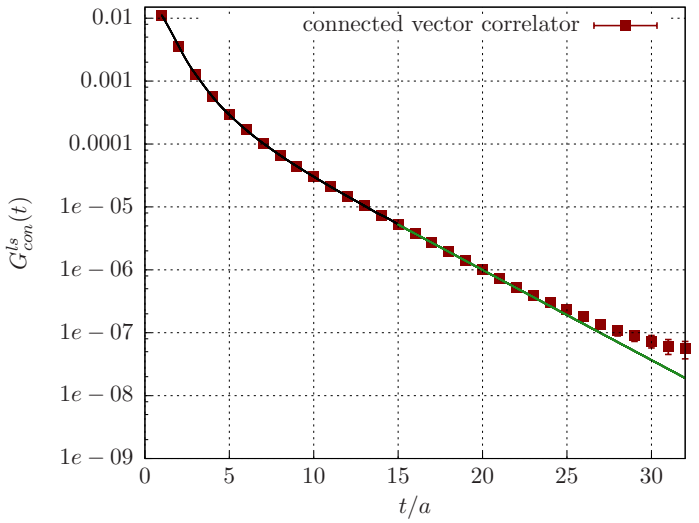

Figure 9.7: The connected vector correlator $G^{ls}_{con}(t)$ for light and strange quarks for E5. The black line up to $t = 15a$ shows the interpolation with cubic splines. The green line starting at $t = 15a$ shows the result of the exponential fit with the fit range $t = 15a$ to $t = 20a$. The deviation of the data from the fit curve for $t \approx T/2$ is due to the periodic boundary conditions and the backward propagating correlator.

is a cubic polynomial. In both regions, the integral can be carried out analytically. The result for the connected hadronic vacuum polarization on the E5 ensemble is plotted in figure 9.8 against the momentum Q^2.

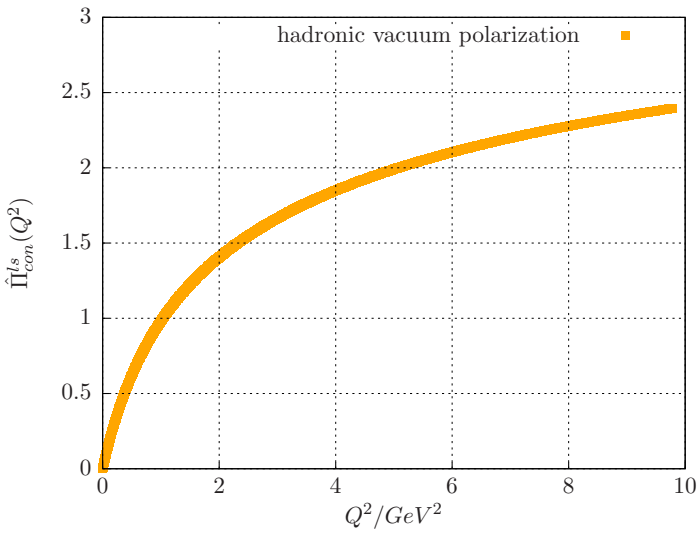

Figure 9.8: The connected contribution to the subtracted vacuum polarization for light and strange quarks plotted against the momentum Q^2 for the E5 ensemble.

9.3.2 *Estimate for the Disconnected Contribution*

To obtain an upper limit for the disconnected contribution to the hadronic vacuum polarization, we repeat the same analysis as for the connected one using the estimate for the disconnected correlator as explained above, i.e.

- Up to $x_0 = 15a$ the disconnected contribution is neglected, i.e. we use

$$G^{ls}(x_0) = \frac{5}{9} G^{l}_{con}(x_0) + \frac{1}{9} G^{s}_{con}(x_0)\,, \tag{9.50}$$

  for the vector correlator as we know from figure 9.4 that the vector correlator is well described by the connected contribution only.

- For $x_0 > 15a$, we use the asymptotic value for the disconnected contribution $G^{ls}_{disc}(x_0) = G^{\rho\rho}(x_0)$, i.e. we use

$$\begin{aligned} G^{ls}(x_0) &= \frac{5}{9} G^{l}_{con}(x_0) + \frac{1}{9} G^{s}_{con}(x_0) - \frac{1}{9} G^{\rho\rho}(x_0) \\ &= G^{\rho\rho}(x_0) + \frac{1}{9} G^{s}_{con}(x_0) \end{aligned} \tag{9.51}$$

  for the vector correlator.

From this approach we obtain the largest possible contribution of the disconnected diagram to the hadronic vacuum polarization which is still consistent with our data. The result for $\hat{\Pi}^{ls}(Q^2)$ with the disconnected estimate is shown in figure 9.9 in red compared to the result from the connected vector correlator in yellow. As expected, the data with the estimate for the disconnected correlator lie below those of the connected one, since the asymptotic value $G^{ls}_{disc}(x_0) = G^{\rho\rho}(x_0)$ is subtracted from the vector correlator $G^{ls}(x_0)$ (cf. equation (9.51)).

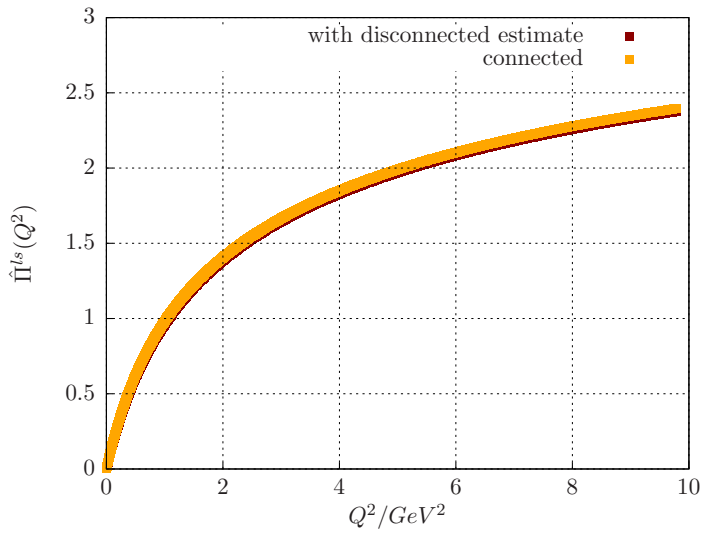

Figure 9.9: The subtracted vacuum polarization for light and strange quarks with an estimate for the disconnected contribution (red) compared to the connected contribution alone.

The statistical errors on the hadronic vacuum polarization $\hat{\Pi}^{ls}(Q^2)$ in the plotted Q^2 region are of the order of $\approx 0.5\%$ and thus, not visible in figures 9.8 and 9.9. To be able to judge if the difference between the connected data and the result using a disconnected estimate is significant, figure 9.10 shows the difference between the red and the yellow data points from figure 9.9. As one can see, this difference is larger than the statistical error and is thus significant.

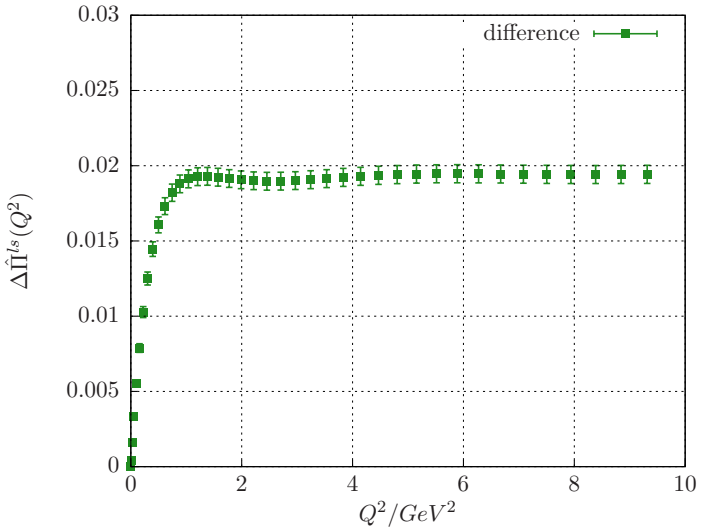

Figure 9.10: The difference $\Delta\hat{\Pi}^{ls}(Q^2)$ between the connected vacuum polarization and the vacuum polarization calculated with the estimate for the disconnected contribution plotted against the momentum Q^2.

9.3.3 *The Hadronic Contribution to* a_μ

In the last step, we will now determine the leading order hadronic contribution to the anomalous magnetic moment of the muon for light and strange quarks from the hadronic vacuum polarization. This calculation will be done once with the vacuum polarization from the connected correlator and once with the disconnected estimate.
To obtain a_μ, one has to integrate $\hat{\Pi}(Q^2)$ over the momentum Q^2 (cf. equation (8.19)),

$$a_\mu^{hvp} = \left(\frac{\alpha}{\pi}\right)^2 \int_0^\infty dQ^2\, K(Q^2)\, \hat{\Pi}(Q^2)\,. \tag{9.52}$$

The electromagnetic integration kernel $K(Q^2)$ is given by [134]

$$K(Q^2) = \frac{1}{m_\mu^2}\ \hat{Q}^2\ Z(\hat{Q}^2)^3\ \frac{1-\hat{Q}^2\,Z(\hat{Q}^2)}{1+\hat{Q}^2\,Z(\hat{Q}^2)^2} \tag{9.53}$$

$$\text{with}\quad Z(\hat{Q}^2) = -\frac{\hat{Q}^2-\sqrt{\hat{Q}^4+4\hat{Q}^2}}{2\hat{Q}^2}\qquad \text{and}\quad \hat{Q}^2 = \frac{Q^2}{m_\mu^2}\,. \tag{9.54}$$

The required integral over Q^2 can be performed numerically using the trapezoidal rule. Actually, one has to integrate up to $Q^2 = \infty$, but in practice, we cut the integral at $Q^2 = 10\ \mathrm{GeV}^2$. This is a justified approximation as one can see in figure 9.11. Here, the integrand

$$\left(\frac{\alpha}{\pi}\right)^2 K(Q^2)\,\hat{\Pi}(Q^2) \tag{9.55}$$

is plotted against Q^2 for the E5 ensemble with the $\hat{\Pi}(Q^2)$ from the connected light and strange vector correlator. Thus, the area under this curve is the connected contribution to a_μ^{hvp}. As one can see, the integrand (9.55) has a maximum at roughly $0.002\ \mathrm{GeV}^2$ and then drops rapidly for larger momenta. In [61] the hadronic vacuum polarization was calculated with the standard method and perturbation theory was used to model $\hat{\Pi}(Q^2)$ for large momenta $Q^2 > 4\ \mathrm{GeV}^2$. The contribution of the region $Q^2 > 4\ \mathrm{GeV}^2$ to a_μ^{hvp} was found to be below 0.07%. Thus, we can be confident that calculating the integral up to $Q^2 = 10\ \mathrm{GeV}^2$ is clearly sufficient and any contribution from higher momenta Q^2 can be neglected.

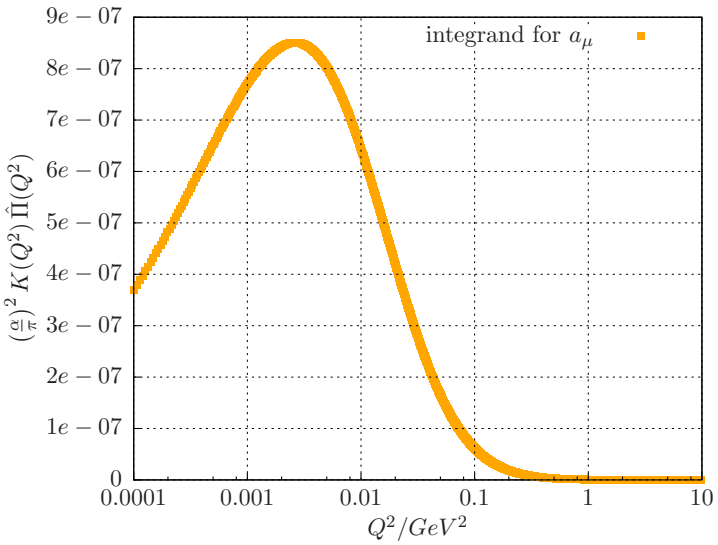

Figure 9.11: The integrand for the calculation of the anomalous magnetic moment of the muon for the E5 ensemble. a_μ^{hvp} is the area under this curve.

Performing the integral (9.52) we find as a result for the hadronic contribution to the anomalous magnetic moment of the muon

$$a_\mu^{\mathrm{hvp}} = (325.0 \pm 4.9) \times 10^{-10} \qquad \text{connected} \tag{9.56}$$

$$a_\mu^{\mathrm{hvp}} = (313.7 \pm 4.5) \times 10^{-10} \qquad \text{with disconnected estimate} \tag{9.57}$$

for the E5 ensemble. As expected, the value calculated with disconnected estimate is smaller, as the hadronic vacuum polarization is smaller as well. The contribution of the disconnected diagram clearly has to be negative, since the asymptotic value of the disconnected vector correlator $G^{ls}_{\mathrm{disc}}(x_0) = G^{\rho\rho}(x_0)$ is

subtracted from the connected correlator for large Euclidean times, where the disconnected contribution becomes important.
One has to keep in mind, that our estimate of the disconnected contribution is as conservative as possible. According to our data, the disconnected correlator cannot contribute more to anomalous magnetic moment of the muon. Thus, the result for a_μ^{hvp} with disconnected estimate (9.57) provides a very conservative bound on the true hadronic contribution to a_μ for light and strange quarks at this pion mass and could in reality be much closer to the result from the connected vector correlator (9.56).

Comparing the result for connected (9.56) and the result including the disconnected estimate (9.57), we find that the latter is $\approx 3.5\%$ smaller. The difference of both values can be used as an upper limit for a systematic error, which arises when neglecting the disconnected contribution

$$a_\mu^{hvp} = \left(325.0 \pm 4.9^{+0.0}_{-11.3}\right) \times 10^{-10} . \tag{9.58}$$

Thus, we can state that for the E5 ensemble the disconnected diagram for the hadronic vacuum polarization contributes at most -3.5% to a_μ^{hvp}.
If one compares the statistical error $\sigma(a_\mu^{hvp})_{stat} = 4.9 \times 10^{-10}$ from the calculation of the hadronic contribution and our upper limit for the systematic error $\sigma(a_\mu^{hvp})_{disc} = 11.3 \times 10^{-10}$ from the disconnected contribution, one finds that at the current accuracy of our calculations the systematic error is larger than the statistical one. Thus, our final result (9.58) can only be improved by reducing the error on the disconnected contribution.

So far, we have done the calculation of the connected and disconnected vector correlator for light and strange quarks for three different gauge ensemble, which are listed in table 9.1. Similar plots for the vector correlator and the hadronic vacuum polarization as shown above for E5 can be found in the appendix in section C.1 for the F6 and F7 ensembles. An overview over the ρ- and ϕ-masses for the three ensembles can be found in section C.2.

β	a[fm]	lattice	m_π[MeV]	$m_\pi L$	κ_s	Label	N_{cfg}
5.3	0.063	64×32^3	455	4.7	0.135546	E5	1000
5.3	0.063	96×48^3	325	5.0	0.135675	F6	300
5.3	0.063	96×48^3	280	4.3	0.135714	F7	250

Table 9.1: The CLS ensembles used to estimate the disconnected contribution to a_μ^{hvp}.

One has to note, that for the F6 and the F7 ensemble, the number of gauge configurations N_{cfg} that have been used is smaller than for the E5 ensemble. Although the number of lattice points is larger and thus we can average over more possible source positions, the error on the disconnected correlator $G^{ls}_{disc}(t)$ is slightly larger compared to E5. Thus, for F6 and F7 the resolution of the ratio

$$-\frac{1}{9}\frac{G^{ls}_{disc}(t)}{G^{\rho\rho}(t)} \tag{9.59}$$

(cf. figure C.3 in the appendix) is slightly worse compared to E5 and thus, we choose a smaller time $t_{cut} = 13a$ for which we assume that the disconnected contribution drops to its asymptotic value to obtain a conservative estimate for the maximum contribution of the disconnected correlator.

The results for the hadronic contribution to the anomalous magnetic moment of the muon from the connected part $a_\mu^{hvp,con}$, with disconnected estimate $a_\mu^{hvp,disc\ est}$ as well as their deviation

$$\Delta a_\mu^{hvp} = \frac{a_\mu^{hvp,con} - a_\mu^{hvp,disc\ est}}{a_\mu^{hvp,con}} \tag{9.60}$$

are compiled in table 9.2 for the three ensembles. One can see that the connected contribution to a_μ^{hvp} becomes larger for lighter pion masses, and, as expected, the results with the disconnected estimate are smaller than the connected ones. We find the deviation Δa_μ^{hvp} to be of the order of $\approx 4 - 6\%$, depending on the ensemble.

ensemble	t_{cut}	$a_\mu^{hvp,con}$	$a_\mu^{hvp,disc\ est}$	Δa_μ^{hvp}
E5	15	$(325.0 \pm 4.9) \times 10^{-10}$	$(313.7 \pm 4.5) \times 10^{-10}$	3.5%
F6	13	$(400.7 \pm 13.4) \times 10^{-10}$	$(380.6 \pm 12.1) \times 10^{-10}$	5.0%
F7	13	$(485.4 \pm 23.5) \times 10^{-10}$	$(457.4 \pm 21.2) \times 10^{-10}$	5.7%

Table 9.2: The results for a_μ^{hvp} calculated for the connected contribution and with disconnected estimate as well as the deviation of both values.

In figure 9.12 these results are plotted against the pion mass m_π^2 to indicate the chiral behavior. The connected contribution to a_μ^{hvp} is shown in red including error bars for the statistical errors only. We use the difference of the connected result and the result including the disconnected estimate as a maximum systematic error that arises from neglecting the disconnected contribution. As already discussed, the disconnected contribution has to be negative as indicated by the asymmetric green error bar in the plot.
Furthermore, one has to note that for all three ensembles, our estimate is as conservative as possible by combining the large time behavior of the Euclidean correlator with our explicit knowledge of the disconnected contribution from our lattice calculations. Thus, the disconnected contribution could well be much smaller than the maximum systematic error that is claimed here.

As one can see, for all three ensembles the systematic error is larger than the statistical one. This indicates that a more precise result for the hadronic contribution to the anomalous magnetic moment of the muon can only be achieved by reducing the error on the disconnected contribution. However, this would require even more effort, either in terms of computer time or better noise reduction techniques for the all-to-all propagators. Without a more precise estimate of the disconnected contribution, it will not be possible to obtain the

hadronic contribution to a_μ from a lattice calculation with an error of $< 1\%$ to be comparable with the determination using $e^+ e^- \to$ hadrons data.

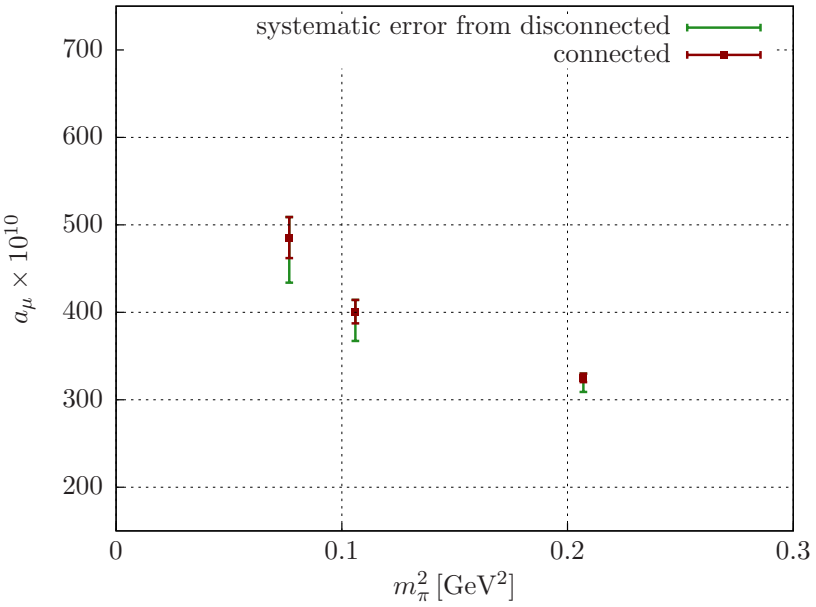

Figure 9.12: The results for the hadronic contribution a_μ^{hvp} to the anomalous magnetic moment of the muon plotted against the pion mass m_π^2. Red points show the results from the connected vector correlator. Green error bars show our conservative estimates for the maximum systematic error that arises from neglecting the disconnected contribution.

10

CONCLUSIONS AND OUTLOOK

We have explicitly calculated the disconnected contribution to the hadronic vacuum polarization using the time-momentum vector correlator. The required disconnected two-point functions have been estimated using stochastic sources and the generalized hopping parameter expansion. Although we have been able to systematically improve our calculation for the combined light and strange quark disconnected correlator $G^{ls}_{disc}(t)$ by computing light and strange quark loops with the same random sources, we still find the disconnected contribution to the hadronic vacuum polarization to be consistent with zero within our current accuracy. However, using the expected behavior of the correlator for large Euclidean times, we are able to give an upper limit for the maximum disconnected contribution to the anomalous magnetic moment of the muon.
Up to a certain timeslice t_{cut}, our data show that $G^{ls}_{disc}(t)$ is negligible compared to the connected correlator. From that timeslice on, we assume that in the case where the disconnected diagram contributes maximally according to our data, $G^{ls}_{disc}(t)$ falls from basically zero to its asymptotic value. This allows us to estimate the maximum systematic error that arises from neglecting the disconnected contribution when calculating a_μ^{hvp} in lattice QCD, and we find this systematic error to be of the order $\approx -5\%$ depending on the gauge ensemble and the available statistics.
In quenched chiral perturbation theory it was estimated that the disconnected contribution can be as large as -10% [29, 30] for the light quarks. This estimate can also be reproduced by our approach. If we did not perform any explicit calculation of the disconnected diagram, we would have to assume, that the disconnected vector correlator drops to its asymptotic value $G^{\rho\rho}(t)$ already at $t_{cut} = 0$. In the case of only the light quarks, one would replace

$$G^{l}(t) = \frac{10}{9} G^{\rho\rho}(t) - \frac{1}{9} G^{l}_{disc}(t) \to G^{\rho\rho}(t) = 0.9 \cdot \left(\frac{10}{9} G^{\rho\rho}(t) \right) . \tag{10.1}$$

Repeating our analysis, we would find a value which is by a factor 0.9 smaller than the result from the connected vector correlator only. Thus, we can state, that even without any explicit knowledge of the disconnected vector correlator, its contribution cannot be larger than -10% in the light quark sector, as stated in [32]. With our explicit calculation of the disconnected correlator for light and strange quarks, we have been able to further reduce this upper limit.

To be compatible with the accuracy of the phenomenological estimate of a_μ^{hvp} (cf. equation (8.11)) using $e^+e^- \to$ hadrons data, one would need a lattice calculation of a_μ^{hvp} with a precision of $< 1\%$. However, the statistical error on the disconnected correlator is large, such that it could still contribute to a level of $\approx 5\%$ to a_μ^{hvp}, which is larger than the statistical error on the connected contribution from our mixed-representation calculation. Assuming that the disconnected contribution is indeed much smaller, e.g. smaller than 1% of

the connected one, it would be desirable to reduce the statistical error on the disconnected vector correlator such that it translates into a systematic error of $< 1\%$ for a_μ^{had}. Therefore one must be able to better resolve the ratio

$$-\frac{1}{9}\frac{G^{ls}_{disc}(x_0)}{G^{\rho\rho}(x_0)} = \frac{G^{ls}(x_0) - G^{\rho\rho}(x_0)}{G^{\rho\rho}(x_0)} - \frac{1}{9}\left(1 + 2\frac{G^{s}_{con}(x_0)}{G^{l}_{con}(x_0)}\right), \tag{10.2}$$

such that one can choose a later timeslice where one assumes that the disconnected contribution jumps to its asymptotic value. To figure out, what amount of statistics would be required, one can choose different values of t_{cut}, up to which the disconnected contribution is neglected as depicted in figure 10.1.

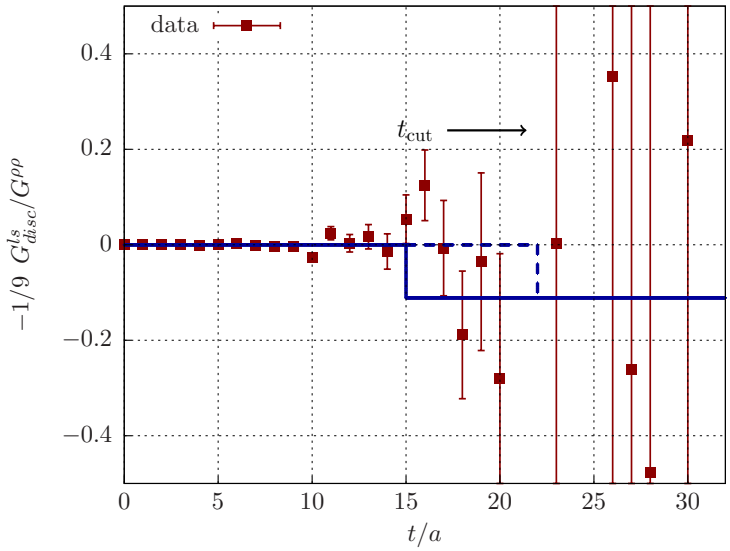

Figure 10.1: Assuming that one could resolve the ratio (10.2) to a better precision, one could choose a larger timeslice t_{cut} up to which the disconnected vector correlator can be set to zero, e.g the dotted line instead of the solid one.

For the E5 ensemble we have repeated the analysis for calculating a_μ^{hvp} with a disconnected estimate choosing different values of t_{cut}. In figure 10.2 the relative deviation of a_μ^{hvp} with disconnected estimate and the connected result

$$\Delta a_\mu^{hvp} = \frac{a_\mu^{hvp,con} - a_\mu^{hvp,disc\ est}}{a_\mu^{hvp,con}} \tag{10.3}$$

is plotted against t_{cut}. For $t_{cut} = 15$ this deviation is the 3.5% quoted above as the systematic error on a_μ^{hvp}. As expected, the deviation from the connected result gets smaller the longer the disconnected contribution can be neglected, i.e. the larger the value of t_{cut}. As one can see, the level of $< 1\%$ is reached at $t_{cut} = 23$.

Thus, to resolve the disconnected contribution to a_μ^{hvp} to be smaller than 1% of the connected one, we would have to clearly distinguish the ratio $-1/9\, G^{ls}_{disc}(x_0)/G^{\rho\rho}(x_0)$ from the asymptotic $-1/9$ up to $t = 23$. Unfortunately the error on the ratio grows exponentially, such that the absolute error at $t = 23$ has reached ≈ 0.66. Thus, one would have to reduce this error by at least a factor

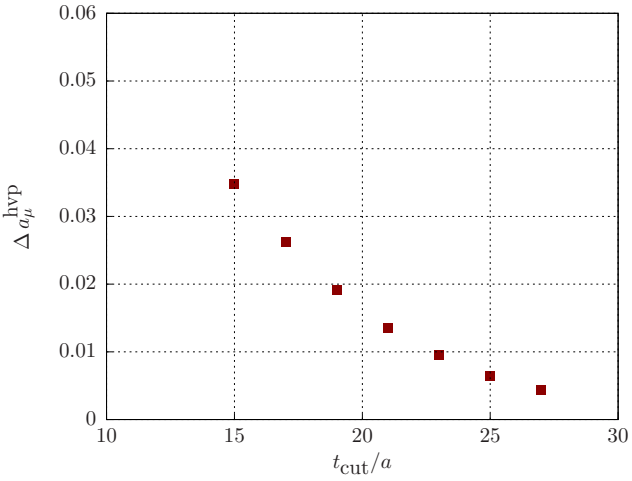

Figure 10.2: The dependence of the relative systematic error $\Delta\, a_\mu^{\mathrm{hvp}}$ from neglecting the disconnected contribution up to t_{cut} for the E5 ensemble.

of 6. However, an error reduction of a factor 6 requires a factor 36 in statistics, which is not affordable at this point.
For the lighter ensembles, such as F6 and F7, even more effort would be needed to reduce the systematic error to a sub-percent level. Figure 10.3 shows the integrand $f(t)$ of the formula for the calculation of the hadronic vacuum polarization with the mixed time-moment correlator (cf. equation (9.44))

$$\hat{\Pi}(Q^2) = \int_0^\infty dt \underbrace{G^{\gamma\gamma}(t)\left[t^2 - \frac{4}{Q^2}\sin^2\left(\frac{1}{2}Qt\right)\right]}_{f(t)} \tag{10.4}$$

for $Q^2 = 0.05\ \mathrm{GeV}^2$. One can see that the integrand has a maximum, which for lighter masses is located at larger values of t. Thus, for lighter masses, a given t_{cut} is closer to the maximum, and thus the difference $\Delta\, a_\mu^{\mathrm{hvp}}$ is larger for smaller masses, even for the same amount of statistics.

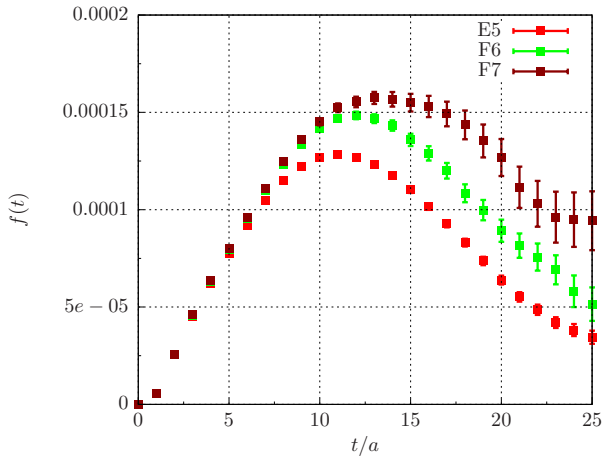

Figure 10.3: The Integrand for the calculation of $\hat{\Pi}(Q^2)$ plotted against t for a momentum of $Q^2 = 0.05\ \mathrm{GeV}^2$.

However, it is not clear how small the disconnected contribution actually is. It is possible that at this stage, we are already close to resolving a signal. An idea of the size of the disconnected contribution could be obtained with phenomenology [147]. It is possible to estimate the first term of the right-hand side of the ratio

$$-\frac{1}{9}\frac{G^{ls}_{disc}(x_0)}{G^{\rho\rho}(x_0)} = \frac{G^{ls}(x_0) - G^{\rho\rho}(x_0)}{G^{\rho\rho}(x_0)} - \frac{1}{9}\left(1 + 2\frac{G^{s}_{con}(x_0)}{G^{l}_{con}(x_0)}\right) \tag{10.5}$$

using the R-ratio (cf. (8.34) and (8.35))

$$\frac{G^{ls}(x_0) - G^{\rho\rho}(x_0)}{G^{\rho\rho}(x_0)} = \frac{\int_0^\infty d\omega\, \omega^2 \left(R(\omega^2) - R_{I=1}(\omega^2)\right) e^{-\omega t}}{\int_0^\infty d\omega\, \omega^2 R_{I=1}(\omega^2)\, e^{-\omega t}}, \tag{10.6}$$

where $R_{I=1}(\omega^2)$ only contains final states with isospin $I = 1$. The second term contains only the light and the strange connected correlators, which could be taken from the lattice. This might give us a hint of the actual size of the disconnected contribution, and one could judge whether or not the current state-of-the-art of lattice calculations allows for resolving the disconnected contribution to the anomalous magnetic moment of the muon. An analysis of this kind remains to be done in future studies.

Besides the contribution of the light and the strange quarks, one can additionally consider a charm quark. Although the charm quark contribution is suppressed in the hadronic vacuum polarization due to its heavier mass, it is on the other hand enhanced compared to the strange contribution by the charge factor 4/9. Recently, the ETMC collaboration [125] and the HPQCD collaboration [148] have found a non-negligible contribution of the charm to a_μ^{hvp} for connected contributions only.
For the mixed-representation method, one would have to include the charm current, such that the electromagnetic current is given by

$$j^{lsc}_\mu = \frac{2}{3}\bar{u}\gamma_\mu u - \frac{1}{3}\bar{d}\gamma_\mu d - \frac{1}{3}\bar{s}\gamma_\mu s + \frac{2}{3}\bar{c}\gamma_\mu c\,. \tag{10.7}$$

Using Wick's theorem one finds for the four-flavor vector correlator

$$G^{lsc}(x_0) = \frac{5}{9}G^{l}_{con}(x_0) + \frac{1}{9}G^{s}_{con}(x_0) + \frac{4}{9}G^{c}_{con}(x_0) - \frac{1}{9}G^{lsc}_{disc}(x_0) \tag{10.8}$$

where one can see that the connected charm correlator $G^{c}_{con}(x_0)$ is enhanced by a factor 4 compared to the strange correlator due to their different charges. However, according to the masses, the charm correlator is exponentially suppressed. For the disconnected four-flavor vector correlator $G^{lsc}_{disc}(x_0)$, one finds

$$\begin{aligned}&\left\langle j^{lsc}_k(x)\, j^{lsc}_k(0)\right\rangle_{disc}\\ &= \left\langle \left(j^{l}_k(x) - j^{s}_k(x) + 2j^{c}_k(x)\right)\left(j^{l}_k(0) - j^{s}_k(0) + 2j^{c}_k(0)\right)\right\rangle_{disc},\end{aligned} \tag{10.9}$$

i.e. one still expects a cancellation of noise as seen in the three-flavor case, when using the same random numbers, but the effect will probably be smaller. However, it is more convenient to first improve the statistical error on the

disconnected contribution for light and strange quarks, before adding the charm and thus more noise.

In general, it is also possible to use the conserved vector current for the disconnected contribution as done for the connected one. The connected and disconnected Wick contractions of a conserved vector current at the sink and a local current at the source are written down in the appendix in section C.3. However, for this thesis we resorted to use two local currents for the disconnected contribution to the vector correlator since this allowed us to use the light quark loops that we had determined for the scalar form factor project without requiring additional computer time.

CONCLUSIONS

The search for physics beyond the Standard Model in the low-energy regime requires high-precision calculations to find possible deviations from experimental results. With growing computer power and the development of new algorithms, lattice QCD has become a powerful tool for the determination of hadronic quantities in the low-energy regime of QCD where a perturbative expansion in the strong coupling constant is not possible.
In this thesis we have concentrated on quantities that receive contributions from Wick contractions with disconnected quark loops. Such disconnected diagrams are computationally more demanding than connected contributions, since they require knowledge of the all-to-all propagator. An exact calculation of the all-to-all propagator is far from being feasible in terms of computational costs and thus one relies on stochastic methods. We found that the generalized hopping parameter expansion is a powerful tool to reduce the statistical error on disconnected loops at fixed computational costs. Using a combination of stochastic sources and the gHPE, we have calculated the quark-disconnected contribution to the scalar form factor of the pion. Additionally, we have determined the corresponding connected contribution to obtain the full form factor. From the Q^2-dependence of the form factor we have extracted the scalar radius. We find that the disconnected contribution to the scalar radius is of the same order as the connected one. Thus, we can conclude that a meaningful result for the scalar radius of the pion can only be obtained when the disconnected contribution is included. Extrapolating our results for the total scalar radius to the physical point we find agreement with a phenomenological value from $\pi\pi$-scattering. Additionally, we have extracted the low-energy constant $\bar{\ell}_4$ from our data.
In another project we investigated the disconnected contribution to the hadronic vacuum polarization, which is the leading order QCD contribution to the anomalous magnetic moment a_μ of the muon. For many years a deviation of $\approx 3\sigma$ has persisted between the Standard Model estimate and the experimental value for a_μ, which might be a possible hint for physics beyond the Standard Model. Currently, the best theoretical estimate of the HVP relies on a semi-phenomenological approach using the cross section of $e^+e^- \to$ hadrons, and a first-principles calculation using lattice QCD is desirable. In the past few years, the error on the connected contribution to the hadronic vacuum polarization from lattice calculations has been significantly improved by several groups, and it would be desirable to achieve the same precision of 1% as the precision of the phenomenological estimate. However, the disconnected contribution is generally neglected. Although we found that the disconnected contribution to the HVP is consistent with zero within its errors, we used the expected time-dependence of the vector correlator to determine an upper limit for the maximum contribution of the disconnected diagram to a_μ, which we find to be smaller than $\approx 5\%$ of the connected contribution. However, to be competitive with the phenomenological result, the disconnected contribution has to be determined more precisely. This

indicates the need for developing even better noise reduction techniques for the stochastic estimation of disconnected quark loops.

The methods that have been developed in this thesis can easily be used also for other quantities with disconnected diagrams, such as the strangeness electromagnetic form factors $\langle N|\bar{s}\gamma_\mu s|N\rangle$ or the strangeness content of the nucleon $\sigma_s = \langle N|\bar{s}s|N\rangle$, which is an important quantity for the search of dark matter [149, 150]. Both quantities are purely disconnected and consist of a nucleon two-point function and a strange quark loop. However, nucleon quantities suffer from an exponentially decaying signal-to-noise ratio $\propto \exp(-(m_N - 3/2\, m_\pi)t_s)$. Thus, the strangeness form factors receive a large statistical error from the nucleon besides the statistical error from the disconnected loop.
Using similar methods as for the hadronic vacuum polarization, one can examine the hadronic contributions to the running of the Weinberg angle $\sin^2(\theta_W)$ [151], which requires the calculation of a vacuum polarization $\Pi_{\gamma Z}$ with a photon on one and a Z boson at the other vertex. In terms of Wick contractions, $\Pi_{\gamma Z}$ receives a contribution from a connected and a disconnected two-point function. As for the HVP we can benefit from noise cancellation when light and strange loops have been calculated with the same stochastic sources for the disconnected contribution [147].

For the future we plan to use the methods developed in this thesis for the calculation of further quantities with disconnected diagrams, such as the strangeness magnetic form factors of the nucleon and the hadronic contribution to the running of $\sin^2(\theta_W)$.

APPENDIX

A

NOTATIONS AND CONVENTIONS

A.1 NATURAL UNITS

In this thesis natural units have been used, i.e.

$$\hbar \equiv c \equiv 1 \,. \tag{A.1}$$

To convert quantities to other unit systems, one uses [34]

$$\begin{aligned} \hbar c &= 197.3269718(44)\,\text{MeV fm} \\ c &= 299792458\,\frac{\text{m}}{\text{s}} \,. \end{aligned} \tag{A.2}$$

A.2 A FEW WORDS ON SU(3)

$SU(N)$ is a non-abelian group consisting of the complex $N \times N$ matrices which are unitary, i.e. $U^\dagger = U^{-1}$, and $\det U = 1$. $SU(N)$ matrices can be described using $N^2 - 1$ real parameters θ_a,

$$U(\theta) = \exp\left(-i\theta_a T_a\right) \,, \tag{A.3}$$

with the generators T_a of the group $SU(N)$.
The generators of $SU(3)$ are the *Gell-Mann matrices* λ_a, i.e. the elements $U(\theta)$ of the group $SU(3)$ can be written as

$$U(\theta) = \exp\left(-i\theta_a \frac{\lambda_a}{2}\right) \,, \tag{A.4}$$

with $a = 1, \cdots, 8$. A particular representation of the Gell-Mann matrices is given by [97]

$$\begin{aligned} \lambda_1 &= \begin{pmatrix} 0 & 1 & 0 \\ 1 & 0 & 0 \\ 0 & 0 & 0 \end{pmatrix}, & \lambda_2 &= \begin{pmatrix} 0 & -i & 0 \\ i & 0 & 0 \\ 0 & 0 & 0 \end{pmatrix}, & \lambda_3 &= \begin{pmatrix} 1 & 0 & 0 \\ 0 & -1 & 0 \\ 0 & 0 & 0 \end{pmatrix}, \\ \lambda_4 &= \begin{pmatrix} 0 & 0 & 1 \\ 0 & 0 & 0 \\ 1 & 0 & 0 \end{pmatrix}, & \lambda_5 &= \begin{pmatrix} 0 & 0 & -i \\ 0 & 0 & 0 \\ i & 0 & 0 \end{pmatrix}, & \lambda_6 &= \begin{pmatrix} 0 & 0 & 0 \\ 0 & 0 & 1 \\ 0 & 1 & 0 \end{pmatrix}, \\ \lambda_7 &= \begin{pmatrix} 0 & 0 & 0 \\ 0 & 0 & -i \\ 0 & i & 0 \end{pmatrix}, & \lambda_8 &= \tfrac{1}{\sqrt{3}} \begin{pmatrix} 1 & 0 & 0 \\ 0 & 1 & 0 \\ 0 & 0 & -2 \end{pmatrix} . \end{aligned} \tag{A.5}$$

abc	123	147	156	246	257	345	367	458	678
f_{abc}	1	$1/2$	$-1/2$	$1/2$	$1/2$	$1/2$	$-1/2$	$\sqrt{3}/2$	$\sqrt{3}/2$

Table A.1: The $SU(3)$ structure constants

The Gell-Mann matrices fulfill the commutation relation

$$\left[\frac{\lambda_a}{2}, \frac{\lambda_b}{2}\right] = i f_{abc} \frac{\lambda_c}{2} \tag{A.6}$$

with the $SU(3)$ structure constants f_{abc}. The f_{abc} are totally antisymmetric in the indices abc. The values of the non-vanishing structure constants are given in table A.1.

A.3 EUCLIDEAN γ-MATRICES

In this work the Euclidean γ-matrices in the chiral representation have been used:

$$\gamma_0 = \begin{pmatrix} 0 & 0 & -1 & 0 \\ 0 & 0 & 0 & -1 \\ -1 & 0 & 0 & 0 \\ 0 & -1 & 0 & 0 \end{pmatrix} \qquad \gamma_1 = \begin{pmatrix} 0 & 0 & 0 & -i \\ 0 & 0 & -i & 0 \\ 0 & i & 0 & 0 \\ i & 0 & 0 & 0 \end{pmatrix}$$

$$\gamma_2 = \begin{pmatrix} 0 & 0 & 0 & -1 \\ 0 & 0 & 1 & 0 \\ 0 & 1 & 0 & 0 \\ -1 & 0 & 0 & 0 \end{pmatrix} \qquad \gamma_3 = \begin{pmatrix} 0 & 0 & -i & 0 \\ 0 & 0 & 0 & i \\ i & 0 & 0 & 0 \\ 0 & -i & 0 & 0 \end{pmatrix} \tag{A.7}$$

In Euclidean metric the γ-matrices fulfill the anti-commutation relation

$$\{\gamma_\mu, \gamma_\nu\} = 2\delta_{\mu\nu}\mathbb{1}\,, \tag{A.8}$$

which can be easily checked for the matrices given in (A.7). Additionally we define

$$\gamma_5 = \gamma_0\gamma_1\gamma_2\gamma_3 = \begin{pmatrix} 1 & 0 & 0 & 0 \\ 0 & 1 & 0 & 0 \\ 0 & 0 & -1 & 0 \\ 0 & 0 & 0 & -1 \end{pmatrix}, \tag{A.9}$$

which fulfills $\gamma_5^2 = \mathbb{1}$ and anti-commutes with the γ_μ, i.e. $\{\gamma_5, \gamma_\mu\} = 0$.

A.4 ERROR ANALYSIS

A.4.1 *Jackknife Procedure*

The statistical errors in this thesis have been calculated using the Jackknife procedure [152]. The idea of the Jackknife procedure is to calculate the quantity

of interest θ once for all N measurements (in our case gauge configurations). Then, the same analysis is repeated with one measurement i (configuration) left out. If one has done that for every measurement i, the variance of the quantity θ is given by

$$\sigma^2 = \frac{N-1}{N} \sum_{i=1}^{N} (\theta - \theta_i)^2 \,, \tag{A.10}$$

where θ_i is the result where measurement i has been left out. The advantage of the Jackknife procedure is that it can be applied also to secondary quantities such as the ratios that have been used for the calculation of the scalar form factor.

A.4.2 χ^2 *Fit*

We use χ^2 fits to fit functions $f(x)$ to a data sample of N (uncorrelated) points (y_i, x_i) with $i = 1, \ldots, N$. The statistical error on y_i is σ_i. The function $f(x)$ depends on M fit parameters a_j, which have to be determined in the fit. The result for the parameters a_j are the values where

$$\chi^2 = \sum_i \frac{(f(a_j; x_i) - y_i)^2}{\sigma_i^2} \tag{A.11}$$

is minimized.

B

SCALAR FORM FACTOR

B.1 RATIOS SCALAR FORM FACTOR

In the following the ratios for the calculation of the scalar form factor are shown for all CLS ensembles used. We have used ratio R_1 (cf. equation (6.2)) and R_3 (cf. equation (6.3)) for the connected and disconnected contributions, respectively. Blue lines in the plots show the results of the global fits. For the fit ranges see B.1.10. The corresponding numerical results are given in B.1.7 - B.1.9.

B.1.1 *Connected - Vanishing Momentum Transfer*

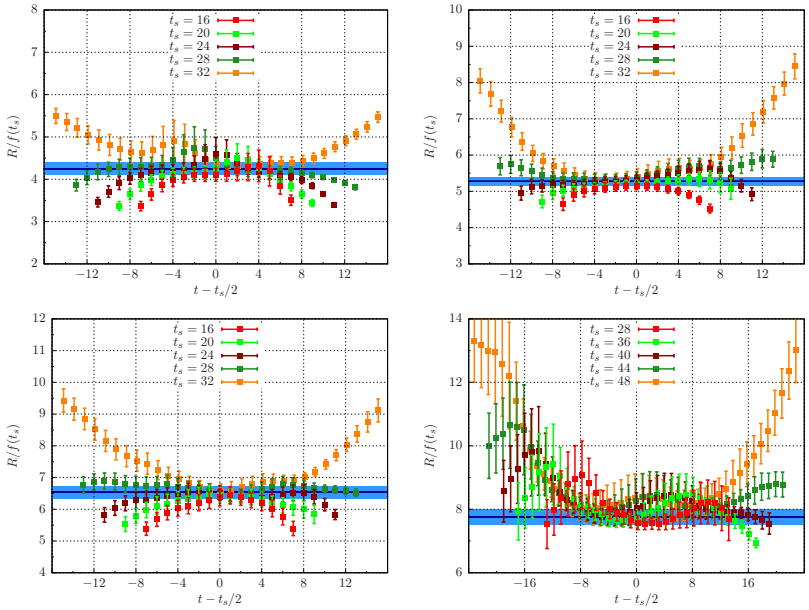

Figure B.1: The connected ratios for vanishing momentum transfer for the $\beta = 5.2$ ensembles. The plots are from left to right, top to bottom: A3, A4, A5, and B6.

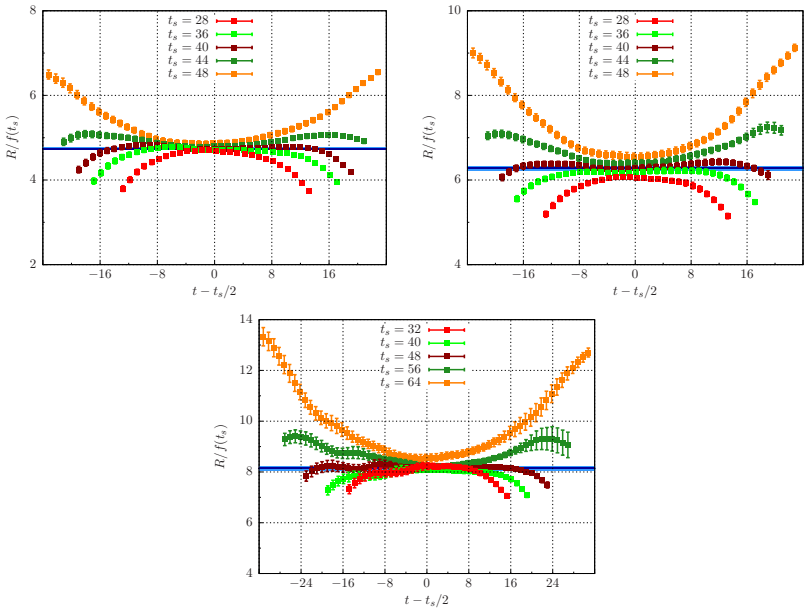

Figure B.2: The connected ratios for vanishing momentum transfer for the $\beta = 5.5$ ensembles. The plots are from left to right, top to bottom: N5, N6, and O7.

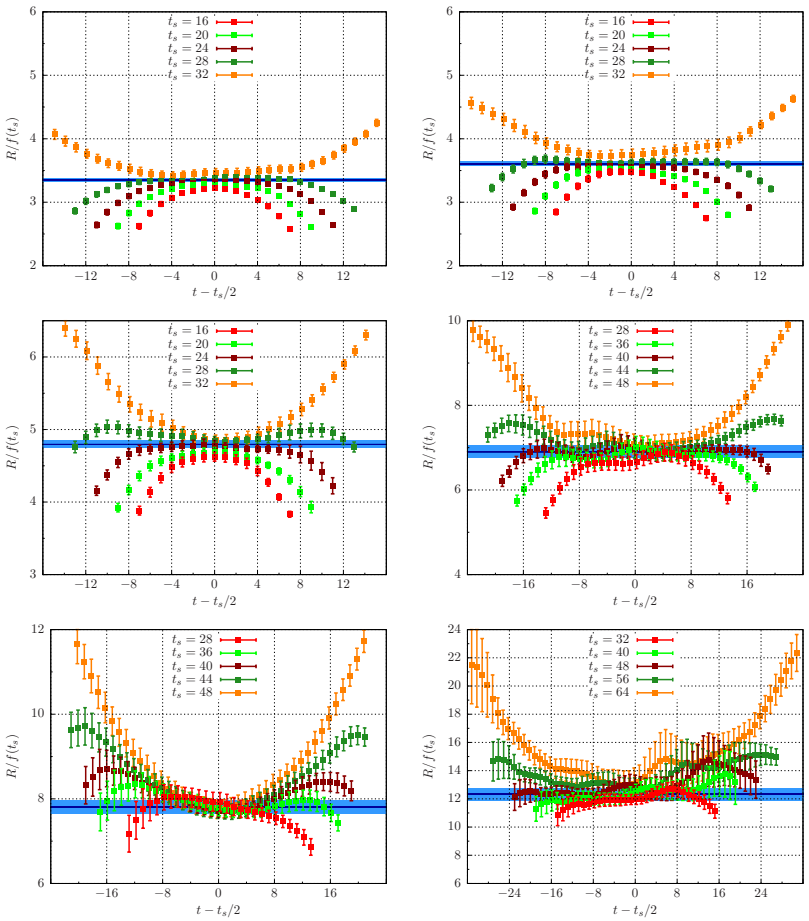

Figure B.3: The connected ratios for vanishing momentum transfer for the $\beta = 5.3$ ensembles. The plots are from left to right, top to bottom: E3, E4, E5, F6, F7 and G8.

B.1.2 *Disconnected - Vanishing Momentum Transfer*

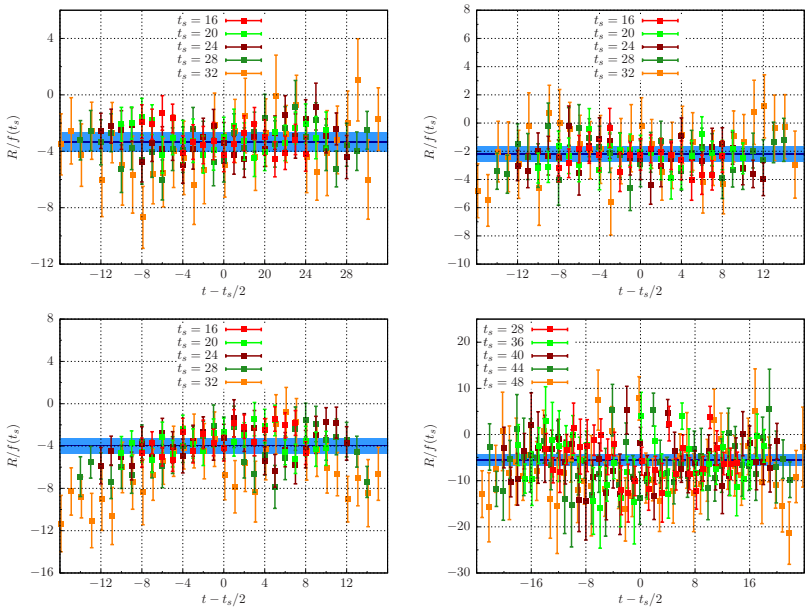

Figure B.4: The disconnected ratios for vanishing momentum transfer for the $\beta = 5.2$ ensembles. The plots are from left to right, top to bottom: A3, A4, A5, and B6.

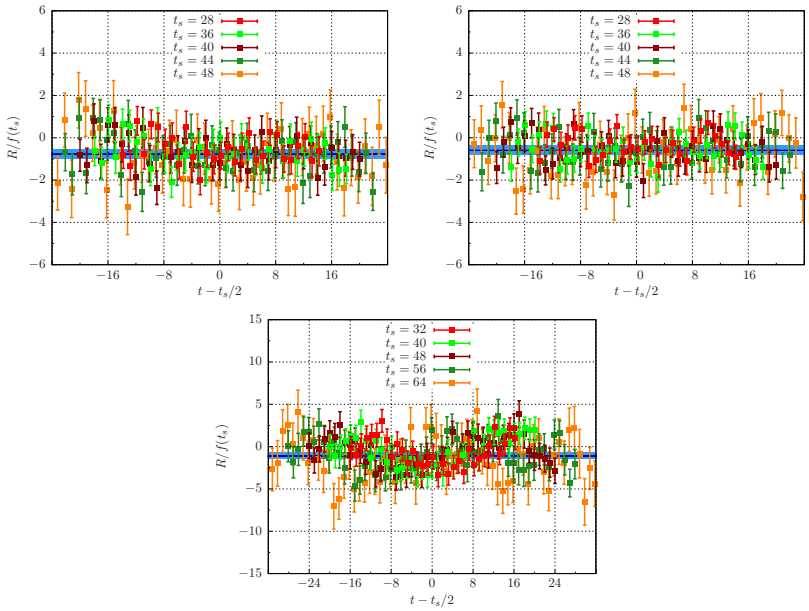

Figure B.5: The disconnected ratios for vanishing momentum transfer for the $\beta = 5.5$ ensembles. The plots are from left to right, top to bottom: N5, N6, and O7.

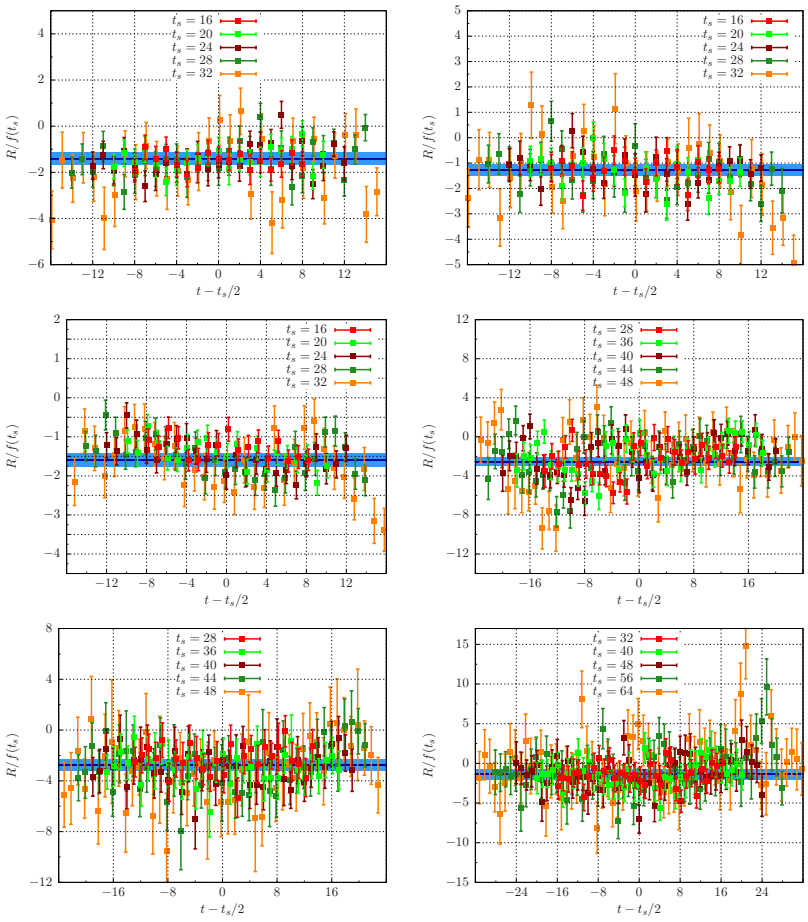

Figure B.6: The disconnected ratios for vanishing momentum transfer for the $\beta = 5.3$ ensembles. The plots are from left to right, top to bottom: E3, E4, E5, F6, F7 and G8.

B.1.3 *Connected - first Non-Vanishing Momentum Transfer*

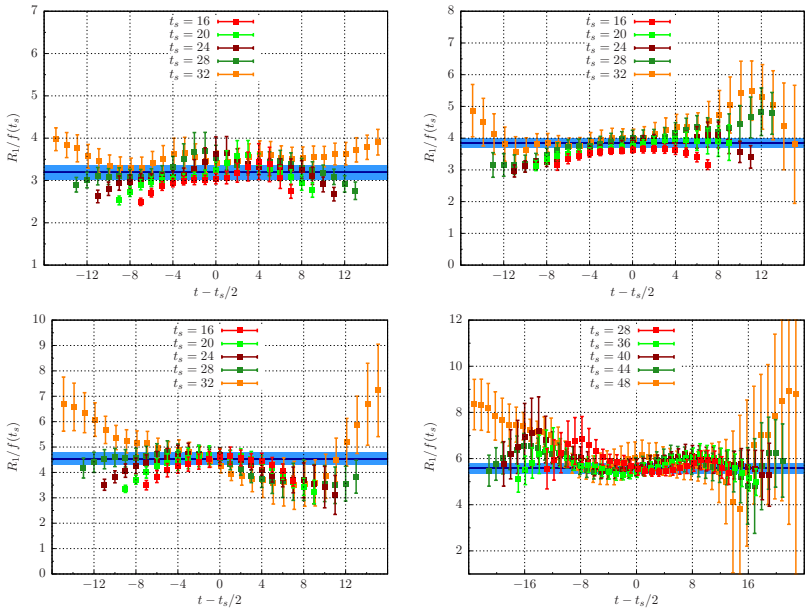

Figure B.7: The connected ratios for the first non-vanishing momentum transfer for the $\beta = 5.2$ ensembles. The plots are from left to right, top to bottom: A3, A4, A5, and B6.

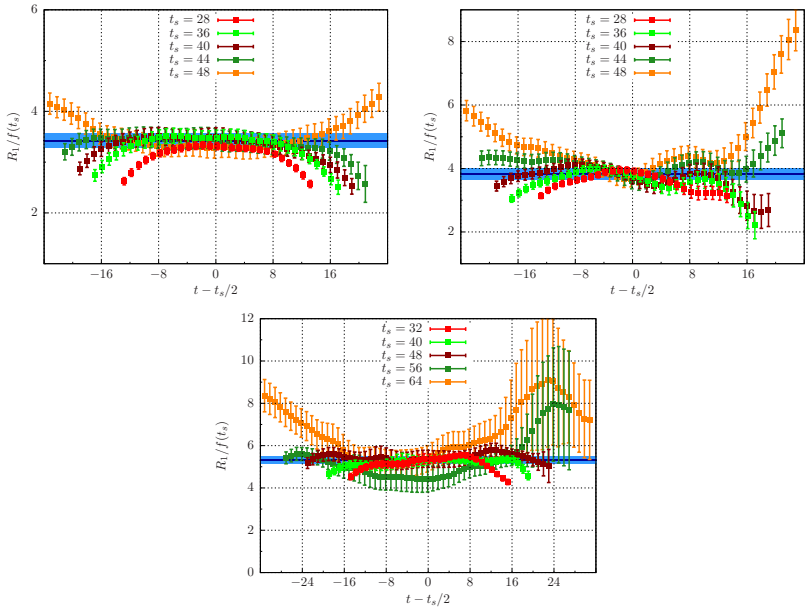

Figure B.8: The connected ratios for the first non-vanishing momentum transfer for the $\beta = 5.5$ ensembles. The plots are from left to right, top to bottom: N5, N6, and O7.

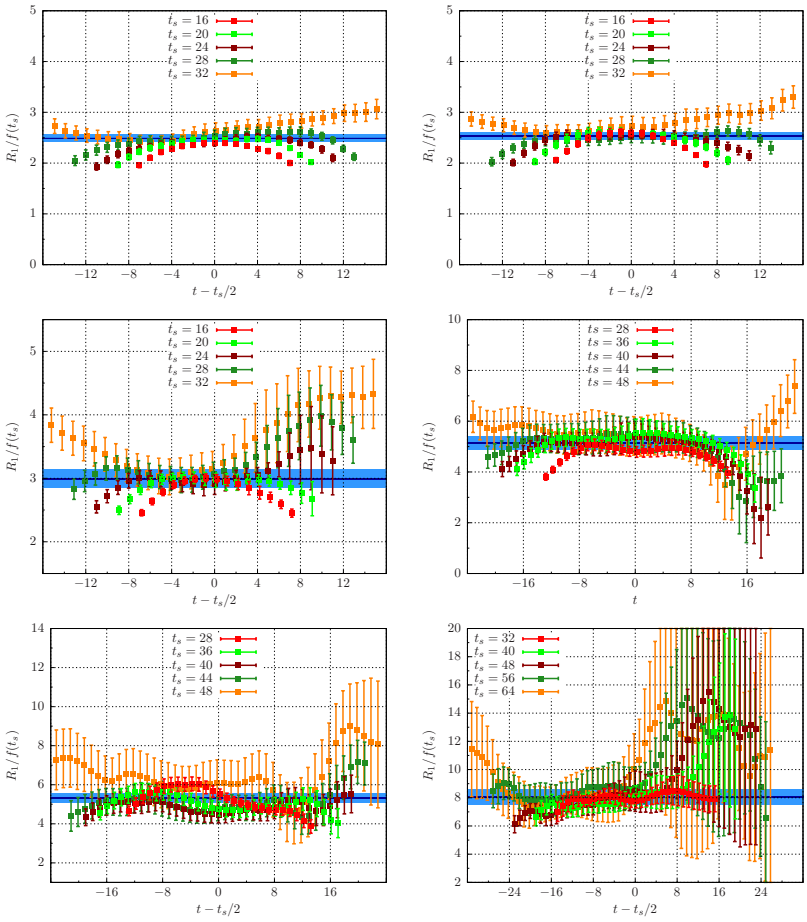

Figure B.9: The connected ratios for the first non-vanishing momentum transfer for the $\beta = 5.3$ ensembles. The plots are from left to right, top to bottom: E3, E4, E5, F6, F7 and G8.

B.1.4 *Disconnected - first Non-Vanishing Momentum Transfer*

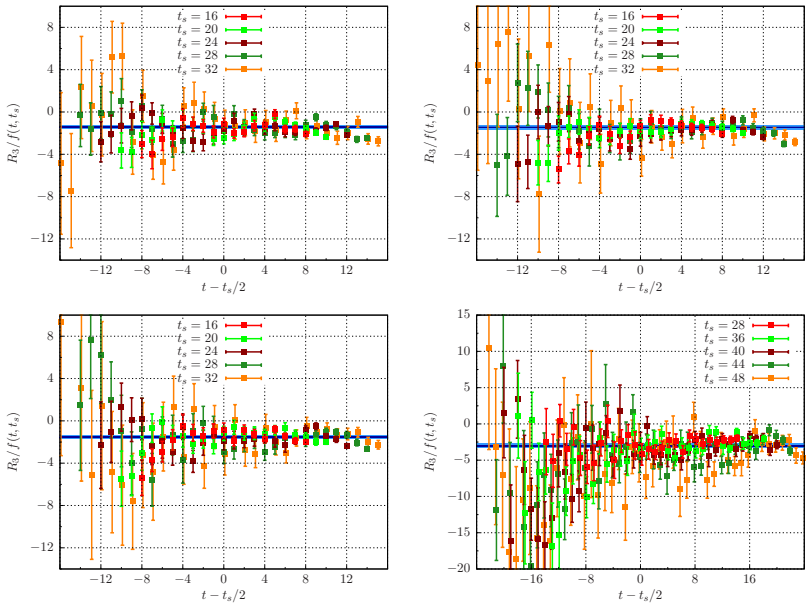

Figure B.10: The disconnected ratios for the first non-vanishing momentum transfer for the $\beta = 5.2$ ensembles. The plots are from left to right, top to bottom: A3, A4, A5, and B6.

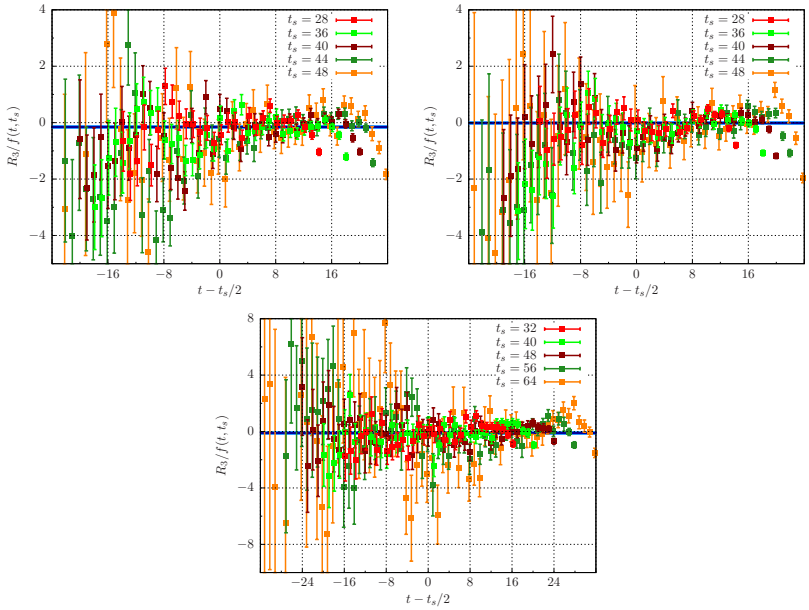

Figure B.11: The disconnected ratios for the first non-vanishing momentum transfer for the $\beta = 5.5$ ensembles. The plots are from left to right, top to bottom: N5, N6, and O7.

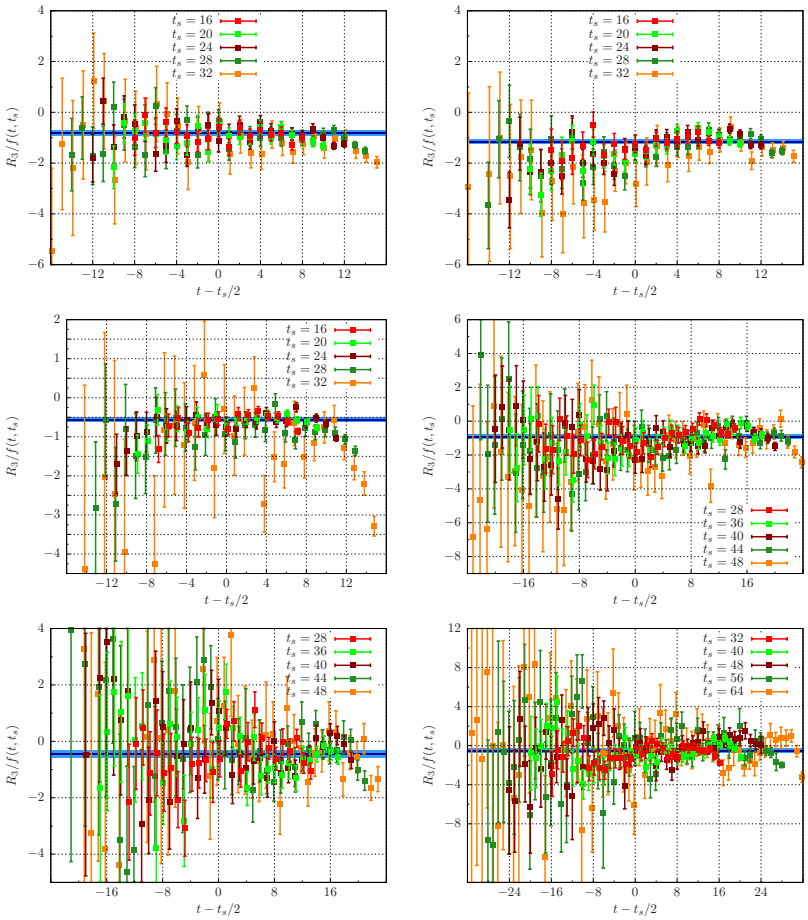

Figure B.12: The disconnected ratios for the first non-vanishing momentum transfer for the $\beta = 5.3$ ensembles. The plots are from left to right, top to bottom: E3, E4, E5, F6, F7 and G8.

B.1.5 *Connected - second Non-Vanishing Momentum Transfer*

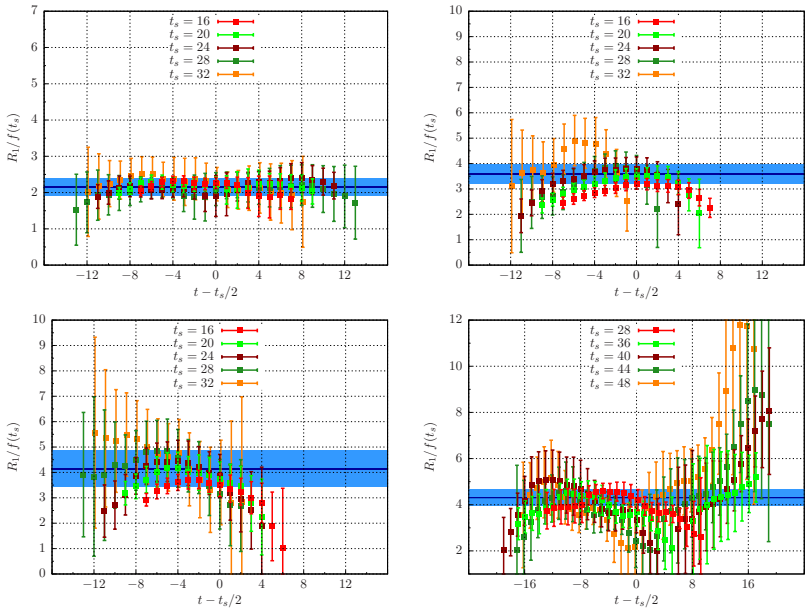

Figure B.13: The connected ratios for the second non-vanishing momentum transfer for the $\beta = 5.2$ ensembles. The plots are from left to right, top to bottom: A3, A4, A5, and B6.

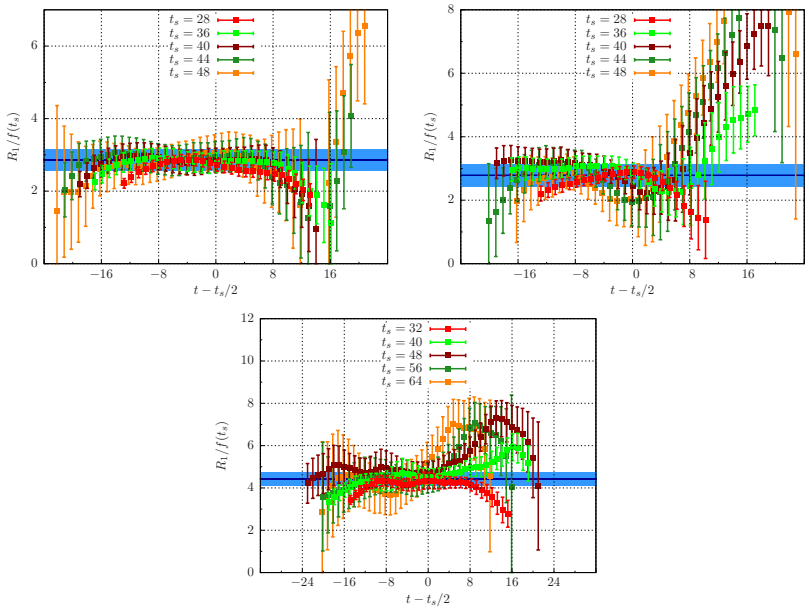

Figure B.14: The connected ratios for the second non-vanishing momentum transfer for the $\beta = 5.5$ ensembles. The plots are from left to right, top to bottom: N5, N6, and O7.

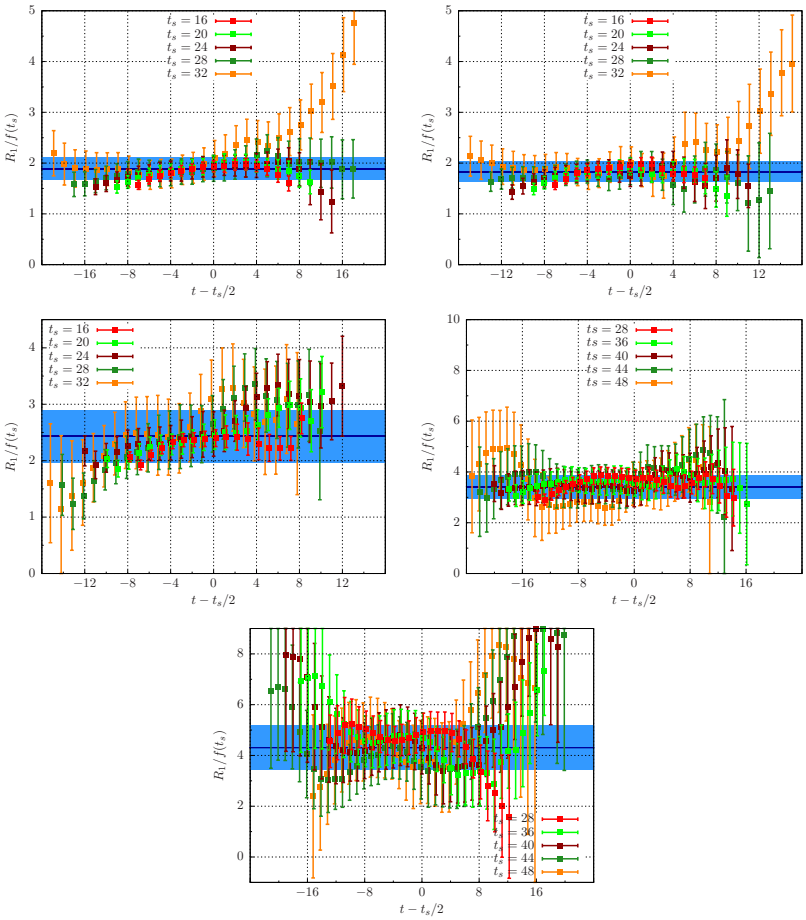

Figure B.15: The connected ratios for the second non-vanishing momentum transfer for the $\beta = 5.3$ ensembles. The plots are from left to right, top to bottom: E3, E4, E5, F6 and F7.

B.1.6 *Disconnected - second Non-Vanishing Momentum Transfer*

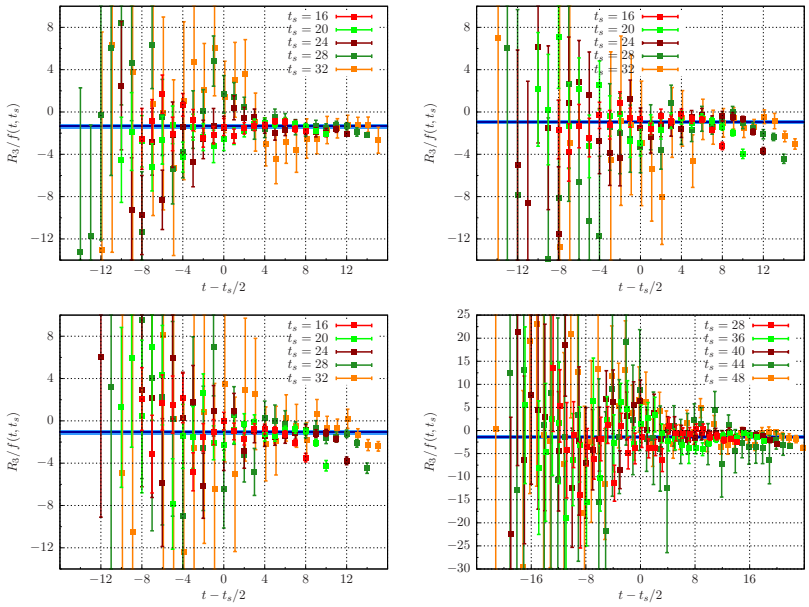

Figure B.16: The disconnected ratios for the second non-vanishing momentum transfer for the $\beta = 5.2$ ensembles. The plots are from left to right, top to bottom: A3, A4, A5, and B6.

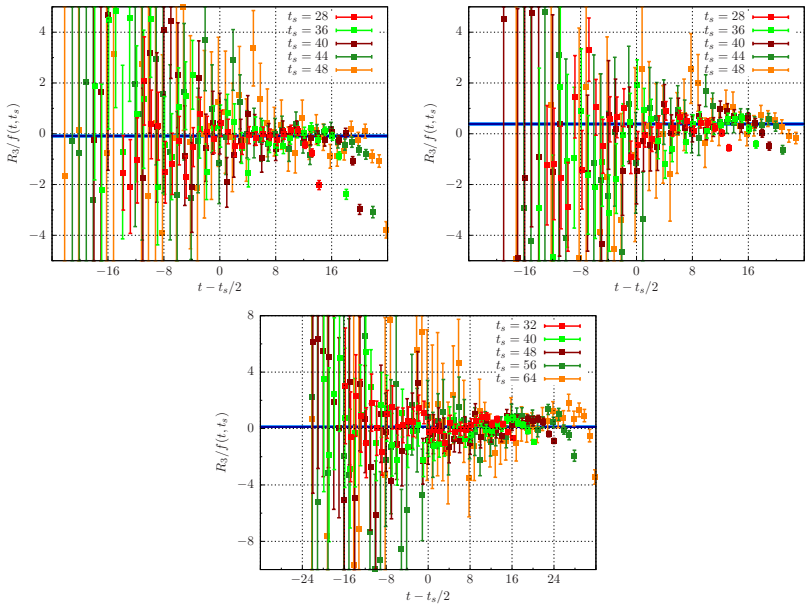

Figure B.17: The disconnected ratios for the second non-vanishing momentum transfer for the $\beta = 5.5$ ensembles. The plots are from left to right, top to bottom: N5, N6, and O7.

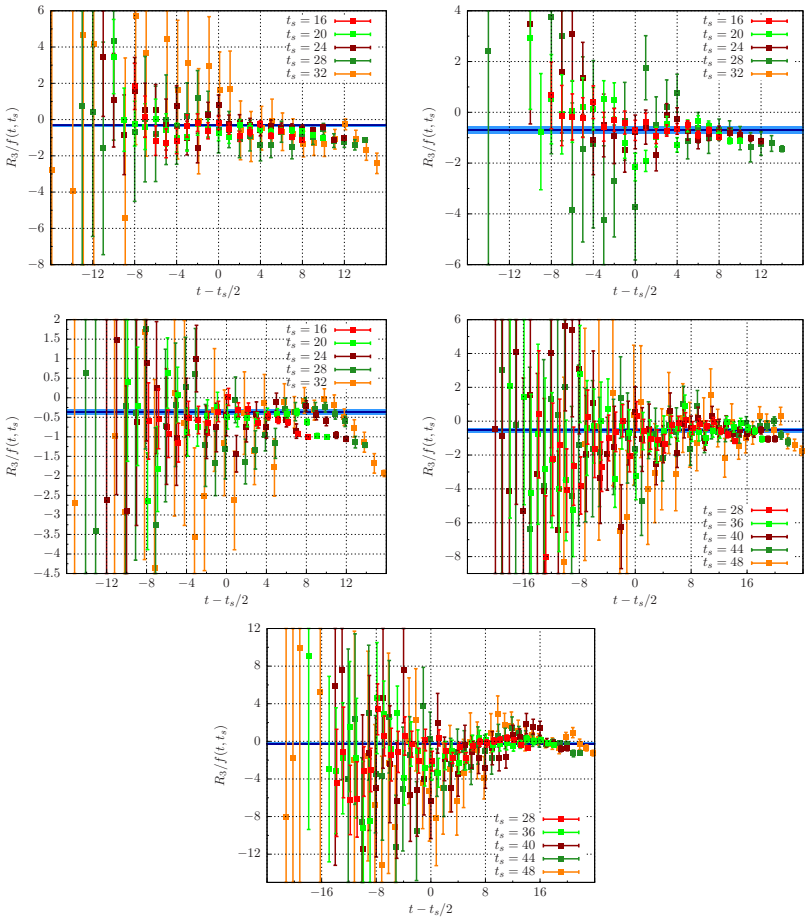

Figure B.18: The disconnected ratios for the second non-vanishing momentum transfer for the $\beta = 5.3$ ensembles. The plots are from left to right, top to bottom: E3, E4, E5, F6 and F7.

B.1.7 *Numerical Results - Vanishing Momentum Transfer*

In the following, we will give the numerical results for the scalar form factor for all ensembles. The form factor data are unrenormalized since Z_s has not been determined.

	connected	disconnected	total
A3	1.61 ± 0.06	-1.28 ± 0.26	2.89 ± 0.29
A4	1.53 ± 0.03	-0.63 ± 0.16	2.16 ± 0.16
A5	1.66 ± 0.05	-1.00 ± 0.19	2.67 ± 0.19
B6	1.66 ± 0.05	-1.18 ± 0.27	2.84 ± 0.28

Table B.1: Numerical results for the scalar form factor for $Q^2 = 0$ for $\beta = 5.2$.

	connected	disconnected	total
E3	1.39 ± 0.01	-0.58 ± 0.10	1.97 ± 0.11
E4	1.39 ± 0.01	-0.49 ± 0.09	1.88 ± 0.09
E5	1.36 ± 0.01	-0.45 ± 0.04	1.82 ± 0.05
F6	1.44 ± 0.03	-0.53 ± 0.09	1.97 ± 0.10
F7	1.39 ± 0.03	-0.50 ± 0.08	1.88 ± 0.09
G8	1.52 ± 0.05	-0.17 ± 0.09	1.69 ± 0.10

Table B.2: Numerical results for the scalar form factor for $Q^2 = 0$ for $\beta = 5.3$.

	connected	disconnected	total
N5	1.03 ± 0.01	-0.17 ± 0.05	1.20 ± 0.05
N6	1.06 ± 0.01	-0.10 ± 0.04	1.16 ± 0.04
O7	1.08 ± 0.01	-1.15 ± 0.05	1.22 ± 0.05

Table B.3: Numerical results for the scalar form factor for $Q^2 = 0$ for $\beta = 5.5$.

B.1.8 *Numerical Results - First Momentum Transfer*

	connected	disconnected	total
A3	1.46 ± 0.08	-0.66 ± 0.07	2.11 ± 0.11
A4	1.45 ± 0.06	-0.55 ± 0.07	2.00 ± 0.10
A5	1.56 ± 0.09	-0.53 ± 0.06	2.10 ± 0.11
B6	1.50 ± 0.06	0.80 ± 0.09	2.30 ± 0.11

Table B.4: Numerical results for the scalar form factor for the first $Q^2 \neq 0$ for $\beta = 5.2$.

	connected	disconnected	total
E3	1.20 ± 0.03	-0.40 ± 0.05	1.61 ± 0.07
E4	1.17 ± 0.04	-0.53 ± 0.04	1.70 ± 0.06
E5	1.11 ± 0.05	-0.23 ± 0.02	1.34 ± 0.06
F6	1.36 ± 0.07	-0.24 ± 0.03	1.60 ± 0.08
F7	1.26 ± 0.06	-0.10 ± 0.03	1.37 ± 0.08
G8	1.39 ± 0.09	-0.09 ± 0.04	1.45 ± 0.10

Table B.5: Numerical results for the scalar form factor for the first $Q^2 \neq 0$ for $\beta = 5.3$.

	connected	disconnected	total
N5	0.93 ± 0.04	-0.04 ± 0.02	0.98 ± 0.04
N6	0.88 ± 0.04	0.00 ± 0.01	0.88 ± 0.04
O7	0.94 ± 0.03	-0.01 ± 0.02	0.95 ± 0.04

Table B.6: Numerical results for the scalar form factor for the first $Q^2 \neq 0$ for $\beta = 5.5$.

B.1.9 *Numerical Results - second Momentum Transfer*

	connected	disconnected	total
A3	1.08 ± 0.12	-0.68 ± 0.10	1.76 ± 0.16
A4	1.53 ± 0.17	-0.39 ± 0.08	1.92 ± 0.18
A5	1.63 ± 0.28	-0.42 ± 0.08	2.05 ± 0.29
B6	1.31 ± 0.11	-0.43 ± 0.10	1.74 ± 0.15

Table B.7: Numerical results for the scalar form factor for the second $Q^2 \neq 0$ for $\beta = 5.2$.

	connected	disconnected	total
E3	1.01 ± 0.12	-0.32 ± 0.07	1.33 ± 0.14
E4	0.93 ± 0.11	-0.36 ± 0.08	1.29 ± 0.13
E5	1.02 ± 0.20	-0.15 ± 0.03	1.17 ± 0.20
F6	1.02 ± 0.14	-0.16 ± 0.04	1.17 ± 0.14
F7	1.17 ± 0.23	-0.07 ± 0.03	1.23 ± 0.24

Table B.8: Numerical results for the scalar form factor for the second $Q^2 \neq 0$ for $\beta = 5.3$.

	connected	disconnected	total
N5	0.88 ± 0.09	-0.02 ± 0.02	0.90 ± 0.09
N6	0.73 ± 0.09	0.10 ± 0.02	0.62 ± 0.10
O7	0.89 ± 0.07	0.03 ± 0.02	0.87 ± 0.07

Table B.9: Numerical results for the scalar form factor for the second $Q^2 \neq 0$ for $\beta = 5.5$.

B.1.10 *Fit Ranges*

In the following we give the fit ranges in t for the ratios for all different values of source-sink separation t_s and momentum transfer Q^2.

		fit range
A3	con mom 0	$t_s = 20$ ($t \in [6, 15]$), $t_s = 24$ ($t \in [6, 17]$), $t_s = 28$ ($t \in [6, 19]$), $t_s = 32$ ($t \in [14, 22]$)
	con mom 1	$t_s = 20$ ($t \in [5, 11]$),$t_s = 24$ ($t \in [5, 15]$), $t_s = 28$ ($t \in [7, 18]$), $t_s = 32$ ($t \in [9, 20]$)
	con mom 11	$t_s = 20$ ($t \in [7, 13]$),$t_s = 24$ ($t \in [7, 14]$), $t_s = 28$ ($t \in [8, 16]$), $t_s = 32$ ($t \in [11, 20]$)
A3	dis mom 0	$t_s = 20$ ($t \in [4, 16]$), $t_s = 22$ ($t \in [4, 18]$), $t_s = 24$ ($t \in [5, 19]$), $t_s = 26$ ($t \in [5, 21]$), $t_s = 28$ ($t \in [6, 22]$), $t_s = 30$ ($t \in [6, 24]$), $t_s = 32$ ($t \in [7, 25]$)
	dis mom 1	$t_s = 20$ ($t \in [5, 17]$), $t_s = 22$ ($t \in [6, 19]$), $t_s = 24$ ($t \in [7, 21]$), $t_s = 26$ ($t \in [8, 22]$), $t_s = 28$ ($t \in [9, 23]$), $t_s = 30$ ($t \in [10, 25]$), $t_s = 32$ ($t \in [11, 27]$)
	dis mom 11	$t_s = 20$ ($t \in [5, 17]$), $t_s = 22$ ($t \in [6, 19]$), $t_s = 24$ ($t \in [7, 21]$), $t_s = 26$ ($t \in [8, 22]$), $t_s = 28$ ($t \in [9, 23]$), $t_s = 30$ ($t \in [10, 25]$), $t_s = 32$ ($t \in [11, 27]$)
A4	con mom 0	$t_s = 20$ ($t \in [6, 14]$), $t_s = 24$ ($t \in [8, 15]$), $t_s = 28$ ($t \in [10, 16]$), $t_s = 32$ ($t \in [14, 19]$)
	con mom 1	$t_s = 20$ ($t \in [8, 11]$),$t_s = 24$ ($t \in [10, 14]$), $t_s = 28$ ($t \in [13, 18]$), $t_s = 32$ ($t \in [13, 21]$)
	con mom 11	$t_s = 20$ ($t \in [8, 13]$),$t_s = 24$ ($t \in [8, 14]$), $t_s = 28$ ($t \in [10, 14]$), $t_s = 32$ ($t \in [14, 15]$)
A4	dis mom 0	$t_s = 20$ ($t \in [4, 16]$), $t_s = 22$ ($t \in [4, 18]$), $t_s = 24$ ($t \in [5, 19]$), $t_s = 26$ ($t \in [5, 21]$), $t_s = 28$ ($t \in [6, 22]$), $t_s = 30$ ($t \in [6, 24]$), $t_s = 32$ ($t \in [7, 25]$)
	dis mom 1	$t_s = 20$ ($t \in [5, 17]$), $t_s = 22$ ($t \in [6, 19]$), $t_s = 24$ ($t \in [7, 21]$), $t_s = 26$ ($t \in [8, 22]$), $t_s = 28$ ($t \in [9, 23]$), $t_s = 30$ ($t \in [10, 25]$), $t_s = 32$ ($t \in [11, 27]$)
	dis mom 11	$t_s = 20$ ($t \in [5, 17]$), $t_s = 22$ ($t \in [6, 19]$), $t_s = 24$ ($t \in [7, 21]$), $t_s = 26$ ($t \in [8, 22]$), $t_s = 28$ ($t \in [9, 23]$), $t_s = 30$ ($t \in [10, 25]$), $t_s = 32$ ($t \in [11, 27]$)

Table B.10: Complete fit ranges for the ratios of the A3 and A4 ensembles.

		fit range
A5	con mom 0	$t_s = 20$ ($t \in [9,13]$), $t_s = 24$ ($t \in [9,19]$), $t_s = 28$ ($t \in [10,21]$), $t_s = 32$ ($t \in [14,19]$)
	con mom 1	$t_s = 20$ ($t \in [6,13]$),$t_s = 24$ ($t \in [8,14]$), $t_s = 28$ ($t \in [8,15]$), $t_s = 32$ ($t \in [15,17]$)
	con mom 11	$t_s = 20$ ($t \in [7,10]$),$t_s = 24$ ($t \in [7,11]$), $t_s = 28$ ($t \in [7,10]$), $t_s = 32$ ($t \in [14,16]$)
A5	dis mom 0	$t_s = 20$ ($t \in [4,16]$), $t_s = 22$ ($t \in [4,18]$), $t_s = 24$ ($t \in [5,19]$), $t_s = 26$ ($t \in [5,21]$), $t_s = 28$ ($t \in [6,22]$), $t_s = 30$ ($t \in [6,24]$), $t_s = 32$ ($t \in [7,25]$)
	dis mom 1	$t_s = 20$ ($t \in [5,17]$), $t_s = 22$ ($t \in [6,19]$), $t_s = 24$ ($t \in [7,21]$), $t_s = 26$ ($t \in [8,22]$), $t_s = 28$ ($t \in [9,23]$), $t_s = 30$ ($t \in [10,25]$), $t_s = 32$ ($t \in [11,27]$)
	dis mom 11	$t_s = 20$ ($t \in [5,17]$), $t_s = 22$ ($t \in [6,19]$), $t_s = 24$ ($t \in [7,21]$), $t_s = 26$ ($t \in [8,22]$), $t_s = 28$ ($t \in [9,23]$), $t_s = 30$ ($t \in [10,25]$), $t_s = 32$ ($t \in [11,27]$)
B6	con mom 0	$t_s = 20$ ($t \in [9,11]$), $t_s = 28$ ($t \in [12,18]$), $t_s = 36$ ($t \in [13,19]$), $t_s = 40$ ($t \in [15,21]$), $t_s = 44$ ($t \in [18,25]$), $t_s = 48$ ($t \in [20,28]$)
	con mom 1	$t_s = 20$ ($t \in [9,12]$), $t_s = 28$ ($t \in [11,20]$), $t_s = 36$ ($t \in [14,21]$), $t_s = 40$ ($t \in [17,24]$), $t_s = 44$ ($t \in [18,24]$), $t_s = 48$ ($t \in [18,20]$)
	con mom 11	$t_s = 20$ ($t \in [8,8]$), $t_s = 28$ ($t \in [8,14]$), $t_s = 36$ ($t \in [8,19]$), $t_s = 40$ ($t \in [10,19]$), $t_s = 44$ ($t \in [15,24]$), $t_s = 48$ ($t \in [19,20]$)
B6	dis mom 0	$t_s = 20$ ($t \in [3,17]$), $t_s = 24$ ($t \in [4,20]$), $t_s = 28$ ($t \in [5,23]$), $t_s = 32$ ($t \in [6,26]$), $t_s = 36$ ($t \in [7,29]$), $t_s = 40$ ($t \in [8,32]$), $t_s = 44$ ($t \in [9,35]$), $t_s = 48$ ($t \in [10,37]$)
	dis mom 1	$t_s = 20$ ($t \in [10,17]$), $t_s = 24$ ($t \in [10,20]$), $t_s = 28$ ($t \in [12,24]$), $t_s = 32$ ($t \in [15,27]$), $t_s = 36$ ($t \in [18,31]$), $t_s = 40$ ($t \in [20,35]$), $t_s = 44$ ($t \in [23,39]$), $t_s = 48$ ($t \in [25,42]$)
	dis mom 11	$t_s = 20$ ($t \in [10,17]$), $t_s = 24$ ($t \in [10,20]$), $t_s = 28$ ($t \in [12,24]$), $t_s = 32$ ($t \in [15,27]$), $t_s = 36$ ($t \in [18,31]$), $t_s = 40$ ($t \in [20,35]$), $t_s = 44$ ($t \in [23,39]$), $t_s = 48$ ($t \in [25,42]$)

Table B.11: Complete fit ranges for the ratios of the A5 and B6 ensembles.

		fit range
E3	con mom 0	$t_s = 24$ ($t \in [7, 17]$), $t_s = 28$ ($t \in [7, 21]$), $t_s = 32$ ($t \in [9, 23]$)
	con mom 1	$t_s = 24$ ($t \in [8, 16]$), $t_s = 28$ ($t \in [8, 20]$), $t_s = 32$ ($t \in [12, 20]$)
	con mom 11	$t_s = 24$ ($t \in [10, 18]$), $t_s = 28$ ($t \in [7, 16]$), $t_s = 32$ ($t \in [7, 17]$)
E3	dis mom 0	$t_s = 24$ ($t \in [3, 21]$), $t_s = 26$ ($t \in [3, 23]$), $t_s = 28$ ($t \in [3, 25]$), $t_s = 30$ ($t \in [3, 27]$), $t_s = 32$ ($t \in [3, 29]$)
	dis mom 1	$t_s = 24$ ($t \in [5, 21]$), $t_s = 26$ ($t \in [6, 23]$), $t_s = 28$ ($t \in [7, 25]$), $t_s = 30$ ($t \in [8, 26]$), $t_s = 32$ ($t \in [9, 27]$)
	dis mom 11	$t_s = 24$ ($t \in [5, 21]$), $t_s = 26$ ($t \in [6, 23]$), $t_s = 28$ ($t \in [7, 25]$), $t_s = 30$ ($t \in [8, 26]$), $t_s = 32$ ($t \in [9, 27]$)
E4	con mom 0	$t_s = 24$ ($t \in [6, 18]$), $t_s = 28$ ($t \in [6, 22]$), $t_s = 32$ ($t \in [10, 22]$)
	con mom 1	$t_s = 24$ ($t \in [6, 15]$), $t_s = 28$ ($t \in [6, 19]$), $t_s = 32$ ($t \in [13, 19]$)
	con mom 11	$t_s = 24$ ($t \in [7, 17]$), $t_s = 28$ ($t \in [7, 17]$), $t_s = 32$ ($t \in [8, 20]$)
E4	dis mom 0	$t_s = 24$ ($t \in [3, 21]$), $t_s = 26$ ($t \in [4, 22]$), $t_s = 28$ ($t \in [4, 24]$), $t_s = 30$ ($t \in [5, 25]$), $t_s = 32$ ($t \in [5, 27]$)
	dis mom 1	$t_s = 24$ ($t \in [6, 21]$), $t_s = 26$ ($t \in [8, 23]$), $t_s = 28$ ($t \in [10, 25]$), $t_s = 30$ ($t \in [12, 26]$), $t_s = 32$ ($t \in [14, 27]$)
	dis mom 11	$t_s = 24$ ($t \in [6, 21]$), $t_s = 26$ ($t \in [8, 23]$), $t_s = 28$ ($t \in [10, 25]$), $t_s = 30$ ($t \in [12, 26]$)
E5	con mom 0	$t_s = 24$ ($t \in [5, 19]$), $t_s = 28$ ($t \in [6, 22]$), $t_s = 32$ ($t \in [12, 20]$)
	con mom 1	$t_s = 24$ ($t \in [7, 14]$), $t_s = 28$ ($t \in [9, 15]$), $t_s = 32$ ($t \in [10, 16]$)
	con mom 11	$t_s = 24$ ($t \in [9, 12]$), $t_s = 28$ ($t \in [11, 13]$), $t_s = 32$ ($t \in [10, 13]$)
E5	dis mom 0	$t_s = 24$ ($t \in [4, 20]$), $t_s = 26$ ($t \in [4, 22]$), $t_s = 28$ ($t \in [5, 23]$), $t_s = 30$ ($t \in [5, 25]$), $t_s = 32$ ($t \in [6, 26]$)
	dis mom 1	$t_s = 24$ ($t \in [9, 21]$), $t_s = 26$ ($t \in [10, 23]$), $t_s = 28$ ($t \in [10, 24]$), $t_s = 30$ ($t \in [10, 26]$), $t_s = 32$ ($t \in [10, 27]$)
	dis mom 11	$t_s = 24$ ($t \in [9, 21]$), $t_s = 26$ ($t \in [10, 23]$), $t_s = 28$ ($t \in [10, 24]$), $t_s = 30$ ($t \in [10, 26]$), $t_s = 32$ ($t \in [10, 27]$)

Table B.12: Complete fit ranges for the ratios of the E3, E4 and E5 ensembles.

		fit range
F6	con mom 0	$t_s = 28$ ($t \in [6,21]$), $t_s = 36$ ($t \in [6,29]$), $t_s = 40$ ($t \in [6,36]$), $t_s = 44$ ($t \in [12,32]$), $t_s = 48$ ($t \in [15,33]$)
	con mom 1	$t_s = 28$ ($t \in [7,21]$), $t_s = 36$ ($t \in [7,29]$), $t_s = 40$ ($t \in [7,29]$), $t_s = 44$ ($t \in [7,30]$), $t_s = 48$ ($t \in [10,31]$)
	con mom 11	$t_s = 28$ ($t \in [8,14]$), $t_s = 36$ ($t \in [7,18]$), $t_s = 40$ ($t \in [7,20]$), $t_s = 44$ ($t \in [11,21]$), $t_s = 48$ ($t \in [11,22]$)
F6	dis mom 0	$t_s = 24$ ($t \in [4,20]$), $t_s = 28$ ($t \in [5,23]$), $t_s = 32$ ($t \in [6,26]$), $t_s = 36$ ($t \in [7,29]$), $t_s = 40$ ($t \in [8,32]$), $t_s = 44$ ($t \in [8,36]$), $t_s = 48$ ($t \in [8,40]$)
	dis mom 1	$t_s = 24$ ($t \in [5,21]$), $t_s = 28$ ($t \in [5,25]$), $t_s = 32$ ($t \in [5,29]$), $t_s = 36$ ($t \in [6,32]$), $t_s = 40$ ($t \in [7,35]$), $t_s = 44$ ($t \in [8,39]$), $t_s = 48$ ($t \in [9,43]$)
	dis mom 11	$t_s = 24$ ($t \in [5,21]$), $t_s = 28$ ($t \in [5,25]$), $t_s = 32$ ($t \in [5,29]$), $t_s = 36$ ($t \in [6,32]$), $t_s = 40$ ($t \in [7,35]$), $t_s = 44$ ($t \in [8,39]$), $t_s = 48$ ($t \in [9,43]$)
F7	con mom 0	$t_s = 28$ ($t \in [6,15]$), $t_s = 36$ ($t \in [13,28]$), $t_s = 40$ ($t \in [18,25]$), $t_s = 44$ ($t \in [18,28]$), $t_s = 48$ ($t \in [19,29]$)
	con mom 1	$t_s = 28$ ($t \in [6,12]$), $t_s = 36$ ($t \in [6,13]$), $t_s = 40$ ($t \in [18,27]$), $t_s = 44$ ($t \in [18,27]$), $t_s = 48$ ($t \in [18,28]$)
	con mom 11	$t_s = 28$ ($t \in [9,14]$), $t_s = 36$ ($t \in [10,20]$), $t_s = 40$ ($t \in [10,20]$), $t_s = 44$ ($t \in [8,29]$), $t_s = 48$ ($t \in [12,28]$)
F7	dis mom 0	$t_s = 24$ ($t \in [4,20]$), $t_s = 28$ ($t \in [5,23]$), $t_s = 32$ ($t \in [6,26]$), $t_s = 36$ ($t \in [7,29]$), $t_s = 40$ ($t \in [8,32]$), $t_s = 44$ ($t \in [8,36]$), $t_s = 48$ ($t \in [8,40]$)
	dis mom 1	$t_s = 24$ ($t \in [3,21]$), $t_s = 28$ ($t \in [4,25]$), $t_s = 32$ ($t \in [7,29]$), $t_s = 36$ ($t \in [12,32]$), $t_s = 40$ ($t \in [16,35]$), $t_s = 44$ ($t \in [20,39]$), $t_s = 48$ ($t \in [23,43]$)
	dis mom 11	$t_s = 24$ ($t \in [3,21]$), $t_s = 28$ ($t \in [4,25]$), $t_s = 32$ ($t \in [7,29]$), $t_s = 36$ ($t \in [12,32]$), $t_s = 40$ ($t \in [16,35]$), $t_s = 44$ ($t \in [20,39]$), $t_s = 48$ ($t \in [23,43]$)

Table B.13: Complete fit ranges for the ratios of the F6 and F7 ensembles.

		fit range
G8	con mom 0	$t_s = 24$ ($t \in [9,20]$), $t_s = 32$ ($t \in [9,18]$), $t_s = 40$ ($t \in [15,31]$),
		$t_s = 48$ ($t \in [18,32]$), $t_s = 56$ ($t \in [18,33]$), $t_s = 64$ ($t \in [24,41]$)
	con mom 1	$t_s = 24$ ($t \in [9,20]$), $t_s = 32$ ($t \in [9,18]$), $t_s = 40$ ($t \in [15,31]$),
		$t_s = 48$ ($t \in [18,32]$), $t_s = 56$ ($t \in [18,33]$), $t_s = 64$ ($t \in [24,41]$)
G8	dis mom 0	$t_s = 24$ ($t \in [5,19]$), $t_s = 28$ ($t \in [6,22]$), $t_s = 32$ ($t \in [7,25]$),
		$t_s = 36$ ($t \in [8,28]$), $t_s = 40$ ($t \in [9,31]$), $t_s = 44$ ($t \in [10,34]$),
		$t_s = 48$ ($t \in [10,38]$), $t_s = 52$ ($t \in [10,42]$), $t_s = 56$ ($t \in [10,46]$),
		$t_s = 60$ ($t \in [10,50]$), $t_s = 64$ ($t \in [10,54]$)
	dis mom 1	$t_s = 24$ ($t \in [12,5]$), $t_s = 28$ ($t \in [14,6]$), $t_s = 32$ ($t \in [16,7]$),
		$t_s = 36$ ($t \in [18,8]$), $t_s = 40$ ($t \in [20,9]$), $t_s = 44$ ($t \in [22,10]$),
		$t_s = 48$ ($t \in [24,11]$), $t_s = 52$ ($t \in [26,12]$), $t_s = 56$ ($t \in [28,12]$),
		$t_s = 60$ ($t \in [30,12]$), $t_s = 64$ ($t \in [32,12]$)

Table B.14: Complete fit ranges for the ratios of the G8 ensemble.

		fit range
O7	con mom 0	$t_s = 32$ ($t \in [15,21]$), $t_s = 40$ ($t \in [17,25]$), $t_s = 48$ ($t \in [19,28]$),
		$t_s = 56$ ($t \in [26,32]$), $t_s = 64$ ($t \in [29,35]$)
	con mom 1	$t_s = 32$ ($t \in [14,19]$), $t_s = 40$ ($t \in [15,27]$), $t_s = 48$ ($t \in [20,29]$),
		$t_s = 56$ ($t \in [21,30]$), $t_s = 64$ ($t \in [28,30]$)
	con mom 11	$t_s = 32$ ($t \in [9,18]$), $t_s = 40$ ($t \in [15,31]$), $t_s = 48$ ($t \in [18,32]$),
		$t_s = 56$ ($t \in [18,33]$), $t_s = 64$ ($t \in [24,41]$)
O7	dis mom 0	$t_s = 32$ ($t \in [5,27]$), $t_s = 36$ ($t \in [6,30]$), $t_s = 40$ ($t \in [7,33]$),
		$t_s = 44$ ($t \in [8,36]$), $t_s = 48$ ($t \in [9,39]$), $t_s = 52$ ($t \in [10,42]$),
		$t_s = 56$ ($t \in [11,45]$), $t_s = 60$ ($t \in [12,48]$), $t_s = 64$ ($t \in [13,51]$)
	dis mom 1	$t_s = 32$ ($t \in [10,27]$), $t_s = 36$ ($t \in [12,30]$), $t_s = 40$ ($t \in [14,33]$),
		$t_s = 44$ ($t \in [16,36]$), $t_s = 48$ ($t \in [18,40]$), $t_s = 52$ ($t \in [20,44]$),
		$t_s = 56$ ($t \in [22,48]$), $t_s = 60$ ($t \in [24,52]$), $t_s = 64$ ($t \in [24,56]$)
	dis mom 11	$t_s = 32$ ($t \in [12,27]$), $t_s = 36$ ($t \in [14,30]$), $t_s = 40$ ($t \in [16,33]$),
		$t_s = 44$ ($t \in [18,36]$), $t_s = 48$ ($t \in [20,40]$), $t_s = 52$ ($t \in [22,44]$),
		$t_s = 56$ ($t \in [24,48]$), $t_s = 60$ ($t \in [26,52]$), $t_s = 64$ ($t \in [28,56]$)

Table B.15: Complete fit ranges for the ratios of the O7 ensemble.

		fit range
N5	con mom 0	$t_s = 36$ ($t \in [10, 26]$), $t_s = 40$ ($t \in [13, 27]$), $t_s = 44$ ($t \in [15, 26]$), $t_s = 48$ ($t \in [20, 26]$)
	con mom 1	$t_s = 36$ ($t \in [13, 23]$), $t_s = 40$ ($t \in [15, 23]$), $t_s = 44$ ($t \in [15, 23]$), $t_s = 48$ ($t \in [17, 31]$)
	con mom 11	$t_s = 36$ ($t \in [16, 26]$), $t_s = 40$ ($t \in [19, 27]$), $t_s = 44$ ($t \in [19, 24]$), $t_s = 48$ ($t \in [20, 27]$)
N5	dis mom 0	$t_s = 32$ ($t \in [6, 26]$), $t_s = 36$ ($t \in [7, 29]$), $t_s = 40$ ($t \in [8, 32]$), $t_s = 44$ ($t \in [9, 35]$), $t_s = 48$ ($t \in [10, 38]$)
	dis mom 1	$t_s = 32$ ($t \in [9, 27]$), $t_s = 36$ ($t \in [11, 31]$), $t_s = 40$ ($t \in [13, 34]$), $t_s = 44$ ($t \in [15, 38]$), $t_s = 48$ ($t \in [17, 41]$)
	dis mom 11	$t_s = 32$ ($t \in [15, 29]$), $t_s = 36$ ($t \in [15, 33]$), $t_s = 40$ ($t \in [20, 36]$), $t_s = 44$ ($t \in [23, 39]$), $t_s = 48$ ($t \in [25, 43]$)
N6	con mom 0	$t_s = 36$ ($t \in [12, 20]$), $t_s = 40$ ($t \in [15, 23]$), $t_s = 44$ ($t \in [17, 25]$), $t_s = 48$ ($t \in [20, 26]$)
	con mom 1	$t_s = 36$ ($t \in [13, 18]$), $t_s = 40$ ($t \in [19, 21]$), $t_s = 44$ ($t \in [21, 26]$), $t_s = 48$ ($t \in [20, 29]$)
	con mom 11	$t_s = 36$ ($t \in [10, 16]$), $t_s = 40$ ($t \in [19, 23]$), $t_s = 44$ ($t \in [20, 26]$), $t_s = 48$ ($t \in [20, 27]$)
N6	dis mom 0	$t_s = 32$ ($t \in [6, 26]$), $t_s = 36$ ($t \in [7, 29]$), $t_s = 40$ ($t \in [8, 32]$), $t_s = 44$ ($t \in [9, 35]$), $t_s = 48$ ($t \in [10, 38]$)
	dis mom 1	$t_s = 32$ ($t \in [9, 27]$), $t_s = 36$ ($t \in [11, 31]$), $t_s = 40$ ($t \in [13, 34]$), $t_s = 44$ ($t \in [15, 38]$), $t_s = 48$ ($t \in [17, 41]$)
	dis mom 11	$t_s = 32$ ($t \in [15, 29]$), $t_s = 36$ ($t \in [15, 33]$), $t_s = 40$ ($t \in [20, 36]$), $t_s = 44$ ($t \in [23, 39]$), $t_s = 48$ ($t \in [25, 43]$)

Table B.16: Complete fit ranges for the ratios of the N5 and N6 ensembles.

B.2 Q^2-DEPENDENCE AND SCALAR RADIUS

B.2.1 *Results Scalar Form Factor and Radius*

		$F_S^\pi(0)$	$Q_1^2\,[\mathrm{GeV}^2]$	$F_S^\pi(Q_1^2)$	$Q_2^2\,[\mathrm{GeV}^2]$	$F_S^\pi(Q_2^2)$	$\langle r^2\rangle_S^\pi\,[\mathrm{fm}^2]$
A3	con	1.61 ± 0.06	0.197	1.45 ± 0.08	0.346	1.08 ± 0.12	0.181 ± 0.040
	tot	2.89 ± 0.29		2.11 ± 0.11		1.76 ± 0.16	0.259 ± 0.051
A4	con	1.53 ± 0.03	0.179	1.45 ± 0.06	0.304	1.53 ± 0.16	0.049 ± 0.041
	tot	2.16 ± 0.16		2.00 ± 0.10		1.92 ± 0.18	0.089 ± 0.076
A5	con	1.66 ± 0.05	0.169	1.56 ± 0.09	0.282	1.63 ± 0.28	0.066 ± 0.063
	tot	2.67 ± 0.19		2.10 ± 0.11		2.05 ± 0.29	0.248 ± 0.097
B8	con	1.66 ± 0.05	0.083	1.50 ± 0.06	0.142	1.31 ± 0.11	0.316 ± 0.085
	tot	2.84 ± 0.28		2.30 ± 0.11		1.74 ± 0.15	0.653 ± 0.112

Table B.17: Numerical results of the (unrenormalized) scalar pion form factor $F_S^\pi(Q^2)$ for three different momentum transfers Q^2 for connected contribution (con) and the total form factor (tot) and the results for the scalar radius $\langle r^2\rangle_S^\pi$ as determined from an uncorrelated linear fit for all $\beta = 5.2$ ensembles.

		$F_S^\pi(0)$	$Q_1^2\,[\mathrm{GeV}^2]$	$F_S^\pi(Q_1^2)$	$Q_2^2\,[\mathrm{GeV}^2]$	$F_S^\pi(Q_2^2)$	$\langle r^2\rangle_S^\pi\,[\mathrm{fm}^2]$
E3	con	1.39 ± 0.01	0.319	1.20 ± 0.03	0.565	1.02 ± 0.12	0.099 ± 0.018
	tot	1.97 ± 0.11		1.61 ± 0.07		1.33 ± 0.14	0.134 ± 0.032
E4	con	1.39 ± 0.01	0.311	1.17 ± 0.04	0.548	0.93 ± 0.11	0.125 ± 0.017
	tot	1.88 ± 0.09		1.70 ± 0.06		1.38 ± 0.13	0.208 ± 0.027
E5	con	1.36 ± 0.01	0.278	1.11 ± 0.05	0.471	1.02 ± 0.19	0.149 ± 0.028
	tot	1.82 ± 0.05		1.34 ± 0.06		1.17 ± 0.20	0.208 ± 0.027
F6	con	1.44 ± 0.03	0.128	1.36 ± 0.07	0.221	1.02 ± 0.14	0.197 ± 0.069
	tot	1.97 ± 0.10		1.60 ± 0.08		1.17 ± 0.14	0.396 ± 0.081
F7	con	1.39 ± 0.03	0.121	1.26 ± 0.06	0.203	1.17 ± 0.23	0.175 ± 0.088
	tot	1.88 ± 0.09		1.37 ± 0.08		1.23 ± 0.24	0.487 ± 0.083
G8	con	1.52 ± 0.05	0.065	1.36 ± 0.09	0.109	–	0.371 ± 0.181
	tot	1.69 ± 0.05		1.45 ± 0.10		–	0.506 ± 0.240

Table B.18: The same as table B.17 for all $\beta = 5.3$ ensembles. For G8 we have only data for two Q^2 and thus the radius has been determined from only two values of Q^2.

		$F_S^\pi(0)$	$Q_1^2\,[\mathrm{GeV}^2]$	$F_S^\pi(Q_1^2)$	$Q_2^2\,[\mathrm{GeV}^2]$	$F_S^\pi(Q_2^2)$	$\langle r^2\rangle_S^\pi\,[\mathrm{fm}^2]$
N5	con	1.03 ± 0.01	0.208	0.93 ± 0.04	0.358	0.88 ± 0.09	0.105 ± 0.035
	tot	1.20 ± 0.05		0.98 ± 0.04		0.90 ± 0.09	0.187 ± 0.044
N6	con	1.06 ± 0.01	0.186	0.88 ± 0.04	0.313	0.73 ± 0.09	0.221 ± 0.043
	tot	1.16 ± 0.04		0.88 ± 0.04		1.62 ± 0.10	0.322 ± 0.047
O7	con	1.08 ± 0.01	0.107	0.94 ± 0.03	0.180	1.89 ± 0.07	0.255 ± 0.053
	tot	1.22 ± 0.05		0.95 ± 0.04		0.87 ± 0.07	0.417 ± 0.073

Table B.19: The same as table B.17 for all $\beta = 5.5$ ensembles.

B.2.2 *Linear Fits to the Q^2-Dependence*

The following plots show the results for the unrenormalized scalar form factor including a linear fit

$$F_s^\pi(Q^2) = F_s^\pi(0)\left(1 - \frac{1}{6}\left\langle r^2\right\rangle_s^\pi Q^2 + \mathcal{O}(Q^4)\right) . \tag{B.1}$$

for the Q^2-dependence to extract the scalar radius.

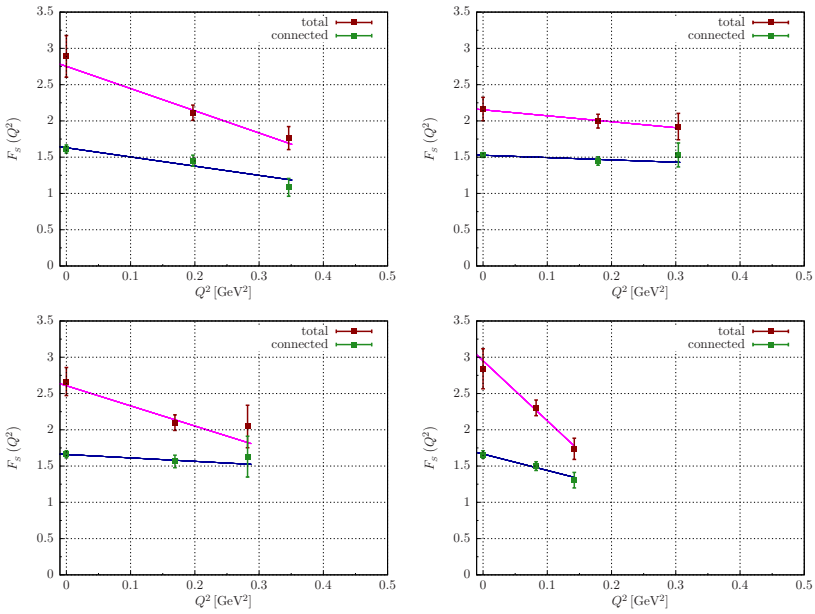

Figure B.19: The Q^2-dependence for the $\beta = 5.2$ ensembles. The plots are from left to right, top to bottom: A3, A4, A5, and B6.

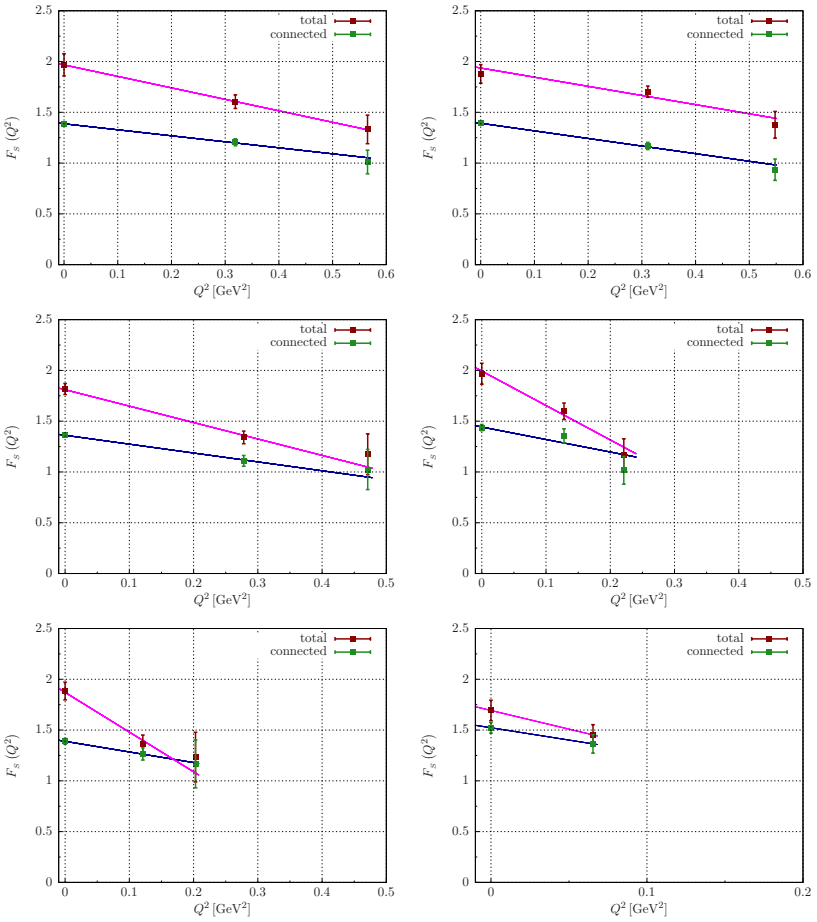

Figure B.20: The Q^2-dependence for the $\beta = 5.3$ ensembles. The plots are from left to right, top to bottom: E3, E4, E5, F6, F7 and G8.

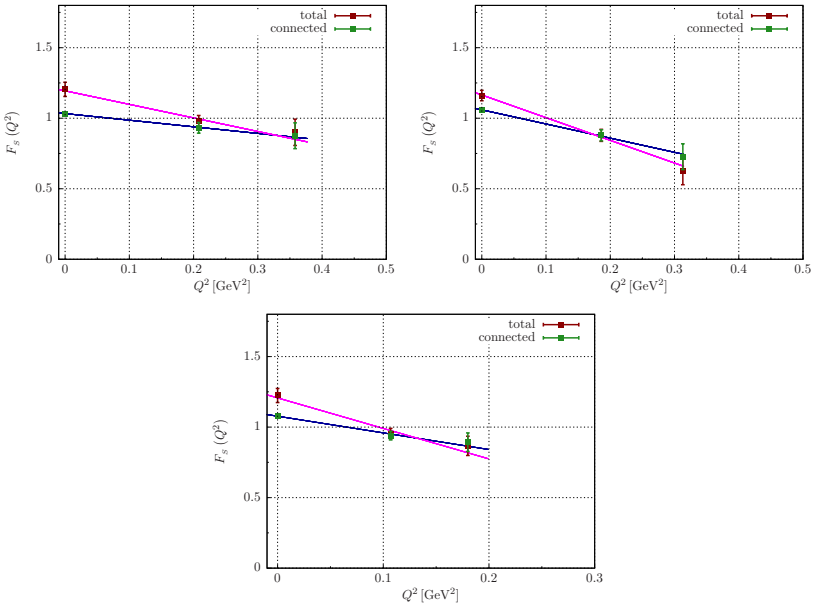

Figure B.21: The Q^2-dependence for the $\beta = 5.5$ ensembles. The plots are from left to right, top to bottom: N5, N6, and O7.

B.2.3 *Comparison of different Fit Ansätze*

The following plots show the comparison of the different ansätze for the Q^2-dependence of the scalar form factor for all ensembles. The plot for the ensembles with $a = 0.063$ fm is the same as figure 6.13. The three different ansätze are:

- a linear curve is matched to the form factor for $Q^2 = 0$ and the smallest non-vanishing Q^2
- a linear function is fitted to the results

$$F_S^\pi(Q^2) = F_S^\pi(0)\left(1 - \frac{1}{6}\left\langle r^2\right\rangle_S^\pi Q^2 + \mathcal{O}(Q^4)\right). \tag{B.2}$$

- a vector meson dominance inspired curve is fitted the data (cf (6.29))

$$F_S^\pi(Q^2) = F_S^\pi(0)\frac{1}{\left(1 + \left(\frac{Q^2}{M^2}\right)\right)^2} \qquad \left\langle r^2\right\rangle_S^\pi = \frac{12}{M^2} \tag{B.3}$$

For G8 we can not make such a comparison, since we have only a signal for the form factor for two momentum transfers. For all other ensembles we find, that the results from all three methods are in agreement with each other.

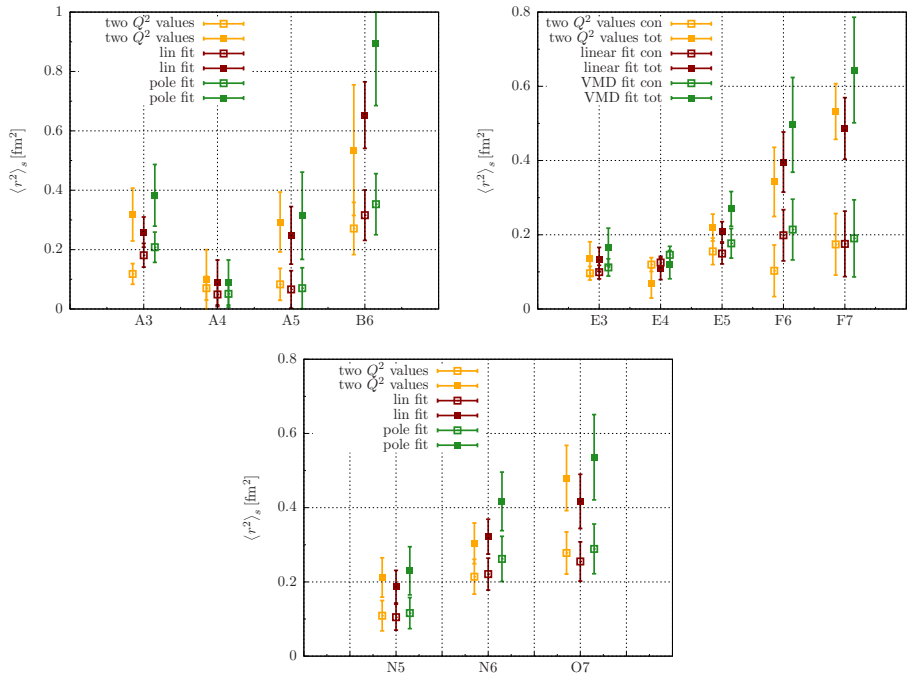

Figure B.22: Comparison of the scalar radius obtained from different ansätze. Yellow points show the results from the first two Q^2 only, red points show the results from a linear fit to all three Q^2 values, and green points show the results from a vector meson dominance fit. Open and closed symbols denote results from the connected and total form factor, respectively. The plots are from left to right, top to bottom: $a = 0.079$ fm, 0.063 fm and 0.050 fm.

B.3 NNLO CHIRAL PERTURBATION THEORY

In next-to-next-to-leading order (NNLO) in chiral Perturbation Theory the scalar radius of the pion is given by [25, 80]

$$\begin{aligned}\left\langle r^2\right\rangle_s^\pi &= \frac{1}{F_\pi^2}\left(-\frac{13}{2N}+6\ell_4^r-6L\right)\\ &+\frac{M_\pi^2}{F_\pi^4}\left[\frac{1}{N}\left(-\frac{23}{192}+88\ell_1^r+36\ell_2^r+5\ell_3^r-13\ell_4^r+\frac{145}{36}L\right)\right.\\ &\left.+\frac{869}{108}\frac{1}{N^2}-24\ell_3^r\ell_4^r+12(\ell_4^r)^2+31k_1+17k_2-6k_4+6r_{S2}^r\right]\end{aligned} \tag{B.4}$$

$$\begin{aligned}\left\langle r^2\right\rangle_v^\pi &= \frac{1}{F_\pi^2}\left(-6\ell_6^r-L-\frac{1}{N}\right)\\ &+\frac{M_\pi^2}{F_\pi^4}\left[-3k_1+\frac{3}{2}k_2-\frac{1}{2}k_4-3k_6-12\ell_4^r\ell_6^r\right.\\ &\left.+\frac{1}{N}\left(-2\ell_4^r+\frac{31}{6}L+\frac{13}{192}-\frac{181}{48N}\right)+6r_{V1}^r\right]\end{aligned} \tag{B.5}$$

The low energy constants at a given scale μ^2 are defined by

$$l_i^r=\frac{\gamma_i}{2N}\left(\bar{\ell}_i+NL\right)\qquad\text{and}\qquad k_i=(4\ell_i^r-\gamma_i L)L \tag{B.6}$$

with

$$L=\frac{1}{N}\log\left(\frac{M_\pi^2}{\mu^2}\right)\qquad\text{and}\qquad N=16\pi^2\,. \tag{B.7}$$

The constants γ_i are given by

$$\begin{aligned}&\gamma_1=\frac{1}{3},\quad \gamma_2=\frac{2}{3},\quad \gamma_3=-\frac{1}{2},\quad \gamma_4=2,\quad \gamma_5=-\frac{1}{6},\\ &\gamma_6=-\frac{1}{3},\quad \gamma_7=0\,.\end{aligned} \tag{B.8}$$

In principle, it would be desirable to fit our results of the scalar radius of the pion with the NNLO χPT expression (B.4). However, the amount of data available is clearly not sufficient to constrain all required low-energy constants.

C.1 VECTOR CORRELATOR AND HADRONIC VACUUM POLARIZATION

The following plots (figures C.1 to C.5) show results for the vector correlator and hadronic vacuum polarization for the F6 and F7 ensemble. Details can be found in chapter 9.

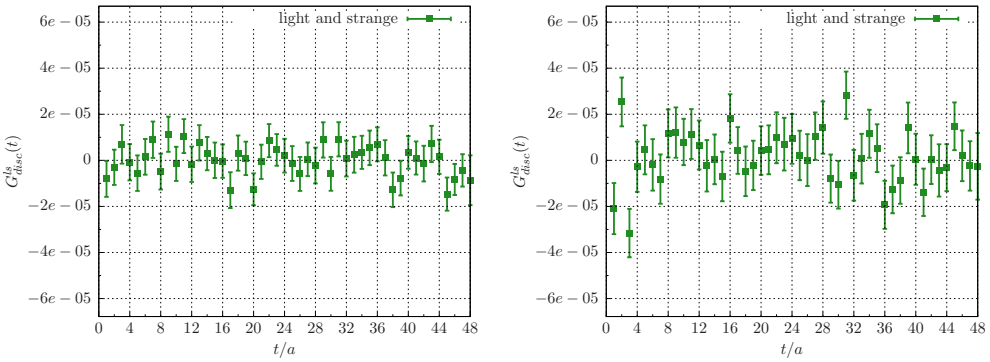

Figure C.1: The disconnected vector correlator for the F6 (left) and F7 (right) ensemble for light and strange quarks. The corresponding plot for the E5 ensemble is the right-hand side of figure 9.3.

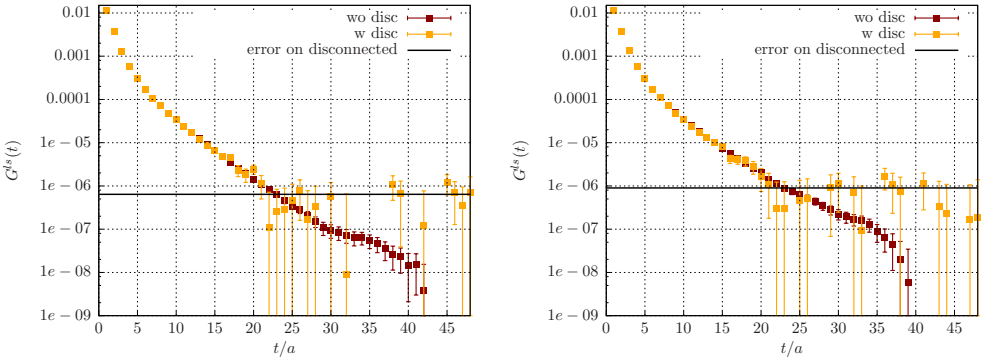

Figure C.2: The vector correlator for the F6 (left) and F7 (right) ensemble for light and strange quarks. The connected result is shown in red, the total vector correlator is shown in yellow. The corresponding plot for the E5 ensemble is figure 9.4.

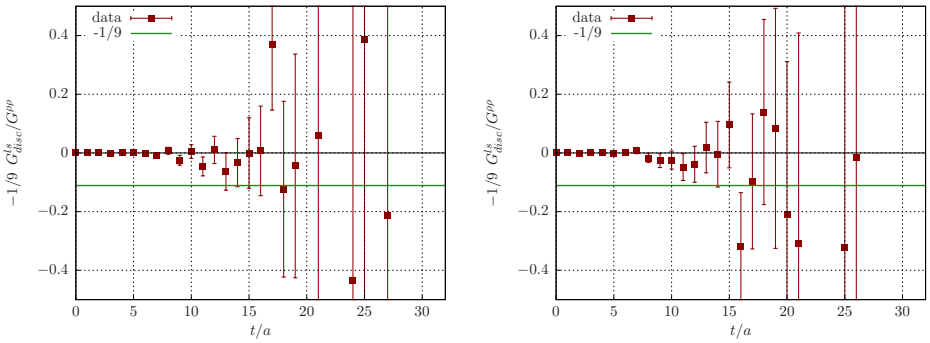

Figure C.3: The ratio of the disconnected correlator G^{ls}_{disc} and the ρ-correlator for the F6 (left) and F7 (right) ensemble. For both ensembles we choose $t_{cut} = 13a$ as the point up to which the disconnected contribution is neglected. The corresponding plot for the E5 ensemble is figure 9.5.

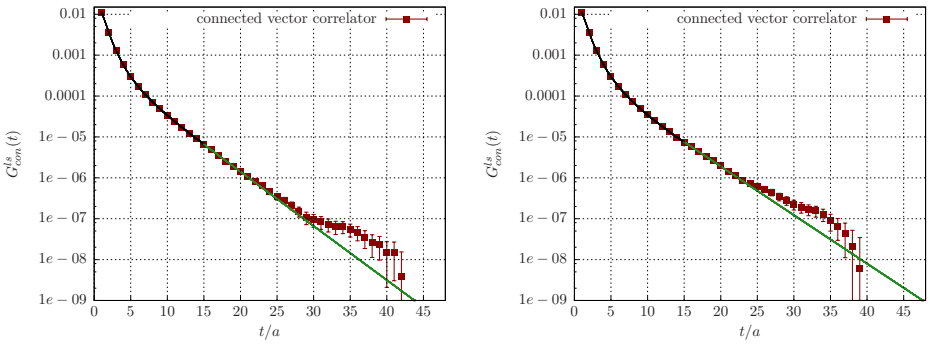

Figure C.4: The vector correlator for the F6 (left) and F7 (right) ensemble. The black line shows the interpolation with cubic splines, the green line the exponential fit. The corresponding plot for the E5 ensemble is figure 9.7.

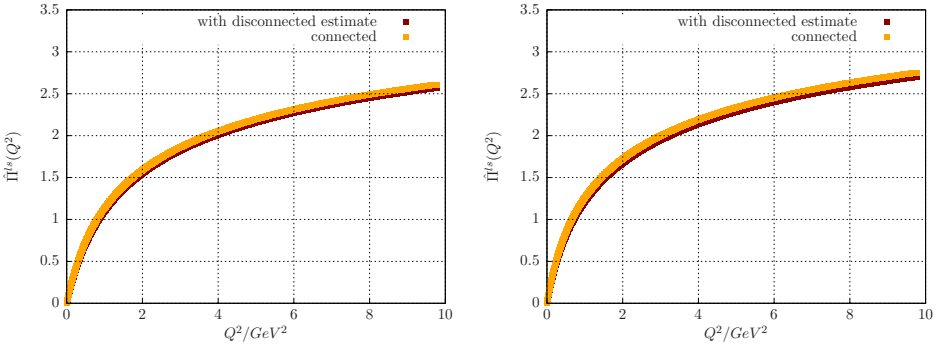

Figure C.5: The subtracted vacuum polarization for light and strange quarks with an estimate for the disconnected contribution (red) compared to the connected contribution alone for F6 (left) and F7 (right). The corresponding plot for the E5 ensemble is figure 9.9.

C.2 VECTOR MESON MASSES

The following plots show the results for the ρ- and ϕ-meson masses from our determination of the hadronic vacuum polarization. This masses have been obtained by fitting exponential functions of the form

$$f(t) = A\ \exp(-m \cdot t) \tag{C.1}$$

to the connected vector correlator for light and strange quarks for the ρ and the ϕ mass, respectively. The black points in both plots show the corresponding experimental value as quoted by the Particle Data Group [34]:

$$m_\rho = 775.26 \pm 0.25\ \text{MeV}\,, \qquad m_\phi = 1019.461 \pm 0.019\ \text{MeV}\,. \tag{C.2}$$

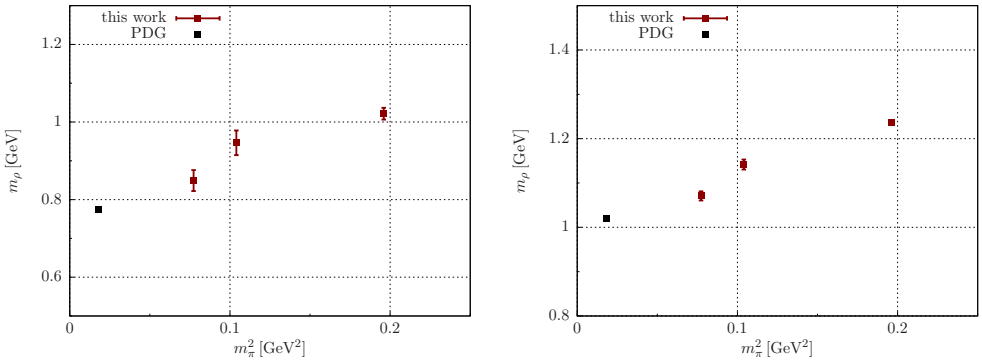

Figure C.6: The masses of the ρ (left) and the ϕ (right) mesons plotted against m_π^2. Red points show the results for E5, F6 and F7 obtained from fits to the vector correlators. The black points show the physical values from [34].

C.3 CONSERVED VECTOR CURRENT

For the calculation of the connected vector correlator a conserved vector current

$$V_\mu^c(x) = \frac{1}{2}\left(\bar{q}(x+a\hat{\mu})(1+\gamma_\mu)U_\mu^\dagger(x)\,q(x) - \bar{q}(x)(1-\gamma_\mu)U_\mu(x)\,q(x+a\hat{\mu})\right) \tag{C.3}$$

has been used at the sink. The connected contraction with a local current $V_\nu(x) = \bar{q}(x)\gamma_\nu q(x)$ at the source is given by

$$\begin{aligned}\left\langle V_\mu^c(x)\,V_\nu(0)\right\rangle_{\text{con}} = \text{Tr}\big[&\gamma_\nu\gamma_5\,S^\dagger(x+a\hat{\mu},0)\,\gamma_5(1+\gamma_\mu)U_\mu^\dagger(x)\,S(x,0)\\ &-\gamma_\nu\gamma_5\,S^\dagger(x,0)\,\gamma_5(1-\gamma_\mu)U_\mu(x)\,S(x+a\hat{\mu},0)\big]\,.\end{aligned} \tag{C.4}$$

The corresponding disconnected contraction is

$$\begin{aligned}\left\langle V_\mu^c(x)\,V_\nu(0)\right\rangle_{\text{disc}} =&\text{Tr}\big[(1+\gamma_\mu)\,U_\mu^\dagger(x)\,S(x,x+a\hat{\mu})\big]\cdot\text{Tr}\,\big[\gamma_\nu\,S(0,0)\big]\\ &-\text{Tr}\big[(1-\gamma_\mu)\,U_\mu(x)\,S(x+a\hat{\mu},x)\big]\cdot\text{Tr}\,\big[\gamma_\nu\,S(0,0)\big]\,.\end{aligned} \tag{C.5}$$

However, for the calculation of the disconnected vector correlator, we have used two local currents.

LIST OF FIGURES

LIST OF TABLES

BIBLIOGRAPHY

[1] V. Gülpers, G. von Hippel, and H. Wittig, "The scalar pion form factor with Wilson fermions," PoS **LATTICE2012**, 181 (2012).

[2] V. Gülpers, G. von Hippel, and H. Wittig, "The scalar radius of the pion in two-flavor Wilson lattice QCD ," PoS **LATTICE2013**, 283 (2013).

[3] V. Gülpers, G. von Hippel, and H. Wittig, "The scalar pion form factor in two-flavor lattice QCD," Phys.Rev. **D89**, 094503 (2014), arXiv:1309.2104.

[4] A. Francis, V. Gülpers, G. Herdoiza, H. Horch, B. Jäger, *et al.*, "The leading hadronic contribution to $(g-2)$ of the muon: The chiral behavior using the mixed representation method," PoS **LATTICE2014**, 127 (2014), arXiv:1410.7491.

[5] A. Francis, V. Gülpers, B. Jäger, H. Meyer, G. von Hippel, *et al.*, "The leading disconnected contribution to the anomalous magnetic moment of the muon," PoS **LATTICE2014**, 128 (2014), arXiv:1411.7592.

[6] A. Francis, V. Gülpers, G. Herdoíza, G. von Hippel, H. Horch, *et al.*, "Lattice QCD Studies of the Leading Order Hadronic Contribution to the Muon $g-2$," (2014), arXiv:1411.3031.

[7] G. Aad *et al.* (ATLAS Collaboration), "Observation of a new particle in the search for the Standard Model Higgs boson with the ATLAS detector at the LHC," Phys.Lett. **B716**, 1–29 (2012), arXiv:1207.7214.

[8] S. Chatrchyan *et al.* (CMS Collaboration), "Observation of a new boson at a mass of 125 GeV with the CMS experiment at the LHC," Phys.Lett. **B716**, 30–61 (2012), arXiv:1207.7235.

[9] P.W. Higgs, "Broken symmetries, massless particles and gauge fields," Phys.Lett. **12**, 132–133 (1964).

[10] F. Englert and R. Brout, "Broken Symmetry and the Mass of Gauge Vector Mesons," Phys.Rev.Lett. **13**, 321–323 (1964).

[11] G.S. Guralnik, C.R. Hagen, and T.W.B. Kibble, "Global Conservation Laws and Massless Particles," Phys.Rev.Lett. **13**, 585–587 (1964).

[12] S.L. Glashow, "Partial Symmetries of Weak Interactions," Nucl.Phys. **22**, 579–588 (1961).

[13] S. Weinberg, "A Model of Leptons," Phys.Rev.Lett. **19**, 1264–1266 (1967).

[14] A. Salam, "Weak and Electromagnetic Interactions," Conf.Proc. **C680519**, 367–377 (1968).

[15] D.J. Gross and F. Wilczek, "Ultraviolet Behavior of Nonabelian Gauge Theories," Phys.Rev.Lett. **30**, 1343–1346 (1973).

[16] K.G. Wilson, "Confinement of Quarks," Phys.Rev. **D10**, 2445–2459 (1974).

[17] S. Aoki *et al.* (JLQCD and TWQCD Collaborations), "Pion form factors from two-flavor lattice QCD with exact chiral symmetry," Phys. Rev. **D80**, 034508 (2009), arXiv:0905.2465.

[18] T. Kaneko *et al.* (JLQCD Collaboration, TWQCD collaboration), "Pion vector and scalar form factors with dynamical overlap quarks," PoS **LATTICE2008**, 158 (2008), arXiv:0810.2590.

[19] T. Kaneko, "Pion form factors from lattice QCD with exact chiral symmetry," PoS **CD09**, 011 (2009), arXiv:0911.5193.

[20] V. Gülpers, *Improved stochastic estimators for disconnected contributions to mesonic form factors in Lattice QCD*, Diploma thesis, JGU Mainz (2011), URL: `http://wwwkph.kph.uni-mainz.de/T//pub/diploma/Dipl_Th_Guelpers.pdf`.

[21] A. Jüttner, "Revisiting the pion's scalar form factor in chiral perturbation theory," JHEP **1201**, 007 (2012), arXiv:1110.4859.

[22] A. Jüttner, "Quark disconnected diagrams in chiral perturbation theory - the scalar form factor," PoS **LATTICE2012**, 196 (2012), arXiv:1212.2559.

[23] J. Gasser and H. Leutwyler, "Chiral Perturbation Theory to One Loop," Annals Phys. **158**, 142 (1984).

[24] J.F. Donoghue, J. Gasser, and H. Leutwyler, "The Decay of a light Higgs Boson," Nucl. Phys. **B343**, 341–368 (1990).

[25] J. Gasser and U.G. Meissner, "Chiral expansion of pion form-factors beyond one loop," Nucl.Phys. **B357**, 90–128 (1991).

[26] B. Moussallam, "N_f dependence of the quark condensate from a chiral sum rule," Eur. Phys. J. **C14**, 111–122 (2000), arXiv:hep-ph/9909292.

[27] G. Colangelo, J. Gasser, and H. Leutwyler, "$\pi\pi$ scattering," Nucl. Phys. **B603**, 125–179 (2001), arXiv:hep-ph/0103088.

[28] J. Gasser and H. Leutwyler, "Low-Energy Theorems as Precision Tests of QCD," Phys. Lett. **B125**, 325 (1983).

[29] A. Jüttner and M. Della Morte, "New ideas for $g-2$ on the lattice," PoS **LAT2009**, 143 (2009), arXiv:0910.3755.

[30] M. Della Morte and A. Jüttner, "Quark disconnected diagrams in chiral perturbation theory," JHEP **1011**, 154 (2010), arXiv:1009.3783.

[31] D. Bernecker and H.B. Meyer, "Vector Correlators in Lattice QCD: Methods and applications," Eur.Phys.J. **A47**, 148 (2011), arXiv:1107.4388.

[32] A. Francis, B. Jäger, H.B. Meyer, and H. Wittig, "A new representation of the Adler function for lattice QCD," Phys.Rev. **D88**, 054502 (2013), arXiv:1306.2532.

[33] X. Feng, S. Hashimoto, G. Hotzel, K. Jansen, M. Petschlies, *et al.*, "Computing the hadronic vacuum polarization function by analytic continuation," Phys.Rev. **D88**, 034505 (2013), arXiv:1305.5878.

[34] K.A. Olive *et al.* (Particle Data Group), "Review of Particle Physics," Chin.Phys. **C38**, 090001 (2014).

[35] M.E. Peskin and D.V. Schröder, *An Introduction to Quantum Field Theory* (Westview Press, 1995).

[36] S. Weinberg, *The Quantum Theory of Fields II* (Cambridge University Press, 1995).

[37] J. Goldstone, A. Salam, and S. Weinberg, "Broken Symmetries," Phys.Rev. **127**, 965–970 (1962).

[38] C. Gattringer and C.B. Lang, *Quantum Chromodynamics on the Lattice* (Springer, 2010).

[39] I. Montvay and G. Münster, *Quantum Fields on a Lattice* (Cambridge University Press, 1994).

[40] H.J. Rothe, *Lattice Gauge Theories* (World Scientific, 1997).

[41] J. Smit, *Introduction to Quantum Fields on a Lattice* (Cambridge University Press, 2002).

[42] H.B. Nielsen and M. Ninomiya, "A no-go theorem for regularizing chiral fermions," Physics Letters B **105**, 219 – 223 (1981).

[43] L. Susskind, "Lattice Fermions," Phys.Rev. **D16**, 3031–3039 (1977).

[44] P.H. Ginsparg and K.G. Wilson, "A Remnant of Chiral Symmetry on the Lattice," Phys.Rev. **D25**, 2649 (1982).

[45] K. Symanzik, "Continuum Limit and Improved Action in Lattice Theories," Nucl.Phys. **B226**, 187 (1983).

[46] B. Sheikholeslami and R. Wohlert, "Improved Continuum Limit Lattice Action for QCD with Wilson Fermions," Nucl.Phys. **B259**, 572 (1985).

[47] M. Lüscher, S. Sint, R. Sommer, and P. Weisz, "Chiral symmetry and O(a) improvement in lattice QCD," Nucl.Phys. **B478**, 365–400 (1996), arXiv:hep-lat/9605038.

[48] M. Lüscher, S. Sint, R. Sommer, P. Weisz, and U. Wolff, "Nonperturbative O(a) improvement of lattice QCD," Nucl.Phys. **B491**, 323–343 (1997), arXiv:hep-lat/9609035.

[49] K. Jansen and R. Sommer (ALPHA collaboration), "O(a) improvement of lattice QCD with two flavors of Wilson quarks," Nucl.Phys. **B530**, 185–203 (1998), arXiv:hep-lat/9803017.

[50] M. Lüscher, "Computational Strategies in Lattice QCD," (2010), arXiv:1002.4232.

[51] M. Lüscher, "Solution of the Dirac equation in lattice QCD using a domain decomposition method," Comput.Phys.Commun. **156**, 209–220 (2004), arXiv:hep-lat/0310048.

[52] M. Lüscher, "Schwarz-preconditioned HMC algorithm for two-flavour lattice QCD," Comput.Phys.Commun. **165**, 199–220 (2005), arXiv:hep-lat/0409106.

[53] S. Duane, A.D. Kennedy, B.J. Pendleton, and D. Roweth, "Hybrid Monte Carlo," Phys.Lett. **B195**, 216–222 (1987).

[54] S. Capitani, M. Della Morte, G. von Hippel, B. Knippschild, and H. Wittig, "Scale setting via the Ω baryon mass," PoS **LATTICE2011**, 145 (2011), arXiv:1110.6365.

[55] P. Fritzsch, F. Knechtli, B. Leder, M. Marinkovic, S. Schaefer, *et al.*, "The strange quark mass and Lambda parameter of two flavor QCD," Nucl. Phys. **B865**, 397–429 (2012), arXiv:1205.5380.

[56] T. Draper, R.M. Woloshyn, W. Wilcox, and K.-F. Liu, "The Pion Form Factor in Lattice QCD," Nucl.Phys. **B318**, 319 (1989).

[57] S. Gusken, "A Study of smearing techniques for hadron correlation functions," Nucl.Phys.Proc.Suppl. **17**, 361–364 (1990).

[58] S. Güsken, U. Löw, K.H. Mütter, R. Sommer, A. Patel, *et al.*, "Nonsinglet Axial Vector Couplings of the Baryon Octet in Lattice QCD," Phys. Lett. **B227**, 266 (1989).

[59] C. Alexandrou, F. Jegerlehner, S. Güsken, K. Schilling, and R. Sommer, "B meson properties from lattice QCD," Phys. Lett. **B256**, 60–67 (1991).

[60] C.R. Allton *et al.* (UKQCD Collaboration), "Gauge invariant smearing and matrix correlators using Wilson fermions at Beta = 6.2," Phys. Rev. **D47**, 5128–5137 (1993), arXiv:hep-lat/9303009.

[61] B. Jäger, *Hadronic Matrix Elements in Lattice QCD*, Phd thesis, Universität Mainz (2013), URL: `http://ubm.opus.hbz-nrw.de/volltexte/2014/3741/pdf/doc.pdf`.

[62] G. Martinelli and C.T. Sachrajda, "A Lattice Study of Nucleon Structure," Nucl.Phys. **B316**, 355 (1989).

[63] K. Bitar, A.D. Kennedy, R. Horsley, S. Meyer, and P. Rossi, "The QCD Finite Temperature Transition and Hybrid Monte Carlo," Nucl.Phys. **B313**, 348–376 (1989).

[64] S. Bernardson, P. McCarty, and C. Thron, "Monte Carlo methods for estimating linear combinations of inverse matrix entries in lattice QCD," Comput.Phys.Commun. **78**, 256–264 (1993).

[65] S.-J. Dong and K.F. Liu, "Stochastic estimation with Z(2) noise," Phys.Lett. **B328**, 130–136 (1994), arXiv:hep-lat/9308015.

[66] W. Wilcox and B. Lindsay, "Disconnected loop noise methods in lattice QCD," Nucl.Phys.Proc.Suppl. **63**, 973–975 (1998), arXiv:hep-lat/9708028.

[67] G.S. Bali, S. Collins, and A. Schäfer, "Effective noise reduction techniques for disconnected loops in Lattice QCD," Comput.Phys.Commun. **181**, 1570–1583 (2010), arXiv:0910.3970.

[68] E. Endress, A. Jüttner, and H. Wittig, "On the efficiency of stochastic volume sources for the determination of light meson masses," (2011), arXiv:1111.5988.

[69] C. McNeile and C. Michael (UKQCD Collaboration), "Decay width of light quark hybrid meson from the lattice," Phys.Rev. **D73**, 074506 (2006), arXiv:hep-lat/0603007.

[70] W. Wilcox, "Noise methods for flavor singlet quantities," , 127–141(1999), arXiv:hep-lat/9911013.

[71] R. Babich, R. Brower, M. Clark, G. Fleming, J. Osborn, *et al.*, "Strange quark contribution to nucleon form-factors," PoS **LAT2007**, 139 (2007), arXiv:0710.5536.

[72] S. Collins, G. Bali, and A. Schäfer, "Disconnected contributions to hadronic structure: a new method for stochastic noise reduction," PoS **LAT2007**, 141 (2007), arXiv:0709.3217.

[73] L. Giusti, P. Hernandez, M. Laine, P. Weisz, and H. Wittig, "Low-energy couplings of QCD from current correlators near the chiral limit," JHEP **0404**, 013 (2004), arXiv:hep-lat/0402002.

[74] H. Neff, N. Eicker, T. Lippert, J. Negele, and K. Schilling, "On the low fermionic eigenmode dominance in QCD on the lattice," Phys.Rev. **D64**, 114509 (2001), arXiv:hep-lat/0106016.

[75] G.S. Bali, H. Neff, T. Duessel, T. Lippert, and K. Schilling (SESAM Collaboration), "Observation of string breaking in QCD," Phys.Rev. **D71**, 114513 (2005), arXiv:hep-lat/0505012.

[76] C. Thron, S.J. Dong, K.F. Liu, and H.P. Ying, "Pade - Z(2) estimator of determinants," Phys.Rev. **D57**, 1642–1653 (1998), arXiv:hep-lat/9707001.

[77] M. Lüscher, "Implementation of the lattice Dirac operator," (2006), unpublished notes.

[78] S. Lemcke, *Charmonium Spektroskopie mit stochastischen Propagatoren in der Gitterfeld-Quantenchromodynamik*, Bachelor thesis, Universität Mainz (2013).

[79] R.P. Feynman, "Forces in molecules," Phys. Rev. **56**, 340–343 (Aug 1939), `http://link.aps.org/doi/10.1103/PhysRev.56.340`.

[80] J. Bijnens, G. Colangelo, and P. Talavera, "The Vector and scalar form-factors of the pion to two loops," JHEP **9805**, 014 (1998), arXiv:hep-ph/9805389.

[81] M. Foster and C. Michael (UKQCD Collaboration), "Quark mass dependence of hadron masses from lattice QCD," Phys.Rev. **D59**, 074503 (1999), arXiv:hep-lat/9810021.

[82] S. Capitani, C. Gattringer, and C.B. Lang (Bern-Graz-Regensburg (BGR) Collaboration), "A Lattice calculation of the pion form-factor with Ginsparg-Wilson-type fermions," Phys. Rev. **D73**, 034505 (2006), arXiv:hep-lat/0511040.

[83] D. Brömmel *et al.* (QCDSF/UKQCD Collaboration), "The Pion form-factor from lattice QCD with two dynamical flavours," Eur. Phys. J. **C51**, 335–345 (2007), arXiv:hep-lat/0608021.

[84] F.-J. Jiang and B.C. Tiburzi, "Flavor twisted boundary conditions, pion momentum, and the pion electromagnetic form-factor," Phys. Lett. **B645**, 314–321 (2007), arXiv:hep-lat/0610103.

[85] T. Kaneko *et al.* (JLQCD Collaboration), "Pion form-factor from all-to-all propagators of overlap quarks," PoS **LAT2007**, 148 (2007), arXiv:0710.2390.

[86] C. Alexandrou and G. Koutsou, "Pion and rho-meson form-factors using four-point functions in N(F) = 2 QCD," PoS **LAT2007**, 150 (2007), arXiv:0710.2441.

[87] P.A. Boyle, J.M. Flynn, A. Jüttner, C. Kelly, H.P. de Lima, *et al.*, "The Pion's electromagnetic form-factor at small momentum transfer in full lattice QCD," JHEP **0807**, 112 (2008), arXiv:0804.3971.

[88] R. Frezzotti, V. Lubicz, and S. Simula (ETM Collaboration), "Electromagnetic form factor of the pion from twisted-mass lattice QCD at $N_f = 2$," Phys.Rev. **D79**, 074506 (2009), arXiv:0812.4042.

[89] O.H. Nguyen, K.I. Ishikawa, A. Ukawa, and N. Ukita, "Electromagnetic form factor of pion from $N_f = 2 + 1$ dynamical flavor QCD," JHEP **1104**, 122 (2011), arXiv:1102.3652.

[90] H. Fukaya *et al.* (JLQCD Collaboration), "Pion form factors in the epsilon regime," PoS **LATTICE2012**, 198 (2012), arXiv:1211.0743.

[91] B.B. Brandt, A. Jüttner, and H. Wittig, "The electromagnetic form factor of the pion in two-flavour lattice QCD," PoS **ConfinementX**, 112 (2012), arXiv:1301.3513.

[92] B.B. Brandt, A. Jüttner, and H. Wittig, "The pion vector form factor from lattice QCD and NNLO chiral perturbation theory," JHEP **1311**, 034 (2013), arXiv:1306.2916.

[93] J. Koponen, F. Bursa, C. Davies, G. Donald, and R. Dowdall, "Pion electromagnetic form factor from full lattice QCD," PoS **LAT2013**, 282 (2013), arXiv:1311.3513.

[94] C.T. Sachrajda and G. Villadoro, "Twisted boundary conditions in lattice simulations," Phys.Lett. **B609**, 73–85 (2005), arXiv:hep-lat/0411033.

[95] J. Flynn, A. Jüttner, C. Sachrajda, and G. Villadoro, "Partially twisted boundary conditions in lattice simulations," PoS **LAT2005**, 352 (2006), arXiv:hep-lat/0509093.

[96] NA7 Collaboration, "A measurement of the space-like pion electromagnetic form factor," Nuclear Physics B **277**, 168 – 196 (1986).

[97] S. Scherer and M.R. Schindler, *A Primar for Chiral Perturbation Theory* (Springer-Verlag Berlin Heidelberg, 2012).

[98] S. Aoki, Y. Aoki, C. Bernard, T. Blum, G. Colangelo, *et al.*, "Review of lattice results concerning low energy particle physics," (2013), arXiv:1310.8555.

[99] C.W. Bernard and M.F.L. Golterman, "Chiral perturbation theory for the quenched approximation of QCD," Phys.Rev. **D46**, 853–857 (1992), arXiv:hep-lat/9204007.

[100] C.W. Bernard and M.F.L. Golterman, "Partially quenched gauge theories and an application to staggered fermions," Phys.Rev. **D49**, 486–494 (1994), arXiv:hep-lat/9306005.

[101] S.R. Sharpe and N. Shoresh, "Physical results from unphysical simulations," Phys.Rev. **D62**, 094503 (2000), arXiv:hep-lat/0006017.

[102] P.A. Boyle, J.M. Flynn., A. Jüttner, C.T. Sachrajda, and J.M. Zanotti, "Hadronic form factors in Lattice QCD at small and vanishing momentum transfer," JHEP **0705**, 016 (2007), arXiv:hep-lat/0703005.

[103] B. Knippschild, *Baryons in the chiral regime*, Phd thesis, Universität Mainz (2012), URL: `http://ubm.opus.hbz-nrw.de/volltexte/2012/3068/pdf/doc.pdf`.

[104] S. Capitani, M. Della Morte, G. von Hippel, B. Jäger, B. Knippschild, *et al.*, "Excited state systematics in extracting nucleon electromagnetic form factors from the lattice," PoS **ConfinementX**, 321 (2012).

[105] C. Davies, private communication (2014).

[106] A. Bazavov *et al.* (MILC Collaboration), "Lattice QCD ensembles with four flavors of highly improved staggered quarks," Phys.Rev. **D87**, 054505 (2013), arXiv:1212.4768.

[107] G.P. Lepage, "Flavor symmetry restoration and Symanzik improvement for staggered quarks," Phys.Rev. **D59**, 074502 (1999), arXiv:hep-lat/9809157.

[108] F.D.R. Bonnet, R.G. Edwards, G.T. Fleming, R. Lewis, and D.G. Richards (LHP Collaboration), "Lattice computations of the pion form-factor," Phys. Rev. **D72**, 054506 (2005), arXiv:hep-lat/0411028.

[109] G.P. Lepage, TASI 89 Summer School, Boulder, CO, Jun 4-30, 198.

[110] M. Della Morte and B. Jäger and T. Rae and H. Wittig, "Improved interpolating fields for hadrons at non-vanishing momentum," PoS **LATTICE2012**, 260 (2012), arXiv:1211.1288.

[111] M. Della Morte, B. Jäger, T. Rae, and H. Wittig, "Improved interpolating fields for hadrons at non-zero momentum," Eur.Phys.J. **A48**, 139 (2012), arXiv:1208.0189.

[112] F. Bernardoni, N. Garron, P. Hernandez, S. Necco, and C. Pena, "Light quark correlators in a mixed-action setup," PoS **LATTICE2011**, 109 (2011), arXiv:1110.0922.

[113] T.W. Chiu, T.H. Hsieh, and Y.-Y. Mao (TWQCD Collaboration), "Pseudoscalar Meson in Two Flavors QCD with the Optimal Domain-Wall Fermion," Phys.Lett. **B717**, 420–424 (2012), arXiv:1109.3675.

[114] R. Baron *et al.* (ETM Collaboration), "Light Meson Physics from Maximally Twisted Mass Lattice QCD," JHEP **1008**, 097 (2010), arXiv:0911.5061.

[115] J. Noaki *et al.* (JLQCD Collaboration, TWQCD Collaboration), "Convergence of the chiral expansion in two-flavor lattice QCD," Phys.Rev.Lett. **101**, 202004 (2008), arXiv:0806.0894.

[116] M. Bruno, D. Djukanovic, G.P. Engel A. Francis, G. Herdoiza, *et al.*, "Simulation of QCD with $N_f = 2 + 1$ flavors of non-perturbatively improved Wilson fermions," (2014), arXiv:1411.3982.

[117] F. Jegerlehner and A. Nyffeler, "The Muon $g-2$," Phys.Rept. **477**, 1–110 (2009), arXiv:0902.3360.

[118] G.W. Bennett *et al.* (Muon G-2 Collaboration), "Final Report of the Muon E821 Anomalous Magnetic Moment Measurement at BNL," Phys.Rev. **D73**, 072003 (2006), arXiv:hep-ex/0602035.

[119] J. Schwinger, "On quantum-electrodynamics and the magnetic moment of the electron," Phys. Rev. **73**, 416–417 (Feb 1948), `http://link.aps.org/doi/10.1103/PhysRev.73.416`.

[120] T. Aoyama, M. Hayakawa, T. Kinoshita, and M. Nio, "Complete Tenth-Order QED Contribution to the Muon $g-2$," Phys.Rev.Lett. **109**, 111808 (2012), arXiv:1205.5370.

[121] C. Gnendiger, D. Stöckinger, and H. Stöckinger-Kim, "The electroweak contributions to $(g-2)_\mu$ after the Higgs boson mass measurement," Phys.Rev. **D88**, 053005 (2013), arXiv:1306.5546.

[122] S.J. Brodsky and E. De Rafael, "Suggested boson - lepton pair couplings and the anomalous magnetic moment of the muon," Phys.Rev. **168**, 1620–1622 (1968).

[123] M. Davier, A. Hoecker, B. Malaescu, and Z. Zhang, "Reevaluation of the Hadronic Contributions to the Muon $g-2$ and to $\alpha(M_Z)$," Eur.Phys.J. **C71**, 1515 (2011), arXiv:1010.4180.

[124] K. Hagiwara, R. Liao, A.D. Martin, D. Nomura, and T. Teubner, "$(g-2)_\mu$ and $\alpha(M_Z^2)$ re-evaluated using new precise data," J.Phys. **G38**, 085003 (2011), arXiv:1105.3149.

[125] F. Burger, X. Feng, G. Hotzel, K. Jansen, M. Petschlies, *et al.*, "Four-Flavour Leading-Order Hadronic Contribution To The Muon Anomalous Magnetic Moment," (2013), doi:\bibinfo{doi}{10.1007/JHEP02(2014)099}, arXiv:1308.4327.

[126] P. Boyle, L. Del Debbio, E. Kerrane, and J. Zanotti, "Lattice Determination of the Hadronic Contribution to the Muon $g-2$ using Dynamical Domain Wall Fermions," Phys.Rev. **D85**, 074504 (2012), arXiv:1107.1497.

[127] M. Della Morte, B. Jäger, A. Jüttner, and H. Wittig, "Towards a precise lattice determination of the leading hadronic contribution to $(g-2)_\mu$," JHEP **1203**, 055 (2012), arXiv:1112.2894.

[128] J. Prades, E. de Rafael, and A. Vainshtein, "Hadronic Light-by-Light Scattering Contribution to the Muon Anomalous Magnetic Moment," (2009), arXiv:0901.0306.

[129] M. Hayakawa, T. Blum, T. Izubuchi, and N. Yamada, "Hadronic light-by-light scattering contribution to the muon $g-2$ from lattice QCD: Methodology," PoS **LAT2005**, 353 (2006), arXiv:hep-lat/0509016.

[130] T. Blum, M. Hayakawa, and T. Izubuchi, "Hadronic light-by-light scattering contribution to the muon anomalous magnetic moment from lattice QCD," (2014), arXiv:1407.2923.

[131] H. Merkel *et al.* (A1 Collaboration), "Search for Light Gauge Bosons of the Dark Sector at the Mainz Microtron," Phys.Rev.Lett. **106**, 251802 (2011), arXiv:1101.4091.

[132] T. Beranek, H. Merkel, and M. Vanderhaeghen, "Theoretical framework to analyze searches for hidden light gauge bosons in electron scattering fixed target experiments," Phys.Rev. **D88**, 015032 (2013), arXiv:1303.2540.

[133] G. Venanzoni (Fermilab E989 Collaboration), "The new muon $g-2$ experiment at Fermilab," Nucl.Phys.Proc.Suppl. **225-227**, 277–281 (2012).

[134] B.E. Lautrup and E. De Rafael, "Calculation of the sixth-order contribution from the fourth-order vacuum polarization to the difference of the anomalous magnetic moments of muon and electron," Phys.Rev. **174**, 1835–1842 (1968).

[135] T. Blum, "Lattice calculation of the lowest order hadronic contribution to the muon anomalous magnetic moment," Phys.Rev.Lett. **91**, 052001 (2003), arXiv:hep-lat/0212018.

[136] M. Göckeler *et al.* (QCDSF Collaboration), "Vacuum polarization and hadronic contribution to muon $g-2$ from lattice QCD," Nucl.Phys. **B688**, 135–164 (2004), arXiv:hep-lat/0312032.

[137] C. Aubin and T. Blum, "Calculating the hadronic vacuum polarization and leading hadronic contribution to the muon anomalous magnetic moment with improved staggered quarks," Phys.Rev. **D75**, 114502 (2007), arXiv:hep-lat/0608011.

[138] D.B. Renner, X. Feng, K. Jansen, and M. Petschlies (ETM Collaboration), "Leading order hadronic contribution to $g-2$ from twisted mass QCD," PoS **LATTICE2010**, 155 (2010), arXiv:1011.4231.

[139] X. Feng, K. Jansen, M. Petschlies, and D.B. Renner, "Two-flavor QCD correction to lepton magnetic moments at leading-order in the electromagnetic coupling," Phys.Rev.Lett. **107**, 081802 (2011), arXiv:1103.4818.

[140] M. Della Morte, B. Jäger, A. Jüttner, and H. Wittig, "Lattice calculations of the leading hadronic contribution to $(g-2)_\mu$," PoS **LATTICE2012**, 175 (2012), arXiv:1211.1159.

[141] F. Burger, X. Feng, G. Hotzel, K. Jansen, M. Petschlies, *et al.*, "Leading-order hadronic contribution to the anomalous magnetic moment of the muon from $N_f = 2+1+1$ twisted mass fermions," PoS **LATTICE2013**, 301 (2013), arXiv:1311.3885.

[142] E.B. Gregory, Z. Fodor, C. Hoelbling, S. Krieg, L. Lellouch, *et al.*, "Leading-order hadronic contributions to $g_\mu - 2$," (2013), arXiv:1311.4446.

[143] C. Aubin, T. Blum, M. Golterman, and S. Peris, "Model-independent parametrization of the hadronic vacuum polarization and $g-2$ for the muon on the lattice," Phys.Rev. **D86**, 054509 (2012), arXiv:1205.3695.

[144] M. Golterman, K. Maltman, and S. Peris, "Tests of hadronic vacuum polarization fits for the muon anomalous magnetic moment," Phys.Rev. **D88**, 114508 (2013), arXiv:1309.2153.

[145] K. Jansen, private communication (2014).

[146] M. Della Morte, R. Hoffmann, F. Knechtli, R. Sommer, and U. Wolff, "Non-perturbative renormalization of the axial current with dynamical Wilson fermions," JHEP **0507**, 007 (2005), arXiv:hep-lat/0505026.

[147] H. Meyer, private communication (2014).

[148] B. Chakraborty, C.T.H. Davies, G.C. Donald, R.J. Dowdall, J. Koponen, *et al.*, "Strange and charm quark contributions to the anomalous magnetic moment of the muon," (2014), arXiv:1403.1778.

[149] T. Falk, A. Ferstl, and K.A. Olive, "New contributions to neutralino elastic cross-sections from CP violating phases in the MSSM," Phys.Rev. **D59**, 055009 (1999), arXiv:hep-ph/9806413.

[150] A.W. Thomas, "Overview of Issues Surrounding Strangeness in the Nucleon," AIP Conf.Proc. **1182**, 933–936 (2009), arXiv:0907.4916.

[151] F. Jegerlehner, "Hadronic Contributions to Electroweak Parameter Shifts: A Detailed Analysis," Z.Phys. **C32**, 195 (1986).

[152] B. Efron, "Bootstrap methods: Another look at the jackknife," Ann. Statist. **7**, 1–26 (01 1979), http://dx.doi.org/10.1214/aos/1176344552.